Electrochemical biosensor development for enhanced detection of pathogens which cause sepsis and hyperinflammation

PhD Thesis

Vincent Vezza

Research Group

Biomedical Engineering

University of Strathclyde, Glasgow

August 3, 2021

This thesis is the result of the author's original research. It has been composed by the author and has not been previously submitted for examination which has led to the award of a degree.

Signed: 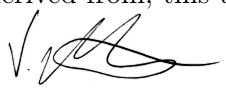

Date: 3/8/2021

Abstract

Sepsis represents a significant and growing challenge within modern healthcare settings. It can deteriorate quickly, potentially leading to fatality. The common characteristic to all sepsis patients is the importance of pathogen identification. Currently, pathogen detection is lengthy (hours to days) and as such is detrimental to patient outcome. Rapid pathogen detection will aid clinicians in source control and help guide targeted treatment in shorter time scales giving patients the best chances for recovery.

Electrochemical biosensors have potential to offer a route to rapid, low cost, multiplexed pathogen identification. The work presented in this thesis represents a series of investigations made to apply electrochemical methods to rapid pathogen detection at the point of care.

The first section presents a literature review exploring sepsis, current detection methods employed and identifying the requirements of an electrochemical biosensor for pathogen detection.

The second section details investigations into suitable platforms on which to construct electrochemical biosensors. Various electrode platforms were investigated and the results from these experiments were used to design custom 'printed circuit board' electrodes.

The ability to form sensing layers composed of biorecognition elements on printed circuit board electrode surfaces is then demonstrated using *Streptococcus pneumoniae* genomic DNA to form a *S. pneumoniae* recognition surface. *lytA* was detectable on this *S. pneumoniae* DNA biosensor in serum samples at 1 pM after 15 minutes of sample

addition at room temperature.

Finally, the development of a simple enzyme-based sensor for SARS-CoV-2 is demonstrated. Detection performances are described for multiple positive and negative controls culminating in clinical sample testing. Viral PCR sample solution clinical samples are shown to be statistically different from a negative sample (P = 1.2E-7). Viral transport medium clinical samples showed multiple positive and negative samples were significantly different with preliminary calculations showing a sensitivity = 80 % and specificity = 67 %.

Acknowledgements

I would like to express my special thanks of gratitude to my supervisor Dr Damion Corrigan for affording me the opportunity to work in his research group. Thank you for your guidance, advice and always having more ideas when I hit brick walls. Also thank you for the many proof-readings of my work. I would also like to thank my second supervisor, Prof. Paul A Hoskisson, for advising and teaching microbiological aspects. I am grateful to Dr David Alcorn for his clinical input giving invaluable advice from a different perspective. For general help and camaraderie I would like to thank my colleagues Paul Williamson, Bukola Omolaiye and with special thanks to Adrian Butterworth, Dr Stuart Hannah, Dr Ewen Blair, Sandy MacDonald and Perrine Lasserre for their help with COVID-19 work and their sense of humour during very difficult times. For allowing access to COVID-19 clinical samples at the Clinical Microbiology Department at Glasgow Royal Infirmary I would like to thank Dr Michael E Murphy, Dr Eoghan Farmer, Fiona Turner, Sandra Higgins and the entire team for helping me test the samples. I would also like to gratefully acknowledge the support of NHS Research Scotland (NRS) Greater Glasgow and Clyde Biorepository. I would also like to thank Dr Simon Evans for his clinical input and review of the section regarding covid-19. A special thank you to Prof. Glenn Burley and Dr Andrea Taladriz Sender for allowing me to work in their lab and giving me invaluable guidance on unique fluorous chemistries. For dealing with many tedious and laborious administrative issues I would like to thank Carol McInnes and Thomas Milne. For helping design and fabricate PCBs I would like to thank Steve Cartwright. To all my friends and family I apologise for being insufferable and thank you for helping me get through this thesis, it was hard work for

you as well as me. I'm sure you never thought I would get here with my obstacles and my encounter with *Neisseria meningitidis*. Thank you to the small subset of reviewers of our paper publications that gave critical yet constructive feedback.

CDT Medical Devices, University of Strathclyde Funded by EPSRC, grant reference number EP/L015595/1

Publications

Papers published from work reported in this thesis

Vezza, Vincent, Adrian Butterworth, Perrine Lasserre, Ewen O. Blair, Alexander MacDonald, Stuart Hannah, Christopher Rinaldi, Paul A. Hoskisson Andrew C. Ward, Alastair Longmuir, Steven Setford, Michael E, Murphy, Damion Corrigan. "An electrochemical SARS-CoV-2 biosensor inspired by glucose test strip manufacturing processes." Chemical Communications (2021).

Vezza, Vincent, Adrian Butterworth, Perrine Lasserre, Ewen O. Blair, Alexander MacDonald, Stuart Hannah, Christopher Rinaldi, Paul A. Hoskisson Andrew C. Ward, Alastair Longmuir, Steven Setford, Michael E, Murphy, Damion Corrigan. "An uncomplicated electrochemical sensor combining a perfluorocarbon SAM and ACE2 as the bio-recognition element to sensitively and specifically detect SARS-CoV-2 in complex samples." Chemarxiv (2020).

Vezza, Vincent, Paul A. Hoskisson., David Alcorn, Damion Corrigan. "Rapid, label free electrochemical detection of *Streptococcus pneumoniae* using *lytA* gene sequences." in preparation, (2021).

Papers published using work not reported in this thesis

Blair, Ewen O., Stuart Hannah, Vincent Vezza, Hüseyin Avcı, Tanil Kocagoz, Paul A. Hoskisson, Fatma D. Güzel and Damion K. Corrigan. "Biologically modified microelectrode sensors provide enhanced sensitivity for detection of nucleic acid sequences from

Mycobacterium tuberculosis." *Sensors and Actuators* Reports 2, no. 1 (2020): 100008.

Corrigan, Damion K., Vincent Vezza, Holger Schulze, Till T. Bachmann andrew R. Mount, Anthony J. Walton and Jonathan G. Terry. "A microelectrode array with reproducible performance shows loss of consistency following functionalization with a self-assembled 6-mercapto-1-hexanol layer." *Sensors* 18, no. 6 (2018): 1891

Crossley, Lisa, Bukola Attoye, Vincent Vezza, Ewen Blair, Damion K. Corrigan and Stuart Hannah. "Establishing a Field-Effect Transistor Sensor for the Detection of Mutations in the Tumour Protein 53 Gene (TP53)—An Electrochemical Optimisation Approach." *Biosensors* 9, no. 4 (2019): 141.

Russell, Christopher Andrew C. Ward, Vincent Vezza, Paul Hoskisson, David Alcorn, D. Paul Steenson and Damion K. Corrigan. "Development of a needle shaped microelectrode for electrochemical detection of the sepsis biomarker interleukin-6 (IL-6) in real time." *Biosensors and Bioelectronics* 126 (2019): 806-814

Contents

List of Figures

List of Figures

List of Figures

List of Tables

List of Tables

List of Tables

Chapter 1

Literature Review

Epidemiology

Sepsis is a severe medical emergency that provides a significant challenge to clinicians and health care systems. The lethality of sepsis is compounded by poor awareness in the general population as well as the difficulty in detecting the condition and the course it is taking promptly. Each path that sepsis can progress along requires differing therapies. It is a challenging condition to define and therefore treat. Currently, it has gone through three major definition iterations. The first of which was introduced at the 1991 Consensus Conference [1]. It split sepsis into four stages (Systemic inflammatory response syndrome (SIRS), Sepsis, Severe sepsis and finally, Septic shock). The second was introduced at the 2001 International sepsis definitions conference [2]. In this iteration more signs and symptoms were added to each stage due to research that concluded there were larger variations in the signs and symptoms. Since then the four stage approach has proven to be sub-optimal in diagnosis and reporting of the disease, as a consequence, at the 2016 Third International Consensus Definitions for Sepsis and Septic Shock [3] the definitions were reduced and streamlined. Now there are only two stages (Sepsis and Septic shock). A summary of the various conferences and definitions is shown in (Figure 1.1).

1991 Consensus Conference

Diagnosis	Signs and symptoms
Systemic inflammatory response syndrome	Patients experiencing at least two of the following symptoms: • Body temperature >38 °C or <36 °C • Heart rate >90 beats per minute • Respiratory rate >20 breaths per minute or arterial CO_2 <32 mmHg • White blood cell count >12 × 10^9 l^{-1} or <4 × 10^9 l^{-1}, or >10% immature forms
Sepsis	Systemic inflammatory response syndrome and proven or suspected infection
Severe sepsis	Sepsis and acute organ dysfunction
Septic shock	Sepsis and persistent hypotension after fluid resuscitation

2001 International Sepsis Definitions Conference

The 2001 definitions of sepsis were very similar to the definitions stated in 1991. Of note, in 2001 it was acknowledged that the signs and symptoms of sepsis are more varied than described in the 1991 definition, and this resulted in the addition of a list of these signs and symptoms for the diagnosis of sepsis.

2016 Third International Consensus Definitions for Sepsis and Septic Shock (Sepsis-3)

Diagnosis	Signs
Sepsis*	• Life-threatening organ dysfunction caused by a dysregulated host response to infection • Organ dysfunction can be identified as an acute change in total SOFA score of ≥2 points‡
Septic shock	• Sepsis in which the underlying circulatory and cellular and/or metabolic abnormalities are marked enough to substantially increase mortality • Clinically defined as sepsis with persisting hypotension that requires vasopressors to maintain the mean arterial pressure at ≥65 mmHg and with a serum lactate concentration >2 mmol l^{-1}

*Of note, the presence of organ dysfunction is central and required in the new 2016 consensus sepsis definition. Until then, organ dysfunction was part of the definition of 'severe' sepsis, a term that was abandoned in the Sepsis-3 definition. ‡The sequential organ failure assessment (SOFA) score is based on six different scores (each classified from 1 to 4 according to increasing abnormality and/or severity), one each for the respiratory, cardiovascular, hepatic, coagulation, renal and neurological systems .

Figure 1.1: A summary of the various iterations of sepsis definitions [4].

Due to all the incarnations of Sepsis definitions, it has been difficult to acquire epidemiological information. Though, a few studies have managed to obtain and analyse some hospital data from sepsis patients. A study of 847 hospitals in 7 U.S states [5] found that the national incidence rate was 3.0 cases per 1,000 population. This produced an estimated national average of 751,000 cases per annum. The incidence for infants $<$ 1 year old was high at 5.3 cases per 1000 which quickly decreased for older children

(0.2 per 1000 aged 5-14 years old). The incidence slowly increases for adulthood to an incidence of 5.3 per 1000 between 60 - 64 years old. For ages 85 upward the incidence dramatically increases to 26.2 per 1000. This demonstrates that the very young and old are significantly more susceptible to sepsis with more than half the patients being 65 years or older. Mortality was found to be 28.6% also seen in [6] with overall higher rates in patients with comorbidities and slightly higher mortality in men than women. This makes sepsis one of the leading causes of deaths in the world, equal with myocardial infarction [7]. Indeed, in the United states it is the leading cause of death of the critically ill outside coronary intensive care units. In the past 20 years there has been an increase in sepsis incidence and related deaths [8, 9], with the trend predicted to continue on this course due to the increasingly ageing population. It is difficult to ascertain if this is a true incidence increase or improved recognition. The mortality rate over the same time period has reduced [10], this is likely due to the combination of earlier sepsis recognition leading to quicker treatment and advances in organ support care in intensive care units (ICUs).

The extent of sepsis prevalence and mortality in the UK is somewhat difficult to gauge. According to the hospital admitted patient care activity 2016-17 statistics [11] provided by NHS England, there were 354,698 diagnoses of the multiple ICD 10 conditions for sepsis. Note ("The data used in this publication are called 'Finished Consultant Episodes' and each episode relates to a period of care for a patient under a single consultant at a single hospital. Therefore, this report counts the number of episodes of care for admitted patients rather than the number of patients"). The Summary Hospital-level Mortality Indicator (SHMI) - Deaths associated with hospitalisation, England, April 2016 - March 2017 statistics [12] showed 15,851 deaths for septicaemia (except in labour) shock criteria. This data is only for reference, the actual prevalence and mortality is most likely very different due to the way these statistics are collected. The data is collected only from English NHS trust hospitals, thus excluding non-hospital cases or other health care centres. The data does warn that the cause of death may be unrelated to the condition the patient is in hospital for, due to the way that diagnosis groups distinguish themselves. A breakdown of the statistics is shown in Table 1.1.

The Sepsis Trust commissioned a report in 2016 that concluded that more than 260,000 people are affected by sepsis and 44,000 deaths occur annually in the UK as a result [13]. As of 2021, this is now 245,000 affected with 48,000 deaths. This is more than breast, bowel and prostate cancer combined and globally 11 million lives per year are lost to sepsis [13]. These statistics come with the caveat that this is a charitable body that has its own interests and an open mind and care must be taken when discussing them. As of late 2019, sepsis has become even more prevalent with the emergence of coronavirus disease 2019 (COVID-19). COVID-19 progression can lead to sepsis [14]. This is viral sepsis rather than bacterial but similar difficulties are common between both. Treatment between the two differ as bacterial sepsis focuses on source control and antibiotics. This approach is not consistent with viral sepsis. The pathogenesis of both can have similarities but this will be complicated by the new virus's own pathogenesis.

Table 1.1: Summary table of ICD 10 codes and classified disease with their relevant preferences[11].

ICD 10 character code and description	All Diagnoses 2015-16	All Diagnoses 2016-17
A02.1 - Salmonella Sepsis	193	184
A22.7 - Anthrax Sepsis	3	3
A26.7 - Erysipebthrix Sepsis	2	3
A28.0 - Pasteurellosis	163	181
A28.2 - Etraintestinal Yersinosis	4	6
A32.7 - Listerial Sepsis	110	114
A39.2 - Acute Meningiococcaemia	63	79
A39.3 - Chronic Meningiococcaemia	1	6
A39.4 - Meningiococcaemia, unspecified	980	910
A40.0 - Sepsis due to Streptococcus, Group A	1,761	2,007
A40.1 - Sepsis due to Streptococcus, Group B	1,497	1,767
A40.2 - Sepsis due to Streptococcus, Group D	414	597
A40.3 - Sepsis due to Streptococcus pneumoniae	2,331	2,974
A40.8 - Other Streptococcal sepsis	4,515	5,695
A40.9 - Streptococcal sepsis, unspecified	1,675	1,957
A41.0 - Sepsis due to Staphylococcus aureus	10,911	12,510
A41.1 - Sepsis due to other specified Staphylococcus	5,402	5,968
A41.2 - Sepsis due to unspecified Staphylococcus	1,936	1,789
A41.3 - Sepsis due to Haemophilus influenzae	269	413
A41.4 - Sepsis due to Anaerobes	913	1,104
A41.5 - Sepsis due to other Gram-negative organisms	34,073	41,510
A41.8 - Other specified sepsis	8,283	9,282
A41.9 - Sepsis, unspecified	182,393	226,058
A42.7 - Actinomyotic Sepsis	19	29
B37.7 - Candidal Sepsis	1,283	1,280
O85.X - Puerperal Sepsis	4,490	5,628
P36 - Bacterial Sepsis of newborn	29,955	32,622
A39.1 - Waterhouse - Friderichsen syndrome E35.1 - Disorders of adrenal glands in diseases clasified elsewhere	31	22
TOTAL Diagnoses	293,670	354,698
Spells of Septicaemia (except in labour), shock	69,785	77,996
Observed Deaths	14,095	15,851
Mortality rate	20.1%	20.3%

Biology of Sepsis

1.1 Current Diagnostics

Sepsis is an extremely challenging illness to diagnose as there is a multitude of signs, symptoms and measurements that can occur that can be attributed to a plethora of other serious and benign medical conditions. Not only are there many potential indications for sepsis that can be non-specific, the diagnostic information markedly varies with cases, even having opposite indications. For example, one septic patient may present with high blood pressure (BP), high temperature and leukocytosis (above normal white blood cell count) and another patient with contradictory but equally valid sepsis symptoms could present with low BP, normal to low temperature and leukopenia (low white cell count). Due to the many permutations that sepsis indications can take, there must be a consideration for every clinician or health professional of "could this be sepsis?". Surprisingly, this may be the most difficult part of detecting sepsis. Once you have at least identified the possibility of sepsis, then following diagnostic protocols will hopefully guide in ruling in/out a sepsis diagnosis. The following sections describe the current diagnostic abilities for sepsis detection. They are split into 3 sections: Signs and Symptoms, Organism Determination and Sepsis Biomarkers.

1.2 Signs and Symptoms

The signs and symptoms of sepsis are varied and potentially non-specific. Steps have been taken to try and mitigate the vast combination of sepsis information. From the 2016 Third international consensus definitions for sepsis and septic shock [3], a set of

guides were established to aid in the detection of sepsis. Starting with the definition of sepsis ("Sepsis is defined as life-threatening organ dysfunction caused by a dysregulated host response to infection"). It is crucial to be able to gauge the level of organ dysfunction in a patient. This is achieved by using the Sequential [Sepsis-related] Organ Failure Assessment score (SOFA score) [15]. It is important to note that the SOFA score is not designed as a predictive assessment of outcome (although it has/can be used in this fashion due to decades of data collection), but is a descriptive measure of complications in the critically ill. It should not be used instead of any other medical management system but as a complementary aid to them. The SOFA score pools together pathological and pathophysiological information from the various organ systems to give a numeric score between 0 - 4 that aids in determining organ dysfunction/failure and potentially eluding to the pathogenesis of the illness. In a general hospital population that is suspected of having an infection, a SOFA score ≥ 2 represents an overall mortality risk of 10%. The systems and measurements used for the SOFA score include Respiration (partial pressure of O_2/ fraction of inspired O_2), Coagulation (platelet count), Liver (Bilirubin density), Cardiovascular (mean arterial pressure), Central Nervous System (Glasgow coma scale) and Renal (creatinine density and urine output). An example of the SOFA score is shown in (Figure 1.2).

	Score				
System	0	1	2	3	4
Respiration					
Pao_2/Fio_2, mm Hg (kPa)	≥400 (53.3)	<400 (53.3)	<300 (40)	<200 (26.7) with respiratory support	<100 (13.3) with respiratory support
Coagulation					
Platelets, $\times 10^3/\mu L$	≥150	<150	<100	<50	<20
Liver					
Bilirubin, mg/dL (μmol/L)	<1.2 (20)	1.2-1.9 (20-32)	2.0-5.9 (33-101)	6.0-11.9 (102-204)	>12.0 (204)
Cardiovascular	MAP ≥70 mm Hg	MAP <70 mm Hg	Dopamine <5 or dobutamine (any dose)[b]	Dopamine 5.1-15 or epinephrine ≤0.1 or norepinephrine ≤0.1[b]	Dopamine >15 or epinephrine >0.1 or norepinephrine >0.1[b]
Central nervous system					
Glasgow Coma Scale score[c]	15	13-14	10-12	6-9	<6
Renal					
Creatinine, mg/dL (μmol/L)	<1.2 (110)	1.2-1.9 (110-170)	2.0-3.4 (171-299)	3.5-4.9 (300-440)	>5.0 (440)
Urine output, mL/d				<500	<200

Abbreviations: Fio_2, fraction of inspired oxygen; MAP, mean arterial pressure; Pao_2, partial pressure of oxygen.

[a] Adapted from Vincent et al.[27]

[b] Catecholamine doses are given as μg/kg/min for at least 1 hour.

[c] Glasgow Coma Scale scores range from 3-15; higher score indicates better neurological function.

Figure 1.2: Sequential [Sepsis-Related] Organ Failure Assessment Score. [3].

To further aid in identifying potential sepsis patients, the qSOFA (quick SOFA) criteria was introduced. It aims to identify suspected infected patients that are likely to have a prolonged ICU stay or die. Again before continuing it is important to note that qSOFA was found to have less accurate predictive performance than other currently used indicators for ICU transfer and death such as Modified Early Warning Score (MEWS) and the National Early Warning Score (NEWS) [16]. It has been advised that qSOFA be used in conjunction with other predictive scoring systems and not instead of. The appealing characteristic of the qSOFA is the fact it only uses three easy to determine criteria: respiratory rate $\geq$ 22 breaths/ min, altered mental status and systolic BP $\leq$ 100 mmHg. In the UK the NEWS2 scoring system has been adopted (Figure 1.3) with it being superior to qSOFA for detecting sepsis with organ dysfunction, admission to intensive care due to an infection and infection-related mortality [17].

Physiological parameter	Score 3	2	1	0	1	2	3
Respiration rate (per minute)	≤8		9–11	12–20		21–24	≥25
SpO_2 Scale 1 (%)	≤91	92–93	94–95	≥96			
SpO_2 Scale 2 (%)	≤83	84–85	86–87	88–92 ≥93 on air	93–94 on oxygen	95–96 on oxygen	≥97 on oxygen
Air or oxygen?		Oxygen		Air			
Systolic blood pressure (mmHg)	≤90	91–100	101–110	111–219			≥220
Pulse (per minute)	≤40		41–50	51–90	91–110	111–130	≥131
Consciousness				Alert			CVPU
Temperature (°C)	≤35.0		35.1–36.0	36.1–38.0	38.1–39.0	≥39.1	

Figure 1.3: Example of a shortened National Early Warning System 2 (NEWS2).

Septic shock is another condition that must be readily diagnosed. It is a subset of sepsis where cellular/metabolic and circulatory irregularities become extensive enough

to increase mortality to considerably higher levels. Septic shock is identified by satisfying the previous sepsis requirements in addition to having persisting hypotension that requires vasopressors (a class of drug that constricts vessels to maintain arterial BP) to maintain a mean arterial pressure $\geq$ 65 mmHg and serum lactate levels 2 mmol/L in defiance of adequate volume resuscitation. If this criterion is met then mortality is over 40%.

There are other diagnostic criteria in use that have added categories such as temperature, heart rate and leukocyte count. These were for aiding in diagnosing the now-defunct SIRS criteria. Other clinical criteria include Deranged homeostasis (oedema, fluid balance and Hyperglycemia) [18]. The stratification tool using the SOFA score issued by the sepsis-3 consensus is shown in Figure 1.4.

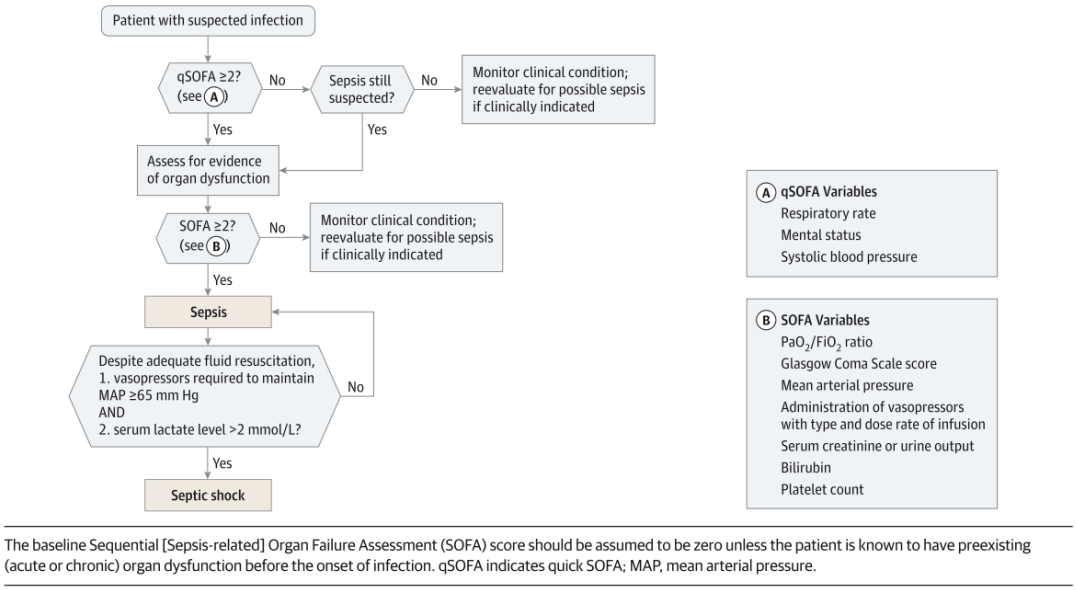

Figure 1.4: Operationalisation of Clinical Criteria Identifying Patients with Sepsis and Septic Shock Sepsis-3 [3].

In the UK the NICE guidelines for Sepsis recognition, diagnosis and early management were used [19] before the adoption of NEWS2. The stratification for this is shown in Figure 1.5. It uses similar criteria to sepsis-3 outlines and SOFA score with its equivalent risk stratification tool. What is important to understand is that there are many criteria used throughout the world all of which are essentially identical when it comes down to

measurements and management. The recent revisions are trying to make diagnosis more streamlined and efficient. Even the criteria that were used for the more outdated sepsis definitions are not without merit but perhaps slightly overcomplicated and may lead to confusion. It appears that at this current diagnostic level, many different criteria used in medical institutions can provide scores and guidelines, but the most difficult part of sepsis diagnosis is confirming pathogen causation and not physiological changes. This means the clinician the most important component in evaluating these scores with the use of common sense, experience and training to properly identify pathogen involvement and sepsis diagnosis. Sepsis requires multiple specialists due to patients that are very young, have comorbidities, or are very old, which can turn all the diagnostic tests on their head. The numbers and guidelines alone are less effective unless processed by an aware and competent clinician. This is what is particularly striking about sepsis, there is no 'magic bullet' that can identify it in a test and then prescribe a treatment. Lives are saved by very well-trained and experienced medical staff that unfortunately are sometimes bested by the disingenuous illness, not to mention the shortages of such staff in developing nations.

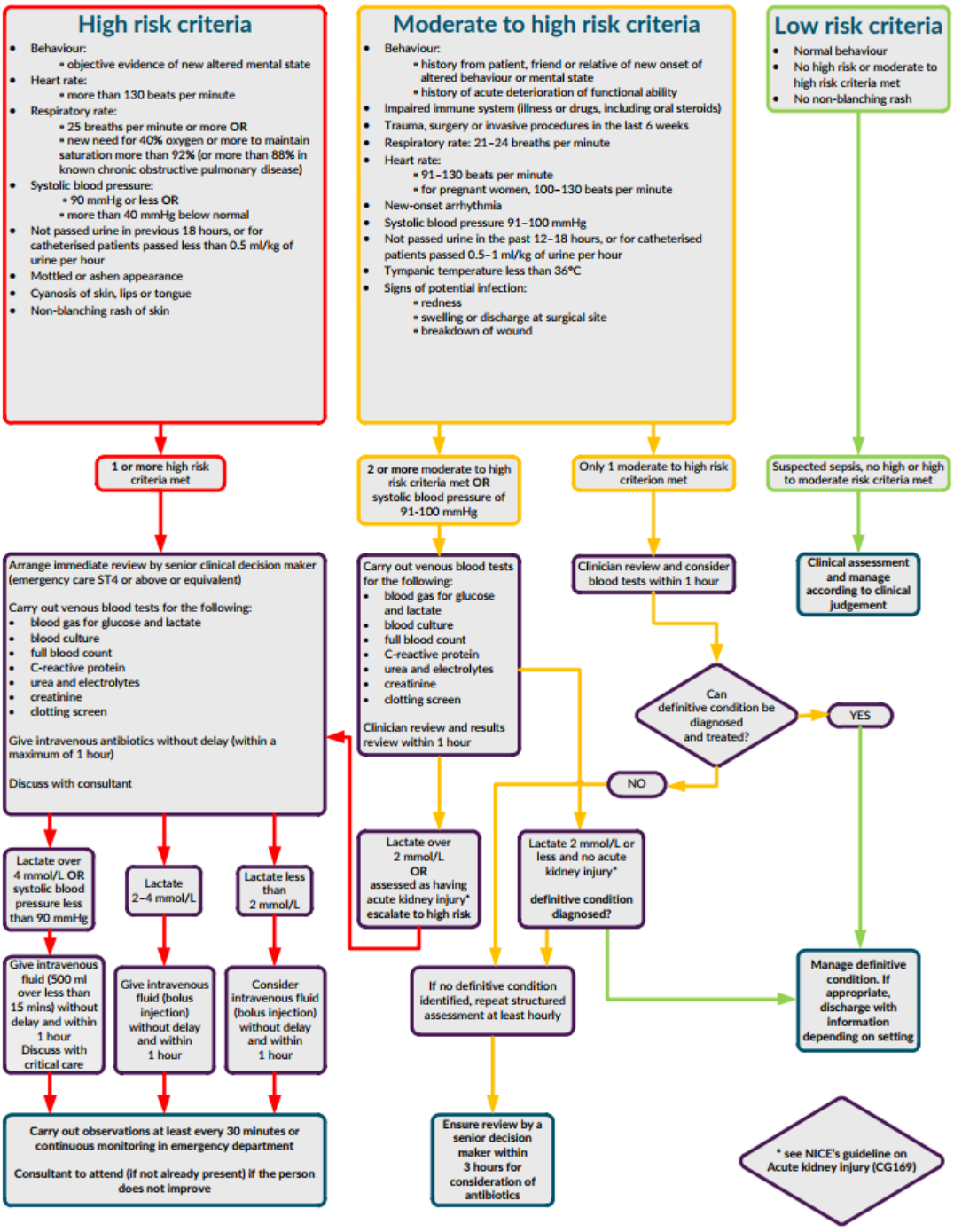

Figure 1.5: Sepsis Risk Stratification Tool [19].

1.3 Organism Identification

A critical step in sepsis management is the identification of the organism that is causing the underlying infection. At least two blood samples should be drawn from the patient (20-30 ml) each. One an anaerobic and one an aerobic sample [20, 21]. This covers pathogens that require oxygen-rich and oxygen-deprived environments to grow. This should preferably be done before the administration of antibiotics as this can interfere with the samples, making detection more difficult. If the infection site is not apparent, scans should be conducted to try and locate an infection site. This is important as if there is a cyst that contains infected fluid this may require drainage. The blood samples are then sent to the laboratory to identify the organism and to perform susceptibility analysis. There are many ways in which the samples can be tested, too many to give detail of all of them in this review however, they can be categorised into a few testing modalities. The modalities discussed are Phenotypic identification, Genotypic identification and mass spectrometer based identification.

1.3.1 Phenotypic Identification

Phenotypic identification first requires a blood sample to return a positive result i.e bacterial growth is present. This can be problematic as in sepsis cases only 30% - 60% of samples become positive [22, 23]. The time to a positive result varies drastically from 2.6 - 127 hours, with a median time of 15 hours [24, 25, 26]. Potential reasons for such variance could be due to:

- Pathogen load (the amount of pathogen present, cells per unit volume blood)
- Type of pathogen and its growth capacity (the maximum pathogen population size allowed by the environment)
- Volume of the blood sample
- Types of blood culture vials used
- Presence of multiple infections (polymicrobial infection)

- Time it takes for a culture bottle to reach an incubator
- Treatment with antibiotics prior to sample recovery

[24, 25, 26]. After a positive blood result, the sample undergoes Gram staining. This determines if the pathogen is a Gram-positive or Gram-negative organism. The Gram result is usually then communicated to the clinician so that antibiotic treatment can be tailored to be more effective against the respective Gram category.

The next step involves streaking the positive blood sample onto a suitable agar plate, the composition of which is often chosen based on the Gram result. This is left to culture, normally overnight. Anaerobes can take longer to subculture. The culture is then put into devices of which there are many (e.g. hundreds) that use biochemical testing to identify the organism i.e. its phenotypic expressions are used to identify it. Susceptibility analysis can also be performed on some instruments to identify any antibiotic resistances. Biochemical testing normally takes 6-8 hours with automation. Thus the total time to identify organisms with phenotypic testing is usually $\geq$ 72 hours, with rarer and more difficult organisms taking longer than this [24, 25, 26]. This method of identification is the gold standard however, with all the issues with blood positivity, biochemical similarities (where more than one type of organisms share some biochemical properties) and time to identification, it is not the most ideal gold standard.

1.3.2 Genotypic Identification

Nucleic acid testing (NAT) is a genotypic method of pathogen identification. This is identification via the pathogens genetic material i.e the nucleic acid sequences in its DNA/RNA constituents [27] (Figure 1.6).

DNA-DNA Hybridisation uses a labelled sequence of DNA from the pathogen and is mixed with an unlabelled DNA sequence to which it is to be compared. Suitable incubation will cause the DNA strands to dissociate and then subsequent forming of hybridised DNA sequences. The higher the similarity between the hybridised strands the stronger the binding between them. The consequence of the different binding strengths will result in a spectrum of temperatures at which strand separation occurs. The DNA

is then heated in steps and washed. The temperature at which the DNA separates determines the similarity between the 2 organisms [28]. Three of the most used techniques: the hydroxyapatite method [29], the optical renaturation rates method [30], or the S1 nuclease method [31] do not give a percentage value of similarity between the two organisms. To achieve this the counts/min of the heterologous DNA is divided by the homologous counts/min and multiplied by 100 to give a percentage value [28]. In general DNA-DNA methods are time-consuming. Faster techniques are explained by [32].

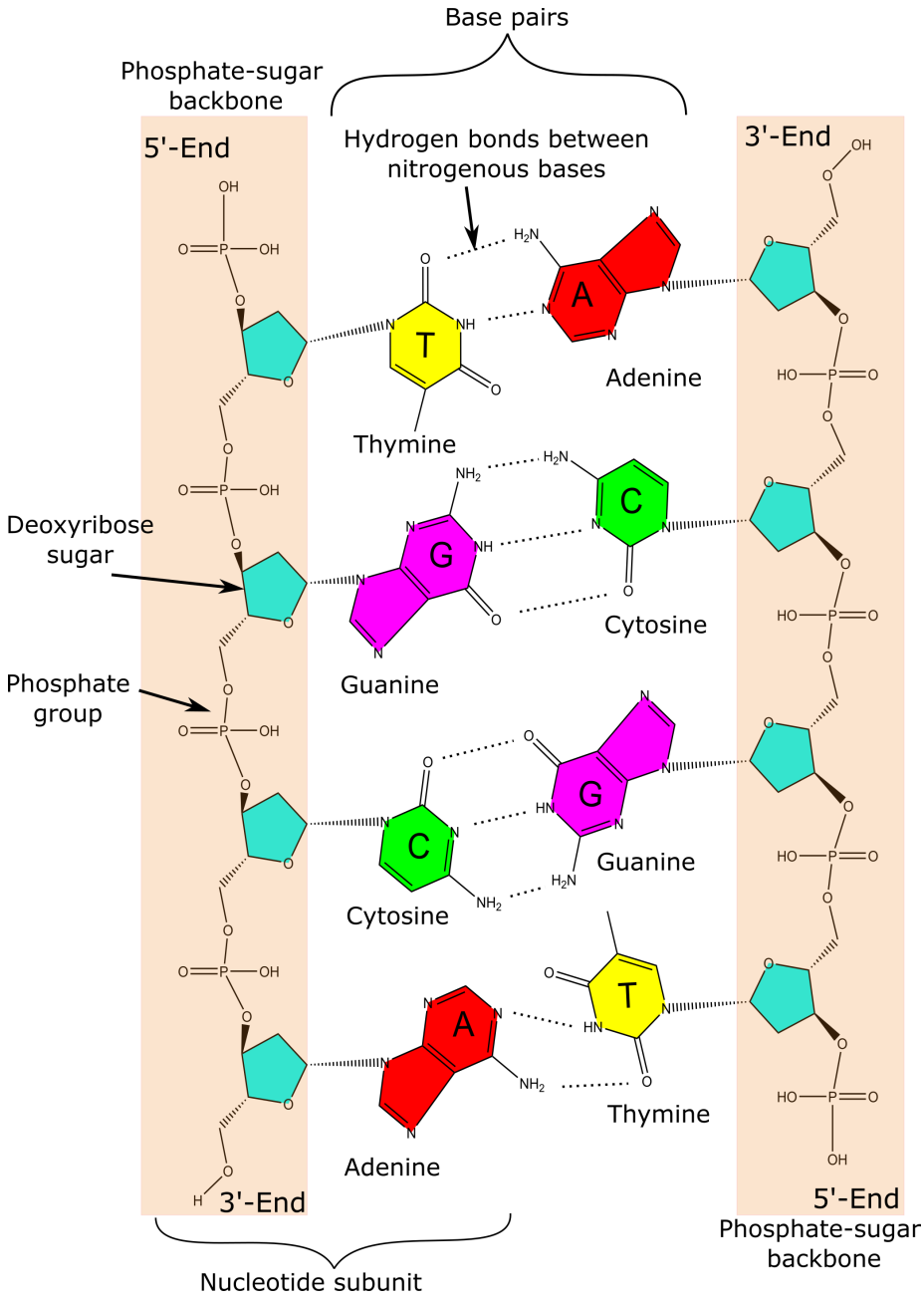

Figure 1.6: Chemical structure of DNA. DNA is made from nucleotide sub-units that bond via hydrogen bonding creating base pairs. Each sub-unit consists of a phosphate group, deoxyribose sugar molecule and one of four nitrogenous bases (adenine (A), cytosine (C), guanine (G) and thymine (T).

Amplified ribosomal DNA restriction analysis (ARDRA)[33] employs an enzyme amplification using primers directed at the conserved regions in the ends of the

small 16S ribosomal bacterial subunit. Tetracutter restriction enzymes allow for digestion following the amplification stage. Comparing patterns from several restriction enzymes with reference strains allows for pathogen identification [28].

16S and 23S rDNA sequencing have complemented traditional phenotypic methods of identification [34, 35, 36]. The 16S and 23S sequences comprise highly stable genetic sequences and highly variable sequences. These sequences are found in all bacteria, thus the stable sequence can be used as a primer for the amplification of the gene. The variable sequences can then be used to determine identification by comparing to primed reference sequences [37, 38].

These are examples of species-specific identification methods i.e they can identify the species of organism. This is sometimes enough but there are variants of each species called strains. Some strains can be benign or beneficial and others highly dangerous to the patient. It is therefore important to be able to identify the strain of a pathogen. The following techniques are examples of strain-specific identification.

Pulse field gel electrophoresis (PFGE) separates DNA molecules larger than 10 kb. This is achieved by applying an electric field and cyclically varying the polarity. The varying fields cause relaxation and elongation of the DNA molecules and will result in bands of various DNA molecules [39]. Bacterial isolates yielding the same PFGE pattern can be considered as belonging to the same strain. Isolates differing by one to three bands are to be considered closely related, by four to six bands possibly related and six or more bands unrelated [28, 40].

Amplified fragment length polymorphism (AFLP) is a technique for detecting polymorphisms in DNA based on the selective amplification of DNA fragments that are obtained by digestion with restriction enzymes. It has high sensitivity, reproducibility and greater resolution than similar identification techniques such as Random amplified polymorphic DNA assay [28, 41].

Ribotyping uses rRNA to identify the pathogen. The DNA from a bacterial colony is extracted and is restricted (cut at specific sequences) into varying fragment lengths using specific restriction enzymes. These fragments then undergo electrophoresis which

separates the fragments by size, these sorted fragments are incubated on a nylon membrane with an enzyme specific DNA probe that will hybridise with the 16s/23s rRNA gene sequence. Finally, an enzyme substrate is added that allows for fluorescence and this signal is used to identify the pathogen [28].

1.3.3 Matrix-Assisted Laser Desorption Ionisation Mass Spectrometry Time of Flight

(MALDI-TOF MS) method does not fit into the categories of phenotypic or genotypic identification. It uses the pathogens physical mass to identify them. The process involves the transfer of a fraction of bacterial colony to a stainless-steel plate and mixed with a matrix solution. Ribosomal proteins crystallise with the matrix on the target plate, these are then irradiated with a pulsed Ultraviolet laser and then accelerated through a 20 keV electric field and into a time of flight measurement device which takes advantage of the charge to mass ratios of the proteins. This will yield an intensity vs charge to mass ratio. The mass spectrum fingerprint can be compared to other spectra in a database. Identification of the pathogen is confirmed when the mass spectra match [42]. Although the identification process is relatively quick when a sample is ready, the requirement of a suitable cultured colony beforehand still keeps positive pathogen identification times high (24-48 hours) [43] which is still a significant improvement on 72 hours. Reliable detection and low costs also make this a desirable method of detection. The main disadvantages being cultivation dependence, relying on reference spectrum and relying on a database to have the spectrum available [42].

1.4 Biomarkers

Being able to detect infections rapidly in patients will change the paradigm for sepsis. On the other hand, not all people with infections have sepsis and for those that do, it is difficult to achieve a qualitative measure of prognoses. It would be beneficial to understand what course a sepsis patient is taking and what systems of the body are involved in the continuing deterioration or improvement. It is hoped that biomarkers

can facilitate these requirements. Currently, there is no single biomarker that gives any definitive answer to the quandaries mentioned. But perhaps the correct combination of biomarkers will allow for a usable diagnoses/prognoses system. There are hundreds of potential biomarkers and most of them have not been tested in any clinically relevant setting. Hopefully, there are very specific biomarkers to sepsis waiting to be discovered. As it stands most if not all biomarkers researched for sepsis can be found in situations other than sepsis making them unreliable for diagnosis. Perhaps with bacterial identification and a handful of biomarkers, it would be sufficient to gauge a sepsis patient in a clinical setting in the future. As there are so many biomarkers, the most common are discussed in this section.

1.4.1 C-reactive protein

C-reactive protein (CRP) is a pentameric protein found in blood plasma. It is produced in the liver in response to an inflammatory event. Its levels tend to peak 24-38 hours after the inflammatory attack. CRP acts to bind dead cells , Gram-positive and negative bacteria and other debris. This bond triggers the complement system which stimulates phagocytosis by macrophages to rid the body of the dangerous materials [44, 45]. The normal concentration of CRP in the body is $\approx$ 5 mg/l and has been used to differentiate between bacterial and viral infections [46, 47]. Levels above 50-100 mg/l have been classed as indicative of sepsis [48, 49]. The issue though, is that CRP is not a specific indicator of sepsis. Autoimmune diseases, some cancers, rheumatoid arthritis and trauma alter CRP levels, as well as some medications such as corticosteroids, have been shown to lower the levels [50, 51]. It is thus dangerous to use CRP levels as a singular guide to any treatment.

1.4.2 Procalcitonin

Procalcitonin (PCT) is the precursor to the hormone calcitonin. Its release is stimulated by pro-inflammatory mediators which are abundant when the body is under attack from a pathogen. In sepsis, PCT is produced mainly by macrophages and monocytic cells. Experimental methods have shown that PCT has been synthesised in other tissues and

organs [52]. PCT acts as a chemokine and stimulates the release of anti-inflammatory cytokines such as nitric oxide synthase (iNOs). In animal sepsis experiments the injection of PCT showed an increase in mortality [53]. Experimental tests on volunteers found that upon injection of PCT, identification of it was obtainable after 2-3 hours and the concentration peaked at 12-48h. The normal concentration range is < 0.5 ng/ml [54, 55]. In sepsis, this oscillates into the hundreds of ng/ml which is complicated by the negative predictive value of PCT i.e levels < 0.2 ng/ml in which bacteremia is higher than 90 % . PCT does have improved sensitivity and specificity than CRP and is used in antibiotic stewardship in the surviving sepsis guidelines [56]. Prolonged use of antibiotics or their use at all contributes to the major issue of antimicrobial resistance. As such an indicator for the safe discontinue of antibiotics would be hugely beneficial. It must be states that a false negative using PCT level is perilous, thus can only be used to aid in clinical decisions, not to be the driving reason for them. There is a campaign attempting to prevent PCT from being used as an antibiotic discontinuance guidance marker due to the lack of positive evidence, as well as supporting evidence that it does not work [57].

1.4.3 Mid-regional fragment of pro-adrenomedulin (MR-proADM)

Adrenomedullin (ADM) is a vasodilator peptide hormone and plays an important role in the inflammation process [58, 59]. It is quickly removed from the circulation making it difficult to detect in plasma. The mid-regional fragment of pro-adrenomedullin (MR-proADM) is more stable in plasma and is indicative of active ADM peptide levels [60]. A review was conducted on MR-proADM as a biomarker for sepsis and septic shock, including relevant studies collected from PubMed, Web of Science and The Cochrane Library search [61]. The review concluded that MR-proADM was identified as a prognostic biomarker able to stratify the mortality risk in sepsis patients with various levels of organ failure. It has the potential for early identification and individual risk assessment of sepsis which could potentially aid in subsequent clinical management. It is again likely that MR-proADM would benefit as one of many biomarkers in a test instead of relying solely on this single marker test. It may also be useful for diagnosis

or prognosis of sepsis and septic shock in patients with burns and malignancy. Normal levels of MR-proADM are below the analytical limit of 0.05 nmol/L [62] those with sepsis have levels $>$ 0.8 nmol/L depending on age, sex and severity [61, 62].

1.4.4 Cytokines (IL-6, IL-8 and IL-10)

Cytokines regulate the immune system by Pleiotropy and have a major and complicated role in the pathophysiology of sepsis. In particular Interleukins 6, 8 and 10 (IL-6, IL-8 and IL-10). IL-6 is a pro-inflammatory cytokine and an anti-inflammatory myokine. It is produced by monocytes, T-lymphocytes, endothelial cells and various other cells. Lipopolysaccharide (the outer membrane of Gram-negative bacteria) or active bacteria introduction to the bloodstream stimulates the release of IL-6. Normal ranges of IL-6 tend to be between 0.2-7.8 pg/ml, with septic patients potentially reaching 1.6 ng/ml i.e 1000 times more [63]. IL-8 is a chemokine and has two main functions. It causes chemotaxis (movement of an organism due to chemical stimulus) in target cells, causing them to migrate to the infected areas. Once there it then induces phagocytosis. Normal serum levels are between 6-41 pg/ml, with sepsis patients up to thousands of times higher 27-66,000 pg/ml [64]. IL-10 is an anti-inflammatory cytokine produced by macrophages, T and B lymphocytes, monocytes and a few other cells. It has a protective role that is characterised by the inhibition of pro-inflammatory mediators such as TNF, IL-8, IL-1, interferon γ and nitric oxide. Normal IL-10 levels are between $<$ 3-10 pg/ml [65], while sepsis patients are between 12-450 pg/ml [66]. High levels of IL-6 and IL-10 have indicated higher mortality for septic patients [67], IL-8 has been shown as a severity marker in septic children [68]. CRP and PCT have greater sensitivity and are more specific than these cytokines. The thought of using them as a way to monitor inflammatory progression has been suggested but no study as yet has shown any evidence that these biomarkers are successful in the management of sepsis treatment [55].

1.4.5 Lipopolysaccharide Binding Protein

Lipopolysaccharide binding protein (LBP) is produced by the liver during the acute phase inflammatory response. It binds to bacterial lipopolysaccharide (LBS) and triggering the immune response by offering it to the cell surface pattern recognition receptors CD14 and TLR4. Normal concentration levels are 5-15 μg/ml and in septic patients 11.8-105 μg/ml [69]. In mice studies, high levels of LPB has been shown to block LPS and reduce mortality in stimulated sepsis [70, 71]. LPB has been shown to be ineffective at distinguishing between infectious and noninfectious conditions but has shown prognostic abilities for sepsis patients [69, 72, 73].

1.4.6 Other

D-dimer is a fibrin degradation product. Sepsis can present with haematological issues and lead to disseminated intravascular coagulation (DIC). This forms clots in affected vessels and thus progress to D-dimer release. Studies are showing its potential ability to indicate bacteremia [74] and even perhaps prognostic measures of how severe the sepsis is in a patient [75]. it has yet to demonstrate diagnostic significance [76]. Normal levels of D-dimer are $\leq$ 250 ng/ml [77], sepsis patients have ranges 500-4573 ng/ml [78].

Presepsin also known as sCD14-ST. As mentioned before LPS and LPB are made present to the glycoprotein CD14 on monocyte and macrophages membrane surfaces. This activates toll-like receptor 4 which induces an outpouring of pro-inflammatory substances. A conglomeration of LPS-LPB-CD14 is shed into circulation and a soluble CD14 (sCD14) is generated called sCD14 subtype (sCD14-ST) i.e presepsin. Presepsin is increased in sepsis and shows little difference between Gram-positive and negative infections [55]. It has been suggested as an early biomarker though, further research is required [79, 80]. Normal levels of presepsin are $\approx$ 365 pg/ml [81], sepsis patients have concentrations ranging from 400-2000 pg/ml, in some case even over 10 times this amount [82].

Table 1.2: Table summarising the biomarkers and their relevant concentrations found in normal and septic patients. Note ng = nano (10^{-9}) grams and pg = pico (10^{-12}) grams.

Biomarker	Normal concentrations	Sepsis concentrations
C-reactive protein	$\approx$ 5 μg/ml [46, 47]	50 - 100 μg/ml [48, 49]
Procalcitonin	$<$ 0.5 ng/ml [54, 55]	fluctuates in the hundreds of ng/ml Note the negative predictive value $<$ 0.2 ng/ml equates to 90 % bacteremia [54, 55]
MR-proADM	below analytical limit of 0.05 nmol/L	$>$ 0.8 nmol/L depending on sex, age and severity
IL-6	0.2 - 7.8 pg/ml [63]	up to 1.6 ng/ml [63]
IL-8	6 - 41 pg/ml [64]	27 - 66,000 pg/ml [64]
IL-10	$<$ 3 - 10 pg/ml [65]	12 - 450 pg/ml [66]
lipopolysaccaride binding protein	5 - 15 μg/ml [69]	11.8 - 105 μg/ml [69]
D-dimer	$\leq$ 250 ng/ml [77]	500 - 4573 ng/ml [78]
Presepsin	$\approx$ 365 pg/ml [81]	400 - 2000 pg/ml (can be in excess of 20,000 pg/ml) [82

1.5 Pathophysiology

Sepsis is the departure from the natural equilibrium that the host body's immune system maintains (homoeostasis), due to an invading infection. The innate immune system (the part of the immune system that immediately responds to an invading pathogen) detects the pathogen via pathogen-associated molecular patterns (PAMPs) via pattern recognition receptors (PRRs) [83]. The innate immune system in everyday cases deals with the invading pathogen by changing the homoeostasis to a more hostile level. Once the pathogen is defeated, homoeostasis returns to the normal level. In the cases that the pathogen prevails the host response can depart homoeostasis and involves an intense release of pro-inflammatory cytokines (cytokine storm). The body always trying to maintain an equilibrium mounts an anti-inflammatory response by releasing anti-inflammatory cytokines. This response is defined as compensatory anti-inflammatory response syndrome (CARS) and can be just as severe as the pro-inflammatory response leading to immunosuppression [84]. The evolution from a hyper-inflammatory state to a hypo-inflammatory state with immunosuppression has been given the name of "immunoparalysis" [85]. The severity of this varies between patients. The host response

can be further disrupted by damage-associated molecular patterns (DAMPs, alarmins). These are released by cells undergoing necrosis and are recognised by most PRRs [86, 87]. This sustains a vicious cycle of immune dysregulation and organ dysfunction. There is evidence that survivors of early sepsis often develop nosocomial (hospital originating) infections with pathogens not ordinarily associated with a healthy immune system. They may also suffer from reactivation of latent viruses [88, 89, 90].

The phenotype of Sepsis in ICU has changed over the years with advances in critical care. Before the 1970s sepsis deaths would usually be from single organ failure and irreversible shock. During the 1970s critical care improved and a new syndrome emerged, multiple organ failure (MOF). This was discovered because patients were living longer and thus mapping the sepsis progression in new territory [91]. Over the next 40 years, intensive care has further advanced and revealed a new syndrome: persistent inflammation immunosuppression catabolism syndrome (PICS). This is characterised by patients not recovering and never reaching the criteria for late MOF. Instead, they show "ongoing protein catabolism with poor nutritional status, poor wound healing, immunosuppression and recurrent infections". This usually results in transfer to long-term care and rarely to a recovery [92].

With improved survival rates of sepsis patients there has been an increase in "second hit infections". These are secondary infections that present after the resolution of the primary insult for admission. This secondary infection is likely due to immunosupresive effects from the initial critical illness. There is a lack of data on comparisons between first and second hit infections. One study found that Gram-negative pathogens were associated with poorer outcomes in the first hit infections [93]. The 90 day mortality of patients that developed Gram-negative pathogens was found to be 43.6 % after elective surgery and 27.9 % following trauma. Compare this to the Gram-positive values of 25.6 % and 20.6 %. The second hit infections were unexpectedly found to show poorer patient outcomes with those developing Gram-positive infections after an initial sepsis diagnosis with Gram-negative pathogen. It was found that the 90 day mortality was 43.6 % for Gram-positive secondary infections versus 40.4 % for Gram-negative secondary

infections. The causes for this inverse behaviour are not fully understood but are likely due to genetic, environmental, immunological and microbiological factors.

As mentioned, the pathophysiology of sepsis involves inflammatory and immune responses, the next Sections describe the various mechanisms of each in the role of sepsis.

1.5.1 Inflammatory Response

Translocation of nuclear factor-κB (NF-κB) from cell cytosol to nucleus initiates the activation of cytokine release, including those that are involved in the inflammation process. Tumour necrosis factor (TNF), interleukin-1 (IL-1), (IL-6), (IL-12) and (IL-18) are pro-inflammatory cytokines involved in sepsis pathogenesis [94]. Inflammation can be split into three systems of influence: the vascular system, the complement system and the coagulation system. Each is interconnected where one can affect the other.

Vascular System

Neutrophil extracellular traps (NETs). When an invading pathogen enters the host, neutrophils (type of white blood cell) are the first line of defence. They attempt to eliminate the pathogen by surrounding the invader and using antimicrobial secretions. They have another method, discovered in the last decade known as NETs. The neutrophils release a fibril matrix made of DNA, histones and serine proteases [95]. NETs are further stimulated by platelets, it has been suggested that a rapid formation of NETs known as NETosis only occur at a certain threshold of platelets [96]. NETs entrap pathogens and eliminate them but they can also cause tissue damage and thrombosis by acting as a scaffold that also entraps platelets and erythrocytes (red blood cells) allowing them to accumulate. Sepsis patients have higher levels of NETs in their system and this is associated with organ damage [97].

Endothelial dysregulation. The endothelium is a lining of the interior of blood and lymphatic vessels. The point where endothelium meets other cells is known as the endothelial barrier. The barriers function (fluid filtration, neutrophil recruitment, haemostasis and vessel tone) is maintained by the glycocalyx, cell cytoskeleton, inter-

cellular adhesion molecules and other supportive proteins [98]. Cell-cell connections are regulated by adherin junctions [99]. When an infection is present, leukocytes and platelets adhere to the endothelium and move towards the infected region. In a septic patient with escalated inflammation, this process is disrupted and leads to failures in the barriers regulation. Both thrombin and matrix metalloproteinase 1 (MMP1) are believed to play a crucial role in the progression barrier dysfunction. PAR1 mediates the effects of them both [100]. Loss of barrier regulation results in intravascular leakage into the extravascular space, tissue oedema and a reduction in microvascular perfusion. Sphingosine-1-phosphate (S1P) is a vascular regulator and has a role in vascular leakage. Activating the S1P receptors (S1PR) on endothelial cells maintains vascular function via the release of various biochemicals [101]. Angiopoietin 1 is also a regulator of vascular function.

Platelets aid in coagulation and maintaining vascular function. Sepsis patients with thrombocytopenia (low platelet count), have an independent associated higher mortality [102]. There is evidence that excessive platelet activation exacerbates organ damage by altering immune cell recruitment and inflammation [103].

Complement system

Small fragments Known as C3a and C5a as anaphylatoxins are released upon the activation of the complement system. They have powerful pro-inflammatory effects that include recruiting and activating leukocytes, endothelial cells and platelets [104]. The unequilibrated compartment system causes tissue damage and organ damage. Blocking C5a signalling has shown improved outcomes in animal models [105]. C3a and C5a have shown differing behaviours in sepsis, C3a antagonist receptor treatment showed a reduction in survival rates whereas C5a antagonist receptor treatment showed improvement [106].

Coagulation system

When a pathogen invades the body, one of the first responses is the activation of the coagulation system. This triggers immune defence mechanisms. Immunothrombosis is

a term recently introduced to represent the interconnectivity between the immune and coagulation systems [107]. In sepsis disseminated intravascular coagulation (DIC) is induced by the highly activated coagulation system. DIC can lead to Microvascular thrombosis (clots) and haemorrhage due to heavy consumption of clotting factors and platelets. The potent activator transmembrane receptor known as tissue factor (TF) is the main driving force of the coagulation systems activation in sepsis [107]. Inhibition of TF in animal sepsis models prevents MOF and mortality in what normally would be a lethal case [107]. Clotting factors FVIIa, FXa, fibrin, thrombin and TF can induce pro-inflammatory signalling via protease-associated pathways (PARs) [108]. There are three anti-coagulant pathways that become jeopardised which leads to higher probabilities of thrombosis in sepsis. The pathways are anti-thrombin, tissue factor pathway inhibitor (TFPI) and protein c system [107]. The protein c system has been shown to be a powerful anti-coagulant such that inhibition of it can turn non-lethal sepsis into a lethal case. In addition to this, it is also an anti-apoptotic and provides protective properties to the vascular system via PAR1 [109]. As for the other pathways, studies have shown that recombinant TFPI and anti-thrombin have inconsistent beneficial effects in sepsis [110, 111, 112].

1.5.2 Immune system

Lymphocytes. T helper cells are an important class of T cells in the immune response. They aid many other immune mechanisms by releasing cytokines or stimulating various cells. Mature T helper cells express surface proteins CD4 and CD8 and are referred to CD4+ and CD8+ T cells. In sepsis, these cells along with B cells and dendritic cells are heavily depleted due to apoptosis (programmed cell death) [113, 114]. T cell exhaustion has also been observed when comparing splenic interferon γ (IFNγ) and TNF levels in sepsis deaths and non-infectious deaths. Harvested CD4+ cells from dead sepsis patients show increased expression of programmed cell death 1 (PD1) whilst macrophages and endothelial cells have expressed programmed cell death ligand 1 (PDL1) which is thought to compromise T cell function [113]. Regulatory T cells (T_{reg}) inhibit monocyte and neutrophil function leading to immunosuppression, these cells are

increased in sepsis patients. Blocking (T_{reg}) cells improves function in experiments [115, 116].

Antigen presenting cells. Reduction in Human Leukocyte Antigen – antigen D Related (HLA-DR) on blood monocytes is a characteristic of immune suppression in sepsis. Dendritic cells have also shown lower expression of HLA-DR which cause the increased release of IL-10, also presenting with increased apoptosis [117, 118].

1.5.3 Antibiotics

Antibiotics are classed by their mechanism of action on organisms. These mechanisms include **inhibiting cell wall synthesis** whereby the antibiotic binds to cell wall components in place of the required component leaving the cell wall uncompleted leading to cell lysis [119]. Antibiotics disrupting **protein synthesis** target the 30S and 50S ribosome subunit of the bacterial cell. These disrupt how m-RNA is translated by these ribosome subunits and leads to faulty instructions to build cell structures, damaging the bacterial cell. **Nucleic acid synthesis inhibitor** antibiotics act by inhibiting the enzyme DNA gyrase. This leads to incorrect DNA supercoiling, condensing of the chromosome, disrupting DNA strand breaks and prevent re-ligation. These are all cytotoxic to the cell and can lead to apoptosis and cell death. **Folic acid metabolism inhibitor** antibiotics work by antagonising folic acid preventing it to work correctly. Since folic acid is an important cofactor of many biomolecules, inhibition disrupts cell division, DNA/RNA synthesis and repair and protein synthesis. All these factors are vital to bacterial cell health and function. Antibiotics can also be classed as a broad-spectrum (effective against Gram-positive and negative bacteria) or narrow-spectrum (effective against bacteria/location in the body). An overview of antibiotic classes can be seen in Figure 1.7. There has not been a new molecule of antibiotic discovered and developed in decades and with antimicrobial resistance becoming ever more prominent there is a need for new antibiotics to treat these resistant pathogens. Recently a few new classes of antibiotic have come on the market ceftolozone/tazobactum, ceftazidime/avibactum and meropenem/vaborbactum. These offer a spectrum against Gram-negative bacteria but these are not new molecules and are not novel [120]. There is research showing

the development of a new type of antibiotic chimeric peptidomimetic antibiotics. These work by binding to lipopolysaccharides and the main component (BamA) which acts to fold proteins into the outer membrane of Gram-negative bacteria [121]. The drug has shown effectiveness against multi-drug resistant pathogens including all Gram-negative members of the ESKAPE pathogens. There is relatively little news of novel antibiotics even though more and more researchers are searching for them.

INHIBIT		CLASIFICATION		ANTIBIOTICS			
Cell Wall Synthesis	Beta Lactams	Penicillins		***Penicinillase – Sensible***			
			Natural Penicillins (narrow spectrum)	Penicillin G: Na, K, Procainic, Benzathine (IV, IM) Penicillin V: VO			
			Aminopenicillins (broad spectrum)	Ampicillin Amoxicillin			
			Penicinillase – Resistant *(very narrow spectrum)*				
			Nafcillin	Oxacillin	Dicloxacillin		
			Antipseudomonal *(extended spectrum)*				
			Carboxipenicillins	Ticarcillin Carbenicillin			
			Ureidopenicillins	Piperacillin Azlocillin Mezlocillin			
		Cephalosporins	1° Generation	Cefazolin	Cephalexine	Cephapirin	
				Cefadroxil	Cephadrine	Cephalotin	
			2° Generation	Cefuroxime	Cefamandole	Cefprozil	
				Cefoxitin	Cefonicid	Cefmetazole	
				Cefotetan	Cefaclor		
			3° Generation	Cefoperazone	Ceftriaxone	Ceftazidime	
				Cefpodoxime	Ceftizoxime	Cefotaxime	
				Cefdinir	Ceftibuten	Cefixime	
				Cefditoren			
			4° Generation	Cefepime	Cefpirome *		
			5° Generation	Ceftaroline			
		Carbapenems		Meropenem	Ertapenem	Doripenem	Imipenem + Cylastatine
		Monobactams		Aztreonam			
		**** ***Beta-lactamase inhib.***		Sulbactam	Tazobactam	Clavulanic Acid	
	No lactam	***Glycopeptides***		Vancomycin	Bacitracin		
				Teicoplanin	Polymyxin B		
Protein Synthesis		***30S***	***Amino-glycosides***	Gentamycin	Neomycin	Streptomycin	
				Amikacin	Tobramycin		
			Tetracyclins	Doxycycline	Demeclocylin *	Minocycline	
				Tetracyclin	Tigecyclin		
		50S	***Oxazolidonones***	Linezolid			
			Streptogramins	Quinupristin/Dalfopristin			
			Cloramphenicol				
			Macrolides	Erythromycin	Azithromycin	Clarithromycin	
			Lincosamides	Clindamycin	Lincomycin		
DNA topoisomerases		***Fluorquinolones***		Ciprofloxacin	Norfloxacin	Levofloxacin	Ofloxacin
				Sparfloxacin	Moxifloxacin	Gemifloxacin	Enofloxacin
		Quinolones		Nalidixic Acid			
Folic Acid Synthesis		***Sulfonamides***		Sulfamethoxazole (SMX)	Ag Sulfadiazine	Sulfasalazine	Sulfisoxazole
		DHFR inhibitors		Trimethroprim (TMP)		Pirymethamine	
DNA (damage)		***Metronidazole***					
mRNA synth.		***Rifampim***					

Figure 1.7: Overview of the classifications of antibiotics [122].

In cases of suspected sepsis, rapid antibiotic treatment is pivotal [19]. The identity of invading pathogen will most likely be unknown, thus it is important to try and deduce an infection source. The source of an infection can help narrow the most effective antibiotics to use. In the event of an unknown source and unidentified infection then broad-spectrum antibiotics must be administered. Examples of broad-spectrum antibiotics include: Amoxicillin; Levofloxacin; Gatifloxacillin; Tetracycline and Chloramphenicol) [123]. According to the Greater Glasgow and Clyde medicines adult therapeutic handbook [124], community or hospital acquired infections with unknown source, should be treated with Benzylpenicillin, Flucloxacillin and Gentamicin. For Penicillin/Beta-lactam allergy, Vancomycin and Gentamicin should be prescribed. If a streptococcal infection is suspected, then treatment is identical as above with the addition of Clindamycin. If *Staphylococcus aureus* bacteremia is suspected then Flucloxacillin or Vancomycin (if beta-lactam allergy) should be prescribed. Local resistance patterns must also be taken into account for antibiotic stewardship. This is achieved with keeping up to date with local bulletins in the region and conversations with experienced microbiologists in the care setting. A summary of antibiotic treatments for sepsis in differing locations and organisms is shown in (Table 1.3).
The three organisms of interest in this review are *Streptococcus pneumoniae*, Neisseria *Neisseria meningitidis* and *Haemophilus influenzae.*

Streptococcus pneumoniae is a Gram-positive encapsulated diplococcus (occurs as pairs of cocci). It is also α-haemolytic (causes red blood cell lysis) and aerobic in growth [123]. It colonises on mucosal areas of the nasopharynx and upper airway [125]. *S. pneumoniae* causes pneumonia; meningitis; bacteremia; endocarditis; septic arthritis; otitis media; sinusitis and rarely peritonitis. Infection with S. *pneumoniae* is known as pneumococcal diseases. Antibiotic treatment involves the administration of any of the following: beta-lactams, macrolide, or a respiratory fluoroquinolone e.g. levofloxacin, moxifloxacin and gemifloxacin [123].

Neisseria meningitidis is a Gram-negative β proteobacterium organism. It is fastidious, can be encapsulated or unencapsulated and is an aerobic diplococcus [126]. *N.*

meningitidis causes mainly meningitis and meningococcemia though, infections in the lungs; joints; respiratory passageways; genitourinary (GU) organs; eyes; endocardium and pericardium are also possible [123]. Infection with *N. meningitidis* is known as meningococcal diseases. Antibiotic treatment typically includes treatment with any of the following antibiotics: ceftriaxone; dexamethasone (steroid); vancomycin; penicillin; and ampicillin are used for immunocompromised patients.

Haemophilus influenzae is a Gram-negative coccobacillus (spherical and rod features). It has the ability to grow aerobically and anaerobically [127]. Childhood infections such as meningitis; bacteremia; septic arthritis; pneumonia; tracheobronchitis; otitis media; conjunctivitis; sinusitis and acute epiglottitis can be caused by *H. influenae*. In adults all the above infections plus endocarditis and urinary tract infections (UTIs) are also possible but uncommon [123]. Antibiotic treatment using β-lactams are usually sufficient [127] but the use of doxycycline, fluoroquinolones, 2nd- and 3rd-generation cephalosporins and carbapenems for more invasive and persistent cases are not uncommon [123].

Table 1.3: Summary of Antibiotic treatments for specific infection cites and organisms [123, 124].

Infection Location	Organism	Antibiotic Treatment
Intra-abdominal	Unknown	Amoxicillin, Metronidazole, Gentamicin, Temocillin, Aztreonam, Vancomycin
UTI	Unknown	Amoxicillin, Temocillian, Aztreonam, Gentamicin
Community-acquired pneumonia (CAP)	Unknown	Clarithromycin, Amoxicillin, Co-amoxiclav, Levofloxacin
Hospital acquired Pneumonia (HAP)	Unknown	Amoxicillin, Temocillin, Aztreonam, Levofloxacin
Central nervous system (Bacterial Meningitis)	Unknown	Ceftriaxone, Chloramphenicol, Dexamethasone (steroid)
NA	Haemophilus *influenzae*	Doxycycline, Fluoroquinolones, 2^{nd} and 3^{rd} generation Cephalosporins and Carbapenims
NA	Streptococcus *pneumoniae*	Beta-lactams, Respiratory Fluoroquinolone (e.g Levofloxacin, Moxifloxacin), Vancomycin, Benzylpenicillin
NA	Neisseria *meningitidis*	Ceftriaxone, Dexamethasone (steroid), Vancomycin, Penicillin, Ampicillin

1.6 COVID-19

COVID-19 was first encountered in Hubei province in China in late 2019. On 30th January 2020, the World Health Organisation (WHO) declared this a global health emergency and on 11th March a pandemic [128] with the infections spreading rapidly

around the world. COVID-19 is a disease caused by the SARS-CoV-2 coronavirus. Coronaviruses are a family of RNA viruses that infect a range of humans and animals. These viruses are divided into four subfamilies: alpha, beta, gamma and delta. Gamma and delta subgroups tend to infect birds and pigs while the alpha and beta infect mammals. The alpha subgroup tends to cause mild respiratory infections such as the common cold and rarely lead to any serious health issues [129]. The beta subgroup can lead to severe respiratory illness and death. These diseases include Middle East Respiratory Syndrome (MERS-CoV), Severe acute respiratory syndrome (SARS-CoV) and the COVID-19 aetiological agent (SARS-CoV-2) [130].

The coronavirus genome encodes four structural proteins: Nucleocapsid protein, Membrane protein, Spike glycoprotein and Envelope protein. There are several other non-structural proteins [131] (Figure 1.8). The capsid protein shell encompasses the RNA and nucleocapsid proteins. The virus replicates by attaching to host cells, in this case, angiotensin converting enzyme 2 (ACE2) receptor. It achieves this by specifically binding the spike protein to the ACE2 receptor for which it has a high affinity. This also facilitates membrane fusion whereby the membranes of cell and virus fuse bringing the virus into the cell in what is now called an endosome. The RNA is then released into the cytoplasm of the cell and hijacks the cells transcription/replication system to build more virions. The virions are then released by a process called exocytosis and can go on to infect other host cells and replicate further [131].

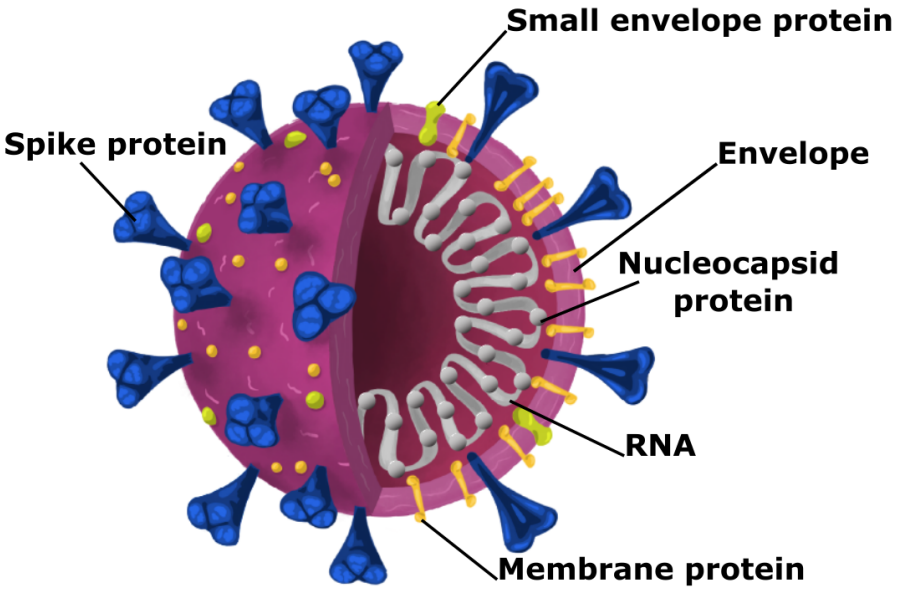

Figure 1.8: Diagram depicting the SARS-CoV-2 anatomy. (Adapted from an image by: Maya Peters Kostman for the Innovative Genomics Institute. https://creativecommons.org/licenses/by-nc-sa/4.0/legalcode

Typical symptoms of COVID-19 are cough, fever, fatigue, anosmia and ageusia [132]. This can progress to or worsen dyspnea. In some cases gastrointestinal symptoms such as nausea, vomiting and diarrhoea occur [133]. The lung response to the virus can be seen in chest X-rays (CXR) as the disease progresses. Typically, early in the disease the lungs remain clear. At 5 - 10 days ground glass opacities (GGO) may appear. From 10 days onward the GGOs may worsen and lung consolidation becomes manifest [134] (Figure 1.9). Although these CXRs may show progression, CT scan is the optimal method for assessing lung damage.

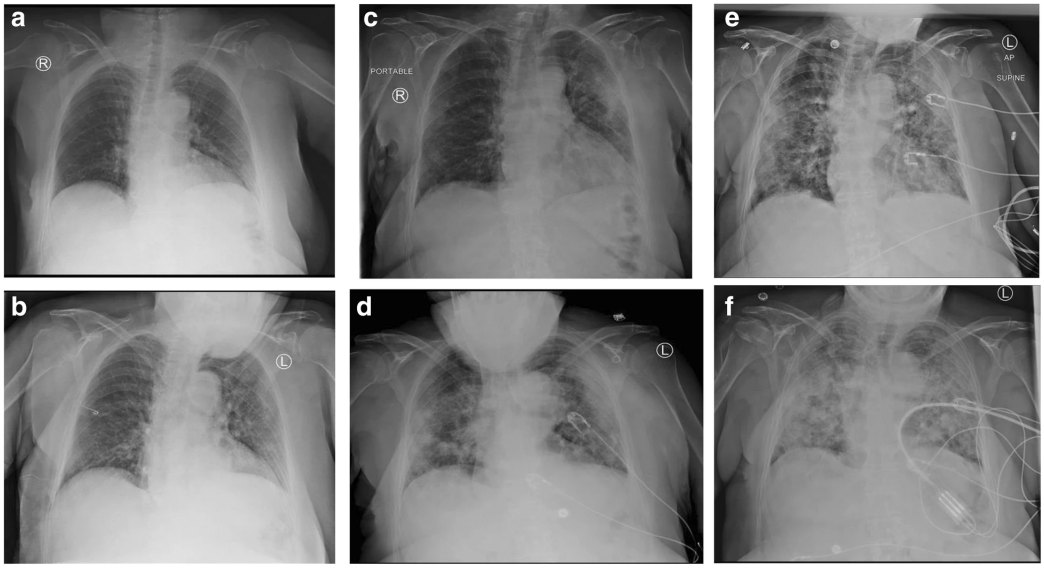

Figure 1.9: Diagram depicting X-rays of SARS-CoV-2 damage of the lungs. Series chest x-rays in an 80-year-old woman with COVID-19 pneumonia. a) Chest x-ray obtained on illness day 5 showed peripheral GGO in the LLZ (score 1). b) Chest x-ray obtained on illness day 7 showed increased extent of the GGO diffusely involving the left lung (score 4). c) Chest x-ray obtained on illness day 11 showed increased extent of the GGO involving the right lung, with increased extent of consolidation involving the left lung diffusely (Total score 8). d) Chest x-ray obtained on illness day 14 showed the development of reticulations in both lungs with increasing extent of involvement of the RUZ. (Total score 8). e) Chest x-ray obtained on illness day 17 showed extensive bilateral consolidations mainly peripherally with increased reticulations (Total score 8). f) Chest x-ray obtained on illness day 18 showed extensive consolidation involving both lungs diffusely (Total score 8). The patient died on illness day 18. (GGO: ground glass opacity. LLZ: left lower zone. RUZ: right upper zone)(Taken from a publication by: [134] https://creativecommons.org/licenses/by/4.0/legalcode

COVID-19 pathogenisis can follow a path to Acute Respiratory Distress Syndrome (ARDS - widespread inflammation in the lungs with difficulty and fast breathing and low blood oxygen levels) and sepsis. Studies have shown that ARDS is closely related to what has been termed cytokine release syndrome. This is a catch all term for elevated cytokine production and presence in the body particularly pro inflammatory cytokines such as IL-6 [135]. This can produce hyperinflamation and is correlated with more severe covid-19 patients [136]. The causes and effects of cytokine release syndrome and hyperinflamation are still poorly understood. It is being debated whether the term cytokine storm is a misleading term [137]. The same set of symptoms have already

previously been identified and was referred to systemic inflammatory response syndrome (SIRS) and was used to define sepsis for decades. Interventions for cytokine release in sepsis have shown mixed results. More research is needed to conclude that cytokine storm is a useful model for understanding covid-19.

Progression to ARDS or sepsis will often result in transfer to the intensive care unit (ICU) if not already there. In ICU patients will receive treatments such as high flow O_2 and continuous positive airway pressure (CPAP - a non-invasive method to maintain adequate oxygenation). This treatment could also be started on the ward or high dependency unit. If this is not effective then intubation (an invasive measure to provide mechanical breathing for the patient) could be performed. For very severe progressions and after careful clinical discussion and subject to availability, a patient may be placed on extracorporeal membrane oxygenation (ECMO - provides some function of the heart and lungs when they are not efficient enough to maintain themselves). Further decline in health results in septic shock and multi-organ failure and can quickly progress to death.

The current method for confirming COVID-19 for the general public is via reverse transcription-polymerase chain reaction (RT-PCR) whereby primers for multiple conserved genomic regions of the viral RNA are amplified. If there is viral RNA present then these should all amplify, if no viral RNA is present then nothing will happen and these are both quantifiable and lead to a positive or negative result. For the general public Nasopharyngeal and throat swabs are provided for testing. This, however, has been shown to have a positive rate of 73 % and 61 % respectively [138]. Bronchoalveolar lavage 93 % and sputum 72 % have higher positive rates but these are tests performed in hospital settings [138]. It can be further confounded by viral load in patients that change the positivity. Combing RT-PCR with antibody tests may improve the sensitivity for COVID-19 detection but is difficult to do as a quick and easy singular test. The best method thus far is an RT-PCR test along with any clinical manifestations but this has drawbacks for asymptomatic or mild symptom patients. The time to result for RT-PCR is only a couple of hours but the number of tests being applied delays the re-

sults up to 24 - 72 hours. To properly bring the pandemic under control a fast, sensitive and specific point of care test would allow for rapid diagnosis and inform individuals to initiate the appropriate self-isolation or clinicians to follow their COVID-19 protocols at much earlier stages.

1.7 Electrochemistry Basics

Electrochemistry combines chemical processes with electrical processes to investigate the behaviours, characteristics and composition of many chemical and biological samples. To investigate the electrochemical properties of samples, the sample (solute/analyte) is placed into a solvent (most commonly water is used) to become a solution. It is advantageous to use a background electrolyte to aid in conduction. Depending on the system in use, two or three electrodes will be placed into the solution. Two-electrode systems are more commonly used for microelectrodes and three-electrode systems for macroelectrodes as three-electrode systems reduce current leakage and potential drop. Microelectrodes have such small current responses that these issues can become minimised and a two-electrode system can be adopted [139]. By applying a potential to the working electrode (measured against the reference electrode) the analyte will thermodynamically and kinetically react which will induce a current that is measured by the counter electrode. Depending on the electrochemical method being performed varying details of the analyte are revealed. The most common electrochemical methods are cyclic voltammetry (CV), pulsed differential voltammetry (DPV), square wave voltammetry (SWV) and electrochemical impedance spectroscopy (EIS).

1.7.1 Electrical Double Layer

When an electrode contacts a solution, an electrical double layer is formed. This happens due to a difference between the charge densities of the metal electrode (q_m) and the solution (q_s). Since charge neutrality must be maintained there must be a redistribution of ions to negate this difference. The metal cannot easily undergo redistribution so the ions in solution reorder. Cations and anions will be attracted or repelled de-

pending on the charge of the metal surface. This will lead to a charge on the metal surface and distribution of cations and ions at or near the metal surface balancing the charge. Two parallel oppositely charged surfaces form which is the essence of a capacitor. This theory describes an electric single layer. The double layer results from a more complicated theory. The Grahame triple-layer model states that the cations and anions will become solvated in solution [140]. They form a solvation shell due to polarity of the diluent molecules (usually water for these examples). In the case of a negatively charge electrode the cations with their solvation shell are attracted to the surface and are maintained at a distance X_2 from the surface (Figure 1.10 A). This layer is known as the outer Helmholtz plane (OHP). Anions can break free of the solvation shell and specifically adsorb onto the metal surface maintaining a distance X_1, also known as the inner Helmholtz plane (IHP). The potential dropped between these layers and the surface is linear (Figure 1.10 B). Beyond these two layers is the diffuse layer and is a gradual change from mostly cations to a more random mixture of both cations and anions leading to the bulk solutions. The potential exponentially decreases over the diffuse layer to the bulk solution. Three layers are described by this theory but the IHP and OHP are usually referred to as a joint term of Helmholtz layer and thus the formation of the electrical double layer.

Because of this capacitor like formation, when the potential of the electrode is changed in an experiment, the surface charge is also changed leading to double layer reorganisation causing a flow of electrodes to and from the electrode. This is registered as a current but is not due to any chemical change at the surface and is a non-Faradaic current. It is an additive current to the desired Faradaic current in experimental conditions. This can lead to misrepresentation in results or obscure Faradaic signals completely. Good experimental design, microelectrodes and suitable measurement techniques can reduce this non-Faradaic current to reveal the electrochemical response of the substance under investigation.

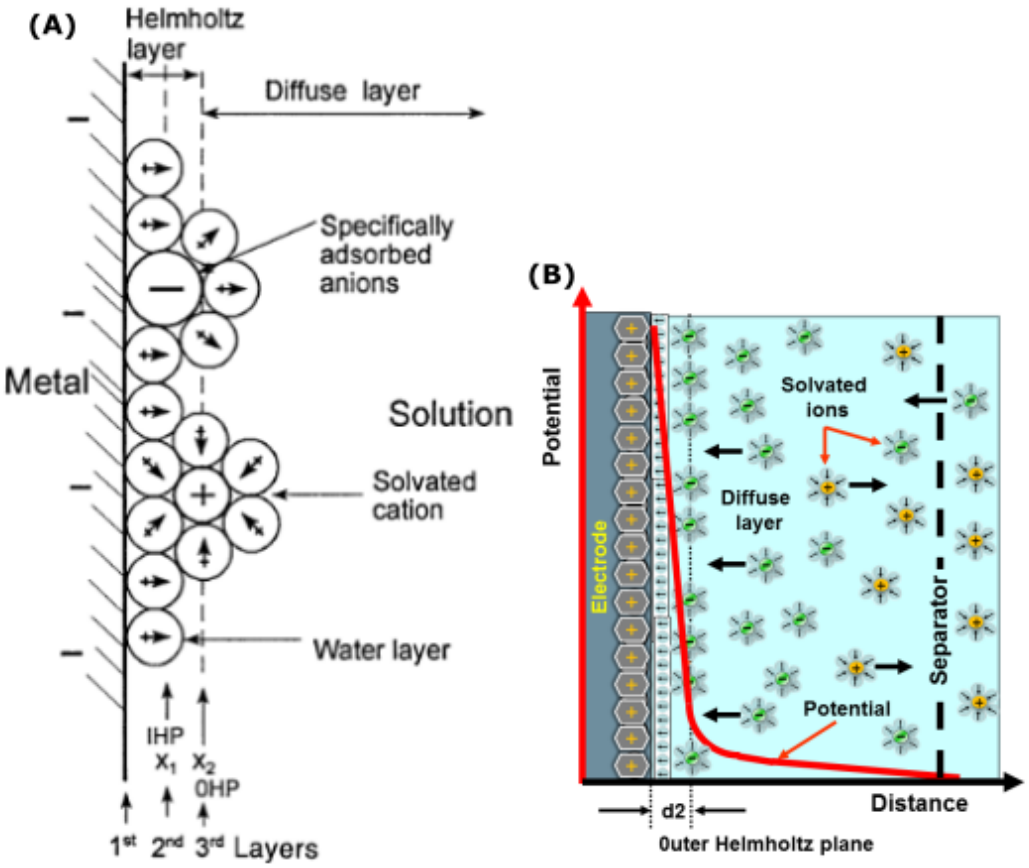

Figure 1.10: Example of Grahame double layer model (A) [140]. Tip of arrows indicate negative end of dipole. Example of how the potential behaves across all the layers of the electrode and solution (B) (Elcap, CC0, via Wikimedia Commons).

1.7.2 Cyclic voltammetry (CV)

In a cyclic voltammetry experiment, a range of potentials are swept whilst recording the resulting current behaviour. This is plotted on a potential vs current (E vs I) graph. Depending on the literature, the positive sweep and negative sweep can be the opposite. Here we define the oxidation (anodic current i_{pa}) to be positive. The experiment begins by first sweeping from a more negative potential to a more positive one. This lowers the energy of the electrons within the electrode. Once the critical energy (dependent on analyte and electrode composition) is passed, it is more energetically favourable for the electrons from the analyte to migrate to the lower vacant energy levels in the electrode. The potentials at which this transfer occurs is related to the standard potential (E^0)

of the analyte. The flow of electrons is measured as a current. Thus when the applied potential approaches the standard potential, a current is produced. This is seen as a peak in the E vs I plot and is called the oxidation peak. Oxidation refers to the fact that the analyte has lost an electron. The potential will then be reversed, applying a more negative potential thus increasing the energy levels in the electrode. Again once the potential is higher than the analyte's standard potential it is energetically more favourable to flow from the electrode to the analyte producing a negative (cathodic) current. This is evident by the appearance of a negative (reduction) peak i_{pc} on the E vs I plot. This completes the cycle and the experiment. An example can be seen in Figure 1.11. The peaks can allude to the standard potentials of the analyte. If multiple peaks are present then more complex reactions are happening in the cell and investigation can identify these reactions. The E vs I plots are known as voltammograms (Figure 1.11).

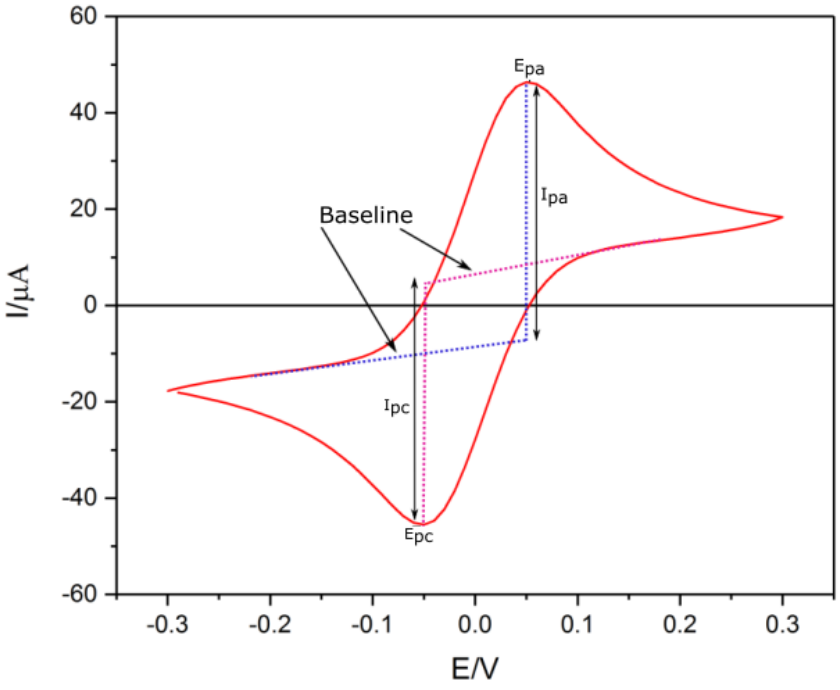

Figure 1.11: A CV voltammogram of a redox couple. i_{pc} and i_{pa} giving the peak cathodic and anodic currents. Note that the peaks must be measured from the current baselines.

The reversible peak current of the cyclic voltammogram response can be calculated using the reversible Randles-Sevcik equation Eqn (1.1).

$$i_p = 0.4463nFAC\left(\frac{nF\nu D}{RT}\right)^{\frac{1}{2}} \tag{1.1}$$

Where i_p is the peak current measured (Amps); n is the number of electrons involved in electron transfer (n = 1 for the redox couples investigated in this study); F is the Faraday constant (C mol^{-1}); A is the effective electrode area (cm^2); C is analyte concentration (mol cm^{-3}); D is the diffusion coefficient of the analyte (cm^2 s^{-1}); R is the gas constant (J K^{-1} mol^{-1}); T the temperature (K) and ν is the potential scan rate (V s^{-1})). The diffusion coefficient reveals information about the diffusion layer and the bulk solution and how the analyte behaves travelling to the electrode surface.

1.7.3 Differential Pulse Voltammetry (DPV)

Anytime a potential ramp is applied with a capacitor like element in the cell as in cyclic voltammetry there is a resulting charging current non-Faradaic in addition to the desired Faradaic currents. Differential pulse voltammetry minimises this charging current allowing a higher resolution and thus being able to detect analytes at 10^{-7}M or lower. This is achieved by applying a less negative baseline potential (E_b) and measuring the current after a time τ'. Just after this measurement a potential pulse (10-100 mV compared to baseline) is applied. A second current measurement is taken at time τ just before this pulse ends. The baseline potential is now increased to a slightly higher potential and the process is repeated see (Figure 1.12a). The waiting time between baseline potential application and the first measurement allows for the charging current to decay to less significant values thus revealing the truer nature of the analyte's electrolysis.

Unlike the voltammograms in CV, the DPV voltammogram plots the difference in current δi = i(τ')-i(τ) against E. When the potential is too negative to induce oxidation there are no Faradaic currents thus δi is essentially zero. When the baseline approaches the formal potential of the analyte $E^{0'}$ then oxidation reactions occur in the waiting

period but still below the maximum possible rate since the concentration of analyte at the electrode surface is not zero. When the pulse is applied, the concentration of analyte is driven lower, resulting in an enhanced flux of analyte to the surface and Faradaic current. Late in the experiment, the maximum rate is achieved and the application of a pulse can no longer increase this rate and δi is again small. These processes produce the overall voltammogram characteristic shape of a peak shown in (Figure 1.12b).

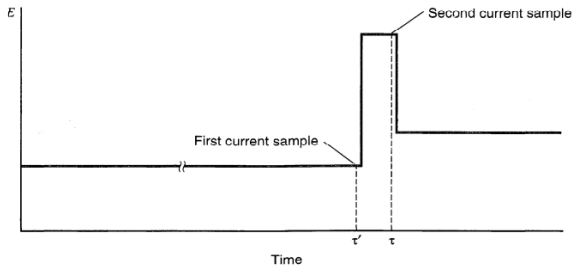

(a) Example of a single differential pulse. i(τ') is where the first current measurement is taken and i(τ) is when the second is measured [141].

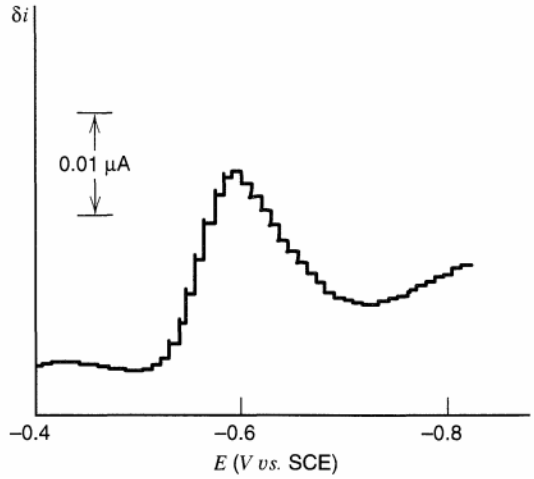

(b) Example of a typical differential pulse voltammogram, note the appearance of a peak that is not seen in other pulsed techniques[141].

Figure 1.12

1.7.4 Square Wave Voltammetry (SWV)

This technique superimposes a square-wave pulse onto a staircase waveform (Figure 1.13 A) [142]. A forward scan current is measured (i_f) halfway through the cycle (or equivalently after the first pulse). The scan direction then reverses and a reverse scan current (i_r) is measured at the end of the cycle (equivalently at the end of the second pulse). This technique therefore produces two voltammograms for analysis. This technique differs from DPV as it uses pulses about the baseline in froward and reverse directions whereas DPV uses a single pulse in the forward direction of the staircase waveform. SWV are usually presented as a single peak voltammogram. This is achieved by taking the difference between the forward and reverse scans $\Delta i = (i_f) - (i_r)$ (Figure 1.13 B). The scan rate is dependent on the frequency which itself is dependent on the pulse width. Varying the pulse width can lead to scan rates between 10 mV/s to 5 mV/s, this is faster than other pulsed techniques and can lead to very fast experiment times. SWV leads to greater sensitivity than DPV and other pulsed techniques. It can achieve much faster scan times and can be applied to a wider range of electrode materials and systems with superior non-Faradaic current rejection leading to improved signal to noise ratios [141].

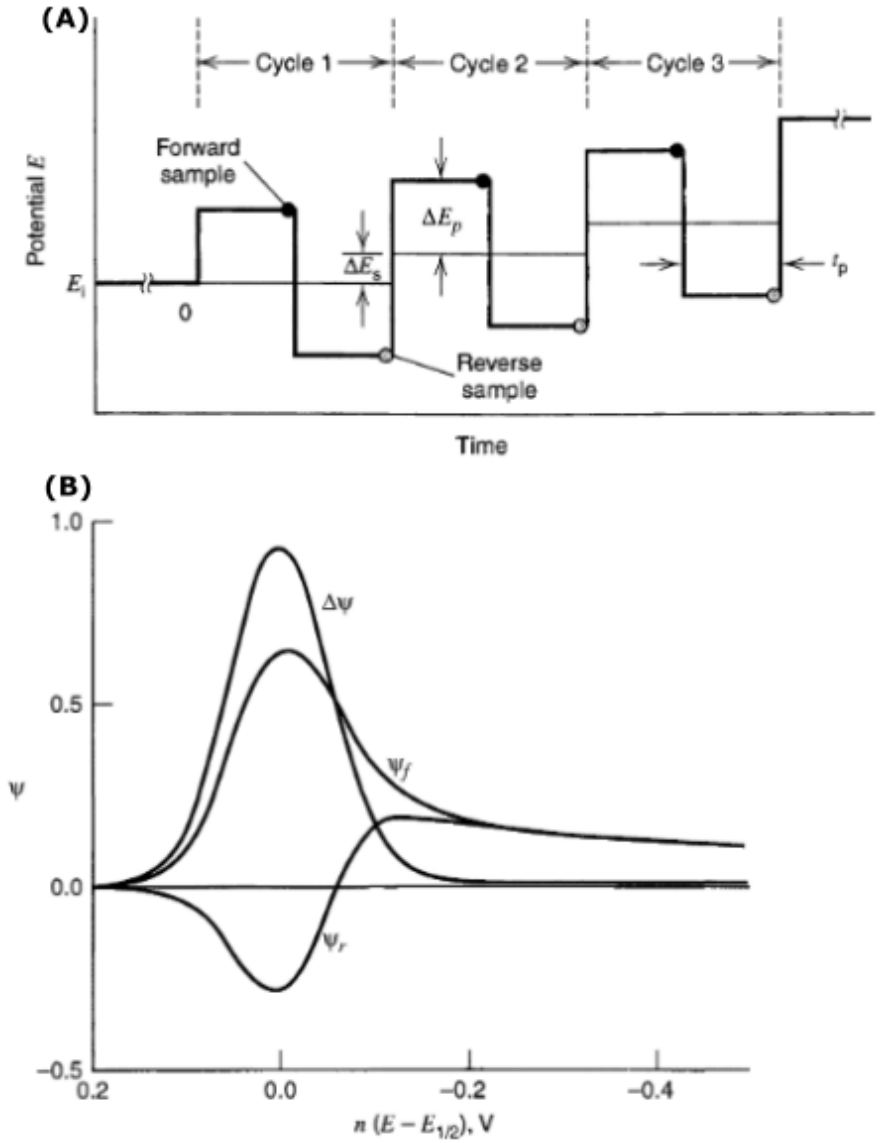

Figure 1.13: Example of the SWV waveform (A) [141]. ΔE_p is the pulse height, ΔE_s is the staircase shift every cycle and t_p is the pulse width. Example of the voltammograms produced by SWV (B) with Ψ being a dimensionless parameter. ΨE_f and ΨE_r are the forward and reverse voltammograms and $\Delta\ \Psi$ represents the voltammogram of the difference between forward and reverse [141].

1.7.5 Electrochemical Impedance Spectroscopy (EIS)

EIS perturbs the electrochemical cell with a small alternating signal and the reaction of this perturbation is recorded, all whilst being in a steady-state. This is beneficial as

electrochemical cells are generally non-linear in their voltage and current relations as seen from the cyclic voltammetry section. By applying a small voltage perturbation, a linear section of the E vs I can be investigated allowing for high precision and extremely stable measurements. Applying an alternating current (ac) potential perturbation to the system will cause the system to depart from a steady-state slightly. Measuring the AC response allows the impedance to be determined. The impedance of the system is in part due to electrolyte properties, diffusion, electrode kinetics and chemical reactions (thermodynamics). To separate all these factors into individual values requires impedimetric analyses which are not derived here though, some important equations and concepts are presented to allow the general idea to be understood. Voltage, current and resistance are related in linear systems via Ohms law Eqn(1.2).

$$R = \frac{V}{I} \tag{1.2}$$

There are more complex resistive behaviours mainly those due to capacitance and inductance in electric circuits. These are dependent on the frequency of the perturbing signal thus do not have such a desirable relationship. Thus restive behaviour that has elements of resistance, capacitance and inductance are given the overall name of impedance. In the electrochemical cell, inductance will play a limited role and is, therefore, neglected and the impedance due to capacitance is governed by Eqn(1.3).

$$Z_c = \frac{1}{i\omega C} \tag{1.3}$$

Where i is $\sqrt{-1}$, ω is angular frequency and C is capacitance. It is evident from this that when the frequency is low, the impedance due to capacitance is high and vice versa for high frequencies. To understand how this reveals information about the cell, the electrochemical cell is modelled simply at first as an equivalent electrical circuit (simple Randles circuit) shown in (Figure 1.14b). Since electrons take the path of least resistance when the frequency is high the current will flow preferentially through the capacitor due to its low impedance, charging the capacitor. As the frequency reduces,

the capacitor becomes fully charged and the current then favours the parallel resistor (R_{ct}) path. The resistor (R_s) models the solution resistance and its effect is to shift the combined parallel charge transfer and double layer capacitance behaviour along the Z' axis. Using excess background electrolyte usually minimises the contribution from the solution resistance. Capturing this information as the frequency is swept from high to low gives the characteristic EIS plot (Nyquist plot) shown in (Figure 1.14a). Observation of the Nyquist plot reveals some behaviours of the sensor system, with further equivalent circuit analysis properties of the electrode, analyte and electrolyte can be discovered, making it a valuable measurement technique.

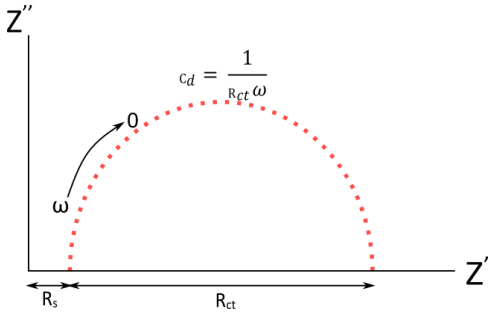

(a) An example of a perfect Nyquist plot where real world factors are not included due to complexity. Solution resistance R_s and charge transfer resistance R_{ct} show the purely real impedance factors and the double layer capacitance C_{dl} shows the purely imaginary impedance. The combination of both as in the Randles circuit gives the semi-circular behaviour.

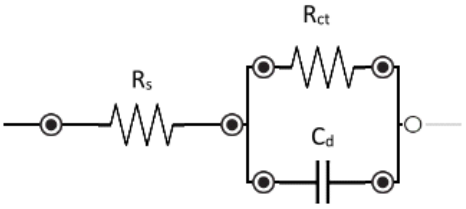

(b) Simple Randles circuit modelling the electrochemical cell.

Figure 1.14

The R_{ct} resistor models the charge transfer resistance and is the resistance to the movement of electrons to and from the analyte and electrode surface. The composition of the surface and adsorption of molecules on it will affect this value. This is why it is a key measurement as it can relay crucial information about the state of the surface. C_{dl} models the double layer capacitance (see Section1.10). This can also reveal information on surface composition and modification by molecules.

Chemical and Bio Functionalisation of Electrode Surfaces

Metal and metal oxide surfaces that are untreated, tend to readily adsorb non-essential organic molecules. This is due to the underlying chemical and physical properties of materials seeking the lowest possible free energy state. These adsorbates allow for this to happen by lowering the free energy state between the metal surface and the surrounding environment [143]. These organic adsorbates also alter the interfacial properties, manifesting as physical or electrostatic barriers, reduction of reactivity of the surface atoms and the electrically insulating film properties. Surface coated with unwanted organic material are not reproducible and do not change chemical functionalities, thus to gain such properties, the use of specific organic molecules are required.

1.8 Self-Assembled Monolayers (SAMs)

SAMs are important organic assemblies for constructing biosensor surfaces. They allow tailoring of the interfacial properties of metal, metal oxide and semiconductor surfaces. SAMs form by the adsorption or chemisorption of organic assemblies from a solution or gas phase to the metal surface. The organisation of the adsorbates is spontaneous and results in crystalline or semicrystalline structures. The molecules that form SAMs have a general form, a headgroup that has chemical functionality that has an affinity for a surface (substrate), a backbone or tail and a terminal functional group. The common head groups are thiols for substrates such as gold, silver, copper, palladium, platinum

and mercury. For surfaces such as silicon, silicon oxide, silane, mica, glass and phosphonates are commonly used [144]. This discussion will focus on gold as it is the electrode material featured in the research. Gold is considered the standard substrate when it comes to SAMs, there are various reasons for this. Gold is easy to obtain in various forms and thin films are easy to prepare via physical vapour deposition, sputtering or electro-deposition. It is easy to pattern using photolithography, micromachining and chemical etching. Gold is highly inert to chemicals and does not oxidise at temperatures below its boiling point and does not react with oxygen at atmospheric pressure. Finally, it bonds strongly to thiols without any sub-reactions taking place and altering the surface chemistry. The high affinity between gold and thiols results in non-essential adsorbed material to be desorbed via displacement [145].

Although many adsorbates can be used to form SAMs, the most commonly used (especially with gold substrates) is the alkanethiols, with general chemical formula $(SH(CH_2)_nR)$. It consists of a thiol (SH) headgroup which is covalently bonded to the tail (alkane chain) where the variable n denotes the number of methylene units $(CH_2)_n$ that compose that particular alkanethiol. R denotes the functional tail group terminating the alkanethiol. An example of the alkanethiol 6-Mercapto-1-hexanol (mercaptohexanol) is shown in (Figure 1.15). Note that this contains an OH functional tail, not all SAM molecules contain the same functional groups at the tail.

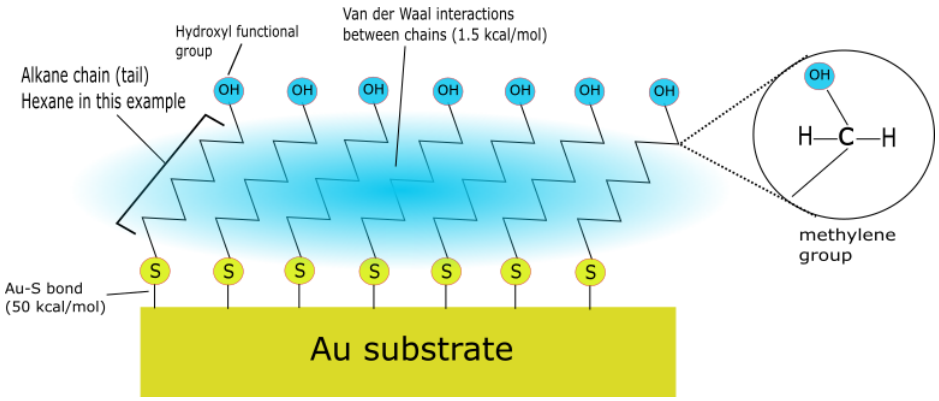

Figure 1.15: Representation of a basic SAM construction. The sulphur of the alkanethiol bonding to the gold substrate, mercaptohexanol contains a hydroxyl functional group at the terminus. Each chain interacts with each other via Van der Waals forces reinforcing the SAM.

A common method for the adsorption of alkanethiols on many metal substrates is to immerse the pretreated clean substrate into a dilute (1-10 mM) ethanolic solution of thiols for 12-18 hours [146]. When the substrate is added to a solution or vice versa, two distinctive kinetic effects occur in the SAM formation. First, due to the large diffusion gradient, the alkanethiols diffuse rapidly to the substrate surface and physisorb. This monolayer is dense and takes milliseconds - minutes to become contiguous. The second stage takes hours to equilibrate as the alkanethiols are reorganised and chemisorb to the surface, creating a crystalline structure where the tails of the thiols rise up [146, 147, 148, 149]. This step minimises defects in the SAM. The Au-S bond strength is believed to be $\approx$ 50 kcal/mol and that of a disulphide bond $\approx$ 62 kcal/mol [150]. As for the fate of the hydrogen atom when the thiol bonds to the substrate, it is still uncertain. The two most likely options are that they form the reductive H_2 gas or the oxidative H_2O [151]. The Au-S bond is sufficient in strength to maintain anchorage of the alkanethiols to the substrate at room temperature but at higher temperatures desorption kinetics become feasible [152]. This may be beneficial as it would allow the removal and reformation of SAMs. There are a number of experimental factors that can affect SAM formation, these include adsorbent concentration, solvent, immersion time, cleanliness of substrate, temperature and alkane chain length [151].

The typical and most studied formation of gold is the Au(1,1,1) structure. When alkanethiols migrate to the surface they are believed to take position in the three gold atom hollows (Figure 1.16a) [153].

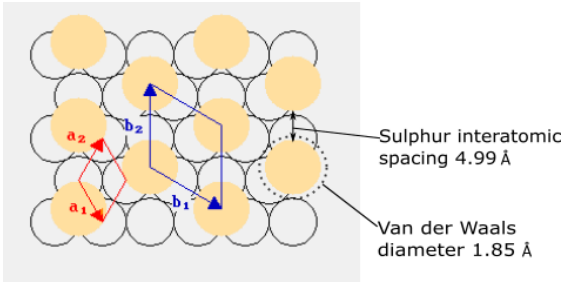

(a) Au(1,1,1) and thiol overlayer lattices sitting in the trifold hollow of the gold atoms. The gold unit vectors are shown in red and the monolayer's in blue. Also shown is the interatomic spacing of the sulphur atoms and their corresponding Van der Waals diameter [154].

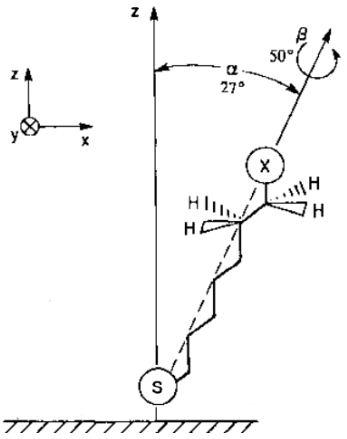

(b) Schematic of the orientation of long chain alkanethiols on gold substrates. Tilt angle α is the angle subtended between the normal axis to the substrate and the thiol. Twist angle β is the angle rotated around the thiol chain's axis [155].

Figure 1.16

From this the characteristic structure of the overlayer of thiols is determined as follows. Define the gold lattice unit vectors a_1 and a_2 as well as the thiol overlayer unit vectors b_1 and b_2 as shown in (Figure 1.16a). Now $|a_1| = |a_2|$ and $|b_1| = |b_2|$. This is evident if you translate the b_1 vector to the ends of the gold unit vectors, which reveals an isosceles triangle with 120° angle. Using the cosine rule Eqn(1.4) the relationship between the gold unit vectors and thiol unit vectors is $b_1 = \sqrt{3}a_1$ with a 30° rotation. This relationship is compactly and concisely put in Woods notation $(\sqrt{3}\text{x}\sqrt{3})\text{R}30°$.

$$\begin{aligned} c^2 &= a^2 + b^2 - 2ab\cos(\theta) \\ b^2 &= 2ab\cos(\theta) \\ b &= \sqrt{3}a \end{aligned} \tag{1.4}$$

With c = a for isosceles triangle and $\cos(30°) = \sqrt{3}/2$.

The sulphur atoms are spaced 4.99 Å, which is 2.7 times the Van der Waals diameter 1.85 Å [155]. This is consistent with the theory that the sulphur-sulphur bonds do not

interact with each other when adsorbed. This distance is also larger than the alkane chains distance of closest approach 4.24 Å thus they tilt upward to maximise interactions [155, 156].

The alkane chains have a tilt angle (relative to the axis perpendicular to the substrate) $\alpha \approx 30°$, a twist angle (rotation about the alkane chain's axis) $\beta \approx 52°$ [146, 155] see figure 1.16b. As previously mentioned the alkane chains help stabilise the SAM due to their Van der Waals interactions with each other, with bond strength ≈ 1.5 kcal/mol.

1.9 DNA SAMs

A DNA biosensor works on the general principle of altering the inherent electrochemical properties of the sensor so that electrical signals measured before and after are distinguishable enough from one another to confirm a detection event. As discussed earlier, the electrochemical cell can be measured by various techniques. One of the best methods for biosensing is the EIS technique as its measurements have high sensitivity to a changing system and by applying a small perturbation [157], it is very gentle in terms of the potentials applied to the biosensor surface. Other techniques have been found to be damaging to biological molecules immobilised on surfaces, in particular DNA.

The DNA biosensor comprises a single stranded DNA (ssDNA) probe oligonucleotide sequence specific to the pathogen of interest immobilised on the electrode surface. The lengths of probe DNA are variable, some systems use optimisation techniques to find the most efficacious length. The probe is most commonly immobilised via a thiol attached to the 5' or 3' end. Thus it is similar to that of the SAM as detailed in the previous section. One difference is in the structure of the tail sequence of the probe. Since the tail is ssDNA, it has a negatively charged phosphate backbone. This induces repulsion between various probes, which results in a lower density coverage of the surface than for uncharged molecules. The probe strands can also droop and adsorb to the surface via base pairs, attaching at incorrect positions reducing the chances of future target binding. Due to these effects, DNA binding is poorly resolved from improperly functionalised surfaces. To improve the electrode functionalisation SAMs are immobilised on the

surface after the ssDNA probe immobilisation stage. They have multiple effects on the system. Firstly, due to their high affinity for the electrode surface, they displace some of the improperly attached ssDNA. This allows certain control over probe coverage. Secondly, the SAMs aid in the probes ability to orientate towards the normal direction of the electrode surface. These effects have shown that when the probes are accompanied by a SAM there is almost 100% target binding [158]. Finally, the SAM reduces the capacitance of the electrode as it increases the capacitance layer thickness and prevents charged ions from reaching the electrode surface [141, 159].

The principle of detection of an EIS based DNA pathogen biosensor uses an indirect method of detection based on charge impedance due to DNA hybridisation on the sensor surface (Figure 1.17 A). When the negatively charged ssDNA probe and SAM are formed on the electrode surface and in the presence of a redox solution (most commonly $Fe\,[(CN)_6]^{3-/4-}$) an equilibrium will form and a charge transfer value will be detectable via the charge transfer resistance R_{ct} on an EIS experiment (Figure 1.17 B). When the target DNA hybridises to form double stranded DNA (dsDNA) there is essentially double the negative charge that was present. With a sufficiently dense DNA SAM, the dsDNA can be thought of as creating negatively charged channels. This has a repulsive nature on the negatively charged redox couple, impeding the route to the electrode surface to undergo a redox reaction thus transferring charge (Figure 1.17 C). This effect can be measured as an increase in the charge transfer resistance during EIS and should be easily noticeable on the corresponding Nyquist plot. Having obtained the before and after hybridisation charge transfer resistances the ratio of the two yields a signal increase which statistical analysis can determine any significant difference that would confirm detection of the pathogen [160]. The signal increase ratio can also be used to optimise the system by performing multiple experiments such as adjusting ssDNA concentration, nucleotide length and temperature, to name a few [161, 162]. These optimisations are important and are potentially different for different pathogens, types of electrode and redox agents used.

Improved EIS biosensing results have been found with the use of peptide nucleic acid

(PNA) instead of the ssDNA. PNA is able to bind to DNA via sequence induced base pair interactions, with the negatively charged backbone of DNA replaced with a neutral peptide-based structure in PNA. Thus, when immobilising the PNA a denser coverage is possible due to the lack of electrostatic repulsion between PNA-PNA strands. Also, once the PNA-alkanethiol SAM is formed and the target DNA added to solution, there is an increase in the amount of hybridised probe-target sequences, again due to the reduced electrostatic repulsion. Increased bound target results in an increased charge transfer resistance [163, 164].

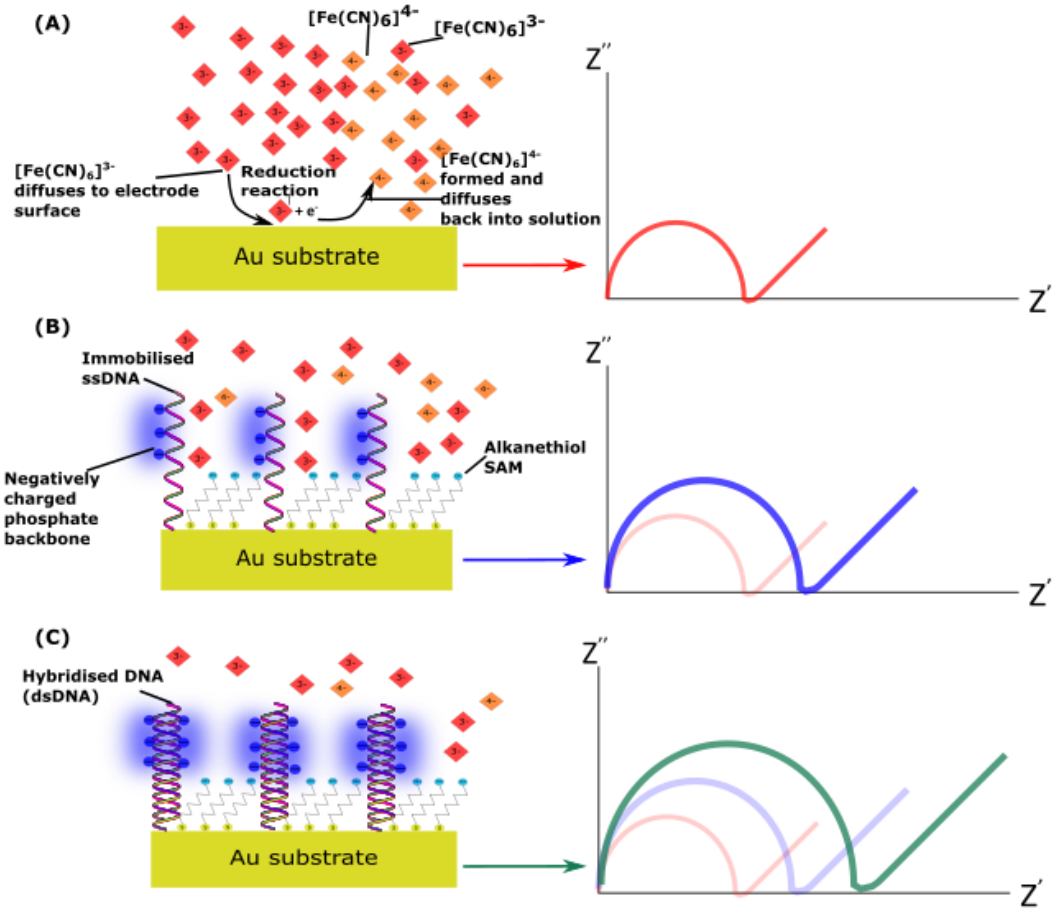

Figure 1.17: A bare electrode reducing $Fe[(CN)_6]^{3-}$ to $Fe[(CN)_6]^{4-}$ unimpeded and the corresponding impedance measurement (A). ssDNA immobilised on the electrode surface with alkanethiol SAM. The negative backbone of the DNA creates some electrostatic repulsion against the anions reducing their flow to the surface increasing the impedance (B). Target DNA hybridises to form dsDNA. This results in an increased negative charge, increasing the electrostatic repulsion and further impeding the ion anion flow to the surface (C).

Microelectrodes and Microelectrode Arrays

The goal of any detection system is to have the most optimised characteristics currently available. In previous sections electrode discussions related to macroelectrodes i.e any device greater than 25 μm in one of its critical dimensions. Macroelectrodes are not the only optimal electrodes for a biosensor. Microelectrodes and microelectrode arrays have many significant enhancements over macroelectrodes, these benefits are listed below.

- Steady-state Faradaic processes develop rapidly due to rapid mass transport.
- Charging current reduction due to small electrode area. Higher Faradaic to non-Faradaic ratios achieved.
- Ohmic drop is reduced due to lower currents. Lower conductivity experiments are therefore possible.
- Accurate CVs at rapid scan rates possible due to reduced charging current.
- Experiments can be conducted on low volumes of analyte due to small electrode dimensions.

1.10 Microelectrodes

Mass transport is a general term relating to the transport of electroactive species in solution to an electrode surface. Three types of transport facilitate the mass transport of ions. They are diffusion due to concentration gradients, convection due to physical force

currents in solution and migration due to electrostatic/dynamic properties. A theory including all three of these components is incredibly complicated. Fortunately, due to quick experiment times, convection can be regarded as negligible and using a background electrolyte that shields ions, allows for migration to be considered negligible. This only leaves diffusion to be considered, reducing the complexity of the studied system.

When a potential is applied to the electrode surface that allows for Faradaic responses to occur, the ion concentration in that region decreases due reduction/oxidation of the species. This results in a concentration gradient from the bulk solution to the electrode surface. This causes the movement of ions from the bulk to replenish this depletion in ion concentration at the electrode surface via diffusion. As time progresses this depleted region gradually increases as more and more of the ions in the bulk solution move to the electrode and undergo redox reactions and is called the diffusion layer. The ratio of electrode surface area and solution volume gives differing types of diffusion behaviour, in particular, decreasing electrode surface area and various geometries show significant diffusion process changes [165]. For Macro disk electrodes the diffusion is planar (perpendicular) to the electrode surface even as time progresses. Microdisk electrodes have time dependent changes in mass transport turning planar diffusion into a combination of planar and radial diffusion see Figure 1.18. As a result, Fick's diffusion law for a microelectrode disk changes from Eqn 1.5 to Eqn 1.6.

$$\frac{\partial c(z,t)}{\partial t} = D\frac{\partial^2 c(z,t)}{\partial z^2} \tag{1.5}$$

$$\frac{\partial c(r,z,t)}{\partial t} = D\left(\frac{\partial^2 c(r,z,t)}{\partial r^2} + \frac{1}{r}\frac{\partial c(r,z,t)}{\partial r} + \frac{\partial^2 c(r,z,t)}{\partial z^2}\right) \tag{1.6}$$

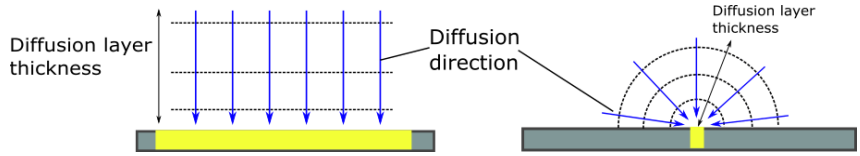

Figure 1.18: Diffusion layer profiles, dotted black lines represent diffusion layer thickness and the blue arrows represent diffusion direction. The figure on the left has diffusion layer thickness smaller than the macroelectrode thus has planar/linear diffusion. The figure on the right has diffusion layer thickness larger than microelectrode so develops planar and radial components giving a hemispherical diffusion.

Chronoamperometry (constant applied potential) experiments have shown the consequences of the mass transport time, electrode area and geometry dependence. In the experiment, the application of a reductive or oxidative potential initiates a diffusion-controlled Faradaic current to flow. The experiment shows that the current density is proportional to the concentration gradient at the electrode surface. As a result for macro disk electrodes with planar diffusion, the time-dependent current obeys the Cotterell equation Eqn1.7. Where i is current, n is number of electrons transferred, F is Faradaic constant, D is diffusion coefficient and t is time.

$$i = \frac{nFAD^{\frac{1}{2}}c}{t^{\frac{1}{2}}\pi^{\frac{1}{2}}} \tag{1.7}$$

When the disk radius becomes small enough i.e when entering the microscale, planar diffusion is accompanied by the radial component adding edge effects at the boundary of the disk see Figure 1.19. This is evidence of a change from planar to a hemispherical type diffusion profile. The time dependence of the diffusion means that the diffusion layer increase in front of the electrode and as a result sees a larger flux of ions to the surface but at larger diffusion layer thicknesses i.e longer times, an equilibrium i.e steady-state emerges and the flux in and out of the hemispherical volume is constant, producing a steady-state current. Therefore, a microdisk electrode's description by the Cotterell equation is modified to a far more complex description (not shown here). It has been shown that in short time regimes the microdisk resembles the macro Cotterell relationship and at longer times i.e when in steady-state, can be modelled by a steady-

state (limiting) current Eqn 1.8. Where the coefficients are the same as in the Cotterell relation with the addition of r for disk radius.

$$i_{ss} = 4rnFDc \tag{1.8}$$

Comparison of these two current relationships clearly shows that macroelectrode disks will produce larger current responses (in similar experimental conditions) compared to micro due to macro having a current dependence on area (r^2) and micro having a dependence on radius (r). The current density of macro devices are usually independent of area and micro is inversely proportional to radius thus, when the electrode radius decreases there is an increase in current density. This coincides with experimental results, showing the improved electric properties of microelectrodes.

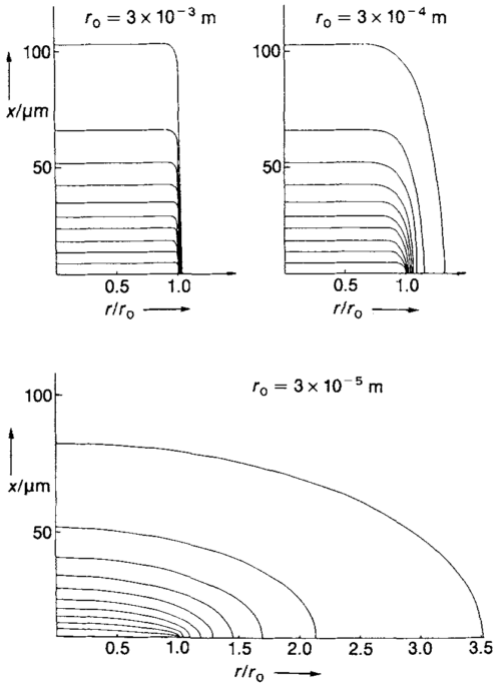

Figure 1.19: Normalised concentration profiles c/c(r,z,t) for disk electrodes of radius 3 mm, 0.3 mm and 30 μm measured after 1 second of experiment start. Concentration is 0 at electrode surface (i.e complete reduction or oxidation at the surface due to large potential pulse) and every concentration curve is 0.1 concentration units apart. [166].

Voltammetry. This is a similar technique to chronoamperometry but instead utilising a linear sweep of potentials is applied in the same manner described in cyclic voltammetry. Microelectrodes in principle produce the same information in these experiments as macroelectrodes. The difference is that microelectrodes reach a steady-state much quicker than macro devices if macroelectrodes even were to reach a steady-state. As mentioned previously short time scales give the normal planar diffusion observed with macroelectrodes and for longer time scales the steady-state is seen thus, by modifying the time of the experiment i.e the scan rate ν (potential per unit time) a microelectrode can be made to mimic a macroelectrode voltammogram. By employing a large scan rate the experiment is quick and resembles macroelectrode responses with peak currents and low scan rates corresponding to longer experiments thus the steady-state is reached and the characteristic sigmoidal plot is seen for microelectrodes. As a consequence of being in the steady-state, currents become independent of time and varying scan rate will not alter the shape and size of the voltammogram. Deviation from the single line sigmoid is often found in real life experiments as the complexities of experimental conditions are difficult to account for. Charging current is one major factor for deviation from the ideal sigmoid with this deviation tending to result in a separation of a single line into two lines that closely follow each other (Figure 1.20). One corresponds to the forward scan and the other for the reverse scan. The deviation is usually most notable in the neck of the CV. Effective electrode cleaning, suitable scan rate and decreasing electrode size will help mitigate large deviations from the ideal sigmoidal profile.

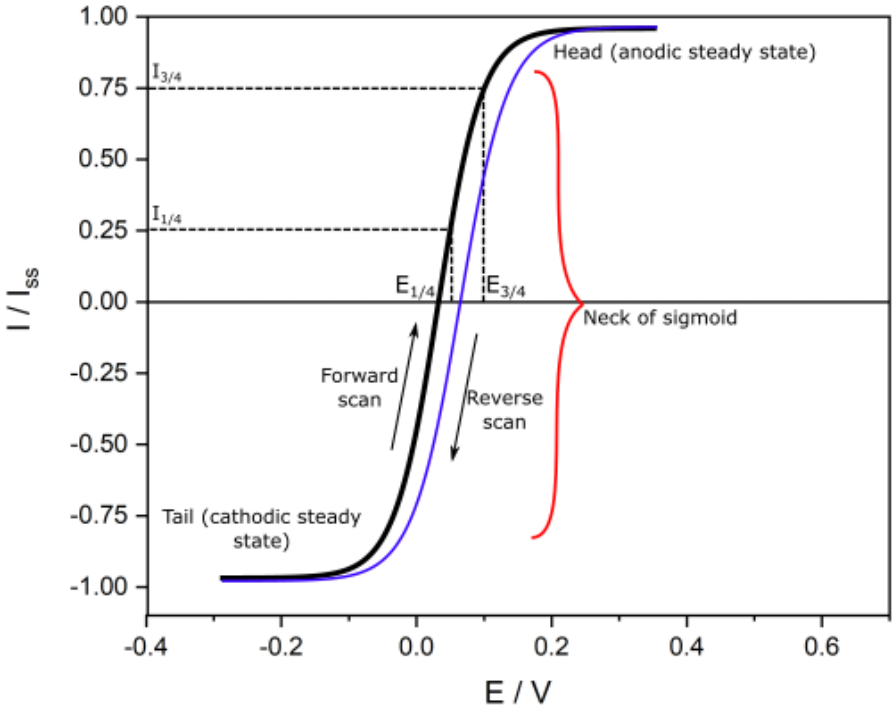

Figure 1.20: Microelectrode CV. This takes the characteristic sigmoidal shape. The anodic steady-state current (head), non-steady-state region (neck) and cathodic steady-state current (tail). Real world CV measurements tend to follow the CV shown by both black and blue lines. An ideal microelectrode under ideal conditions will tend toward the single black line. Analysis of reversibility requires quartile potentials ($E_{3/4}$ and $E_{1/4}$) these are obtained by finding the abscissa that corresponds to the quartile current ordinates ($I_{3/4}$ and $I_{1/4}$).

Charging current is seen in all electrochemical experiments, this is due to the double layer that forms at the electrode surface. As a consequence, there will be a superposition of important Faradaic currents and the unwanted charging current. The non-Faradaic current obscures the true values under investigation. The charging current is proportional to the capacitance of the double layer and the capacitance is proportional to area. By reducing the radius, i.e as with microelectrodes, the capacitance drops and so does the current associated with it. Since the Faradaic current is dependent on the radius, the ratio of Faradaic to non-Faradiac is proportional to the inverse of the radius i.e the

signal to noise ratio improves with reducing electrode radius. Giving microelectrodes superior signal attributes compared to macroelectrodes.

Ohmic IR drop results from the resistance of the electrolyte solution. When a current flows due to a potential E, this would be incorrectly measured, due to the resistance of the solution R_s. The actual measured potential would be E_{eff} = E - iR_s. The Ohmic drop can be decreased by increasing the conductivity of the solution thus lowering the current. Standard practice on macroelectrodes implement a three working electrode system with the reference electrode in close proximity to the working electrode minimising the distance ions will have to travel between the two electrodes in the solution. Electronic feedback was also introduced to reduce Ohmic drop which for most reasonable experiments should cause very few issues nowadays. Microelectrodes have a much lower current associated with them and this results in a significant reduction in the Ohmic drop. It has been shown that under a steady-state diffusion controlled experiment, the Ohmic drop is solely dependent on the electrolyte conductivity. The reduction is so effective that it even allows for low conductivity solutions to be investigated.

1.11 Statistical Analysis

1.11.1 Box Plots

Box plots take obtained data and arrange it into easily visualised and comparable pictographs. The box plot consists of the median and mean of the data. This will be encapsulated in a box and whisker which defines the range of the data (max value - min value) 100 % of the data (Figure 1.21). The box represents the quartile ranges of the data. From the minimum value to the beginning of the box (lower quartile) represents where 25 % of the data lies. From the lower quartile to the end of the box (upper quartile) i.e the length of the entire box represents where 50 % of the data lie. This is called the interquartile range (IQR) (upper quartile - lower quartile). From the minimum whisker to the upper quartile represents 75 % of the data. Sometimes outliers are present and these are represented as dots outside the range of the box and whisker. The criteria for outlier rejection is 1.5*interquartile range. If the data set is normally

distributed the median and mean will tend to coincide about the middle of the box. A deviation from normal distribution is represented by a shift of the median and mean. If the median tends towards the lower quartile this results in positively skewed data (there are a higher frequency of large values) the mean tends to be greater than the median in positively skewed data. Negatively skewed data is the reverse of this with a median nearer the upper quartile (there is a higher frequency of small values) the mean tends to be smaller than the median.

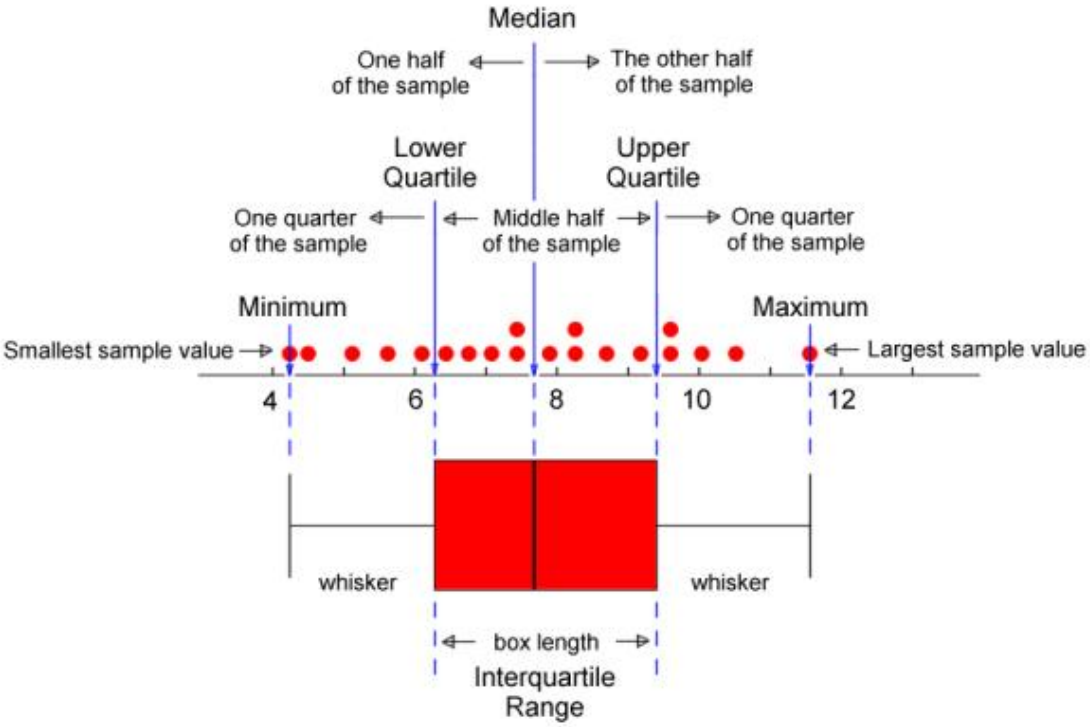

Figure 1.21: Example of a box plot [167]

To compare boxes the position of the median and IQRs is important. If two boxes do not overlap then there is a difference between the two groups. If the median of one data set lies outside the IQR of another data set then they are likely different.

1.11.2 Percentage Change Bar Graphs

When trying to evaluate the measured signal changes between various treatments, it is beneficial to use percentage change. This is easily calculated using Eq 1.9.

$$\left(\frac{\text{New treatment signal}}{\text{Old treatment signal}}\right) - 1 \tag{1.9}$$

If multiple measurements have been made (in most cases it will be multiple electrodes measuring in a single experiment) the mean of the percentage changes from each measurement is taken and plotted on a bar graph with the accompanying standard deviation error. Ideally, for non-control experiments, large signal changes and small standard deviation errors are sought. For control experiments i.e for specificity, small percentage changes and small standard deviation errors are desirable. Overlapping of errors usually indicates that there is likely no difference between groups.

1.11.3 Limit of Detection

To obtain a quantitative indication of the signal response of an electrode to a treatment and input signal, a limit of detection was calculated. The Y-axis limit of detection Y_{LOD} is a measure of how the dependent signal responds to variation of the independent signal or how the ordinate responds to the abscissa. There are many ways to calculate this but the method used here was as follows. Plot the measured signal response versus the independent variable. If the data is non-linear either linearise using linearization methods (commonly transform into a linear-log plot) or find a linear region of the data and perform linear regression. The software used to perform linear regression (Origin Pro 2020a) outputs the Y-intercept value (Y_i) and an associated standard deviation (SD_i). The Y_{LOD} is then calculated from these values using Equation 1.10 [168].

$$Y_{LOD} = Y_i + 3SD_i \tag{1.10}$$

The X-axis limit of detection X_{LOD} is simply the value obtained when the Y_{LOD} is

inputted into the equation of the linear regression and gives an indicated limit as to what independent signal the sensor under test may be able to distinguish from noise.

1.12 Conclusion

The impact of sepsis on global health and finance is immense with the condition costing tens of billions per country and affecting millions of people every year. It is one of the largest contributors to antibiotic resistance which is still probably the largest health crisis faced today. Rates of sepsis are predicted to increase in the future due to the increasingly ageing population.

The pathophysiology of sepsis, in general, follows a known path with the body's immune system reacting to foreign pathogens via an inflammatory response. The inflammatory and immune response flood the body with messengers and mediators to fight such invaders. Unfortunately, the body goes into a complex overdrive dilating vessels in some places leading to arterial pressure drops, constricting it in other areas, reducing blood and oxygen to organs and creating micro-clots. Many other complications can arise making it challenging to treat. If untreated or treatment fails, these effects lead to multi-organ failure then death, with the mortality rate in the developed world between 20-40 %.

The current methods of detection for sepsis are pathogen identification, biomarkers from centralised lab tests such as lactate and physiological symptoms. The identification of bacteria is problematic as it can take up to 72 hours to identify certain bacteria. Rapid bacterial identification would allow for critical information to reach an experienced clinician sooner potentially allowing for quicker treatment and a higher likelihood of the correct use of antibiotics if required, improving patient outcome and reducing the footprint on antimicrobial resistances due to targeted treatment rather than broad-spectrum treatment. Broad-spectrum treatment exposes the bacteria to more of our medicinal arsenal, providing an environment in which to adapt.

To improve detection times, a transition away from purely microbiological techniques, to a combined microbiology and electrochemistry paradigm would be beneficial. Electrochemical techniques such as cyclic voltammetry, differential pulsed voltammetry and

electrochemical impedance spectroscopy are sensitive, rapid, cheap and require less complicated steps in the process of detection, than current techniques. By functionalising an electrode with specific probe DNA for a particular organism and using self-assembled monolayer techniques to further functionalise the electrode, the electrochemical properties of the electrode are changed and are measurable using the techniques mentioned above. The change is a consequence of the DNA and SAM altering the impedance of the electrode via electrostatics due to the negatively charged phosphate groups within DNA and physical blocking by SAMs. When target DNA from a clinical sample is added to the electrode and hybridises with the probe DNA, the impedance is again altered. Measurement of a significant change confirms the presence of a particular pathogen. When designed properly, this works only with the specified bacterial DNA and no other, at least not at significant levels. This results in high sensitivity and specificity from biosensor devices. Similar functionalisation can be undertaken to detect biomarkers for sepsis such as CRP, procalcitonin and IL-6 to aid further sepsis diagnosis and prognoses.

Using microelectrodes and microelectrode arrays instead of the commonly used macroelectrodes allows for vastly improved detection characteristics. Microelectrodes and arrays bring faster mass transport thus quicker times to result. Improved sensitivity is found due to large reductions in physical processes that introduce error, such as Ohmic drop and charging current. Smaller currents due to the micro size of the electrode also increase sensitivity. Multiple electrodes in one chip i.e an array of microelectrodes, each individually addressable, will allow for multiple types of bacterial and biomarker detection's concurrently.

The amount depends on how many electrodes fit in a specified device. This would allow for multiple screening of bacteria, much like in the laboratory and has gained the name of lab-on-chip. These benefits allow biosensor devices to be small and have low power outputs giving bedside diagnostic tests. The relative simplicity of operation allows for clinician use and no requirement for specifically trained professionals. This all potentially sums to rapid and accurate diagnoses of invading pathogens (bacterial/viral/fungal) and biomarkers putting relavant information in clinicans hands sooner allowing for the best possible chances for improved patient outcome and reducing the

impact on antibiotic resistance benefiting and potentially saving millions (fiscally and in terms of mortality).

Chapter 2

Examining Microelectrodes as a Potential Biosensor Platform

2.1 Introduction

Microelectrodes have been theorised and demonstrated to give improved performances over macroelectrodes due in part to their hemispherical diffusion behaviour. This increases the diffusion of redox ions to the surface, reducing the mass transfer rate-limiting factors to a point that the kinetic elements become the rate-limiting factors [141, 169, 170] (Section 1.9). Due to their small surface area microelectrodes give superior Faradaic to non-Faradaic current ratios allowing for improved signal measurements. Microelectrodes show reduced iR drop allowing for use in resistive solutions and improved investigations of analytes without being affected by background ions to aid in conduction.

In this chapter, 25 μm diameter glass pulled gold disk microelectrodes were investigated for their potential use in DNA biosensing. Whilst a large number of electroanalytical studies have been performed with microelectrodes, relatively little literature exists on SAM formation and sensor performance for such devices and although glass pulled microelectrodes are not ideal for biosensor deployment due to their design and the need to perpetually regenerate the surface, they were able to provide insight into some of the mi-

croelectrode behaviours and performance factors that would be beneficial for biosensing. The information gained from these biosensor measurements could later be used to inform the design of individual sensor arrays. The cleaning of glass pulled microelectrodes was investigated first using CV. Similar approaches to those used for gold macroelectrodes were initially tested, but due to the behaviour of the microelectrodes, it was shown that these methods had to be adapted to attain an optimum clean surface. Biosensor performance was investigated beginning with determining whether 3-mercapto-1-propanol (MCP) or 6-mercapto-1-hexanol (MCH) was the optimum molecule to supplement DNA probe immobilisation when forming a SAM layer on the electrode surface. It was found that both molecules produced similar responses making a conclusive determination difficult. MCH was chosen due to its slightly improved consistency.

Target DNA concentration responses were investigated next with a comparison of three different experimental conditions. These conditions allowed the exploration of electrochemical behaviour in response to electrochemical cell configuration; redox buffer strength and composition; wash stringency and incubation times.

Finally, an alternative SAM surface chemistry was investigated. Perfluorocarbon SAM modification was developed in the Department of Pure and Applied Chemistry at the University of Strathclyde. This offered potential for improved SAM capabilities using fluorocarbon chains, which in theory provide reduced surface fouling by contaminants, and potential for surface regeneration without mechanical polishing. For the fluorous system, the probe is tagged with fluorocarbon chains (Figure 2.1) allowing for adsorption into the fluorous SAM via the fluorous effect (tendency for fluorocarbon chains to self-interact avoiding interactions with other molecules) [171, 172]. The fluorous effect can be exploited by introducing solvent wash steps that disrupt the fluorine-fluorine interactions, allowing for the fluorous tagged probe to be removed, ignoring the covalently bonded fluorous SAM, resulting in the potential for surface regeneration and sensor reusability.

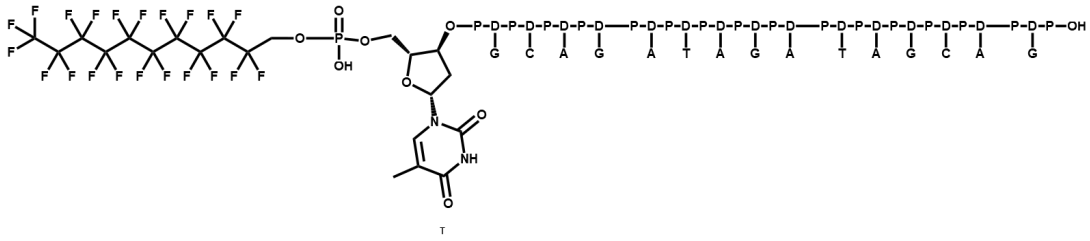

Figure 2.1: Fluorous tagged probe DNA molecule. The DNA sequence is bonded at the 5' end to the prefluoroudecane moiety.

2.2 Materials & Methods

All measurements were taken using a PalmSens4 potentiostat running PSTrace software from Alvatek electrochemical solutions (Houten, Netherlands). The electrodes used were 25 μm diameter glass pulled gold microelectrodes (referred to microelectrodes in this section) and 1.6 mm diameter gold polycrystalline macroelectrodes (referred to macroelectrodes in this section) both purchased from IJ Cambria (Llanelli, UK). Unless otherwise stated the cell setup consists of a working electrode (WE) in this case the microelectrodes and a platinum electrode obtained from Metrohm (Runcorn, UK) as both counter (CE) and reference (RE).

2.2.1 Chemicals

Chemicals used in this work are listed in Table 2.1.

Table 2.1: List of chemicals used in this work.

Chemical	**Composition**	**Supplier**
De-ionised water (resistivity $\geq$ 18 MΩcm)	DI	Sigma-Aldrich
Ethylenediaminetetraacetic acid	EDTA	Metalor technologies Ltd
Hydrochloric acid	HCL	Sigam-Aldrich
Magnesium chloride	$MgCl_2$	Sigma-Aldrich
Methanol	CH_3OH	Sigam-Aldrich
Nitric acid	HNO_3	Sigam-Aldrich
Perfluorodecanethiol	PFT	Sigma-Aldrich
Phosphate buffered saline tablets	PBS	Sigma-Aldrich
Potassium chloride	KCL	Sigma-Aldrich
Potassium hydroxide	KOH	Sigma-Aldrich
Potassium ferricyanide	$K_3[Fe(CN)_6]$	Sigma-Aldrich
Potassium ferrocyanide	$K_4[Fe(CN)_6]$	Sigma-Aldrich
Potassium nitrate	KNO_3	Sigma-Aldrich
Sodium citrate tribasic	SCT	Sigma-Aldrich
Sulfuric acid	H_2SO_4	Sigma-Aldrich
Toluene	C_7H_8	Sigam-Aldrich
3-Mercapto-1-propanol	MCP	Sigma-Aldrich
6-Mercapto-1-hexanol	MCH	Sigma-Aldrich

2.2.2 Buffers

Buffers and their compositions used in this work are shown in Table 2.2. De-ionised water (2.1) was used to make all aqueous solutions.

Table 2.2: List of buffers used and their compositions

Buffer	**Composition**
Acid piranha solution	18 M H_2SO_4 and 30 % H_2O_2 (ratio = 3:1 v/v)
Aqua regia solution	95 % NHO_3, 30 % HCL and H_2O (ratio = 1:3:6 v/v)
Immobilisation buffer (IB)	0.4 M phosphate buffer pH 7.2, 1 M KCl, 5 mM $MgCl_2$ and 1 μM EDTA)
Redox buffer 1	1 mM Potassium ferricyanide/Potassium ferrocyanide in 100 mM KNO_3
Redox buffer 2	5 mM Potassium ferricyanide/Potassium ferrocyanide in 100 mM KNO_3
Redox buffer 3	1 mM Potassium ferricyanide/Potassium ferrocyanide in 1 mM KCl
Redox buffer 4	1 mM Potassium ferricyanide/Potassium ferrocyanide in 0.2 mM KCl
Redox buffer 5	5 mM Potassium ferricyanide/Potassium ferrocyanide in 0.2 mM KCl
Rinse buffer	200 mM PBS + 800 mM KCl pH 7
PBS buffer	200 mM PBS pH 7.8

2.2.3 Probe and Target sequences

A list of probe and target oligonucleotide sequences used and where they were manufactured/purchased is presented in Table 2.3. Note MRSA is methicillin-resistant staphylococcus aureus.

Table 2.3: List of probe and target oligos and their manufacturer

oligonucleotide	**Sequence 5' - 3'**	**Manufacturer**
MRSA probe	[ThiC6]ACTAGGTGTTGGTGAAGATATAACC	Sigma-Aldrich
MRSA target	GGTATATCACCAACACCTAGT	Sigma-Aldrich
TP53 control	GGCACAAACACGCACCTCAAA	Sigma-Aldrich
Fluorous tagged probe	$CF_3(CF_2)_7CH_2CH_2$TGCAGATAGATAGCAAG	University of Strathclyde, Department of Pure and Applied Chemistry
Target for tagged probe	ACGTCTATCTATCGTC	University of Strathclyde, Department of Pure and Applied Chemistry

2.2.4 KOH Cleaning

The microelectrodes were measured by CV in their uncleaned state to establish an uncleaned baseline. This was true for all future unclean tests. All measurements were taken in redox buffer 1 (Table 2.2). The electrodes were then electrochemically cleaned by running 5 CV cycles with a potential window -1.2 V to 0.2 V in 50 mM KOH + 10 mM KCl. They were subsequently tested by CV in redox buffer 1. Following this, the electrodes were electrochemically cleaned as before for 10 cycles and retested.

2.2.5 Coarse Mechanical Polishing and Electrochemical Cleaning

The microelectrodes were tested by CV in their uncleaned state in redox buffer 1. They were then mechanically polished using 400 grit sandpaper (RS Components Ltd, Corby) for two minutes employing a figure-eight motion. They were then rinsed with DI water and sonicated for one minute in DI water. The electrodes were then mechanically polished for a further two minutes on 800 grit sandpaper (RS Components Ltd, Corby) using the same technique. They were again rinsed, sonicated and finally, CV measurements were recorded. The electrodes were then electrochemically cleaned in 0.1 M H_2SO_4 + 100 mM KNO_3 for 5 cycles in a potential window - 0.5 V to 1.5 V. Measurements were then taken in redox buffer 1. For KOH cleaning, electrodes were mechanically polished as described above then cycled 5 times in 50 mM KOH + 100 mM KNO_3 in a potential window of - 1.2 V to 0.2 V.

2.2.6 Fine Mechanical Polishing

The electrochemical cell in these experiments consisted of 25 μM microelectrode as working electrode, platinum counter electrode and saturated 3 M KCL Ag/AgCl reference purchased from IJ Cambria (Llanelli, UK). Redox buffer 1 was used for obtaining CV measurements. All microelectrodes were mechanically polished with fine alumina powder also purchased from IJ Cambria. They were submerged in acid piranha solution for 15 minutes to remove any organic contamination. They were polished using 0.3 mm diameter alumina powder on a polishing pad using the figure-eight motion for two minutes. The electrodes were then rinsed and sonicated in DI water for one minute. They were then polished in the 0.1 mm diameter powder using the same parameters as the previous polish. They were rinsed and sonicated as before. A final polish in 0.05 mm diameter powder and sonication was performed. One group of electrodes n = 4 were further cleaned in the redox buffer by subjecting the electrodes to 1.5 V for 20 seconds, -1.25 V for 20 seconds and 0 V for 5 seconds. CV measurements were then taken. The second group had no other cleaning methods performed and were tested immediately after polishing.

2.2.7 Scan Rate Micro vs Macro

Redox buffer 2 was used for measurements in this experiment. Both micro (n = 2) and macro (n = 3) electrodes were electrochemically cleaned in the redox buffer by running 10 CV cycles in a potential window of - 1.2 V to 0.5 V. After cleaning CV measurements were performed on both sets of electrodes for 10, 25, 50 and 100 mVs^{-1} scan rates.

2.2.8 MCP vs MCH SAMs

For all the remaining experiments, the microelectrodes were cleaned using a 15-minute acid piranha bath and the fine polishing techniques described unless otherwise stated. Redox buffer 1 was used to take all measurements in this section. The electrodes were then incubated in 3 μM MRSA Probe DNA in immobilisation buffer (Table 2.2) for 18 hours at 4 °C. After incubation, they were washed in rinse buffer (Table 2.2). Two electrodes were then incubated in 1 mM MCP in immobilisation buffer and two

electrodes in 1mM MCH in immobilisation buffer for 1.5 hours to form the SAM. They were then washed in the same rinse buffer as above and DPV and EIS measurements were obtained. The two electrode groups were then incubated in TP53 target DNA as a non-specific binding control (Table 2.3) for 30 minutes. They were next washed in rinse buffer and tested again. A DI water wash then removed any hybridised and non-specifically bound target DNA. Following this, the electrodes were subsequently incubated in 2.5 μM fully complementary target DNA (Table 2.3) for 30 minutes. They were washed in rinse buffer, tested and washed with DI water to again remove hybridised DNA. These procedures were repeated for 5 μM and 10 μM specific MRSA target concentrations.

2.2.9 Electrode Response to Functionalisation Parameters

Three treatment groups were employed in functionalising and testing biosensor performances. These treatments all followed the same general biosensor electrode preparation e.g. probe formation, alkanethiol back-filling and SAM formation and finally, target hybridisation. The buffer and solution concentrations, washing steps, incubation times and cell configuration were variables. Table 2.4 summarises the various conditions for each group. Groups 1 and 3 utilised the standard three-electrode cell configuration used in previous experiments. Group 2 used a two-electrode cell configuration consisting of working electrode and a combined platinum RE and CE. All electrodes (n = 5) were incubated at 4 °C in probe solutions using 1 mM immobilisation buffer as the diluent. MRSA probe DNA (Table 2.3) concentrations and incubation times were (group 1 = 3 μM for 20 hr, group 2 = 3 nM for 18 hours and group 3 = 3 nM for 43.5 hr). Group 1 electrodes were then washed with PBS buffer (Table 2.2), groups 2 and 3 were washed with DI water to remove unbound DNA. The electrodes were then incubated at room temperature in SAM solutions, group 1 = 25 mM MCH in 1 mM immobilisation buffer for 1 hr, group 2 and 3 = 3 nM MCH in DI water for 1.5 hr. The electrodes were washed in a DI water bath to remove unbound contaminants for all groups then tested.

All electrochemical tests in these experiments were performed in redox buffer 1 for groups 1 and 2 and redox buffer 3 for group 3. The electrodes were then incubated in

target DNA solutions at room temperature for 30 minutes using 1 mM immobilisation buffer as diluent. PBS buffer was used to remove unspecifically bound target DNA before testing. Group 1 incubations consisted of four concentrations 25 μM TP53 target DNA control, 25 μM, 50 μM and 100 μM specific MRSA target DNA (Table 2.3). All five electrodes were incubated in TP53 first, tested, then washed with DI water to remove hybridised DNA and incubated in the next concentration (smallest to highest). This process was repeated for all concentrations. Groups 2 and 3 had the five electrodes partitioned so that incubations occurred in a single DNA concentration only. Group 2 had two electrodes in 100 μM, two in 50 μM and one in 25 μM. Group 3 had two in 30 nM, two in 15 nM and one in 7.5 nM, as a result of only having five electrodes. The splits resulted in n = 1 for the lowest concentrations and no control DNA.

Table 2.4: Table of group conditions. Note immobilisation buffer = IB. Group 1 electrodes incubated in all target DNA concentrations. Group 2 and 3 electrodes partitioned into smaller groups and incubated in single target DNA concentrations.

Preparation	Group 1	Group 2	Group 3
Cell configuration	3 electrode cell (WE, platinum RE and CE)	2 electrode cell (WE, combined platinum RE and CE)	3 electrode cell (WE, platinum RE and CE)
Redox buffer	Redox buffer 1	Redox buffer 1	Redox buffer 3
Probe DNA	3 μM in 1 mM IB 20 hr @ 4 °C	3 nM in 1 mM IB 18 hrs @ 4 °C	3 μM in 1 mM IB 43.5 hr @ 4 °C
Probe wash	PBS buffer	DI water	DI water
SAM (MCH)	25 mM in 1 mM IB 1 hr @ room temp	3 nM in DI water 1.5 hr @ room temp	3 nM in DI water 1.5 hr @ room temp
SAM wash	DI water	DI water	DI water
Target concentration	25 μM TP53 control DNA, 25 μM, 50μM and 100 μM specific DNA in IB buffer 30 mins @ room temp	25 μM, 50μM and 100 μM specific DNA in IB buffer 30 mins @ room temp	7.5 nM, 15 nM and 30 nM specific DNA in IB buffer 30 mins @ room temp
Target wash	PBS buffer	PBS buffer	PBS buffer
Hybridised DNA removal	DI water bath	NA	NA

2.2.10 Fluorous SAM and Probe Modification

All incubation stages were performed at room temperature for all fluorous experiments. All fluorous SAM experiments used a two-electrode electrochemical cell, working and combined counter reference using platinum wire. All measurements were taken using redox buffer 4 (Table 2.2) unless otherwise stated. The various conditions that were applied to the electrodes in this section were not performed in a single experiment but over multiple experiments. Thus there are repeats and various combinations of the conditions. These are laid out clearly in the results section.

An important note for fluorous based SAM experiments is that the base SAM layer is immobilised before the probe is introduced as the probe binds to the SAM, not the gold electrode surface (Figure 2.1). This is the reverse of the standard alkanethiol SAM formation procedure. All electrodes (n = 5) were incubated in perfluorodecanethiol (PFDT) using toluene as a diluent. The concentrations used were 1 μM, 317 nM and 34.9 nM. The last two concentrations were chosen to give lower concentration responses. The electrodes were incubated for 1 hr, 2hr and 24 hr. The electrodes were tested after being washed with DI water, pure methanol and 10 % methanol.

After the SAM stage underwent testing, the electrodes were incubated in 1 μM probe DNA (Table 2.3) with DI water as the diluent. The incubation times were 1 hr, 2 hr, 19 hr and 24 hr. The electrodes were washed with toluene and nitrogen dried before being tested. They were replaced in solution for the next incubation time point.

2.2.11 Target Detection on Fluorous Modified SAMs

After functionalising with fluorous SAM and fluorous tagged probe the electrodes were incubated in target DNA (Table 2.3). The diluents used were DI water and 1 mM KCL. The concentrations of target DNA used were 10 nM, 1 μM and 10 μM. The various incubation times were 1 hr, 2 hr, 19 hr, 24 hr and 4 days. The electrodes were tested between incubations after being washed with DI water or sodium citrate tribasic (SCT).

2.2.12 Reusability of Fluorous Biosensors

The electrodes were washed using a 30 minute 30 % methanol - 30-minute toluene - 30 minute 30 % methanol protocol to remove the hybridised fluorous tagged probe leaving the fluorous SAM attached to the electrode surface. The electrodes were then incubated with 1 μM probe DNA in DI water for 1 hr, the same solution as the first probe incubations. They were subsequently tested after a toluene wash and dried with nitrogen.

The electrodes were then incubated for a second time in target DNA. The concentrations were 33.3 nM and 10 μM diluted using DI water or 1 mM KCL. The incubation times were 30 minutes and 1 hr. The electrodes were washed with DI water or SCT and tested.

2.3 Results & Discussion

2.3.1 Cleaning of Microelectrodes

The electrode surface is the foundation on which DNA-SAM biosensor elements are formed. It is therefore of vital importance that the surface is adequately clean before any biosensor functionalisation is performed. Electrode measurements are a result of electron transfer to and from a redox species and electrode surface. If the electrode surface is contaminated, it can hinder electron transfer which will result in incorrect interpretation of the kinetics for the reaction [173]. In addition, surface contamination leads to improper SAM formation, further affecting sensor performance.

For gold electrodes, there are many well-researched methods for cleaning the surface of impurities [173]. This is true for all types of gold electrodes. Various cleaning methods were investigated with microelectrodes to find optimal performances. Comparing to the macroelectrode was beneficial as microelectrodes have their own distinctive behaviours [166, 174]. Therefore, by confirming an absence of macro behaviour and a comparison to micro behaviour in literature, gave further confidence in successful surface preparation.

Determining the effectiveness of cleaning techniques commonly employs the use of CVs.

Certain electrochemical behaviours will be present in a CV of clean electrodes, the profile of the CV is one such behaviour. Microelectrodes have in general a slender sigmoidal shape (Figure 1.20) with low capacitive currents and steady-state currents at each of the cathodic and anodic regimes, this behaviour results from equation Eqn 1.8. The explanation for this was discussed in Section 1.9. Departure from this sigmoidal shape is a sign of electrode contamination or a change in diffusion profiles due to large scan rates. Therefore, a visual gauge of successful cleaning can be observed from the CV profile whilst employing a suitable scan rate (0.1 - 1 V/s). Using measured steady state currents and rearranging equation Eqn 1.8 in terms of area A, a qualitative characteristic of cleanliness can be obtained, the real working area (A_{real}) of the electrode. This is a measure of how much surface area is available for redox reactions. If the surface is contaminated, this will usually give a reduced (A_{real}) value compared to a clean surface. Note during the calculation of (A_{real}) only the anodic current was used to determine the area, thus a D_{ox} (ferricynaide) value of 0.726E-5 cm^2/s was used [175]. Often this real working area is taken as a percentage of the geometric area of the electrode [176]. The geometrical area is that expected from calculating the area from the electrode's size and shape, i.e. πr^2. A parameter %Real can be therefore calculated using (%Real = (A_{real}/A_{geo}*100)). This will most probably differ from 100% since the electrode surface is not strictly two-dimensional, containing valleys and peaks at the atomic level as well as deeper scratches due to surface damage.

Another measure of surface contamination can be obtained from the CV voltammogram. With the use of peak separation i.e., if the redox peaks (macroelectrodes) and steady-state currents (microelectrodes) are within the Nernstian limit [177]. The redox couples (potassium ferricyanide and potassium ferrocyanide) used throughout this thesis can behave quasi-reversibly [178] at a scan rate of 0.1 V/s as such, can deviate from the Nernstian limit but should be within acceptable limits. It has been shown that during EIS experiments that CN^- ions are released and etch the gold surface making repeatable measurements difficult [179]. Although EIS is not employed in this section it is throughout the rest of this chapter and research and should be kept in mind that potential cyanide ion damage to the gold surface may be occurring during electrochem-

ical experiments, causing further departure from the Nernstian limit. Macroelectrodes in a Nernstian regime should also produce ratios of peak cathodic (I_{pc}) and anodic current (I_{pa}) = 1 and the separation peak potentials (E_{pc} - E_{pc}) = ΔE_p = 59/n mV, where n is number of electrons transferred in reaction. In the case of the redox buffer used in this study n = 1 thus ΔE = 59 mV (this value is a special case when the temperature is 298 K). Microelectrodes steady-state currents instead of peak currents, cathodic (I^c_{ss}) and anodic (I^a_{ss}) = I^{ss}_{ratio} = 1. The separation peak potential does not exist for microelectrodes thus the Tomes criterion [141] was used ($E_{3/4}$ - $E_{1/4}$) = ΔE_{ss} = 56 mV. Comparing measured results to these values provides adequate evaluation of surface contamination. Real world processes and behaviours deviate from theoretical assumptions and are therefore beneficial only as a guide. when comparing values to determine surface cleanliness it should not be expected to see measured values match theoretical values exactly. A list of all the cleaning parameters and their corresponding results are summarised in (Table 2.5).

Table 2.5: Table of cleaning parameters and their corresponding values. In an ideal theoretical reversible Nernstian system ΔE_{ss} has a theoretical limit value of 56 mV, I^{ss}_{ratio} = 1 and %Real = 100 %. All electrochemical cleaning was preformed using a potential window of -0.5 - 1.8 V and a sca rate of 0.1 V/s.

Cleaning Method	**%Real**	$\mathbf{I^{ss}_{ratio}}$	$\mathbf{\Delta E_{ss}}$(mV)
KOH cleaning			
Uncleaned	50.4	0.92	151
5 cycles	87.5	0.86	47
10 cycles	137	1.08	60
Coarse mechanical polishing + Electrochemical cleaning			
Uncleaned	30	0.68	225
Coarse mechanically polished	135	0.85	41
Coarse mechanically polished + H_2SO_4	140	0.71	57
Coarse mechanically polished + KOH	210	0.87	33
Fine polishing			
fine polished + electrochemical cleaning	240.8 ± 194	1.126 ± 0.37	144 ± 0.08
fine polished only	103 ± 15	0.79 ± 0.028	37.8 ± 0.005

KOH cleaning

KOH cleaning techniques are a common method for removing contaminates on gold electrodes [173]. They also tend to be less aggressive (damaging to the electrode surface) cleaning techniques and were employed as a benchmark for other cleaning techniques. Microelectrodes were cleaned in KOH for 5 CV cycles and 10 CV cycles to show the effect of this common electrochemical cleaning method for gold electrodes. The CVs of uncleaned, 5 cycles KOH and 10 cycles KOH are shown in Figure 2.2. The unclean CV showed little resemblance to a sigmoidal curve and did not meet the criteria for a reversible redox reaction implying an unsuitable electrode surface. The calculated %Real = 50.4 % and the ratio of cathodic and anodic steady-state currents was $I^{ss}_{ratio} = 0.92$. This was close to the expected value for a reversible Nernstian system $I^{ss}_{ratio} = 1$. It must be noted, however, that this CV response did not have a complete steady-state current and therefore the currents at the furthest edges of the potential window were used as approximations. This was true for all the following analyses of microelectrode CVs that did not show complete steady-state currents. This will be a suitable approximation in a full steady-state system but will have limitations on non-steady-state systems.

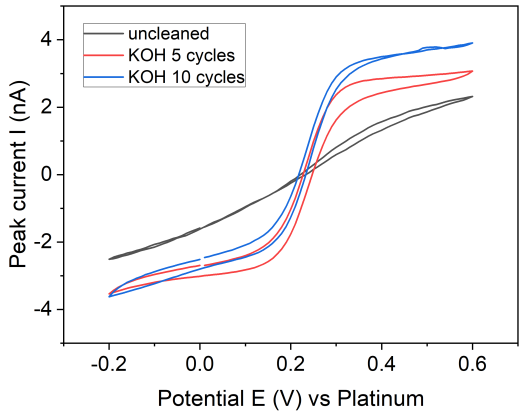

Figure 2.2: CVs obtained in redox buffer 1 of uncleaned microelectrode and after, 5 cycles CV and 10 cycles CV cleaning in 50 mM KOH with a potential window of - 0.2 V to -1.2 V (vs Platinum).

ΔE_{ss} = 151 mV, this was about three times the theoretical limit (56 mV), thus adding further evidence that the electrode surface was contaminated.

The CV (red) obtained after 5 cycles in 50 mM KOH showed a good approximation to the ideal sigmoidal shape and had a calculated %Real = 87.5 %, an improvement over the uncleaned surface. It presented with a good steady-state anodic current but the cathodic current demonstrated a slight negative slope. I^{ss}_{ratio} = 0.86 which was further from unity than the unclean electrode. This was most likely due to the non-steady-state slopes in both CVs and as such was still a reasonable approximation of a reversible system. ΔE_{ss} = 47 mV was below the theoretical limit of 56 mV for a one-electron transfer reversible system. This can happen if the redox molecules adsorb onto the electrode surface. Peak or steady-state current separation is due to the mass transport of the redox molecules. If the molecules adsorb onto the surface, there is a signal component not dependent on mass transport shortening the current separation [180] leading to sub-Nernstian values. This behaviour is an example of a quasi-reversible system. It was clear though, that this CV indicated a cleaner electrode surface compared to the uncleaned electrode. There still appeared to be contamination present evidenced by the sloping cathodic current tail and the larger deviation from unity for the current ratios.

The 10 cycle KOH cleaning results (blue) showed higher steady-state currents and a thinner neck (lower forward and reverse scan separation i.e reduced charging currents see (Section 1.9)) compared to 5 cycles which were evidence of a cleaner surface. It does, however, deviate from a steady-state current at both anodic and cathodic currents indicated by the slight sloping at the head and tail of the CV. I^{ss}_{ratio} = 1.08 which was close to unity and ΔE_{ss} = 60 mV which was within 6 mV of the theoretical limit. These results suggested a relatively clean electrode surface by showing that the electrochemical reactions were behaving in a Nernstian manner as demonstrated in the literature [141, 169, 170]. A %Real = 137 % provided the best value of the three treatments so far.

It was obvious from visual observation of the CVs that the cleaning methods improved the contamination levels of the electrode surface. With 10 KOH perhaps showing a slight decline as evidenced by the sloping head and tail, this may be due to random and or systematic errors though the deviations in slope gradient were small compared to 5

cycles. The quantitative parameters proved to be a useful guide but also demonstrated the measured vs theoretical differences discussed earlier. Also, note that approximations in the steady-state currents were used due to some CVs having sloped cathodic and anodic currents instead of the optimal flat steady-state currents. This added further deviation in the calculations of these parameters. The comparison was still suitable as all CVs used the same approximation method and therefore were self-consistent within the analysis. It appeared that KOH cleaning between 5 - 10 cycles produced the optimal cleaning effect for gold microelectrodes. Further cycles in KOH did not produce improved changes in the CV responses, in some cases, electrodes experienced a decline.

Coarse mechanical polishing and electrochemical cleaning

Following the results of KOH cleaning, it was apparent that the steady-state currents contained a background slope. To improve this behaviour, the microelectrodes underwent coarse mechanical polishing before electrochemical cleaning. KOH was again employed as an electrochemical cleaning technique in addition to H_2SO_4 used as a more aggressive chemical cleaning agent for comparison.

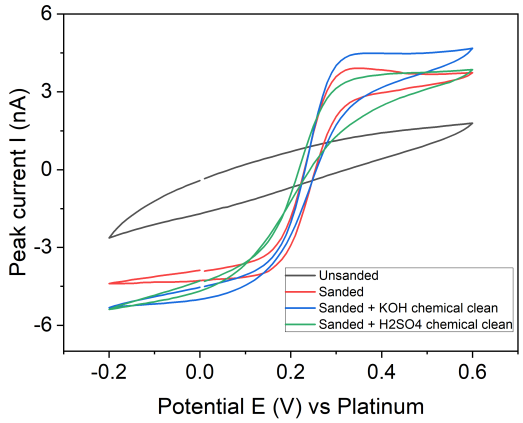

Figure 2.3: CVs obtained in redox buffer 1 of unpolished microelectrode and after, coarse polishing only, coarse polishing + 5 cycles 0.1 M H_2SO_4 and coarse polishing + 5 cycles 50 mM KOH. with a potential window of -0.5 V to 1.5 V for H_2SO_4 and 0.2 V to -1.2 V for KOH (vs Platinum).

As expected, the untreated surface produced no sigmoidal current response (Figure 2.3).

The cleaning parameters were $I^{ss}_{ratio} = 0.68$, $\Delta E_{ss} = 225$ mV and %Real = 30 %. These values were indicative of an unclean surface that was unable to facilitate the desired redox reactions.

The sigmoidal profile was present in the coarse polish only treatment although was accompanied by a small peaking anodic current suggesting a slight deviation from microelectrode behaviour (Figure 2.3). The cathodic current was as expected for microelectrodes. The current ratio $I^{ss}_{ratio} = 0.85$ showed improvement from the unpolished surface. The quartile potential separation was significantly improved with a value of $\Delta E_{ss} = 41$ mV and a %Real = 135 % was obtained. From these results, it was apparent that coarse polishing alone can bring an unclean surface into a mostly microelectrode regime and Nernstian state. These values were similar to the KOH 5 cycles cleaning method, having slightly better CV profiles.

The combined coarse polishing plus H_2SO_4 for 5 cycles treatment showed similar steady-state currents as coarse polishing only and saw the removal of the small anodic peak current behaviour (Figure 2.3). The cathodic current showed the reappearance of the sloping behaviour seen with KOH cleaning. The reverse scan current intersected the forward scan current, giving a distorted overall profile. $I^{ss}_{ratio} = 0.71$ (reduction from the coarse polish only treatment), $\Delta E_{ss} = 57$ mV gave the closest value to the theoretical limit and %Real = 140 % suggested a cleaner electrode surface than coarse polishing only. Though, it was also true that chemical cleaning can have adverse effects on the surface as evidenced by the current ratios, altered sigmoidal CV neck shape and cathodic sloping current. The use of H_2SO_4 may have been too aggressive physically damaging the surface when removing contaminants. A return to a less aggressive chemical was implemented to test this hypothesis.

The final treatment composed of coarse polishing plus KOH cleaning (as it showed the most favourable results in the previous experiment). The CV displayed increased steady-state currents compared to the other treatments suggesting reduced impedance and a respectable sigmoidal profile although the sloping cathodic current was still present with a shallower gradient compared to the H_2SO_4 treatment. The calculated cleaning

parameters were I^{ss}_{ratio} = 0.87, ΔE_{ss} = 33 mV and %Real = 210 % indicating a clean electrode surface and reversible system.

All cleaning treatments exhibited greater than 100 % %Real as expected. Again, the quartile potential separations mostly showed lower values than the Nernstian limit eluding to the adsorbed redox couples on the electrode surface. Electrochemical cleaning seemed to damage or alter the surface producing augmented CV profiles with self-intersecting currents and sloping at the cathodic regions. These results demonstrated that the coarse polishing plus KOH electrochemical cleaning technique produced the cleanest electrode surface so far. It was apparent that the coarse mechanical polishing was effective at removing contamination from the surface but the grit of the polish pad left large scratches on the gold surface. It was beneficial to investigate whether polishing these scratches to a smooth finish could further increase the performance of the electrode.

Fine mechanical polishing

The previous section showed that electrochemical cleaning tended to disturb the microelectrode CV. It was also likely that the coarse mechanical polishing process left large scratches on the electrode surface. In an attempt to avoid this, electrochemical cleaning was substituted with fine mechanical polishing. With access to more microelectrodes, it was possible to carry out more measurements and achieve more repetitions. Figure 2.4A showed the CVs from four microelectrodes that were coarsely polished and electrochemically cleaned (this served as a control).

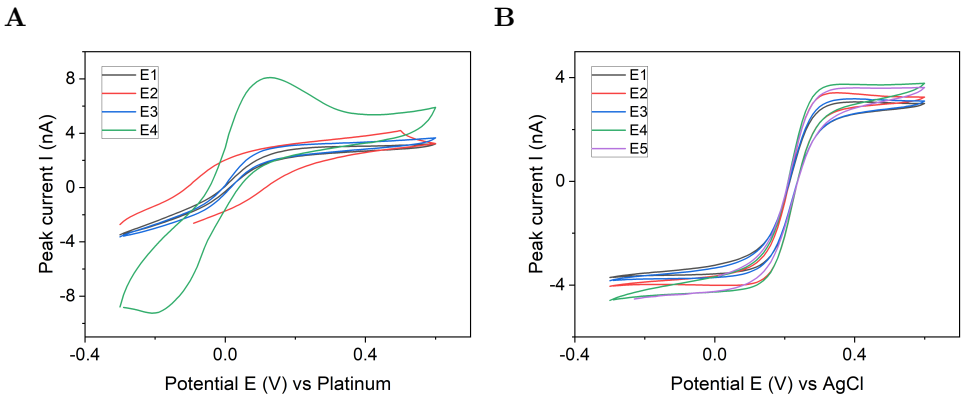

Figure 2.4: CV response of polished and electrochemically cleaned microelectrodes n = 4 (A). The electrochemical clean consisted of holding the electrodes at 1.5 V for 20 s then - 1.25 V for 20 s and finally 0V for 5 s. Electrodes two and four displayed the worst responses with electrode two having no appreciable CV profile and four having a purely anodic response that was more macro in behaviour, evidenced by the peak current. Only polished microelectrodes n = 5 (B). Measurements taken in redox buffer 1 (vs Ag/AgCl).

The CVs varied in size and profile producing an average $I^{ss}_{ratio} = 1.126 \pm 0.37$. This was close to unity which suggested reversibility. This behaviour was produced for two of the CVs (electrodes two and three), and it was visibly clear from the other two CV profiles they were not reversible. $\Delta E_{ss} = 144 \pm 0.08$ mV showed the irreversible nature of the system. %Real = 240.8 ± 194 % was large and as previously discussed high values can be a sign of a clean surface, but in this case, the high current of electrode four had skewed the area calculations to larger values. Although some parameters produced values that suggested the system was a reversible Nernstian state, the large variation in CV shape and sizes most likely cancelled upon averaging leading to agreeable values. A quick visual inspection provides obvious evidence that these electrodes were not in a suitably clean state.

For electrodes that only underwent fine mechanical polishing, the following CVs were obtained (Figure 2.4B). The CV profiles were sigmoidal with flat steady-state currents at both anodic and cathodic currents, all of which were closely situated to one another demonstrating consistency across the devices. $I^{ss}_{ratio} = 0.79 \pm 0.028$ was not as close to unity as expected but was consistent over the five electrodes and appeared to be the

value that thoroughly cleaned microelectrodes will produce. The deviation from unity could also be linked to adsorbed redox molecules on the surface skewing the current behaviour, which was seen many times with the sloping tail in cathodic reactions. The evidence for adsorbed material was further supported with ΔE_{ss} = 37.8 ± 0.005 mV. This matched many of the single electrode values seen in previous sections. These two parameter values showed evidence of a clean electrode surface in a reversible Nernstian system, slightly skewed by adsorbed redox molecules. The small errors gave confidence in device consistency and this was the correct behaviour for these electrodes in this redox medium. %Real = 103 ± 15 % again showed good evidence for a clean and finely polished surface being similar to the geometrical area with low associated error values across the electrodes.

Although higher values are sometimes still suitable indicators of cleanliness, they have also been shown to be a sign of surface damage or alteration as evidenced by the worsening cathodic current sloping seen in previous sections. As mentioned with the current ratios, this may be due to the previous cleaning methods suitably cleaning the surface while simultaneously also making it facilitate higher adsorption increasing the currents which affect all the parameters calculated.

Further fine polishing and cleaning did not improve the CVs obtained in (Figure 2.4B). It was concluded that microelectrode contamination removal was possible using different cleaning techniques. However, electrochemical cleaning methods may damage or alter the gold surface in such a way that adsorption of redox molecules is more favourable resulting in sloped cathodic currents with, I^{ss}_{ratio} values shifted from unity, ΔE_{ss} values falling below the theoretical Nernstian limit of 56 mV and larger calculated %Real area values. Even with approximations being made on calculations due to non-steady-state currents and deviations from ideal CV profiles, the results instilled confidence that the surface was suitably clean and usable for biosensor functionalisation experiments. It must also be noted that in Figures 2.2, 2.3 and 2.4B the profiles all displayed a positive shift in the equilibrium potential. This is most likely due to contamination or issues with the working/reference electrodes.

The optimal cleaning method was demonstrated to be fine mechanical polishing resulting in smooth, consistent and exemplar CV profiles. The values did not match exactly to theoretical values due to the inevitable differences between real world and theory but were considered to be good approximations. These calculated parameters out-competed other electrode platforms available at the time: for example, screen printed electrodes (SPEs) where peak separations could be > 100 mV. The parameters calculated for the finely polished electrodes still showed signs of adsorption but produced smaller associated errors. From these values, it was concluded that this was the standard behaviour of microelectrodes utilising this redox couple. The fine mechanical polishing method was adopted as the preferred method of preparing glass pulled microelectrodes for future experiments.

Microelectrodes and macroelectrodes

It was shown in previous sections that glass pulled microelectrode electrochemical responses were as expected compared to literature. As further evidence that the microelectrodes were behaving as expected, they were compared to macroelectrodes, specifically their CV profile and dependence of scan rate on current outputs. Macroelectrodes in the presence of a reversible redox medium should have a linear relationship between current and the square root of the scan rate ($\nu^{1/2}$). This occurs because faster scan rates prevent the diffusion layer from growing quickly meaning diffusion is still strong resulting in higher currents. As the scan rate slows the diffusion layer has more time to expand resulting in longer diffusion times of the redox molecule and smaller currents [141, 169, 170]. (Figure 2.5A) showed the CV responses of a macroelectrode at 10, 25, 50 and 100 mV/s. The peak currents increased with scan rate as stated in the literature. Also, note the peak current potentials remain fixed i.e. they are independent of scan rate. This should be the case for a reversible system [141, 169, 170]. The reduction peaks are distorted displaying more of spiked peak than a smooth peak. This is most likely due to contamination from Prussian blue, a pigment produced by oxidation of ferrous ferrocynaide salts. (Figure 2.5B) demonstrated the dependence on the square root of scan rate on current. Both anodic and cathodic current responses were linearly

dependent on $\nu^{1/2}$ again confirming a reversible Nernstian system.

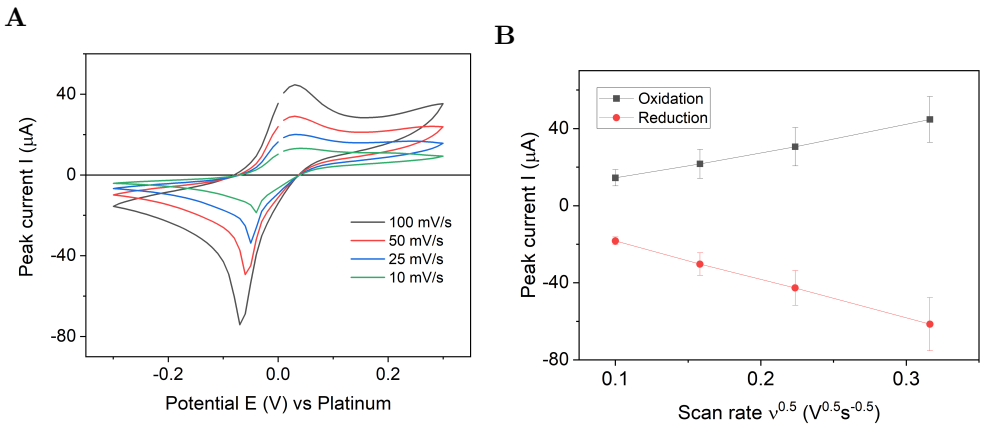

Figure 2.5: CV response of macroelectrode due to varying scan rates (A). The corresponding current response to the square root of the scan rate (B). Scan rates used were 10, 25, 50 and 100 mV/s (Vs platinum). Measurements taken in redox buffer 2.

Microelectrode steady-state currents should be independent of $\nu^{1/2}$, this is due to the change from linear diffusion to hemispherical diffusion (Section 1.9) [170]. Figure 2.6A showed the steady-state currents remained mostly unchanged by the various scan rates. The necks of the CV slightly shifted; this was most likely due to a small dependence on scan rate due to the brief formation of a linear diffusion profile in these regions. The steady-state current was shown to have no dependence on ($\nu^{1/2}$) (Figure 2.6B) as evidenced by the flat constant line response for both anodic and cathodic currents. The final scan rate data point seemed to slightly deviate from the flat line. This could be due to a random measurement deviation from what was expected or could be the beginning of the failure of this independence of ($\nu^{1/2}$). As the scan rates become fast enough the non-Faradaic currents can become large enough to obscure the Faradaic currents and thus gain dependence on ($\nu^{1/2}$). This usually happens at much higher scan rates than 100 mV/s and is an unlikely reason for this. It was noted that 10 - 100 mV/s is the standard working range for biosensor measurements, so any further investigation outside this range would have been purely for indulgence.

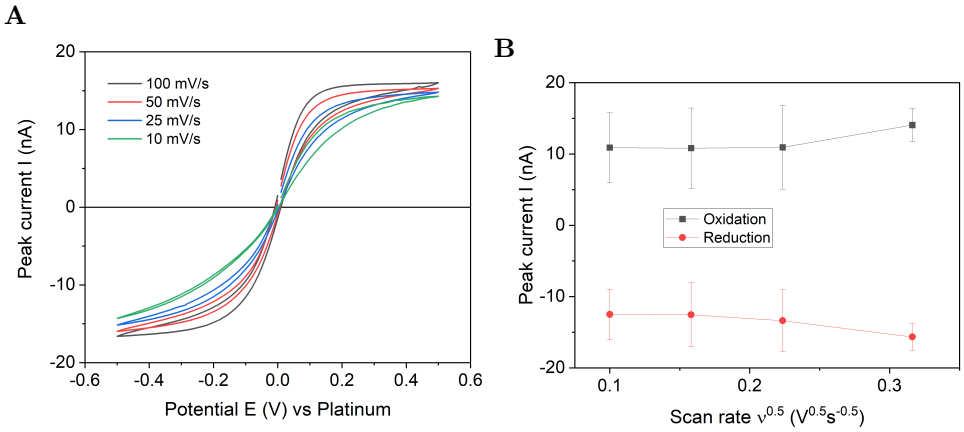

Figure 2.6: CV response of microelectrode due to varying scan rates (A). The corresponding current response to the square root of the scan rate (B). Scan rates used were 10, 25, 50 and 100 mV/s (Vs platinum). Measurements taken in redox buffer 1.

It was shown that glass pulled microelectrodes produced the correct behaviour displaying no steady-state current dependence on scan rate and thus ($\nu^{1/2}$), this was further supported by direct comparison to the macroelectrodes that showed peak current dependence on scan rate due to a planar diffusion profile. The information presented in the cleaning technique and microelectrode behaviour sections showed that the glass pulled electrodes were optimally cleaned and appropriately prepared for biosensor functionalisation, beginning with the immobilisation of probe DNA and alkanethiol SAM onto the electrode surface. The optimal SAM molecule to supplement the probe DNA was examined next.

2.3.2 Optimising for DNA Detection

MCP vs MCH as the diluent in a DNA SAM

Due to differences between micro and macro electrodes such as electrode area, electrochemical behaviour and diffusion profiles, there was potential that SAM formation on the electrode surface would also be different. Therefore, the supplementary SAM molecules already optimised for macroelectrodes may require modification to be fully optimised for microelectrodes. To investigate SAM molecule performance two routinely used chemicals in SAM formation were compared. MCP and MCH (Table 2.1) were

used to form a SAM supplementing already immobilised MRSA DNA. A well-formed SAM should show a significant signal difference between the clean surface stage and immobilised SAM stage.

From the data obtained from Appendix A.1A, no conclusive determination could be made on which chemical modification was most optimum. However, MCP produced a less varied EIS signal change and larger DPV signal change compared to MCH.

The type of molecule used in forming SAMs can affect target binding efficiency [181, 182]. It was therefore not only important to find the optimum SAM forming molecule, but also the molecule that optimised target DNA hybridisation, as this was a crucial factor for biosensor performance. MCP and MCH were tested at various functionalisation stages, these being SAM, 2.5 μM, 5 μM, 10 μM target DNA and TP53 target control stages.

From the DPV and EIS target DNA hybridisation results (Appendix A.2), there was no substantial evidence that MCP outperformed MCH. It was concluded to continue with MCH as the alkanethiol molecule for SAM formation on microelectrodes. With the optimal SAM molecule determined, it was necessary to find the best target hybridisation response. This was a critical stage for biosensor functionality.

Target DNA hybridisation response to various experimental parameters

The investigation into optimal target DNA hybridisation response employed various experimental setups and functionalisation parameters. It was possible to conceptualise why functionalisation parameters could lead to different target hybridisation responses but the effect of electrochemical cell setup was not clear and was included in the analysis. Investigation into the response to various target DNA concentrations for two different electrochemical cell setups and functionalisation preparations were undertaken by separating the electrodes into multiple groups summarised in (Table 2.4) and described in Section (2.2.9).

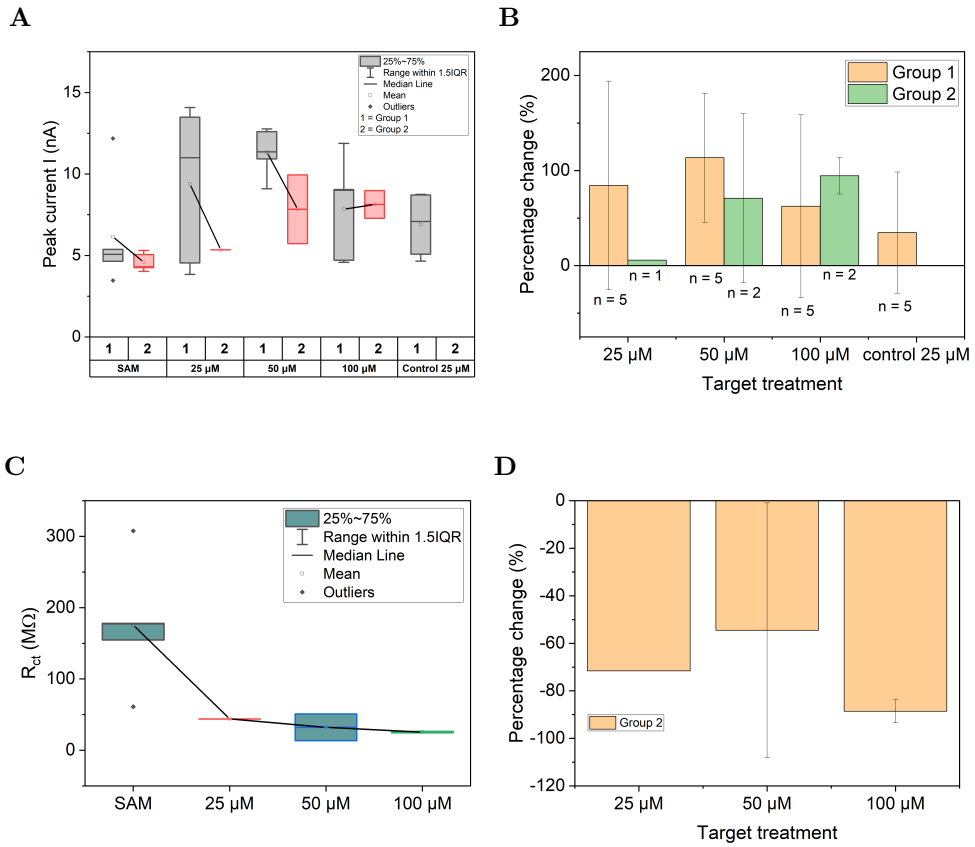

Figure 2.7: Box chart of group 1 and group 2 incubations data for SAM, 25 μM, 50 μM, 100 μM and control stages (A), DPV signal percentage changes for target DNA stages vs SAM stage (B) corresponding EIS box chart data (C) and EIS signal percent change (D). Measurements taken in redox buffer 1. DPV settings (potential window -0.2 - 0.6 V, scan rate 0.1 V/s, E pulse 0.2 V and t pulse 0.02 s. EIS settings (E_{dc} vs OCP = 0.0 V, frequency range: 0.1 Hz to 100 kHz). Group 1 is a three electrode electrochemical cell (CE = platinum and RE = platinum) with incubations of 3 μM probe, 25 mM MCH SAM and successive target incubations for all electrodes. Group 2 is a two-electrode electrochemical cell (combined RE and CE = platinum) with 3 nM probe, 3 nM MCH SAM and split single target incubation's.

Figure 2.7 showed the DPV and EIS responses to 25 μM, 50 μM, 100 μM complementary target DNA and 25 μM TP53 non-specific DNA (control) concentrations. Group 2 had no EIS data due to high noise levels, even when grounded in a Faraday cage. No target DNA control was present due to lack of electrodes (5 electrodes were partitioned into 3 target DNA hybridisation concentrations therefore there were no electrodes left for target DNA control testing). Figure 2.7A showed that the SAM data in both groups

were similar and so there was consistent SAM formation on microelectrodes even with the SAM concentrations differing by a magnitude of 10^6 between the two groups.

Upon the addition of target DNA, the response became more varied as indicated by the larger data spread. Group 2 had a small dose-dependent trend supported by the signal percentage change (Figure 2.7B) displaying an increasing current response to increasing target concentration. The 50 μM target incubation showed particularly significant variation, this could be due to the nature of SAM formation which is known to be variable [183] but these microelectrodes had already been shown to have highly variable responses discussed in limitations of work. Group 1 incubations failed to produce a dose-dependent response and was more peak-like behaviour with the maximal response at 50 μM. This was again confirmed by the signal percentage change data peaking at 50 μM with 110 % response. The target DNA control incubation showed an appreciable signal when compared to the other incubations and therefore was not suitably specific. The errors on all successive incubations overlapped. The box chart EIS data for group 2 produced a slight dose response (Figure 2.7C) but the signal percentage change data (Figure 2.7D) did not match this, with 50 μM producing the smallest signal change out of the three concentrations.

The data obtained for groups 1 and 2 showed that cell configuration (group 1 = three-electrode setup and group 2 = two-electrode setup) did not appear to affect target DNA response. The SAM was shown to produce similar responses between the groups even with an 8 million times concentration difference.

The most likely factors contributing to target DNA hybridisation performance was probe concentration and target DNA incubation method i.e. all electrodes sequentially exposed to all concentrations (group 1) versus partitioning of electrodes for different target incubations (group 2). Group 2 exhibited the best performance with every target incubation stage being likely significantly different from the SAM stage but errors on the percentage changes make successful target DNA detection difficult to ascertain. Group 1 did not have a significant difference at 25 or 50 μM but did at the higher concentrations. EIS measurements confirmed group 2's DPV box chart response but did

not fully confirm the percentage change data, presenting with peak behaviour instead of dose-dependent behaviour. Having shown potential signs of target DNA detection at micromolar concentrations, nanomolar concentration responses were then studied to investigate the sensitivity of the microelectrodes.

Figure 2.8 presents DPV and EIS data obtained from 7.5 nM, 15 nM and 30 nM target DNA incubations.

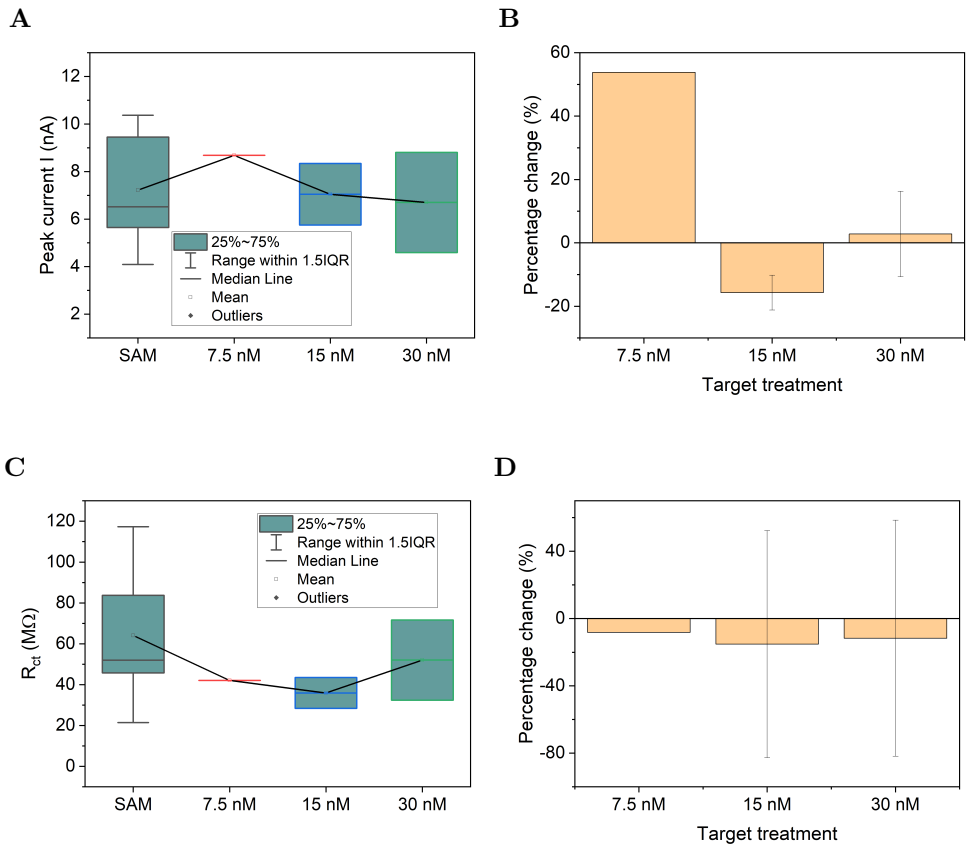

Figure 2.8: Box chart of data for SAM, 7.5 nM, 15 nM and 30 nM stages (A), DPV signal percentage changes for target DNA stages vs SAM stage (B) corresponding EIS box chart data (C) and EIS signal percent change (D). Measurements taken in redox buffer1 (Vs platinum). EIS settings (E_{dc} vs OCP = 0.0 V, frequency range: 0.1 Hz to 100 kHz).

The DPV box chart data (Figure 2.8A) did not show an overall dose response if the SAM stage was included as a data point (i.e the blank). The target stages had a decreasing trend with small data spread. This trend was not present in the percentage

change data (Figure 2.8B) with the response varying between positive and negative values. It was again the middle concentration (15 nM) that appeared to break the trend. The errors were improved compared to the higher concentration data (Figure 2.7). The DPV data demonstrated that the microelectrodes did not have an improved performance in response to lower target DNA concentrations, displaying smaller signal responses, similarly large errors and no likely statistical significance between any of the groups.although accompanied by lower signal changes.

EIS data did not produce a dose response with either raw data (Figure 2.8C) or percentage change (Figure 2.8D). The data again experienced a small spread as was the case with the corresponding DPV and was also smaller than the higher concentration EIS data. The percentage change produced smaller signals and errors compared to the higher concentration data but the errors were still significant compared to the signal, which showed little change between the target concentrations. There were no target stages significantly different from the SAM stage. Although significant differences were not achieved the responses remained promising and guided future experiments (discussed later) to use even smaller target DNA concentrations on a better sensor platform.

Successful alkanethiol SAM formation was shown and potential signs of subsequent target DNA detection at micromolar were observed. The potential for target DNA response at nanomolar was gleaned however more research would be required to successfully demonstrate this. This raised the question, could this performance be reproduced and improved upon using other SAM immobilisation chemistry techniques?

2.3.3 Perfluorocarbon SAMs

Having shown successful standard alkanethiol SAM surface formation and potential target DNA responses with glass-pulled microelectrodes, it was decided to test a more advanced SAM chemistry with the potential advantages of facile layer preparation and surface regeneration. We were afforded the opportunity to work with a unique chemistry thanks to the work being done in the University of Strathclyde, Department of Pure and Applied Chemistry in the lab of Professor Glenn Burley. Instead of using alkanethiols,

perfluorocarbons were substituted. This fluorous modification had been shown to deliver stable amphiphobic structures on surfaces [171]. Due to their inherent lack of interaction with other molecules via the fluorous effect (a propensity to favour fluorine-fluorine interactions ignoring unfavoured interactions with other elements) [172], fluorous SAMs can offer improved anti-fouling properties over other materials. The fluorous effect allows fluorous tagged probes to adsorb into the fluorous SAMs. This self-interaction also provides the ability to remove the fluorous tagged probe molecules using solvent washing, which ignores the underlying fluorous SAM covalently immobilised on surfaces, resulting in regenerative surfaces. This fluorous SAM surface modification was investigated next.

The results from these fluorous SAM investigations consisted of raw DPV data groups presented as box charts and signal percentage changes between various functionalisation stages. The DPV signals were colour coded explaining what measurements to compare and sectioned into datasets. In the box charts, the colours also indicated the concentration used in the experiment. Thus, care must be taken when reading the graphs as not all bars are directly comparable. Care must also be taken in what order the functionalisation stages progress. Previously the probe layer was formed first then the alkanethiol was added to create the full SAM. In the case with fluorous SAM modification, the SAM was generated first and then the fluorous tagged probe DNA was attached to it via the fluorous effect (Figure 2.9). Fitting the EIS data with equivalent circuits proved to be difficult due to the variations in profiles between electrodes. It was therefore decided that EIS data be excluded from the analysis. If EIS was to be used as a measurement technique for a final device it would be more beneficial to consider the change in a select few frequencies rather than trying to fit complex shapes of the full frequency spectrum.

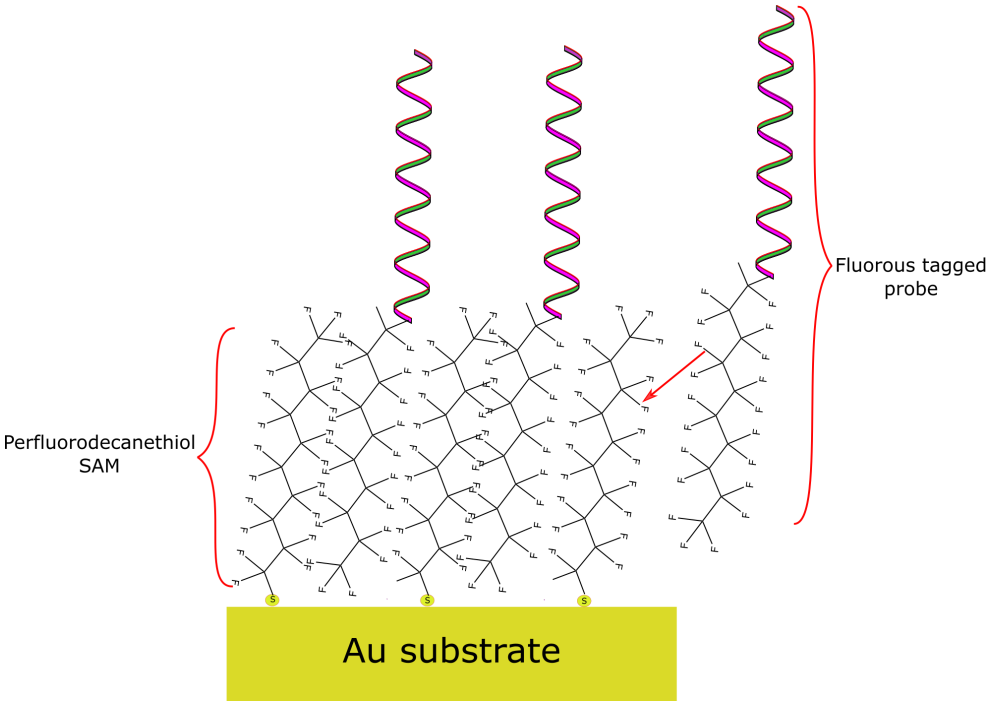

Figure 2.9: Fluorous tagged probe DNA attaches to fluorous SAM (perfluorodecanethiol) via the fluorous effect. Note that the SAM stage comes before the probe stage. This is reversed from previously seen functionalisations.

Table 2.6: Table of fluorous immobilisation conditions. Methanol is shortened to Me. Dataset 4 used redox buffer 5. It was also partitioned into two smaller groups at the target stage onwards n = 3. NA denotes that experiments never took place.

Preparation	**Dataset 1**	**Dataset 2**	**Dataset 3**	**Dataset 4**	
SAM				**Group A**	**Group B**
Concentration	1 μM	1 μM	317 nM	34.9 nM	
Diluent	PFDT	PFDT	PFDT	PFDT	
Incubation time	1hr, 2hr and 24hr	1hr and 24hr	1hr	24hr	
Washes	DI	99 % methanol (Me) Nitrogen dried	10 % methanol (Me) Nitrogen dried	10 % methanol (Me) Nitrogen dried	
PROBE					
Concentration	1 μM	1 μM	1 μM	1 μM	
Diluent	DI	DI	DI	DI	
Incubation time	2hr and 24hr	2hr and 24hr	1hr and 19hr	1hr	
Washes	Toluene Nitrogen dried	Toluene Nitrogen dried	Toluene Nitrogen dried	Toluene Nitrogen dried	
TARGET					
Concentration	1 μM	1 μM	10 μM	1 nM	10 μM
Diluent	DI	DI	DI	KCL	KCL
Incubation time	1hr and 4days	1hr and 24hr	2hr and 19hr	1hr and 19hr	1hr and 19hr
Washes	DI	DI	DI	SCT	SCT
DNA Removal					
Procedure	30 mins 30% methanol bath - 30 mins toluene bath - 30 mins 30% methanol bath				
2^{nd} PROBE					
Concentration	NA	NA	1 μM	1 μM	NA
Diluent	NA	NA	DI	DI	NA
Incubation time	NA	NA	1hr	0.5hr	NA
Washes	NA	NA	Toluene Nitrogen dried	Toluene Nitrogen dried	NA
2^{nd} TARGET					
Concentration	NA	NA	10 μM	33.3 nM	NA
Diluent	NA	NA	DI	KCL	NA
Incubation time	NA	NA	1hr	0.5hr	NA
Washes	NA	NA	DI	SCT	NA

2.3.4 Fluorous SAM and Probe Immobilisation

SAM immobilisation

Various incubation times, concentrations of the SAM forming molecule PFDT and contamination removal solution washes were employed investigating fluorous SAM immobilisation (Table 2.6). Electrodes (n = 5) were incubated in PFDT solution for a specified duration. Washing with chemical solutions (this is denoted in brackets in the graphs) and tested. Following this the electrodes were incubated in the preceding target concentration, this procedure was repeated until all concentrations were tested. This allowed for interrogation of SAM density and stability dependence on concentration, incubation time and washing solution used in removing unbound PFDT after incubations. DI water was used as the contamination wash for all stages for this SAM immobilisation study.

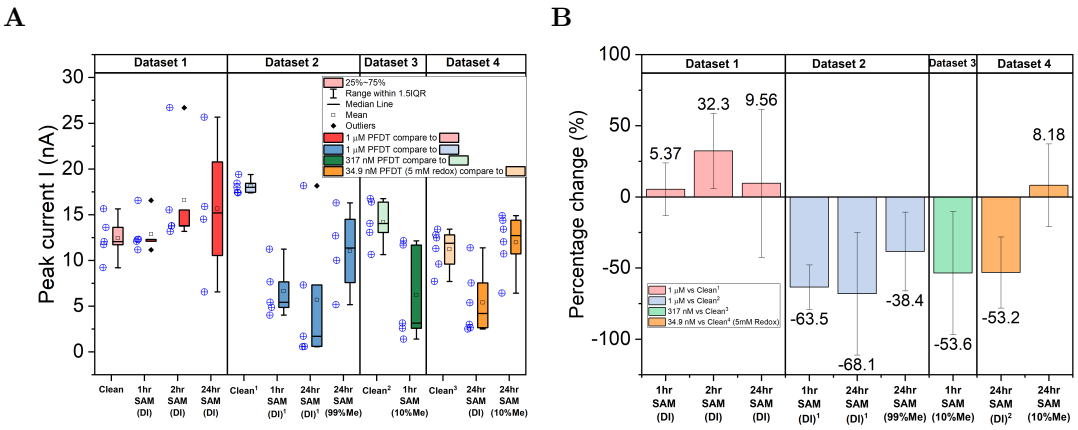

Figure 2.10: DPV measured data from fluorous SAM experiments presented in box charts (A). Note that the current is normalised by redox buffer concentration as dataset 4 used 5 times stronger buffer. Percentage changes are between various fluorous SAM immobilisation times and the clean stage (shown in legend)(B). Terms in brackets () represent the agent used to wash the electrodes before measuring. Dataset 4 data is divided by 5 i.e the redox concentration (5 mM) for scale and comparison purposes. Here methanol has been shortened to Me to save space. Superscripts act as track keeping devices for identical stages in different datasets.

Figure 2.10A showed box chart data for all datasets. Dataset 1 presented with an increasing DPV current in response to increasing incubation time. The 1hr and 2hr SAM

were almost identical to the clean stage indicating that a very sparse SAM formed. (Figure 2.10B) agreed with increases in current from the box chart data showing a peak mean current at 2hrs. The means were large due to one extreme data point skewing the calculation. The increasing current response was paradoxical behaviour, the current was expected to decrease due to the adding of material to the clean surface and therefore reducing the effective working area for electron exchange with redox ions. Possible reasons for the increasing current behaviour could be due to the formation of multiple smaller microelectrode areas. This would occur if a dense SAM formed in a non-uniform manner over most of the electrode surface. This could lead to microelectrode sized regions completely unaffected by PFDT molecules forming multiple microelectrode regions, increasing the current response [183, 184, 185]. Data from experiments conducted by colleagues also observed this behaviour and it appeared the current increase was due to the SAM molecules displacing contaminated material on the surface producing a cleaner environment leading to easier redox couple movement to the surface.

Datasets 2-4 behaved as expected with decreasing current response with incubation time. Figure 2.10A showed this negative response was reduced by using methanol as a washing step in place of DI water. With all methanol stages showing a current rebound compared to DI water washes. This could indicate that the DI water washes were not removing significant amounts of unbound PFDT (PFDT that is self-interacting with other thiol bound PFDT molecules, but itself is not bound by thiol to the electrode) adding to the blocking effect. Methanol can disrupt the fluorous self-interactions and bring the unbound molecules back into solution for removal. After the methanol washes the responses rebounded towards the clean signal and in the case of dataset 4 it slightly surpassed the clean signal evidenced by an 8 % signal increase (Figure 2.10B). The percentage change also supports dataset 2's methanol wash current reduction with the signal almost halving to - 38%. The data suggested that the immobilised SAM forms rapidly, perhaps within the first few hours. Incubation past this rapid formation acts to capture unbound PFDT via fluorous self-interactions and not via thiol immobilisation to the surface. It was, therefore, likely that 1 or 2 hr SAM incubation with a methanol wash will result in similar results as the longer incubations with methanol wash. This was

evident in (Figure 2.10B) with 1hr SAM (10%) in dataset 3 having a more significant signal than the 24hr SAMs with methanol washes in datasets 2 and 4. This signal which was due purely to immobilised SAM was even comparable to the 24 hr SAM's (DI), which contained large signals due to contamination, demonstrating a well-formed fluorous SAM for dataset 3.

It can also be seen that the concentration of PFDT seemed to have little effect on the current response. Comparing 24hr SAM (DI) from dataset 2 and 24hr SAM (DI) dataset 4 (Figure 2.10A). They showed similar current ranges and the data both displayed similar spreads. As a result, their means and medians were similar providing strong evidence equivalent SAMs had formed. Even though dataset 4 used a PFDT concentration 29 times weaker than dataset 2. This was similar for 24hr SAM (99%Me) dataset 2 and 24hr SAM (10%Me). Again, having similar data spreads and resulting average currents.

From these experiments, it was shown that fluorous SAMs were likely to form in short time frames 1 to 2 hrs with additional times providing more contamination for removal with no further benefit to the immobilised SAM. The SAM density and structure was not obviously dependent on the concentration used (34.9 nM - 1 μM). Methanol washing was more effective than DI water at removing unbound PFDT contamination. Dataset 3's SAM forming protocol (Table 2.6) was shown to be the most optimal.

Fluorous tagged probe immobilisation into PFDT SAMS

With the fluorous SAMs immobilised on the electrode surfaces the next step was to immobilise the probe DNA. The probe DNA contained a fluorous tag the same length as the PFDT molecule. The binding between the two was due to the fluorous effect. All probe DNA concentrations were 1 μM and DI water was used as a diluent. All electrodes (n = 5) were washed with toluene and nitrogen dried before measuring.

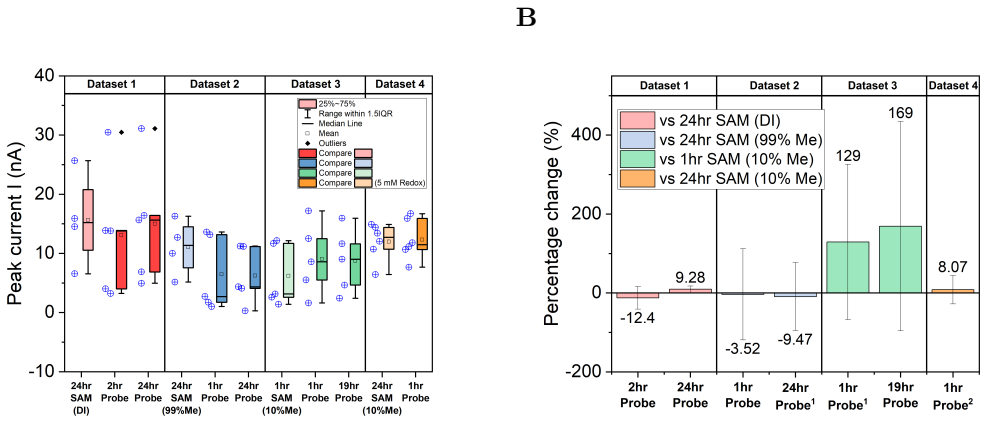

Figure 2.11: DPV measured data from fluorous tagged probe DNA experiments presented in box charts (A). Note that the current is normalised by redox buffer concentration as dataset 4 used 5 times stronger buffer. Percentage change is between various fluorous tagged probe immobilisation and the previous SAM stage (B). Terms in brackets () represent the agent used to wash the electrodes before measuring. Dataset 4 data is divided by 5 i.e the redox concentration for scale and comparison purposes. The probe concentration was 1 μM in DI water for all datasets and the electrodes were washed with toluene and nitrogen dried before testing. Here methanol has been shortened to Me to save space. Superscripts act as track keeping devices for identical stages in different datasets.

The data in Figure 2.11 showed both increasing (datasets 3 and 4) and decreasing current behaviour (datasets 1 and 2) when probe DNA was applied to the SAM. Dataset 1 presented with a current decrease after a 2hr probe incubation and then an increase thereafter. The SAM formation results for this dataset from the previous section showed that the SAM was most likely to be sparse. It could be the case that the probe DNA quickly occupied the SAM due to lack of binding sites resulting in the expected current decrease due to extra blocking of the redox ions. Then, with further incubation, the equilibrium rate reaction favouring probe immobilisation was shifted to a point favouring probe dissociation back into the bulk solution thus reducing the probe coverage and causing a current rebound. This SAM density and probe binding affinity relationship could also explain the behaviour shown in dataset 2 with current decreases for both 1 hr and 24 hr incubation times. As previously demonstrated with the SAM data, dataset 2 appeared to form a denser SAM than dataset 1. It would therefore take more time

to occupy the SAM (more binding locations). This keeps the equilibrium rate reaction favouring probe immobilisation present for longer. If or when the equilibrium shifts to favour probe desorption was clearly past the 24hrs measured in the experiment.

Datasets 3 and 4 showed current percentage change increases, conversely, the box chart data showed little difference between SAM and probe stages even though the average currents were both increased from the SAM stage. The likely cause of this was minimum values from the SAM stage became maximum values of the probe stage, thus giving massive current changes as evidenced by the large percentage changes in (Figure 2.11B). This would mean electrodes that measured having the lowest currents at the SAM stage i.e. denser SAMs have demonstrated a large positive current change upon probe binding. Electrodes that measured higher currents at the SAM stage i.e. less dense SAM now show small decreases upon probe binding like datasets 1 and 2. This suggested that denser fluorous SAMs affect larger current responses to probe adsorption likely due to more probe molecules being adsorbed. There appeared to be critical SAM densities that upon DNA binding either further enforced the structure of the SAM that allowed redox ions to easily reach the surface (current increase) or enforced restructuring of the SAM that impeded ion flow further. Forming uniform dense SAM layers is exceptionally challenging and is why there is such active research in its development. Being able to control SAM density and structure would perhaps be the most significant achievement in the pursuit of reproducible biosensors.

Due to the opposing signal changes accompanied with large errors and lack of group separation in the box plots. It was not possible to confirm probe DNA was successfully immobilised into the SAM. The density and structure of the underlining SAM stage appeared to affect the behaviour of any SAM-probe structure formed upon probe immobilisation. The SAM density may impose a dependence on the equilibrium reaction position either favouring probe immobilisation or removal. It also potentially affected the dual SAM-probe structure either causing a blocking action or opening to redox ions affecting the current responses. Although probe immobilisation could not be confirmed there responses after probe incubation. Therefore it is possible probe DNA was immo-

bilised but not able to be statistically confirmed using these electrode platforms. Target DNA was introduced next to investigate the the response on the assumption that there was some Probe DNA immobilised.

Target DNA detection on fluorous modified surface

The detection of target DNA is the most vital function of the biosensor. This was studied using various concentrations, incubation times, two types of diluent solutions using two types of washing solutions.

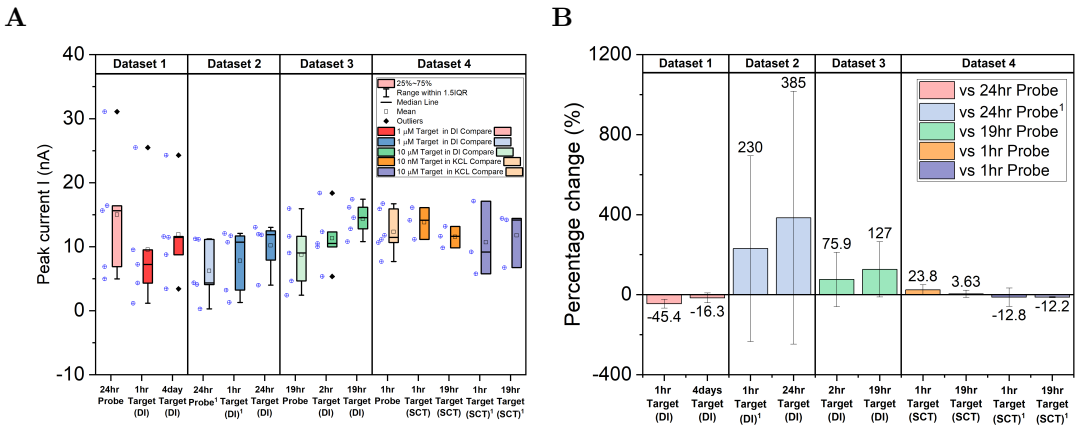

Figure 2.12: DPV measured data from target DNA hybridisation on fluorous modified surface experiments presented in box charts (A). Note that the current is normalised by redox buffer concentration as dataset 4 used 5 times stronger buffer. Percentage change is between the various target times and the probe stage (B). Terms in brackets () represent the agent used to wash the electrodes before measuring. Dataset 4 data is divided by a factor of 5 i.e. the redox concentration for scale and comparison purposes. Here methanol has been shortened to Me to save space. Superscripts act as track keeping devices for identical stages in different datasets.

The overall current response for all datasets displayed increasing behaviour upon target addition (Figure 2.12). This was opposite to what was commonly seen on macroelectrodes and again showed this paradoxical current trend on microelectrodes.

1hr target (DI) from dataset 1 and 19hr target (SCT)^1 from dataset 4 showed current decreases on target binding. This behaviour was most evident by observing the individual electrode responses when target DNA was added. The electrodes demonstrated both

increases and decreases across all datasets. The electrode responses within each sample group tended to randomly change instead of showing a more ordered change upon target incubation. This behaviour acted to cancel out any large electrode responses upon averaging the data as can be seen in Figure 2.12B demonstrating low percentage changes. This again suggested a complex dependence on the density and structure of the SAM-probe-target complex on the surface.

There was a potential dependence between incubation time and signal response. Datasets 1 and 4 showed decreased signals at longer incubation times where datasets 2 and 3 showed improved signals with 24hr target (DI) and 19hr target (DI), 19 hr being likely different from the probe stage giving evidence of successful target DNA detection. The difference between longer and shorter incubation times seemed to be a narrowing of the data range and this suggested that the hybridised structure was in a more settled or ordered state at longer times (19 hours).

The use of washing agent did not appear to affect the results with both DI and SCT showing poorer outcomes in datasets 1 and 4 and improved outcomes in datasets 2, 3 and 4.

The current response lacked a clear dependence on concentration as the 1 μM and 10 μM concentrations showed both positive and negative current responses. In experiments with colleagues out of this project scope, there was evidence of target DNA concentration dependence on the current response on both macro and microelectrode devices. The only supporting evidence here was the comparison between the data in dataset 4 where the lower concentration showed an increased response and the higher concentration showed a decreasing one. This agreed with the lab results of other experiments within the group and is still being actively investigated (see Section 2.3.5).

There were again some signs of response to target DNA, with 19 hr incubation from dataset 3 being the only likely significantly different event. The electrochemical responses displayed both increasing and decreasing current behaviour to target DNA addition. The increasing current behaviour was the more probable behaviour and produced more dominant responses than the decreasing current behaviour. There was no

conclusive evidence for dependencies on diluent and washing solution. Longer incubation times tended to increase the current signal in a positive direction, even if the initial current response was negative. One of the benefits of using fluorous SAMs was the potential for surface regeneration. This would be achieved by removing the probe-target via chemical washing, ignoring the underlying fluorous SAM. This reusability was investigated next.

Reuse of fluorous modified surfaces

The reusability of biosensors would offer unique advantages to point of care testing in clinical and more crucially community care settings. It would drive the cost of the devices down as new devices would not be required for every test performed. SAM based biosensors are currently thought of as single-use, disposable devices and work on surface regeneration could potentially overcome this limitation. To investigate the reuse capabilities of fluorous modified microelectrodes the potentially formed probe-target complex from the previous section was removed (DNA wash). This was achieved by disrupting the fluorous self-interactions between the SAM and the tagged probe by submerging the electrodes in 30 % methanol for 30 minutes, toluene for 30 minutes and again in 30 % methanol for 30 minutes. This had been demonstrated in the literature [186] to successfully remove the probe-target complex leaving the SAM intact. After removal, a new probe layer was formed for 0.5 hr and 1 hr incubation times. Target DNA was then introduced with various concentrations, incubation times, diluents and washing solutions see (Table 2.6).

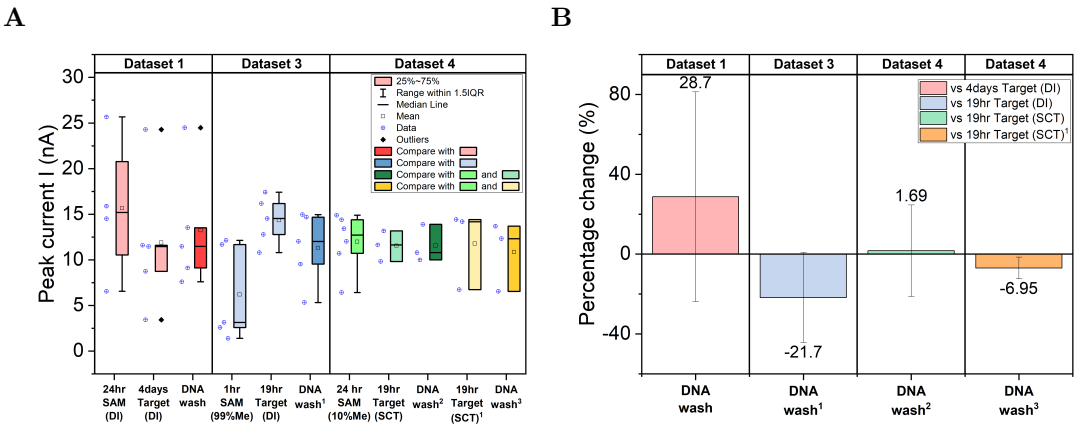

Figure 2.13: DPV measured data from the removal of the probe-target complex (DNA wash) on fluorous modified surface experiments presented in box charts (A). The complex was removed by submerging electrodes in 30 % methanol for 30 minutes, toluene for 30 minutes and again in 30 % methanol for 30 minutes. Note that the current is normalised by redox buffer concentration as dataset 4 used 5 times stronger buffer. Percentage change is between the various DNA wash stages and the previous target stage (B). Terms in brackets () represent the agent used to wash the electrodes before measuring. Dataset 4 data is divided by 5 i.e. the redox concentration for scale and comparison purposes. Here methanol has been shortened to Me to save space. Superscripts act as track keeping devices for identical stages in different datasets.

Fluourous Tagged Probe-Target Complex Removal. Figure 2.13A showed the group behaviour of the electrodes after the DNA wash. Both the original SAM data and the previous target stage data was included to give two comparison points. It was expected that there should be a departure away from the target stage in a direction towards the original SAM stage as this should be the only remaining layer. It was not expected to exactly match the original SAM signal as the SAM structure has undergone many modifications in the functionalisation process.

Dataset 1 showed a current increase, moving away from the target stage in the direction of the original SAMs higher positive current signal as expected. This was supported by the positive percentage change (30%) (Figure 2.13B). The data also broadens compared to the target stage. The original SAM stage still had a broader IQR but indicated that the DNA wash tended toward the same behaviour. The DNA wash was on the verge of likely statistical difference from the target stage. Dataset 3 similarly showed a

departure from the previous target stage towards the original SAM stage. This time, however, the change was a decreasing one supported by a -21 % percentage change. Data broadening was seen much like in the original SAM, in this case, the DNA wash stage was again on the verge of likely difference from both SAM and target stages. This was strong evidence that there had been significant removal of the probe-target complex. Dataset 4 showed little differences between all stages. DNA wash^2 had a small shift and broadening in the data bringing it more in line with the SAM stage but the target stage had considerable overlap with the SAM stage meaning significant differences between them would be difficult to achieve. Small changes were similarly found for DNA wash^3. The percentage changes were evidenced by small percentage changes of 1.69 % and -6.95 % respectively. There was some evidence for probe-target removal in datasets 1 and 3 and small removal in dataset 4.

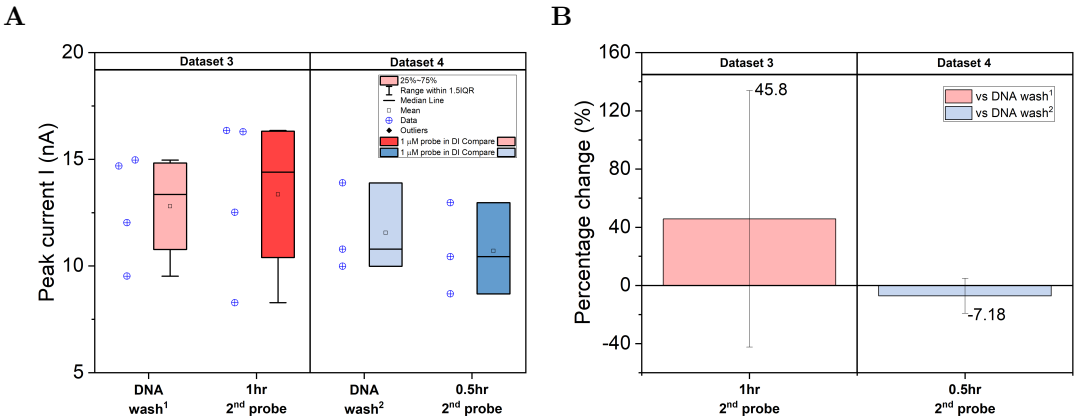

Figure 2.14: DPV measured data from probe immobilisation on restored fluorous modified SAM surface experiments presented in box charts (A). Probe DNA was diluted in DI water to 1 μM for incubation. The electrodes were washed with toluene and nitrogen dried before testing. Note that the current is normalised by redox buffer concentration as dataset 4 used 5 times stronger buffer. Percentage change is between the 2^{nd} probe stages and the previous DNA removal stage (B). Superscripts act as track keeping devices for identical stages in different datasets.

Second Fluorous Tagged Probe Immobilisation. Potential removal of the probe-target complex was followed by the formation of a new probe layer (2^{nd}). Dataset 1 did not receive applications of second probe or target due to the experiment concluding at the DNA wash stage. Dataset 3 showed a small positive current shift on the application

of probe DNA. There was broadening of the data and increases in the average currents (Figure 2.14A) supported by a 45 % percentage current increase (Figure 2.14B). Dataset 4 showed a negative current shift, supported by a percentage decrease of (- 7 %). This evidence suggested that dataset 3 had seen probe immobilisation and dataset 4 had seen a reduced amount of immobilised probe but was still present in small amounts for further functionalisation. no differences between the groups was evident and so statistical confirmation was not possible.

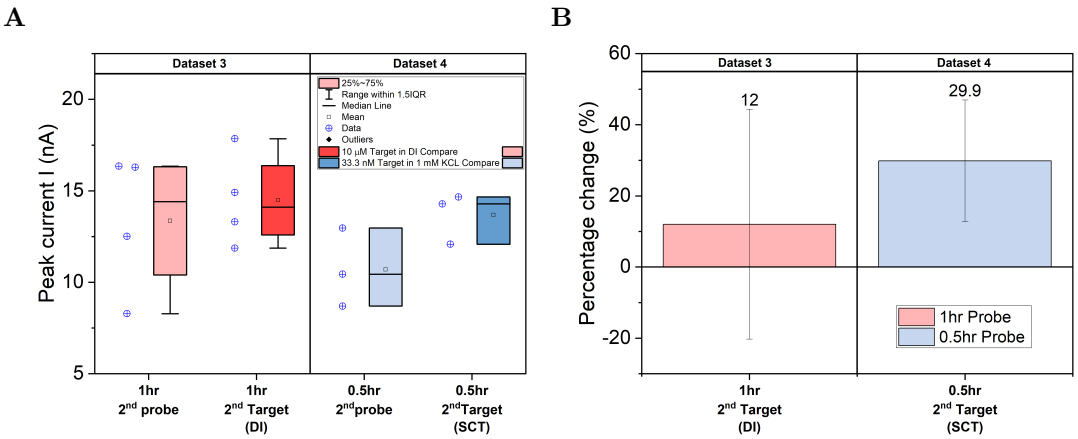

Figure 2.15: DPV measured data from target hybridisation on restored fluorous modified SAM-probe surface experiments presented in box charts (A). Note that the current is normalised by redox buffer concentration as dataset 4 used 5 times stronger buffer. Terms in brackets () represent the agent used to wash the electrodes before measuring. Dataset 4 data is divided by 5 i.e. the redox concentration for scale and comparison purposes. Percentage change is between the 2nd target stages and the previous 2nd probe stage (B). Superscripts act as track keeping devices for identical stages in different datasets.

Second Target Hybridisation. The final piece of evidence for reusability was again the most critical aspect of the biosensor, i.e. target DNA detection. In dataset 3 10 μM target DNA in DI water was incubated for 1hr and washed with DI water before testing. Dataset 4's 33.3 nM target DNA in KCL was incubated and washed in SCT before testing.

Dataset 3 showed a current increase with the mean current increasing (Figure 2.15A). This was supported by a 12 % current percentage increase (Figure 2.15B). The data

also narrowed which was evident in the first target incubation. There was no significant difference between the two stages. Dataset 4 showed a positive current shift with the average current increasing supported by a 29.9 % current percentage change, this behaviour was opposite to the first target incubation which produced small current decreases. Data range narrowing was observed in all target groups (first and second hybridisations) suggesting that this was a characteristic of target binding, producing a more consistent surface. This could be due to the formation of the more rigid helical DNA producing a more consistently permeable environment for redox reactions. The target stage in dataset 4 was likely statistically different compared to the probe stage meaning successful target DNA detection was achieved. This occurred at 0.5 hr, which was a respectable detection time and outperformed the longer incubation times of dataset 3 and many of the first target incubations. This was the case even though there was little empirical evidence of large amounts of probe DNA being immobilised at the second probe stage. This led to the conclusion that there was little target DNA being bound but accompanied by respectable signal. This could mean that a less dense probe layer can facilitate a larger signal change on target binding, again demonstrating the biosensor was very sensitive. Conversely, it may be the case that significant probe DNA was bound previously but was not able to represent large measured signal changes to make this obvious. This detection also occurred at 33.3 nM of target DNA the smallest concentration tested. Lower concentrations might have produced larger signal changes. In this experiment, the diluent and washes with dissolved salts displayed the best results which agreed with the literature though, this behaviour was not evident in the first target incubation.

Potential successful low concentration target detection was shown for dataset 4 on a restored SAM-probe surface demonstrating the potential for surface regeneration and high sensitivity of the fluorous SAM. This gave promising signs for future use of this type of surface chemistry. However, limitations of the microelectrodes were present throughout and more research is required to achieve statistical confirmation. These limitations are discussed in the next section.

2.3.5 Limitations of Work

There were some limitations discovered during experiments with glass pulled microelectrodes. There were sample size losses during some experiments and data variability produced by large signal changes by one or two electrodes within a data group. The variable nature of all electrodes was still evident following identical and meticulous preparations. Large percentage change errors arose by including outliers identified in the box charts and was presented this way for transparency. Although an accepted statistical technique for outlier rejection, it was not as rigorous as other methods. These other methods were not applied because they are only statistically reliable for larger n values. Consequently, it was realised that the electrodes were contributing to most issues discussed. It was concluded that DNA experiments suffered due to being performed on these microelectrodes. The cleaning techniques and both SAM surface modifications produced promising results but along with the DNA experiments would have benefited from using a different platform to supplement them.

Current responses throughout the experiments showed both increasing and decreasing behaviours. In the case of target DNA hybridisation the most common and widely adopted theory of signal change in DPV for biosensors is that, as more target DNA hybridises negative charge increasingly accumulates at the electrode surface, which repulses the negatively charged redox couples thus lowering the current signal [160], the opposite was observed here. There have been opposing theories stating that when the target DNA hybridises the newly formed duplex becomes more rigid and stands straighter allowing for channel formation giving the redox couple an easier path to travel to the electrode surface thus increasing the current [187, 188]. The reason why sometimes one is seen over the other is speculated to be due to SAM density [189]. A dense SAM will not facilitate suitable spacing between hybridised DNA to allow for a channel to form thus repulsion dominates. With a sparser SAM, the spacing allows room for channel formation [190]. It could be that microelectrodes and their different diffusional behaviour and the methods used in these experiments more readily formed a SAM that allowed for channel formation increasing redox flow to the surface. From

other experiments performed in the lab a target DNA concentration dependence on the direction of current response had been seen in macroelectrode experiments, but this was not common. This behaviour was more typical in microelectrode experiments carried out within this project and presented later and also by colleagues. This was a phenomenon on electrode devices and most notably on microelectrode devices. At the time of writing this was still being actively investigated by the group.

2.4 Conclusions

Established macroelectrode cleaning techniques were systematically adopted for use with microelectrodes. The microelectrodes were able to be cleaned to some degree using KOH electrochemical cleaning alone, but evidence of contamination remained (sub-optimal CV profile). The addition of a preceding coarse mechanical polishing stage improved the performance further but electrochemical cleaning after could on occasion be detrimental to the surface as was shown for H_2SO_4 cleaning. KOH cleaning was less aggressive and was an improvement over H_2SO_4 but still had negative effects. Acid piranha solution cleaning followed by a sequence of alumina fine polishing demonstrated the most optimal results, producing respectable CV profiles and optimum cleaning parameter values: I^{ss}_{ratio}, ΔE_{ss} and %Real area. It was also shown that electrochemical cleaning post polishing and acid cleaning had adverse effects.

MCH was found to be the optimum molecule for effective SAM formation. There was little difference in the experiments between MCH and MCP with MCH being chosen because of a moderate signal enhancement following target DNA hybridisation, a critical stage for a biosensor. MCP would also be a suitable choice and is unlikely to cause any significant differences in the outcome of experiments.

Target concentration experiments showed that the microelectrodes were unable to reliably detect target DNA in the micromolar (25 - 100 μM) and nanomolar (7 - 30 nM) range using different probe and SAM concentrations as well as different electrochemical cell configurations. DNA detection experiments revealed significant errors in most measurements and a changing DPV current behaviour, with only one experiment showing

an obvious dose response.

SAMs formed using PFDT were found to vary randomly between dense and sparse SAM immobilisations. When the dense SAMs were washed with methanol there was a relatively small change in signal due to most of the surface being covered in immobilised SAM and when unbound SAM contamination was removed by the wash, a well-blocked surface remained. A sparsely populated immobilised SAM resulted in higher measured currents. This was shown to potentially affect the probe signals measured after the SAM wash, i.e. less probe binding for the sparse SAMs. This also led to smaller target signals as there was less probe DNA for the target to hybridise. The data also suggested that SAM and probe DNA immobilisation happened quickly (within a few hours) and incubation past this point only added to the amount of unspecifically bound material to the PFDT SAM. There were glimpses of the functionalised surface responding to target DNA across multiple experiments with longer target incubations being more pronounced, however statistical significance was unlikely. It was also shown that signs of surface regeneration were present after at least one removal of the probe-target layer and re-immobilisation of a new probe layer. After subsequent re-incubation in target DNA the responses tended toward expected values however were not significant between the stages.

Microelectrodes were tested with different SAM chemistries and while there was promise in these systems, they were not suitable for biosensor development because the microelectrodes were found to be laborious to use and variable in response, making statistical differences difficult to obtain. Consequently, the search for a new sensor format capable of underpinning biosensor development e.g. PCBs was necessary.

Chapter 3

Printed Circuit Boards As Biosensors

3.1 Introduction

It was demonstrated in the previous chapter that DNA oligonucleotide detection was not statistically possible on the glass pulled microelectrodes tested. These platforms allowed for a proof of concept but, reached their limit as an experimental platform for progressing biosensor research. This was due to several limitations that were associated with these systems which included: large overall electrode size resulting in congested electrochemical cells (making the connection to multiplexer a complex and tedious task), low sample sizes (low number of repeats) due to the geometry of the electrode-multiplexer system, unreliability, difficulty functionalising (each electrode incubated in separate vials), high cost and time consuming to buy or manufacture. Ultimately, these limitations lead to a reduced amount of experiments and repeat measurements within each experiment. Small sample sizes provided poor statistics for experiments.

To improve experimental throughput, statistics and to move towards a final usable device, a new electrode platform was required. A custom solution was needed to account for the performance issues which singular electrode measurements present. In this chapter printed circuit boards (PCBs) were investigated as a potential sensor platform.

PCBs have many benefits such as easy customisation (many software programs that allow PCB development to almost any shape, design and size); established and varied manufacturing allowing for quick, precise and bulk production at low cost with various metal plating finishes available from suppliers. Increased electrode numbers can be manufactured on smaller surfaces resulting in higher sample sizes within smaller time intervals. Due to the maturation of PCB systems and their extensive incorporation in modern electronic devices, they can be easily integrated into equipment such as the potentiostat used for electrochemical measurements. They can have additional electronics easily incorporated onto or conjoined to the electrode system of the end goal device. PCB biosensors have been reported in the literature with a wide range of research applications undertaken [191, 192, 193, 194, 195, 196]. The first PCBs designed in this work were designated PCB P1 and consisted of eight working electrodes of various diameters (Table 3.3) around a circular reference electrode and annular counter electrode (Figure 3.1A) and were manufactured in the lab. The goal of this device was to determine 1) if the copper pads and traces could be successfully plated with gold. 2) if they could be easily and quickly interfaced with the potentiostat measurement system and 3) Did the gold surface finish result in a suitable electrochemical response [141, 169, 170, 197] that would warrant further investigation into potential biosensor properties.

With promising results from the PCB P1 design, commercially manufactured PCBs were purchased. The design was changed to eight working electrodes of equal diameter and rectangular reference and counter electrodes. This was a more spatially efficient configuration. Two versions of this design were purchased (Table 3.3). One that was gold plated by the manufacturer (Figure 3.1B) these devices were designated PCB P2. The other version remained non-plated and allowed for various plating methods to be tested in the lab (Figure 3.1C), these devices were designated PCB P3. Using a 3rd party manufacturer allowed for a larger number of devices to be tested and a potentially higher quality device. Successful electrochemical responses typical of gold were witnessed on both boards with P3 having superior behaviour although with a lack of reproducibility. Neither device at the time would have been suitable to continue as the biosensor platform. The lack of reproducibility was addressed with the purchase of PCBs

from a specialist PCB biosensor company (BIOTIP biodevice technology IP). These biosensors were designated PCB P4 (Figure 3.1D) and their electrochemical responses were shown to be optimal and reproducible. These results led to the adoption of PCB P4 as the new suitable platform for biosensor development for the remainder of the research undertaken in this PhD.

3.2 Materials & Methods

3.2.1 Chemicals

Chemicals used in this work are listed in Table 3.1.

Table 3.1: List of chemicals used in this work.

Chemical	**Composition**	**Supplier**
Acetone		Sigma-Aldrich
Ammonia hydroxide	NH_4OH	Sigma-Aldrich
Bright electroless gold plating solution		Sigma-Aldrich
De-ionised water (resistivity $\geq$ 18 MΩcm)	DI	Sigma-Aldrich
ECF 60 (electroplating solution)		Metalor technologies Ltd
Ethanol		Sigma-Aldrich
Hydrogen peroxide	H_2O_2	Sigma-Aldrich
Isopropyl alcohol	IPA	Sigma-Aldrich
Phosphate buffered saline tablets	PBS	Sigma-Aldrich
Potassium hydroxide	KOH	Sigma-Aldrich
Potassium ferricyanide	$K_3[Fe(CN)_6]$	Sigma-Aldrich
Potassium ferrocyanide	$K_4[Fe(CN)_6]$	Sigma-Aldrich
Sulfuric acid	H_2SO_4	Sigma-Aldrich
6-Mercapto-1-hexanol	MCH	Sigma-Aldrich

3.2.2 Buffers

Buffers and their compositions used in this work are shown in Table 3.2. De-ionised water (3.1) was used to make all aqueous solutions.

Table 3.2: List of buffers used and their compositions

Buffer	**Composition**
Acid piranha solution	18 M H_2SO_4 and 30 % H_2O_2 (ratio = 3:1 v/v)
Base piranha solution	NH_4OH and 30 % H_2O_2 (ratio = 3:1 v/v)
1 mM redox buffer	1 mM Potassium ferricyanide/Potassium ferrocyanide in 0.1 x PBS
5 mM redox buffer	5 mM Potassium ferricyanide/Potassium ferrocyanide in 0.5 x PBS
10 mM redox buffer	1 mM Potassium ferricyanide/Potassium ferrocyanide in 1 x PBS

3.2.3 PCBs and Manufacturers

A list of PCB designs and where the various iterations of PCB designs were manufactured/purchased is presented in Table 3.3. PCB P2-P3 used a polymer solder resist (manufacturers did not revel exact polymer) to insulate the tracks. PCB P1 used a manually applied nitrocellulose layer to insulate tracks.

Table 3.3: List of PCB boards, dimensions and their manufacturer. For circular electrodes the diameter is given, annulus electrodes the area is given and rectangular electrodes, width and height are given.

PCB Design	Dimensions	Manufacturer
Prototype PCB P1	WE1 = 0.2 mm WE2 = 0.457 mm WE3 = 0.711 mm WE4 = 0.965 mm WE5 = 1.016 mm WE6 = 1.0668 mm WE7 = 1.1118 mm WE8 = 1.168 mm CE = 175.93 mm^2 RE = 6 mm	Steven Cartwright (University of Strathclyde)
Prototype PCB P2	WE = 1mm CE = 8x15 mm RE = 2x15 mm	P & M services (Rochdale) Ltd
Prototype PCB P3	WE = 1mm CE = 8x15 mm RE = 2x15 mm	Quick-teck Electronics Ltd (Royston, UK)
PCB P4	WE = 1 mm CE = 2 mm RE = 3.365 mm^2	BIOTIP biodevice technology IP

3.2.4 Probe and Target sequences

A list of probe and target DNA sequences used and where they were manufactured/purchased is presented in Table 3.4.

Table 3.4: List of probe and target DNA and their manufacturer

DNA	Sequence 5' - 3'	Manufacturer
lytA probe	[ThiC18]TGCCGAAAACGCTTGATACA	Sigma-Aldrich
lytA target	TGTATCAAGCGTTTTCGGCA	Sigma-Aldrich

3.2.5 Gold Plating PCB Electrodes

PCBs P1 and P3 were gold plated in the lab using various combinations of plating solutions, plating times and plating currents to determine if electro-deposition was possible and the optimum plating parameters? PCB P2 was plated by the manufacturer (Table 3.3). They would not disclose the details of the solutions or methods of plating employed. All that was known was it consisted of a hard gold plating, i.e. a thin nickel layer plated onto the copper before the gold layer was added. Examples of the different PCB boards are shown in (Figure 3.1).

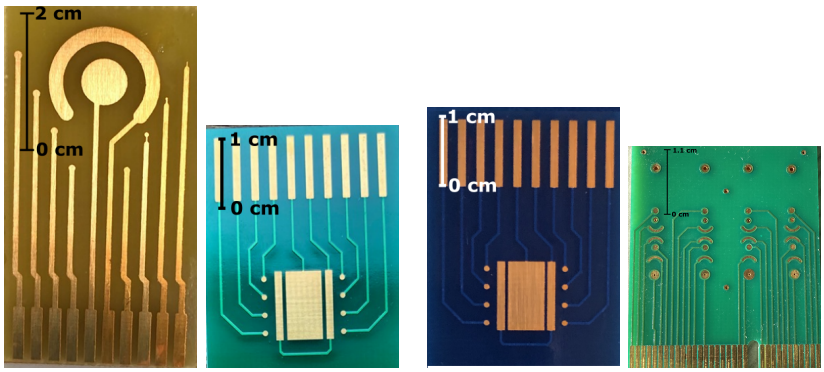

Figure 3.1: PCB P1 (A). Commercially fabricated and hard gold plated PCB P2 (B). New design to increase efficiency and allow for accessory addition. Commercially fabricated bare copper PCB P3 (C). Same in design as B but obtained without gold plating. PCB P4 (d).

3.2.6 Electrochemical Set-up for Gold Plating and Cleaning

All measurements were obtained using a PalmSens4 potentiostat running PSTrace software from Alvatek electrochemical solutions (Houten, Netherlands). All boards used the same electrochemical cell setup for the plating process. The cell consisted of a platinum counter electrode (CE), silver-silver chloride reference electrode (RE) and the electrodes of the PCB connected to a ten-pin connector that was electrically bridged across all contacts including working electrodes (WE) and submerged in plating solution (Table 3.1). The bridge allowed for current to flow to all electrodes so they could all be plated simultaneously (Figure 3.2).

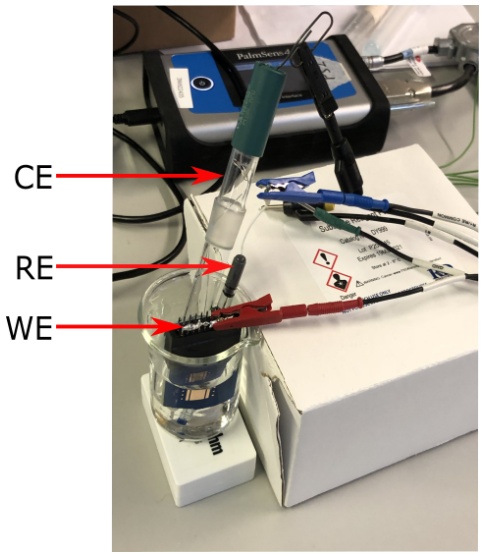

Figure 3.2: Electrochemical cell configuration for gold plating PCB boards using platinum counter electrode (CE), silver-silver chloride reference electrode (RE) and bridged working electrodes (WE) on PCB.

For electrochemical cleaning methods PCBs P1, P2 and P3 used their built-in gold counter and reference electrodes. A MUX8-R2 multiplexer (Alvatek) in combination with PalmSens4 and connector box (Metrohm Runcorn, UK) that connects the multiplexer cables to a ten-pin connector into which the PCBs can be inserted was used. PCB P4's configuration consisted of a platinum counter, silver-silver chloride reference and was connected to the multiplexer via a custom PCI connector (Figure 3.3). For main experiment measurements after plating and cleaning, the PCB's own counter and reference (Gold) was used. The measurement buffer was aliquoted over all electrodes and the surface tension of the buffer maintained electrode coverage.

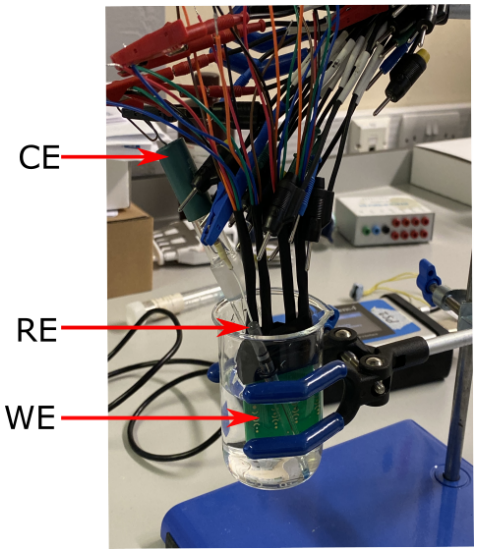

Figure 3.3: Electrochemical cell configuration for cleaning PCB P4 boards, platinum counter electrode (CE), silver-silver chloride reference electrode (RE) and multiplexed working electrodes (WE) on PCB connected to custom PCI connector in 50 mM KOH.

3.2.7 Cleaning of Gold PCB Electrodes

Once each board had obtained a gold surface finish it was essential to clean the gold surface to remove any impurities and contaminants. The PCBs were subjected to various cleaning methods to determine the effect of each cleaning method and also aiming to discover the optimal cleaning protocol. Cleaning methods performed included mechanical, chemical and electrochemical cleaning using solvents, acids and bases shown in (Table 3.1). PCB P4 had a specific cleaning protocol supplied by the manufacturer and was as follows: 1) Organic layer removal was achieved by submerging the PCB in 50 mM KOH and 35 % H_2O_2 for 15 minutes. 2) the PCB was rinsed with DI water and dried with nitrogen gas. 3) PCB electrochemically cleaned in 50 mM KOH with the electrochemical cell configuration discussed previously (Figure 3.3). 4) Cyclic voltammetry was performed for 15 scans running in a potential window of -1.2 V to 0.6 V vs Ag/AgCl reference with a scan rate of 0.1 V/s. On completion of the scans, the boards were rinsed in DI water and dried with nitrogen readying them for use.

3.2.8 DNA Detection on PCB Electrodes

After successful gold plating and surface cleaning the boards were tested using oligonucleotide DNA functionalisation and hybridisation for DNA detection. DNA experiments would be the PCBs primary purpose thus, it was critical that the surfaces could be biochemically functionalised allowing for signal changes when complementary target DNA hybridised with its counterpart immobilised on the surface of the electrode. PCBs P1 and P2 were incubated in 3 μM of *lytA* probe DNA (Table 3.4) for 20 hours at 4 °C. The boards were then washed with DI water and incubated in 1 mM MCP for 1 hour at room temperature forming the functionalised SAM surface for DNA detection. The boards were rewashed to remove non-specifically bound DNA and alkanethiol molecules. The boards were then incubated in 1 μM of target DNA for 1 hour at room temperature. A further wash with lower stringency 1 x PBS was performed so that any hybridised DNA was not removed. The boards were tested between each treatment stage using DPV and EIS (sometimes SWV). Signal changes between the SAM stage and target stage determined whether DNA detection had occurred.

PCB P3 boards underwent the same SAM functionalisation stages though their target incubation was different. The boards were subjected to 50 pM and 500 pM target concentrations, each incubated for 30 minutes at room temperature. They were then washed with 1 x PBS and tested as above. Following this, the board was washed to remove hybridised DNA using DI water and incubated in the 500 pM target concentration. The same washing and testing protocols were used as with the previous concentration.

3.3 Results & Discussion

3.3.1 Gold Plating on PCB Electrodes

Gold based biosensors were the primary target in the project. Since PCBs P1 and P3 were bare copper sensors they had to be plated in the lab to achieve a gold surface layer for further biosensor experiments. A combination of electro and electroless plating was employed in forming gold surfaces on the PCBs. PCB P1 was a proof of concept device

made in the university. The board was submerged in bright electroless solution at 50 °C for various duration's: fresh, 5 minutes and 10 minutes.

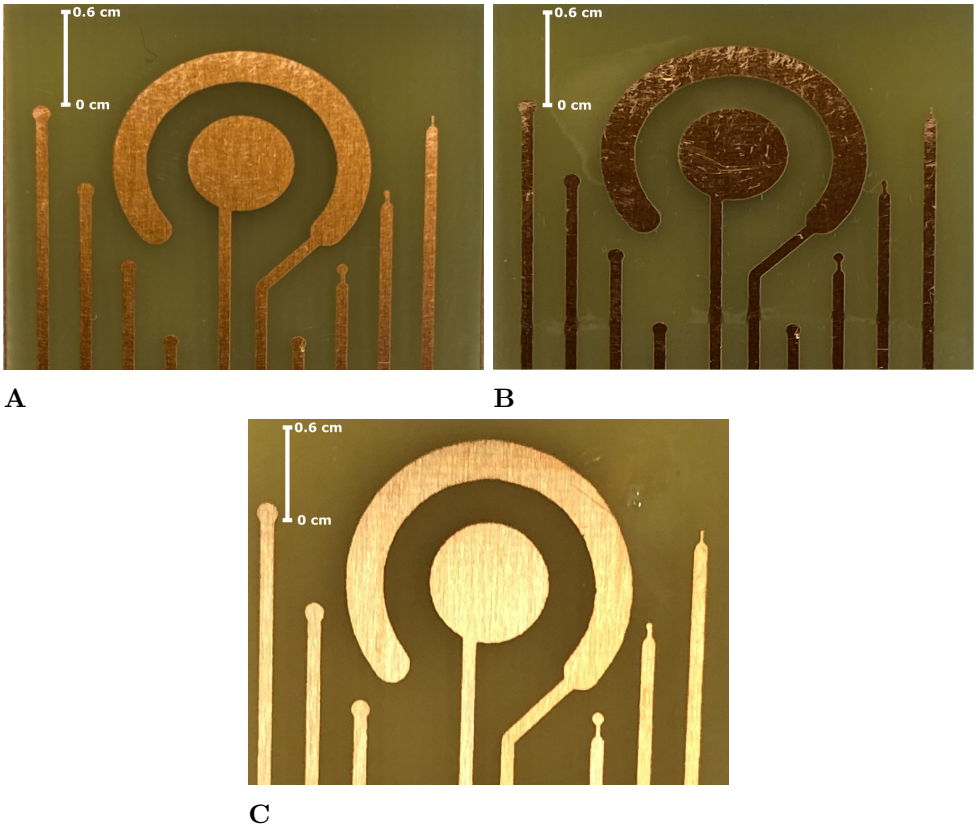

Figure 3.4: PCB P1 after bright electroless solution immersion at 50 °C for Fresh (A). 5 minutes (B) 10 minutes (C).

Electroless plating for under 10 minutes still displayed hints of underlying copper through the deposited gold layer and was re-submerged into solution for further plating (Figure 3.4). A full gold appearance was obtained after 10 minutes. Only devices made using this 10-minute plating protocol underwent electrochemical testing as the others had insufficient gold coverage.

PCB P3 was a commercially non-plated board allowing for plating experiments to be performed. The PCB was firstly subjected to the electroless gold plating protocol used on PCB P1, i.e. 10 minutes in 50 °C bright electroless gold plating solution (Figure 3.5).

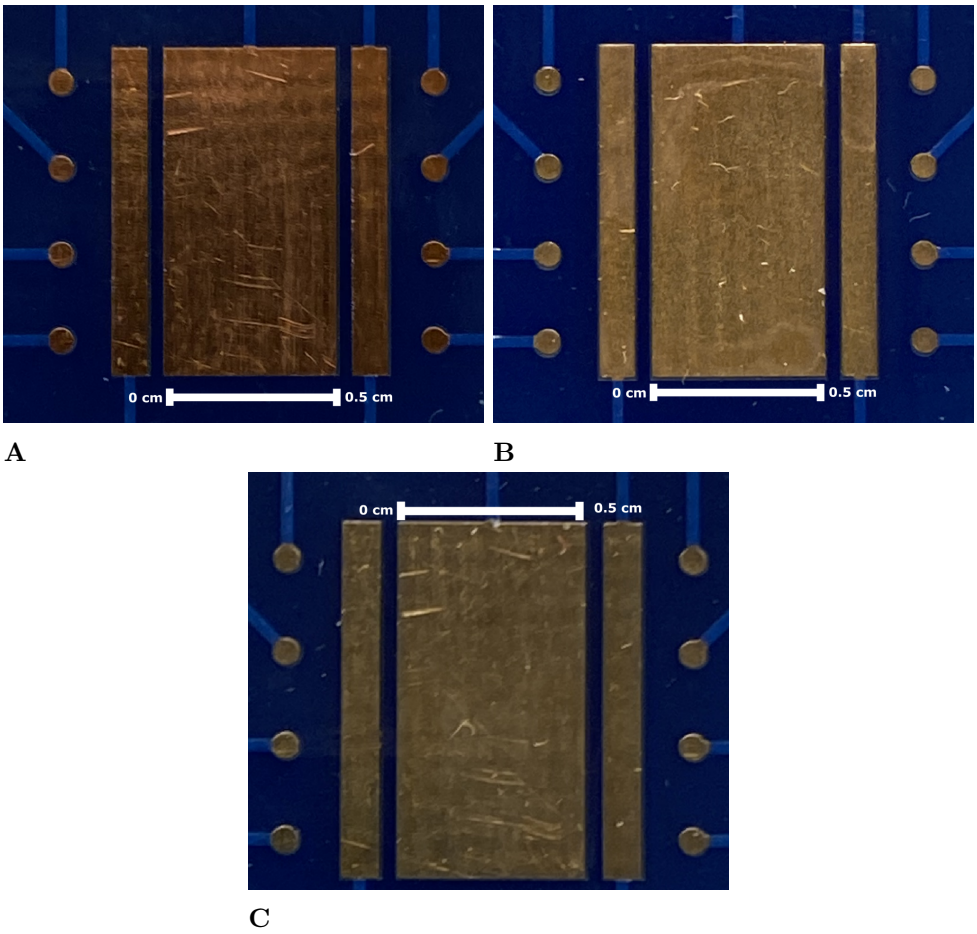

Figure 3.5: PCB P3 box fresh (no plating) (A). After bright electroless solution immersion at 50 °C for 10 minutes (B). After previous electroless treatment plus galvanostatic electroplating using ECF 60 solution at - 2.5 μA for 10 minutes (C).

Longer exposure times in solution proved to cause minimal changes to the visual appearance and the electrochemical response of the gold surface (Figure 3.5B). The response was overall encouraging of an electrochemical response typical of gold (discussed in section 3.3.2). The electrochemical response was still not optimal. This was hypothesised to be due to the absence of full gold coverage on the electrodes. For this reason, the PCB underwent a second gold plating, this time utilising electroplating techniques. After the initial 10-minute electroless plating treatment the PCB was electroplated for 10 minutes, using two different applied currents - 2.5 μA and -4 μA. Different applied currents were implemented to investigate the effect of current magnitude on optimal gold

coverage. The visual appearance of the gold and the electrochemical response (Figure 3.5C) failed to produce any substantial differences between the two applied currents. An example chronopotentiometry of the gold plating response is shown in Figure 3.6.

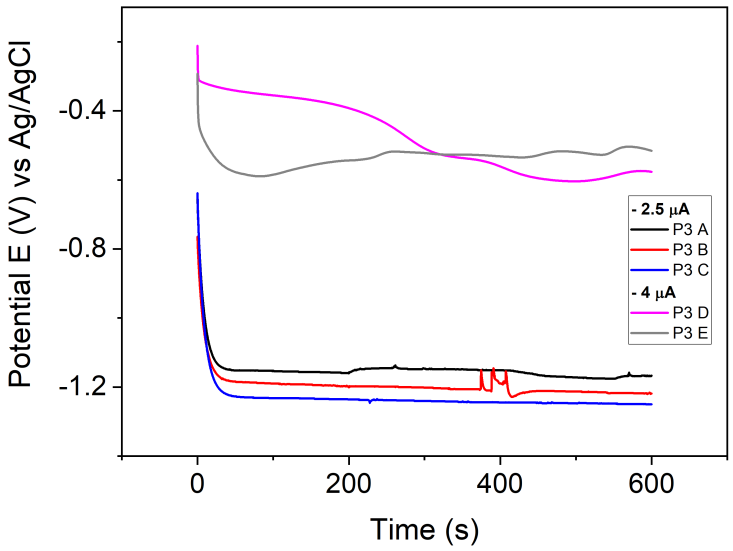

Figure 3.6: Example of a chronopotentiometry plot during electroplating of P3 board in ECF 60. Two currents were used - 2.5 μA and - 4 μA vs Ag/AgCl. Letters are used to denote separate boards. Total area plated $\approx$ 7.8832 cm^2.

These plots displayed the potential response to the applied current as a function of time, revealing the dynamics of gold atoms adsorbing onto the electrode surface forming the gold layer. For example, gaps in the gold layer resulting from non-uniform layer growth were evident from spikes in the potential. These spikes decayed to the steady state potential when uniformity was achieved.

The boards that received - 4 μA treatment showed about half the steady state potential of the - 2.5 μA potential. This was an inverse linear dependence between current and resulting measured potential. The - 4 μA treatment also displayed difficulty in obtaining and maintaining a steady state response evidenced by the long duration before the steady state potential was reached and then displaying an oscillating behaviour about the steady state potential instead of producing a consistent plateau. This could be a result of the current being too large for the surface area of the PCB resulting in

the diffusion of gold to the surface becoming chaotic creating more pronounced non-uniformities. There was no distinguishable benefit between the two currents. The -2.5 μA currents were was used for future electroplating as it produced less chaotic chronopotentiometric behaviour.

3.3.2 PCB Electrode Cleaning

All PCBs were subjected to electrochemical cleaning techniques. P1 - P3 underwent 20 cycles in 0.1 M H_2O_2 with a potential window -0.4 to 1.2 V vs gold. P4 underwent 15 cycles in 50 mM KOH with a potential window of -1.2 to 0.6 vs saturated Ag/AgCl.

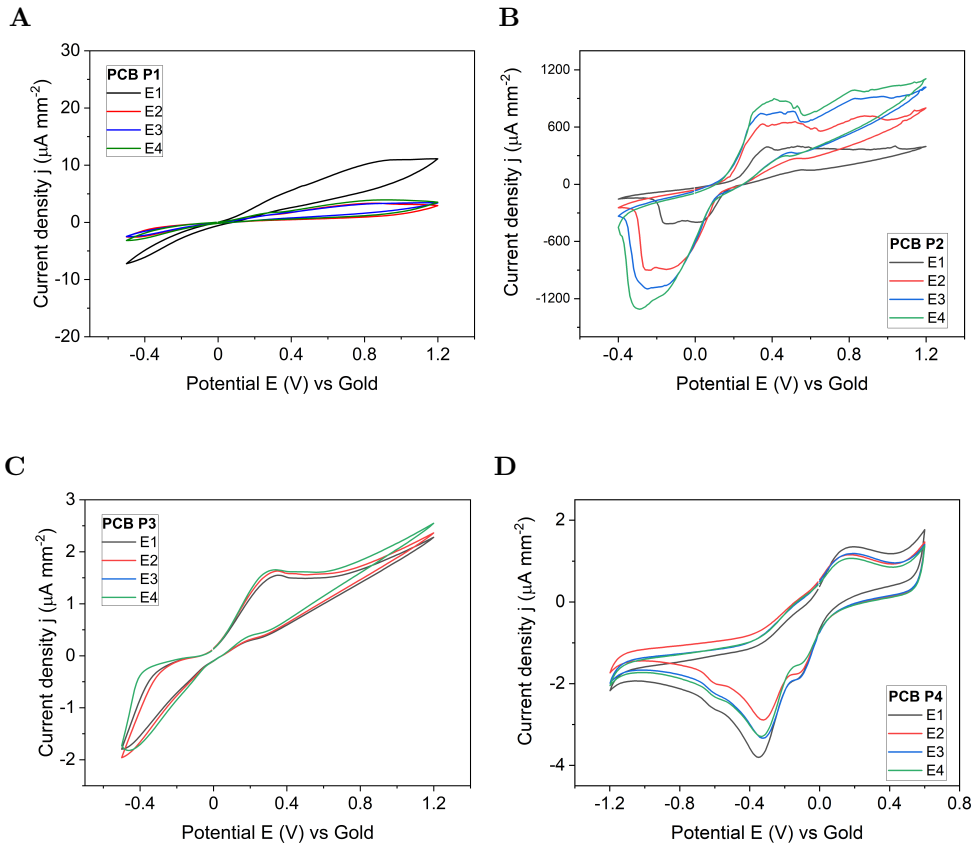

Figure 3.7: Electrochemical cleaning CVs of PCB P1 (A), PCB P2 (B), PCB P3 (C) and PCB P4. A, B and C underwent 20 cycles in 0.1 M H_2O_2 with a potential window -0.4 to 1.2 V vs gold. D P4 underwent 15 cycles in 50 mM KOH with a potential window of -1.2 to 0.6 vs saturated Ag/AgCl. Note electrodes are labelled E1, E2, ...

PCB P1's CV presented without obvious oxidation and reduction peaks, but the begin-

nings of a redox profile were apparent. This was likely due to heavy contamination or poor gold coverage and was not a suitable cleaning CV profile.

PCB P2's electrochemical cleaning CV showed square gold oxidation and reduction peaks at 0.4 V and – 0.4 V. The reason for these peaks was due to a current limiting effect when gold was re-plating and stripping from the surface. This was attributed to the almost complete removal of the gold layer (Figure 3.8). Normally the gold oxidation peak is due to the removal of a superficial layer of gold molecules from the electrode surface. In this case, the gold was almost completely removed leading to a limited current response due to the lack of remaining gold molecules available to effect further current responses. This resulted in the plateau and square peak profile. The reverse was true for the reduction peak. It began with re-plating some gold molecules producing a decreasing current response, but the gold did not completely re-plate leaving large areas bare and limited the current once again. The current range was large and indicated problems with the gold plating on the board. These are discussed in more detail in the electrochemical analysis (Figure 3.3.3). A smaller oxidation peak at 0.8 V was present in some responses, it was unclear what the second oxidation peak represented, perhaps gas evolution.

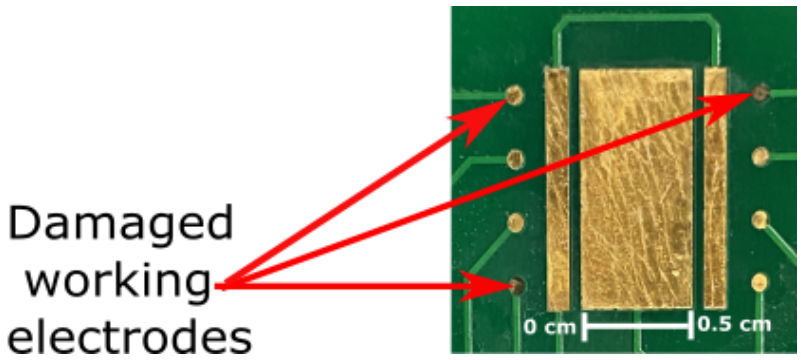

Figure 3.8: The damage experienced on PCB P2 working electrodes during electrochemical cleaning. The gold was removed and the underlying copper tarnished.

PCB P3 presented with an oxidation peak accompanied by a significant amount of background current evidenced by the sloping response at higher potentials. A distinct reduction peak was absent, this could be due to gold removal and damage to the un-

derlying copper making the surface unable to re-plate gold metal ions. This was a promising profile, but more work would be needed if electrochemical cleaning was to be a sufficient method of PCB preparation. PCB P4 showed smooth gold oxidation and reduction peaks at 0.4 and - 0.4 V respectively. The CV profile was as expected for a clean and responsive gold surface. No other cleaning techniques were necessary for PCB P4.

PCB chemical cleaning

The initial cleaning of the PCB P2 boards composed of a 20-minute H_2SO_4 0.1 mM bath, 20-minute ethanol bath, 10-minute acetone bath, 20 minutes IPA bath and 2-minute base piranha bath. None of these techniques produced any substantial change in the electrochemical response. Acid piranha and base piranha baths were then investigated as a method to effectively clean the electrode surface. The boards were submerged in acid piranha for 20 seconds and then base piranha for the same amount of time before being submerged in DI water to remove residual piranha solutions and dissolved organic material. The acid piranha damaged the PCB substrate (Figure 3.9). It was a matter of submerging long enough to clean the electrodes but not long enough for the substrate to dissolve to an unusable state.

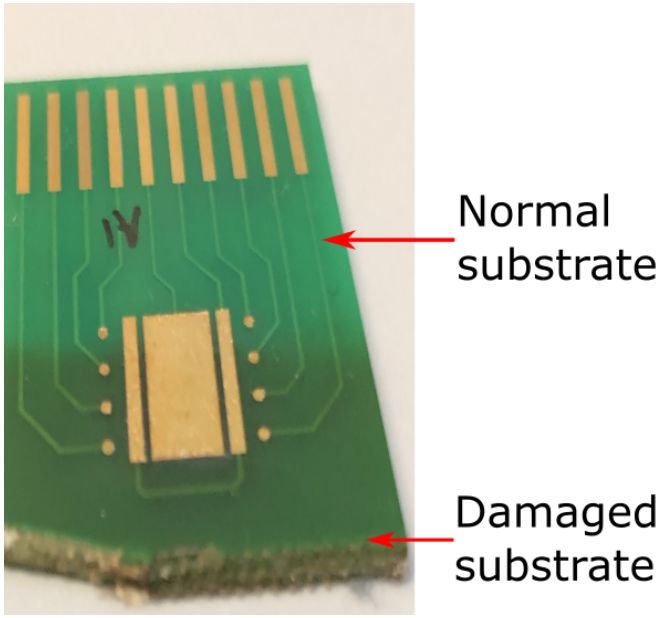

Figure 3.9: The damage done to the PCB substrate after being submerged in acid piranha. The board starts to rapidly dissolve in the solution. The substrate darkens progressively up the board via capillary action.

PCB P1 did not undergo any chemical cleaning. PCB P3 used acid and base piranha solutions discussed above. PCB P4 used a 50 mM KOH in 35 % H_2O_2 solution bath, immersed for 15 minutes. The electrochemical response to these cleaning methods is discussed in section 3.3.3.

3.3.3 PCB Electrochemical Responses (Redox buffer)

The electrochemical responses (CV, SWV and EIS) were measured after the gold plating and cleaning techniques outlined in the previous sections. The responses aid in determining if the PCBs were suitable for further testing or can revel information as to why it was not suitable.

Electrochemical response of Gold Plated Electrodes

PCB P1's electrochemical response to electrochemical cleaning showed small redox peaks (Figure 3.10A). These peaks occurred at various currents for each electrode, this can be explained by the fact that the electrodes were all different sizes with smaller

electrodes tending towards microelectrode behaviour i.e. a steady-state current instead of peak current. The electrodes that did form peaks often had large peak separation, indicating a non-reversible system as a result of a lack of a suitably clean/functional surface. This was as expected for a recently plated and uncleaned surface.

PCB P3 was subjected to 10-minute 0.1 mM H_2SO_4 acid bath cleaning before testing. The electrochemical response to 10-minute electroless plating and 10-minute 0.1 M 0.1 M H_2SO_4 acid bath (Section 3.3.1) is shown in Figure 3.10B.

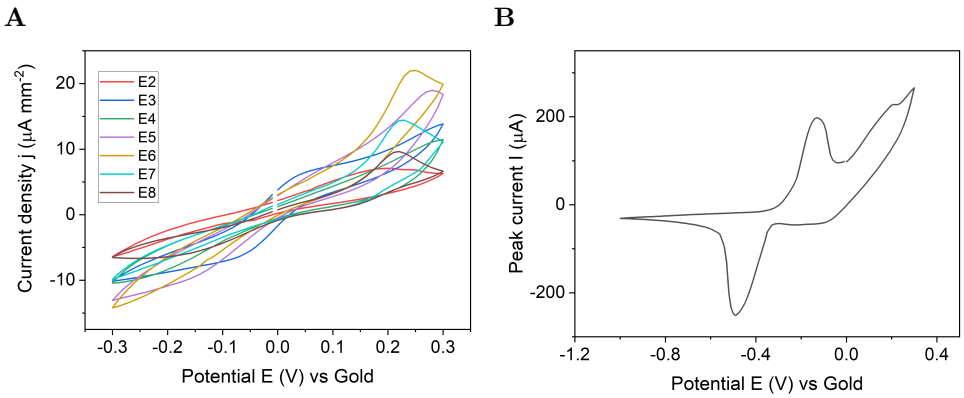

Figure 3.10: Example of PCB P1 CV electrochemical response to electroless gold plating (A). An example of PCB P3 CV electrochemical response to electroless gold plating (B). Both electroless platings consisted of plating for 10 minutes at 50 °C in bright electroless gold plating solution and then subsequent 10-minute 0.1 M H_2SO_4 acid bath. All measurements were taken in 5 mM redox buffer.

The CV demonstrated appropriate shape and definition but the potentials at which the peaks occurred were shifted to more negative regions than expected for gold and produced high currents (- 200 μA and 200 μA). There were hints of a second peak occurring at 0 V. An initial hypothesis for this was that due to copper and gold exposure from the lack of complete gold coverage, produced a mixed metal response. To investigate this, the board was electroplated after the initial electroless treatment, determining if this improved the gold coverage. The same response was found suggesting the extra plating did not suitably increase the gold layer thickness resulting in complete coverage.

Electrochemical response after electrochemical cleaning

PCB P1 CVs showed little peak forming redox behaviour (Figure3.11A). The four electrodes shown were the smallest ones tested so these were more likely to have a mix of macro and micro behaviour as can be seen with E1 (smallest) having very little peak behaviour and E4 (largest) showing peak behaviour. The peaks were all accompanied by large background currents as evidenced by the large sloping current response that failed to level off at the extremum potentials. The DPV response showed the expected and well-formed peaks at about 0 V though, due to background currents the peaks resulted in a slight sloping behaviour with E1 showing a large current shift compared to the others (Figure 3.11B). A second peak formation was evident past 0.4 V and was likely due to insufficient gold coverage or surface contamination.

The EIS responses were appropriate for some electrodes, E3 for example produced semi-circular behaviour with a Warburg region (Figure 3.11C). Others failed to form this response and displayed varying profile shapes. This data confirmed what PCB P1's cleaning CV was eluding to (Figure 3.7A), that there was likely insufficient gold coverage to allow for a complete electrochemical response typical of gold and that stubborn contamination from the gold plating process was likely further compounding this issue. The results were promising for a first attempt with an in-house fabricated and plated system.

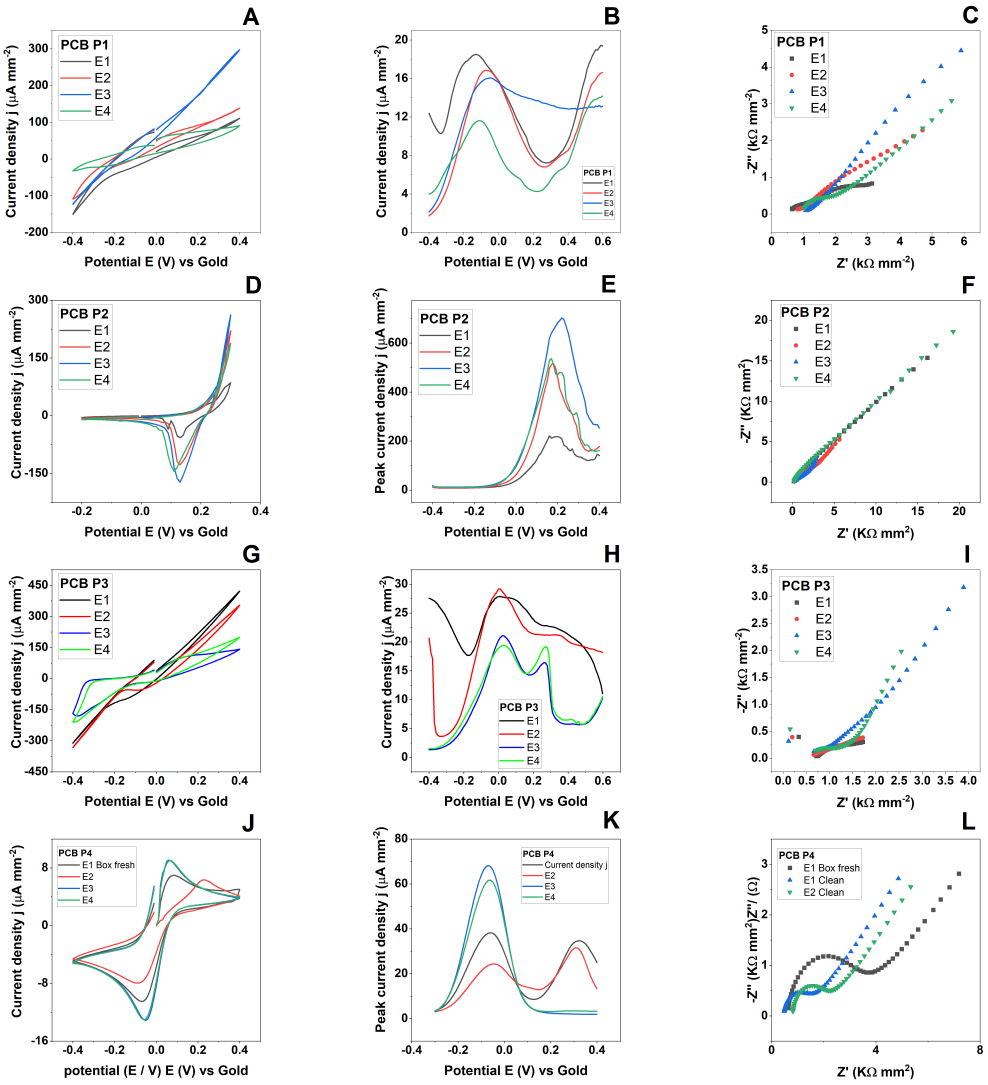

Figure 3.11: CV response of PCB P1 (A), DPV response (B) and EIS response (C) to electrochemical cleaning (Figure 3.7A). CV response of PCB P2 (D), DPV response (E) and EIS response (F) to electrochemical cleaning (Figure 3.7B). CV response of PCB P3 (G), DPV response (H) and EIS response (I) to electrochemical cleaning (Figure3.7C). CV response of PCB P4 (J), DPV response (K) and EIS response (L) to electrochemical cleaning (Figure3.7D). The current was normalised using current density (Current/Area) and impedance values were normalised by multiplying by area (Impedance*Area) Measurements were taken in 1mM redox buffer and note electrodes are labelled (E1, E2, ...). EIS measurement settings used (E_{dc} vs OCP = 0.0 V, PCBs P1 to P3 frequency range: 1 Hz to 10 kHz and PCB P4 frequency range: 1 Hz to 50 kHz).

PCB P2 did not produce the expected electrochemical response of gold upon immediate

use (Figure 3.12). This was not entirely unexpected as the surface was likely to be contaminated from the plating process, warehouse storage and packaging process. This was evident in Figure 3.12A which showed an atypical CV profile (see Figure 1.11 for typical profile) lacking a fully defined oxidation peak and a complete lack of any discernible reduction peak. The lack of proper redox behaviour was further exemplified in Figure 3.12B with a distinct lack of obvious DPV peak currents. This suggested that the redox couple was unable to access the electrode surface to undergo redox reactions, which was consistent with the surface suffering from heavy contamination. Further evidence for surface contamination can be seen by the appearance of large impedance values upon EIS investigation (Figure 3.12C) with values in the MΩ range, which were not typical for electrodes with this geometric surface area and chosen redox buffer concentration. MΩ impedance values were more consistent with microelectrodes or from electrodes functionalised with very dense SAMS. These values would make sense if interpreted as a result due to a contaminating barrier impeding the redox ions from reaching the surface reducing the rate at which the redox ions can react, thus reducing the current i.e. increasing the impedance.

This evidence made it clear that it was necessary to adequately clean the electrodes, to generate the purest surface possible to allow for the optimal electrochemical response and the most efficient functionalisation of the surface with molecules and biomolecules i.e. forming SAMs. H_2SO_4 0.1 mM electrochemical cleaning using a potential window of -0.5 V to 1.2 V for 20 scans was the first successful cleaning method to produce a significant change in electrochemical response (Figure 3.11).

Although electrochemical cleaning managed to effect a change in the electrochemical response of PCB P2, the behaviour was still not ideal. Electrochemical cleaning in H_2SO_4 CV showed redox peaks, but their shape, roughness and position were not typical of a clean gold surface. This behaviour may be explained by the fact that the electrochemical cleaning damaged the board by stripping the gold (oxidation of gold) and nickel layers tarnishing the copper sub-layer as shown in the previous section (Figure 3.8).

The potential window has a well-established range for gold redox reactions in H_2SO_4

and is non-damaging to gold surfaces [141]. Reducing the potential window to -0.3 V and 0.3 V still managed to remove the gold layer and tarnish the underlying copper. This could be due to poor gold adherence to the underlying metal surfaces (nickel and copper) and/or poor gold coverage leaving holes in the surface exposing the nickel and copper, resulting in a three-metal working electrode. Copper exposure was unlikely as the electrodes when later immersed in a base piranha bath remained undamaged. It was noticed in chemical cleaning experiments that copper is rapidly removed from the PCB substrate when directly exposed to base piranha.

The supplying company did not reveal details on their plating methods, so it was difficult to determine possible explanations for the ease of gold removal during voltammetric experiments. To continue with experiments, the cleaning CVs were halted at a potential where the gold redeposited (reduction of gold occurs) on the working electrodes. This in general left a non-uniform gold coverage, or where heavy copper tarnishing was present, no apparent gold was observed. This can be seen from Figure 3.11D as a shift in the potential where the CV peaks form (0.18 V), ideally the peaks should be located on either side of 0 V. The fact this was shifted indicated that there were other metals present affecting the reference potential. This was a slight improvement from the box fresh stage in that there were now both reduction and oxidation peaks, though lacking definition. Figure 3.11E showed the emergence of a peak current, with the current peaking at high values and the peak potential shifted to 0.2 V confirming the shift seen in the CV. This combined with figure 3.11G displaying low impedance indicated that the cleaning method had removed contaminants producing better current and impedance responses. Unfortunately, this removal process was too aggressive and removed the gold along with the contaminants exposing the copper beneath leading to extreme currents and impedances. The EIS response had also departed from its ideal semi-circular profile meaning it lost a majority of its capacitive behaviour. This behaviour was a result of the formation of a double layer at the surface. If the surface was not relatively smooth and uniform, this would affect double layer formation. The generation of an uneven surface with multiple defects forcing complex double-layer formation resulting in the departure from ideal capacitor behaviour was seen. This was due to the gold and nickel

being stripped and redeposited many times damaging the copper sub-layer.

PCB P3's CV response showed complete failures for E1 and E2 (Figure 3.11G). E3 and E4 showed a deformed redox profile occurring around the expected 0 V region. The DPV results showed sub-optimal responses for E1 and E2, and dual peaks around 0 V for E3 and E4 (Figure 3.11H). The slight sloping was a result of background current, the dual peak was most likely due to contamination and areas of incomplete gold coverage. The EIS responses were not ideal for any electrode with E3 and E4 having the better profile with the small appearance of semi-circular behaviour (Figure3.11I). All these results demonstrated this method of surface cleaning was not desirable.

Some of **PCB P4's** abilities were already witnessed via a demonstration at the University of Bath. Confidence in its performance was therefore high and with very little time left to finish experiments in the PhD project only a concise test on two electrodes were conducted to confirm the presence of the required performance.

The CV response produced ideal profiles with peaks located at appropriate potentials (Figure 3.11) even for the box-fresh stage though, cleaning improved the definitions of the CV. DPV responses showed well-defined peaks at suitable potentials, resulting in minimal non-Faradaic currents (Figure 3.11K). The EIS data showed low R_{ct} values and well defined semi-circular with Warburg behaviour (Figure 3.11L). This data suggested that the board had a uniform hard gold layer able to withstand electrochemical cleaning. After undergoing cleaning the boards appeared to be free from major contaminants. This data was an example of what the ideal electrochemistry typical of gold should look like and was expected for a suitable biosensor platform. DNA experiments were later performed on these boards, but these are discussed briefly at the end of this chapter and in-depth in preceding chapters.

Electrochemical Response after chemical cleaning

Electrochemical cleaning success proved to be dependent on the quality of the gold on the PCB with PCB P4 (successful) and PCB P2 (unsuccessful) being exemplars of this. Consistency within a PCB type was also an issue with some cleaning attempts

being more beneficial than others. To clean the electrode surfaces on PCBs P2 and P3 chemical cleaning was investigated. The electrochemical responses of the boards after various chemical cleaning protocols are presented here. PCBs P1 and P4 did not undergo chemical cleaning experimentation as P1 showed enough of a response with electrochemical cleaning to continue with (P1 was also a prototype that was unlikely ever going to be the chosen device) and P4 showed excellent responses from electrochemical cleaning.

PCB P2 electrochemical response to chemical cleaning. Since electrochemical cleaning was damaging to the electrode surface on P2 boards, chemical cleaning was substituted to attempt to improve the response. The electrochemical response due to 20-second acid piranha + 20-second base piranha was significantly improved (Figure 3.12D, E and F) compared to the electrochemical cleaning response.

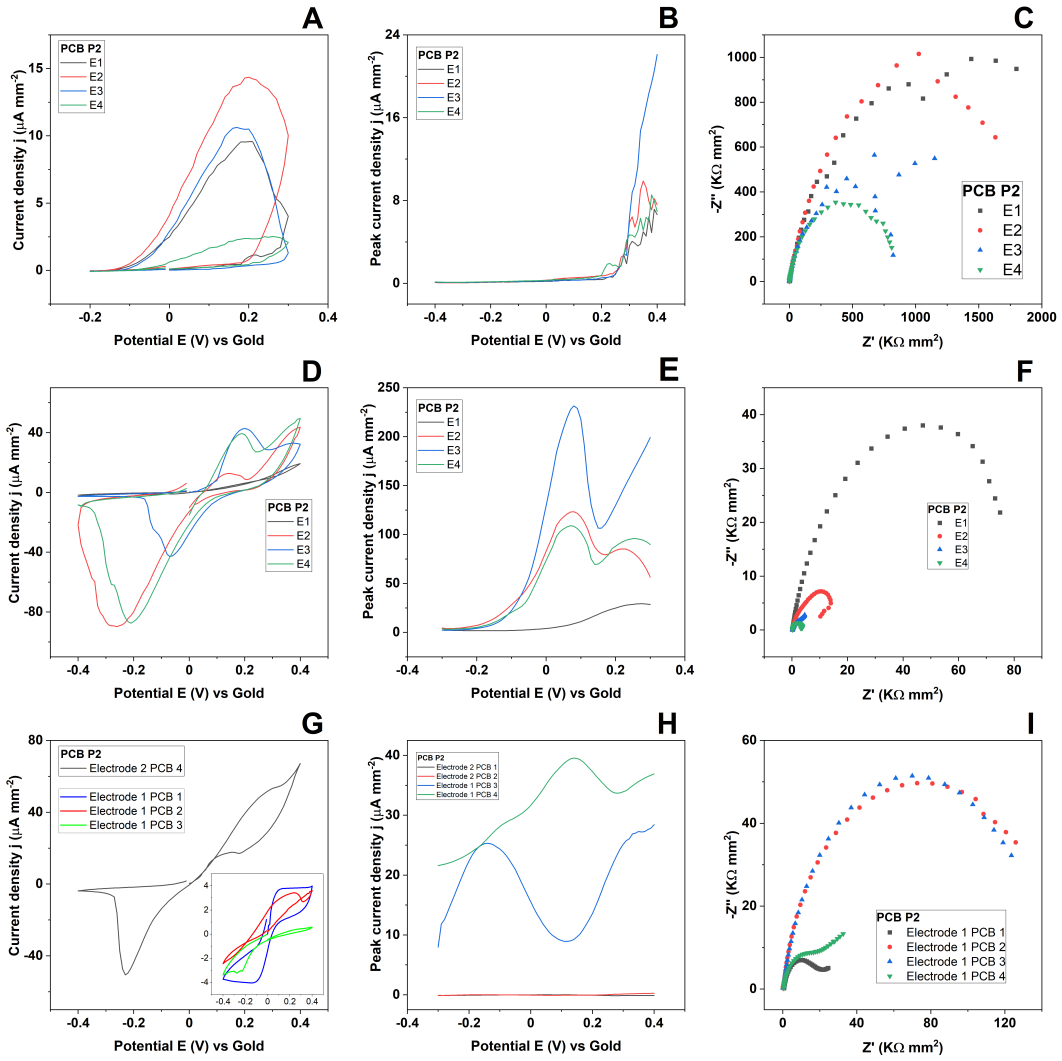

Figure 3.12: CV response of PCB P2 (A), DPV response (B) and EIS response (C) of a box-fresh device (no cleaning). CV response of PCB P2 (D), DPV response (E) and EIS response (F) to 20 seconds each acid and base piranha. CV response of PCB P2 (G), DPV response (H) and EIS response (I) to 10 seconds acid and 1-minute base piranha. The current was normalised using current density (Current/Area) and impedance values were normalised by multiplying by area (Impedance*Area) Measurements A to F were taken in 1mM redox buffer and note electrodes are labelled (E1, E2, ...). Measurements G to H were taken in 5 mM redox buffer and note that it is a single electrode from multiple boards. All EIS measurement settings used (E_{dc} vs OCP = 0.0 V, frequency range: 1 Hz to 50 kHz).

The CVs showed a mixture of well-defined oxidation peaks and reasonable reduction

peaks. The redox peaks occurred at various potentials between -0.25 V to 0.2 V approaching ideal peak positions. Peak separation indicated a non-reversible system though, electrode 3 may have been reversible. Comparatively (Figure 3.12A) and (Figure 3.11D) did not present any of these characteristics. The DPV response contained smooth current peaks located at a reasonable potential between 0 V to 0.1 V although these peaks contained non-Faradaic currents at potentials higher than the main peak (Figure 3.12E). The peaks should be roughly symmetric about the peak potential. As discussed in (Section 2.5.4), DPVs minimise these non-Faradaic currents thus to be still present reveals information about the surface. Since the double layer was the main cause of non-Faradaic currents, there was further evidence suggesting the surface of the electrodes suffered from non-uniform coverage. A more complicated double layer resulted from this, allowing for a significant charge to build resulting in additional unwanted current responses.

The effects of departure from an ideal double layer were also apparent in Figure 3.12F. Although there was a return to the desired semi-circular EIS profile, the response had progressed further along an inward curving path instead of producing a linear Warburg response. This continued inward curving behaviour developed loops and was indicative of induction processes on the electrode surface, sometimes called low-frequency hook [198]. Induction usually occurs at lower frequencies and is thought to be a result of the slower alternating current frequency allowing more time for the analyte to interact with the surface and adsorb [199]. Inductive loops are seen in battery electrochemistry because of multiple metal layers that combine to form more complicated local electric potentials. This is especially prominent if the concentrations of the metals change, producing local electric potentials that supply the paradoxical current response. Adsorption of materials can also create these local potentials. The P2 boards utilised three different metals (copper, nickel, and gold) thus may have played a role in the formation of these loops, perhaps in conjunction with adsorbed material from the redox buffer. The nature of inductive loops is very complicated and has an entire field dedicated to researching them. Further investigation of these loops was not performed as it was not within the scope of the project and rarely occurred in experiments.

The piranha treatment tested so far improved the electrochemical responses of the PCB. The responses continued to be non-optimal and it appeared that a trade-off between wanted and unwanted characteristics between the electrochemical cleaning and piranha treatments developed.

To further optimise and streamline PCB surface cleaning techniques, changes were made to the piranha protocol to reduce board damage (as was seen in section 3.3.2) caused by acid piranha. The 20-second acid piranha bath was reduced to 10 seconds and the base piranha bath duration was increased from 20 seconds to 1 minute. The concentration of redox buffer was changed from 1 mM to 5 mM (Table 3.2). The reason for changing the buffer concentration was due to findings in other experiments that this was a more suitable buffer to produce electrochemical responses on PCB boards. Four P2 boards were used in this experiment, for completeness the box-fresh measurements with the new redox buffer were provided (Appendix B.1). EIS data was not included for box fresh measurements. One electrode from each of the four boards was used during this experiment whereas, in the last section it was four electrodes from one board. This method was adopted to show electrochemical behaviour across the boards.

The box-fresh data was similar to the initial boards using 1 mM redox as expected, producing poorly defined CV and DPV peaks. The piranha treated boards showed improved CV profiles. Some of these responses were not resolvable at this scale due to the eclipsing current range on PCB 4 in Figure 3.12G, an inset graph of the other electrode CVs showed their responses on a readjusted scale.

These CVs were still not ideal, much like the initial experiments. The DPVs (Figure 3.12H) had sporadic peak position or the presence of flat lines. These appeared in the initial cleaning experiments but were rare and became more prominent in these further cleaning attempts. Therefore, there was the occasional use of electrode 2 in the data. Electrode 1 on some PCBs experienced peculiar behaviour giving a diminished response to the applied potential. This was thought to be a connection issue between the board and multiplexer. It was common to see a lack of response on CV and DPV and then see a response with EIS (Figure 3.12I). This suggested that it was unlikely to be a connection

issue but EIS is a far more sensitive measurement technique on the electrode surface than the voltammetric tests. Consequently, it could be possible that a response could be induced even with a poor connection. This behaviour of flat line response was also seen on electrode 2 measurements. To rule out connection issues an examination of various combinations of boards, multiplexers and connectors was performed. It was found that changing any one of these variables could fully or partially resolve the issues. It was also observed that the problematic channels could suddenly start working again without intervention. This behaviour was quickly addressed and its effects were minimised.

PCB P3 electrochemical response to chemical cleaning. PCB P3's electrochemical responses to chemical cleaning techniques were tested after their dual gold plating processes were completed. At this stage of PCB development, many months of work had been accomplished. It was crucial to return to the main outlines of this research i.e pathogen detection. To facilitate this, a less methodical approach was adopted in investigating the suitability of these PCB sensors. The cleaning methods investigated here used only piranha solutions as they had already proved to be optimal for other PCBs. The electrochemical responses to 10 minutes in base piranha cleaning are shown in Figure 3.13.

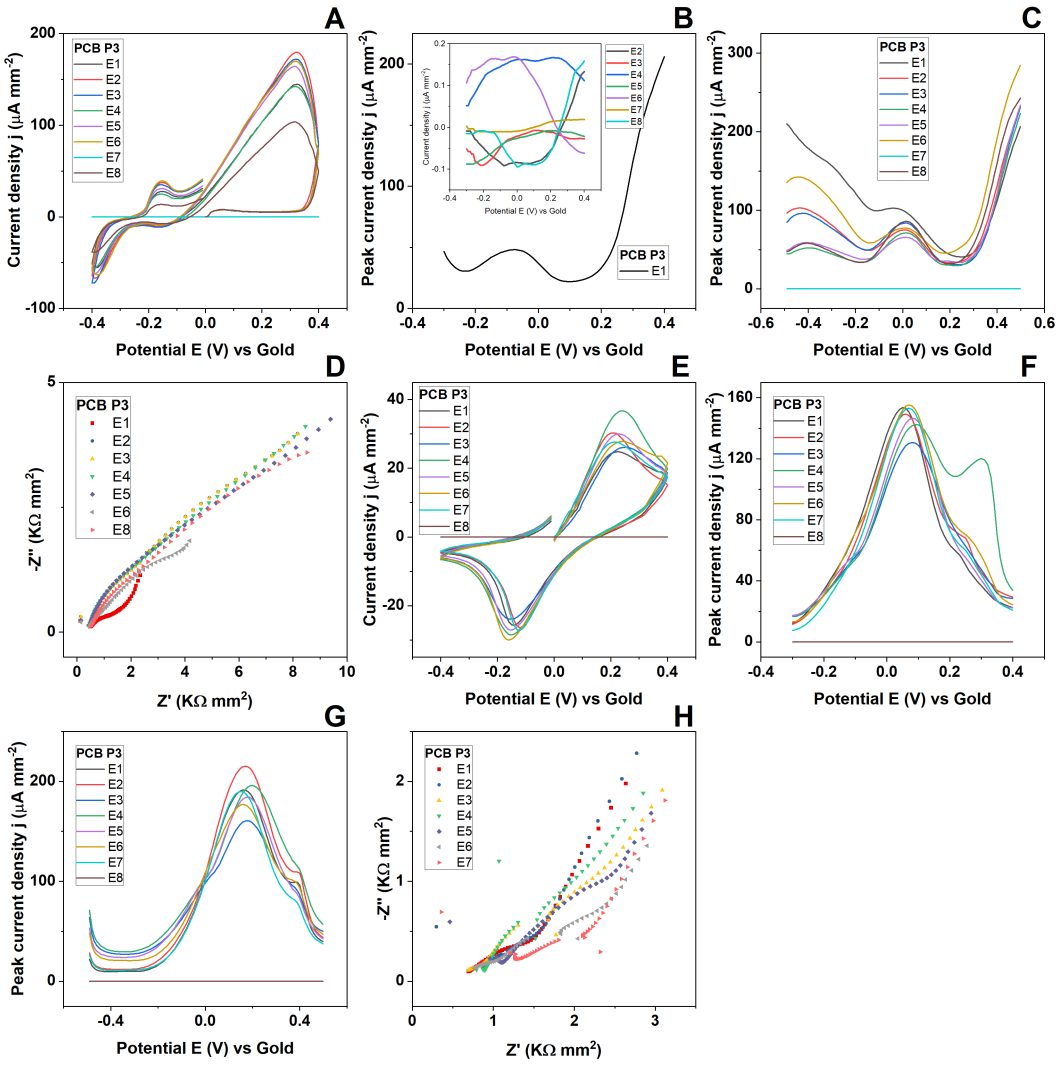

Figure 3.13: CV response of PCB P3 (A), DPV response (B), SWV response (C) and EIS response (D) of 10 minutes electroless plating plus 10 minutes electroplating and 10-minute base piranha cleaning. CV response of PCB P3 (E), DPV response (F), SWV response (G) and EIS response (H) to 10 minutes electroless plating plus 10 minutes electroplating and 10 seconds acid piranha. The current was normalised using current density (Current/Area) and impedance values were normalised by multiplying by area (Impedance*Area). Measurements were taken in 5mM redox buffer. All EIS measurement settings used (E_{dc} vs OCP = 0.0 V, frequency range: 1 Hz to 50 kHz). Note electrodes are labelled (E1, E2, ...).

The base piranha DPV measurements were substandard (Figure 3.13B) with electrode E1 producing the only reasonable response with the rest of the electrodes displaying

random responses most likely noise, at 1000th the current of electrode E1. SWV produced peaks for many of the electrodes although with a significant non-Faradaic current about the peak (Figure 3.13C). EIS measurements lacked semi-circular behaviour (Figure 3.13D) and were comparable to the electrochemical responses seen previously Figure (3.11I). CV measurements displayed signs of the general sought after behaviour (Figure 3.13A) but had two current peaks with increasing potential (the second beginning at 0 V) and formed the more massive oxidation peak in an anti-clockwise progression instead of a clockwise one (not discernible from the graph). There was no normal reduction peak behaviour. The boards also appeared to become damaged if submerged longer than 1 minute.

A 10-second acid piranha cleaning method was then tested to determine if it could affect a better response than the base piranha method. The results obtained showed an improvement (Figure 3.13). SWV measurements had improved peaks that were well defined and saw a reduction in non-Faradaic current slopes around the peaks (Figure 3.13G). DPV results showed current peaks at suitable current levels with no noise, again non-Faradaic currents were minimal (Figure 3.13F). EIS measurements were unable to be improved with significant discontinuities at 60 Hz frequency across many electrodes (Figure 3.13H). This was thought to be due to noise introduced to the system. Mains noise can be common in un-grounded EIS experiments though, this would typically manifest around 50 Hz (UK mains frequency). The exact source of the noise was not able to be discerned. Fortunately, the noise quickly resolved itself. The CV data showed a vast improvement in profile with oxidation and reduction peaks located in a more respectable potential window proving that this was a reversible reaction and continuing to be more in line with the typical electrochemical response typical of gold (Figure 3.13E).

After many months of trials, these piranha cleaning methods were able to enhance the PCB P2 and P3 board's electrochemical performances to an impressive level. Though, further, improvement was not possible due to time restrictions. PCB P4 demonstrated the best performances of all boards using chemical + electrochemical cleaning. Even

with most of the PCB responses not being equal and PCB P4 showing a clear dominance, they were all at a stage where they produced usable electrochemical signals. Therefore, before fully deciding which of these boards were suitable as a biosensor platform, SAM formation and DNA detection experiments were investigated.

DNA functionalisation and hybridisation on PCBs. A more in-depth analysis of PCB P4's performances is discussed in Chapter 4.

An example of its DNA performance was described here along with comparisons to the best DNA performances found using the other three PCB designs shown in the previous sections. This data was combined into Figure 3.14 for easier comparison. SAM functionalisation was identical on all boards and measurements taken in 5 mM redox buffer. Target concentrations were different across the boards and should be taken into consideration when comparing between boards.

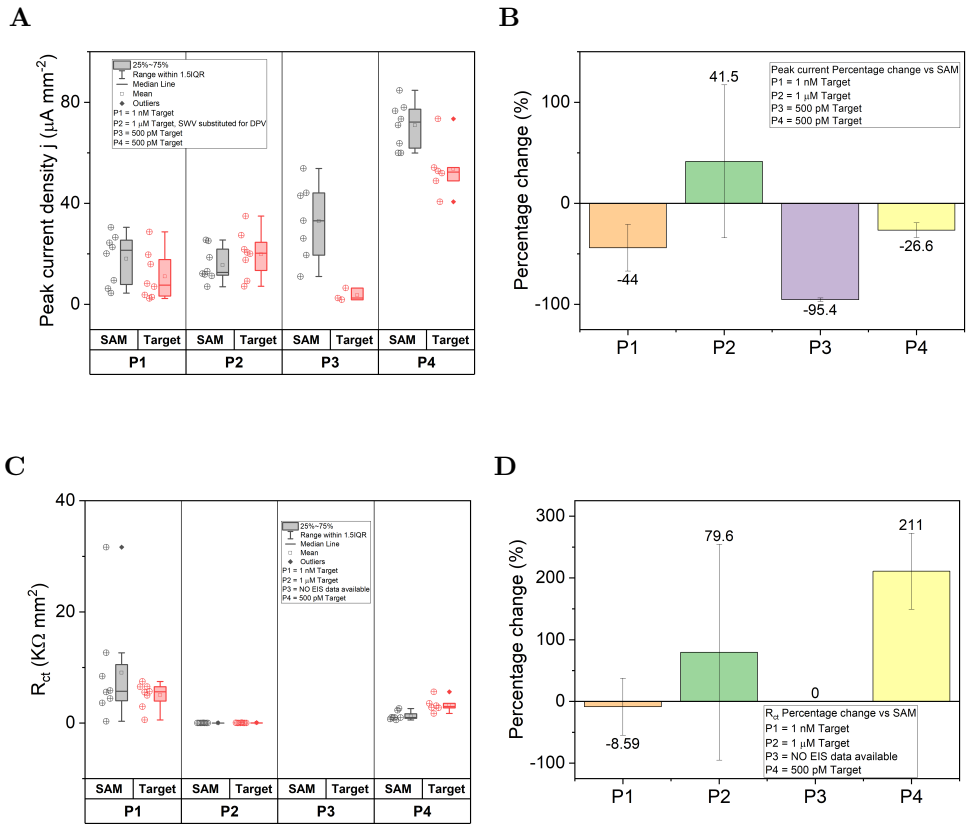

Figure 3.14: Example DPV raw data response of all PCB boards (A) to the addition of various *lytA* target DNA concentrations and their DPV percentage changes (B). Corresponding EIS raw data (C) and Percentage changes (D). All measurements taken in 5 mM redox buffer. EIS settings (E_{dc} vs OCP = 0.0 V, frequency range: 1 Hz to 50 kHz). n= 8 unless otherwise indicated. The n value is represented as the sum of the data points (circle with crosshair) on the box charts.

The DPV responses are shown in Figure 3.14A. PCB P1 showed average current decreases upon target addition with the current range and spread remaining similar. This current decrease was supported by a -44 % percentage current decrease (Figure 3.14B). The target group was unlikely different from the SAM as most data points overlapped. PCB P2 showed average current increases with similar current ranges and distributions to P1 (Figure 3.14A). This was supported with a 41.5 % current percentage change (Figure 3.14B). The target group was not different from the SAM group as the target median lay within the SAM IQR. PCB P3 showed large average current decreases upon target DNA addition with the current range and distribution also reducing significantly

(Figure 3.14A). This was accompanied by a loss of 4 electrodes. A -95 % current percentage change emphasised the large current reduction (Figure 3.14B). The target group was likely different from the SAM group as there was no data overlap between the two. PCB P4 also showed large average current decreases with the current range remaining roughly the same and the distribution becoming more compacted around lower current values (Figure 3.14A). Two outliers were detected allowing for the conclusion that the two groups were likely different as there was no data overlap between the SAM and target groups. If the outliers were included the outcome would have been that the two groups are still likely different as the target median still lay outside the IQR but with reduced confidence. A percentage change of -26 % confirmed the decreasing response (Figure 3.14B). The P4 board also lost two electrodes between SAM and target stages. This was a connection issue with the PCI interface and the potentiostat. This was due to the introduction of an unfamiliar interface system. Practice using the interface resolved the issues quickly.

The EIS data for PCB P1 showed a mean impedance decrease (Figure 3.14C) with the impedance range decreasing and the distribution becoming more compact around the median. A small impedance decrease was also seen -8.59 % percentage change (Figure 3.14D). The two groups were not different as the target median lay within the SAM groups IQR. PCB P2 showed extremely small impedance values with the average impedances increasing upon target addition (Figure 3.14C). This was not discernible from the graph due to the axis scaling it was nonetheless, obvious from the 76.6 % percentage increase in impedance (Figure 3.14D). The two groups were not significantly different as the target median lay within the SAM IQR. As mentioned in previous analysis, EIS fits were not possible on this P3 data so there was no box chart or percentage change data. PCB P4 showed small average impedance increases, with the impedance range and distribution remaining similar (Figure 3.14C). The percentage change in impedance was 211 %(Figure 3.14D), this was a comparatively large signal. The target group was likely different from the SAM group as the target median lay outside the SAM IQR and maximum data value.

PCB P1 was unable to show successful 1 nM target DNA detection using DPV and EIS. PCB P2 had no target detection with DPV and EIS techniques, it also proved difficult to clean with severe electrode damage occurring when electrochemical cleaning under what should have been suitable conditions. PCB P3 also gave an impressive performance using dual plating techniques performed in the lab and was able to successfully detect 500 pM target DNA using DPV. P3 showed poor EIS profiles that resulted from difficulties in fitting the data to equivalent circuits, it suffered from a loss of electrodes at various functionalisation stages. If it had been more consistent it would have been a suitable biosensor platform for project progression. Ultimately PCB P4 showed all the impressive abilities that P1 and P3 displayed and improved upon them. The device was able to detect 500 pM target DNA using both DPV and EIS techniques. The PCB was consistent after the connector interface problems were resolved and demonstrated improved error performance compared to the other three PCB designs. It was for these reasons that PCB P4 was chosen as the biosensor platform for future project experiments.

3.4 Conclusions

As seen in the previous chapter, the need for a high throughput device with consistent electrochemical response was required to reduce experimental complexity and duration while increasing sample repeats for improved statistical analysis. PCB technology was investigated in this chapter to determine if such sensors demonstrate these requirements.

Prototype PCB P1 was quickly designed, fabricated, and tested to give a proof of concept of electrochemical responses typical of gold on a PCB device. It was successful in showing that gold electroless plating was possible on PCBs with copper traces and pads. The PCB also showed the ability to be cleaned to a suitable enough level that DNA experiments were able to be performed. PCB P1 provided enough promising data to warrant testing of better quality commercially manufactured boards with a redesigned, more efficient layout using various plating methods (industrially and lab self-plating).

PCB P2 was commercially fabricated and hard gold plated and showed a lack of electrochemical response to solvent, acid and electrochemical cleaning with the latter causing the removal of the gold layer and copper sub-layer tarnishing. Only 10-second exposure to acid piranha was able to clean and precondition the surface enough to elicit an electrochemical response. The electrochemical behaviours were poor with incomplete CVs lacking reduction peaks, rough DPV profiles with peaks at unreasonable potentials and EIS measurements giving a mixture of appropriate semi-circular response and unwanted linear responses. Though the responses were not optimal they were still tested for SAM formation and DNA hybridisation. The data showed that SAMs were able to form although produced highly variable DPV and EIS signals. Changes in these signals upon DNA hybridisation occurred suggesting some response to target DNA. These signal changes were not consistent across multiple PCBs and had significant errors thus preventing a trustworthy and reliable confirmation of DNA detection. It was concluded that the P2 boards were not a suitable platform to continue with due to inconstant responses (most likely due to inadequate gold coverage).

PCB P3 was found to have an optimal plating protocol consisting of 10 minutes in bright electroless gold plating solution at 50 °C followed by 10 minutes electroplating in ECF 60 solution at a current of -2.5 μA. 10-second acid piranha bath again gave the best cleaning response. The board showed improved CV profile and the appearances of reduction peaks in response to this cleaning method. The DPV peaks were also improved and occurred at sensible potentials but suffered from non-Faradaic currents present about the current peaks. SWV also showed good peak current definition and EIS showed a poor linear response rather than the semi-circular response. DNA testing showed impressive signal changes upon target DNA addition. The changes were more substantial, more consistent and had reduced errors compared to P2. 500 pM target DNA was successfully detected using DPV but not with EIS. The conclusions on the P3 board were similar to P2. Even with the superior performances compared to P1 and P2 the reliability was not sufficient enough to continue putting time and resources into its optimisation, partly due to unavoidable time constraints. Even though this board's development was discontinued there was full confidence that further work on the board

would yield a reliable and suitably performing board for biosensor applications.

PCB P4, the commercially acquired PCB showed excellent responses across all measurements giving exemplary responses to each technique upon electrochemical cleaning. DNA tests were performed with 500 pM target detection using DPV and EIS. Having already worked on the P4 boards in a workshop at the University of Bath and the quick testing performed in the lab it was the logical choice to confirm this board as the biosensor platform to finish the remaining experiments in this PhD research. With a biosensor platform chosen, experiments on bacterial DNA detection was next investigated.

Chapter 4

Electrochemical Detection of *Streptococcus pneumoniae*(DNA Biosensor)

4.1 Introduction

Streptococcus pneumoniae is a Gram-positive aerobic encapsulated diplococci (Figure 4.1) (occurs as pairs of cocci). It is also α-haemolytic (causes red blood cell lysis) [123]. It colonises mucosal areas of the nasopharynx and upper airway [125] and is responsible for the majority of community-acquired pneumonia [200, 201] that have a recorded organism identified. It is a common cause of the upper respiratory infections (URI) such as otitis media and sinusitis. Further progression of the bacteria can lead to invasive pneumococcal diseases (IPD) [202] which includes: pneumonia, meningitis, bacteremia, endocarditis, septic arthritis and rarely peritonitis. These invasive diseases and sepsis lead to about 2 million global deaths per year [203] with the fatality rate between 11 % - 30 % [204].

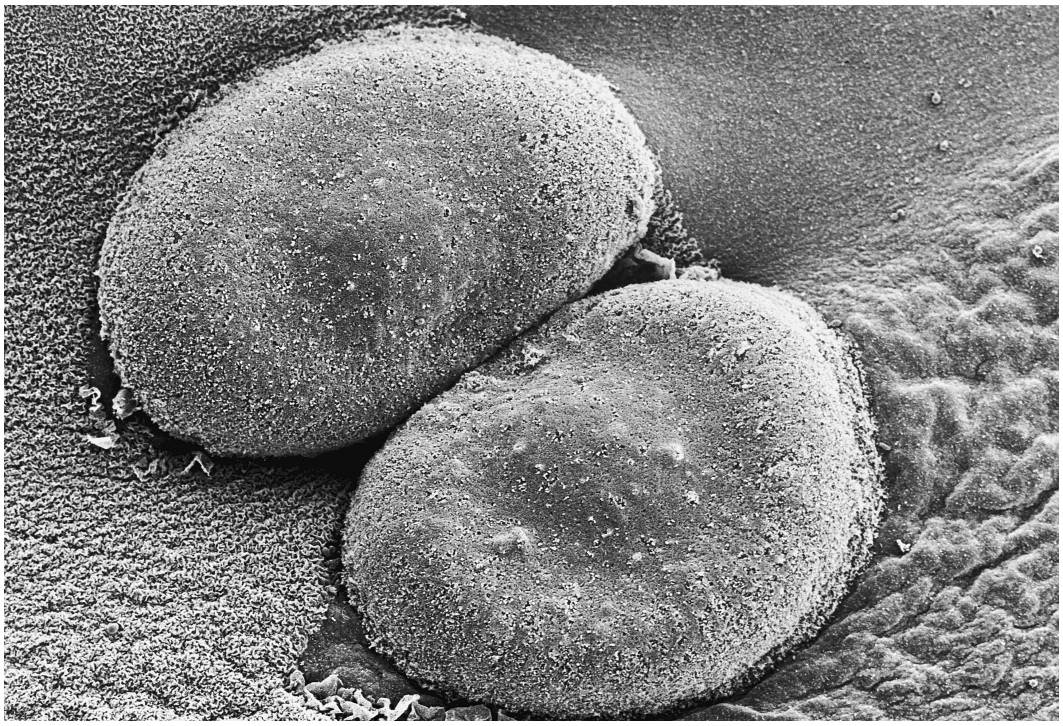

Figure 4.1: SEM of *Streptococcus pneumoniae* colony. Credit: SEM of Streptococcus pneumoniae colony. Credit: Debbie Marshall. Attribution 4.0 International (CC BY 4.0). Creative Commons Attribution (CC BY 4.0) terms and conditions https://creativecommons.org/licenses/by/4.0.

Current detection times take hours to days for results (see section 1.3) . Pneumococcal urinary antigen tests can provide a time to result upon sample application in 15 minutes [205]. This has a caveat of having to equilibrate the device, patient urine sample and reagents to room temperature before hand. The procedure requires multiple steps. Whilst not complicated it is not as simple as sample addition then wait for result. Studies show improved specificity over standard culture techniques for community acquired pneumoniae however, often state that a limitation of the study is that the results may not be generalisable to other patient populations [206, 207, 208]. Technologies that can minimise these limitations, would represent a significant step enhancement in sepsis diagnosis and management. Electrochemical biosensors offer simple, low cost and real time accurate detection [209, 210]. By functionalising PCB electrodes with a DNA probe sequence that specifically binds a truncated sequence from the *S. pneumoniae lytA* gene

which encodes the major autolysin LytA, a label free *S. pneumoniae* biosensor platform was developed. It has been shown that *lytA* is specific to *S. pneumoniae* even though *S. pseudopneumoniae* and streptococci from the mitis group (SMG) contain a *lytA* like gene that is similar (up to 80 % sequence homology). *lytA* was distinguishable between these *lytA* like alleles [211, 212] allowing for accurate and specific detection using PCR techniques. Amplification of a 235 pb from the *lytA* gene has been shown to electrochemically distinguish *S. pneumoniae* from similar streptococci [213]. In this chapter it was shown that using a *lytA* probe and a 20 bp sequence from the *lytA* gene [213] and PCB P4 biosensor platform that this target was detectable at 10 pM in PBS with a calculated limit of detection (LoD) = 4.5 pM. The amplified 235 bp *lytA* using primers form [213] was detectable at 1 pM in complex human serum with a 15 minute time to result at room temperature.

4.2 Materials & Methods

All measurements were taken using a PalmSens4 potentiostat running PSTrace software from Alvatek electrochemical solutions (Houten, Netherlands). The electrodes used were custom in house fabricated microelectrodes, SEP1 BIOTIP multichannel electrode PCB platform discussed in chapter 3, 1.6 mm diameter gold polycrystalline macroelectrodes (referred to macroelectrodes in this section) using a 1.6 mm platinum macroelectrode as combined counter and reference electrode unless otherwise stated. Both purchased from IJ Cambria (Llanelli, UK).

4.2.1 Chemicals

Chemicals used in this work are listed in Table 4.1.

Table 4.1: List of chemicals used in this work.

Chemical	**Abbreviation**	**Supplier**
De-ionised water (resistivity $\geq$ 18 MΩcm)	DI	Sigma-Aldrich
Hydrogen peroxide	H_2O_2	Sigma-Aldrich
Phosphate buffered saline tablets	PBS	Sigma-Aldrich
Potassium chloride	KCL	Sigma-Aldrich
Potassium ferricyanide	$K_3[Fe(CN)_6]$	Sigma-Aldrich
Potassium ferrocyanide	$K_4[Fe(CN)_6]$	Sigma-Aldrich
Sulfuric acid	H_2SO_4	Sigma-Aldrich
Tris(2-carboxyethyl)phosphine	TCEP	Sigma-Aldrich
3-Mercapto-1-propanol	MCP	Sigma-Aldrich
6-Mercapto-1-hexanol	MCH	Sigma-Aldrich

4.2.2 Buffers

Buffers and their compositions used in this work are shown in (Table 4.2). De-ionised water (4.1) was used to make all aqueous solutions.

Table 4.2: List of buffers used and their compositions

Buffer	**Composition**
Acid piranha solution	18 M H_2SO_4 and 30 % H_2O_2 (ratio = 3:1 v/v)
Redox buffer 1	1 mM Potassium ferricyanide/Potassium ferrocyanide in 1 M KCl
Redox buffer 2	0.02 mM Potassium ferricyanide/Potassium ferrocyanide in 10 mM KCl
Redox buffer 3	0.1 mM Potassium ferricyanide/Potassium ferrocyanide in 0.1 M KCl
Redox buffer 4	5 mM Potassium ferricyanide/Potassium ferrocyanide in 0.5 x PBS
Redox buffer 5	2 mM Potassium ferricyanide/Potassium ferrocyanide in 0.5 x PBS
Rinse buffer	1 x PBS

4.2.3 Oligonucleotide Sequences

A list of probe and target oligonucleotide sequences used and where they were manufactured/purchased is presented in (Table 4.3).

Table 4.3: List of probe and target oligonucleotides and their manufacturer

oligonucleotide	**Sequence 5' - 3'**	**Manufacturer**
lytA probe	[ThiC6][SP18]TGCCGAAAACGCTTGATACA	Sigma-Aldrich
lytA target	TGTATCAAGCGTTTTCGGCA	Sigma-Aldrich
lytA Forward primer	TTGGGAACGGTTGCATCATG	Sigma-Aldrich
lytA Reverse primer	TCGTGCGTTTTAATTCCAGCT	Sigma-Aldrich
$bla_{\text{OXA-1}}$ Forward primer	AACAGAAGCATGGCTCGAAA	Sigma-Aldrich
$bla_{\text{OXA-1}}$ Reverse primer	TGGTGTTTTCTATGGCTGAGTT	Sigma-Aldrich

All experiments used the same protocol for probe functionalisation. A 3 μM + 15 μM TCEP solution of *lytA* probe (Table 4.3) was left to incubate overnight at room temperature on electrode surfaces. A PBS wash was then implemented to remove unspecifically bound DNA. The surface was then backfilled with either 1 mM MCH or MCP in 5 mM TCEP for 1 hour at room temperature with a subsequent PBS wash for removal of unspecifically bound material.

lytA primers and probes (Table 4.3) were taken from [213]. $bla_{\text{OXA-1}}$ (OXA) (Table 4.3) were co-designed with a colleague (Mr Adrian Butterworth), a skilled molecular biologist who gave advice and training in primer design. The OXA primers were designed using *E. coli* plasmid pEK499 genome sequence from [214]

4.2.4 Custom Fabricated Microelectrodes and Macroelectrodes

30 μm, 100 μm diameter custom fabricated electrodes (Figure 4.2) and macroelectrodes were utilised in investigating *lytA*'s electrochemical behaviour. *lytA* target was used in various concentrations taking advantage of two testing formats. These formats used various types of redox buffer (Redox buffers 1 - 3 Table 4.2). The two testing formats composed of 1) 30 minutes of *lytA* target incubation followed by a PBS wash to remove unbound material then electrochemical testing followed by a DI wash to remove hybridised DNA. The next target concentration was then incubated. This was repeated until all concentrations were tested. 2) the electrodes were placed into redox solution and continuous measurements were taken for 8 hours. Increasing *lytA* target concentrations were added at various time intervals giving a live response of hybridisation on the electrodes.

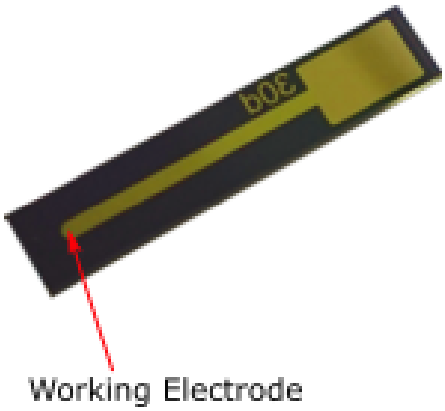

Figure 4.2: Example of the custom fabricated microelectrodes. The working electrode is very small and not visible in this figure. It is located at the end of the gold strip which connects it to the larger gold bond pad.

4.2.5 Custom PCB Electrodes

PCB P4 from Chapter 3 were used in these experiments with *lytA*. Redox buffer 1 (Table 4.2) was used to take measurements. These boards utilised their own inbuilt gold counter and reference electrodes. Experiments using PCB P4 utilised MCP instead of MCH and redox buffer 4 (Table 4.2). Multiple *lytA* target concentrations were incubated for 30 minutes at room temperature. Followed, by a PBS wash to remove unbound material then testing. The next target concentration was then incubated. This was repeated until all concentrations were completed.

4.2.6 PCR Amplification

PCR amplifications were performed using a minipcr mini8 thermal cycler and electrophoresis gels used The blueGel electrophoresis system (minipcrbio, Cambridge, MA, USA). Quantification of PCR samples used a Qubit 4 Fluorometer (Thermo Fisher). The 235 bp *lytA* amplicons were amplified from *S. pneumoniae* genomic DNA TIGR4 [ATCC BAA-334] from (LGC Standards, Middlesex). OXA was amplified from *E. coli* plasmid pEK499. Asymmetric PCR was achieved by lowering the concentration of forward primer, therefore, creating an unequal amount of forward and reverse segments to hybridise. This resulted in a higher concentration of single stranded target amplicon.

Asymmetric Digoxigenin (DIG) amplification was achieved by using the same technique as with the asymmetric amplification, substituting a DIG PCR mix (Sigma-Aldrich) in place of standard PCR mixes. This incorporates the DIG into the sequence being amplified. Later HRP Anti-Digoxigenin antibody [HRP.21H8] (Abcam) specifically binds to the DIG on the target sequence allowing for HRP aided TMB oxidation that can be chronoamporemetrically reduced and detected.

4.2.7 PCR Amplicons in PBS

All experiments in this section used PCB P4, MCP back-fill instead of MCH and redox buffer 5. Different types of 235 bp PCR amplicons (positive control) and 115 bp OXA PCR amplicons (negative control) targets were utilised in these experiments. The different amplicon types were normal PCR *lytA* and OXA requiring preheating to 95 °C to denature the DNA strands, Asymmetric *lytA* and OXA PCR amplicons not requiring heat treatment and Asymmetric DIG-labelled *lytA* and OXA PCR amplicons. All amplicons were diluted in 1 x PBS and multiple concentrations of the various types of target amplicon were tested after a 15-minute incubation at room temperature. PBS and 0.05% tween washing steps were performed after target incubation and before measurement. DIG-labelled PCR amplicons also allowed for chronoamperometric testing by incubating anti DIG antibodies (1:1000 dilution from stock) for 30 minutes at room temperature. Followed by a 20 second per electrode 1 x PBS wash, then 10 μl of TMB was added to each electrode for 20 minutes. Chronoamperometry was then performed with an applied E_{dc} of - 0.15 V for 2 seconds.

4.2.8 PCR Amplicons in Human Serum

PCB P4, MCP back-fill and redox buffer 5 were again used. Normal *lytA* and OXA PCR amplicons were heated to 95 °C for 5 minutes to denature the double stranded DNA then spiked into 100 % human serum from human male AB plasma, USA origin, sterile-filtered (Sigma-Aldrich) to make various target concentrations. The first concentration was incubated on the electrodes for 15 minutes at room temperature then washed with 0.05% tween, tested then washed with PBS and then incubated in the next target

concentration. This was repeated until all concentrations were completed.

4.3 Results & Discussion

4.3.1 *lytA* Detection using Custom Fabricated Micro and Macro Electrodes (30 micron vs 100 micron)

The mean DPV peak current percentage change response between *lytA* probe and 1, 10, 10^2, 10^3 and 10^4 nM target on 30 μm and 100 μm custom fabricated microelectrodes (Figure 4.3A) showed an absence of clear dose response. The 100 μm electrodes could be said to have had decreasing dose response after 1 nM. The 30 μm electrode showed a variable response with no pattern. The DPV peak current data (Figure 4.3B) exemplified this behaviour presenting with large data spreads with none of the target stages being significantly different from the SAM stage.

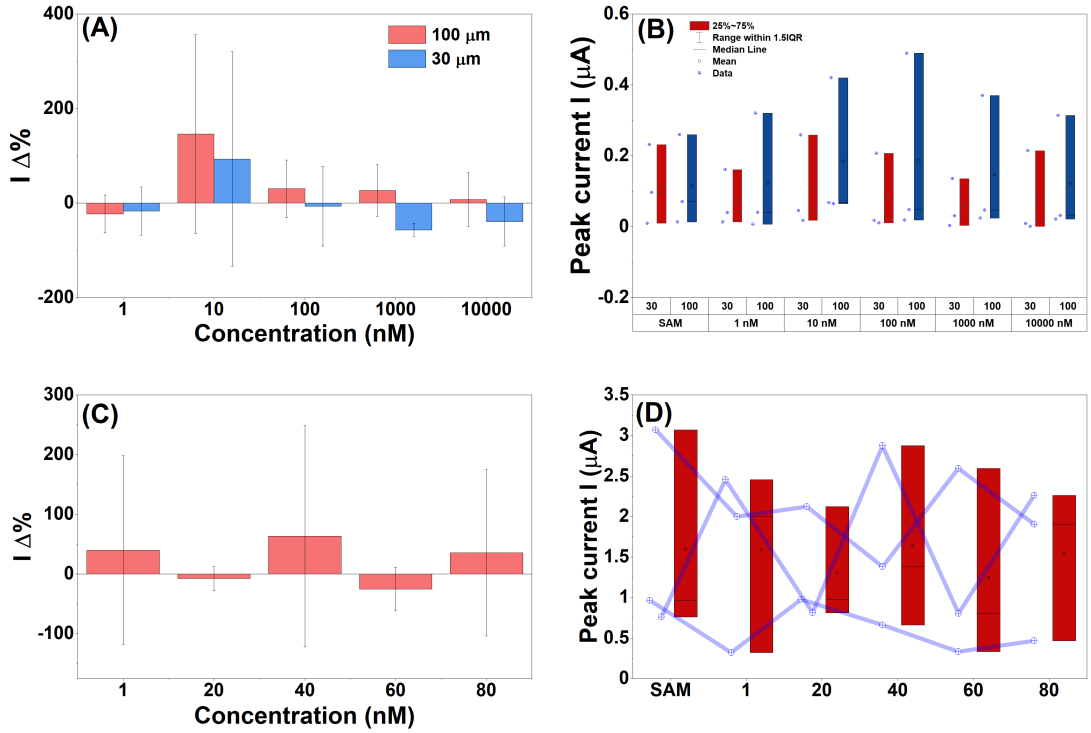

Figure 4.3: *lytA* complementary target response on fabricated microelectrodes. Mean DPV peak current percentage change in response to increasing target concentration on 30 μm and 100 μm electrodes (A). The corresponding DPV peak current raw data (B). Mean DPV peak current percentage change in response to a smaller target concentration range on 30 μm (C). The corresponding DPV peak current raw data (D). measurements performed in Redox buffer 1. n = 3

A repeat experiment was performed using 30 μm electrodes and a smaller target range: 1, 20, 40, 60 and 80 nm. The response (Figures 4.3C and 4.3D) were similar to that seen in the previous experiment presenting with fluctuating DPV percentage changes and an obvious lack of significant difference between the target stages and the SAM stage. EIS data contained enough noise to make circuit fitting challenging. These poor responses were unlikely due to the new *lytA* DNA sequences and were attributable to the custom microelectrode format. To investigate this possibility, electrodes from a new fabrication batch were tested using continuous measurements in response to target DNA and performing a comparative experiment using the gold standard polycrystalline gold macroelectrodes in a continuous measurement format.

4.3.2 Continuous Measurements of *lytA* Hybridisation using Custom Micro and Macro electrodes

One 30 μm custom microelectrode was measured continuously in a 5 mM and a 0.02 mM redox solution (Redox buffers 4 and 2 Table 4.2) in response to 50, 500, $5x10^3$, $5x10^4$ and $5x10^3$ pM target additions. A limit of one microelectrode per experiment was necessary, due to the difficulty with multiplexing these electrodes in the continuous measurement format. The 5 mM redox response (Figure 4.4A) showed a similar fluctuating mean DPV percentage change that was seen previously. The DPV peak current data (Figure 4.4B) was slightly different than previous, with small data spreads for the target stages, although this still did not result in a dose response or significant difference from the SAM. The large spread in data for the SAM stage made statistical differences difficult to obtain. The reason for the large data spread was due to the presence of a large current spike just before the first target addition (Figure 4.4E). In these continuous measurement experiments, the means were obtained by averaging 3 repeated measurements for each target concentration. This took approximately 15 minutes to gather the measurements thus a signal drift could account for some of the data spread response. The overall current response was a decreasing one displaying erratic current changes, though these usually became stable given enough time (Figure 4.4E).

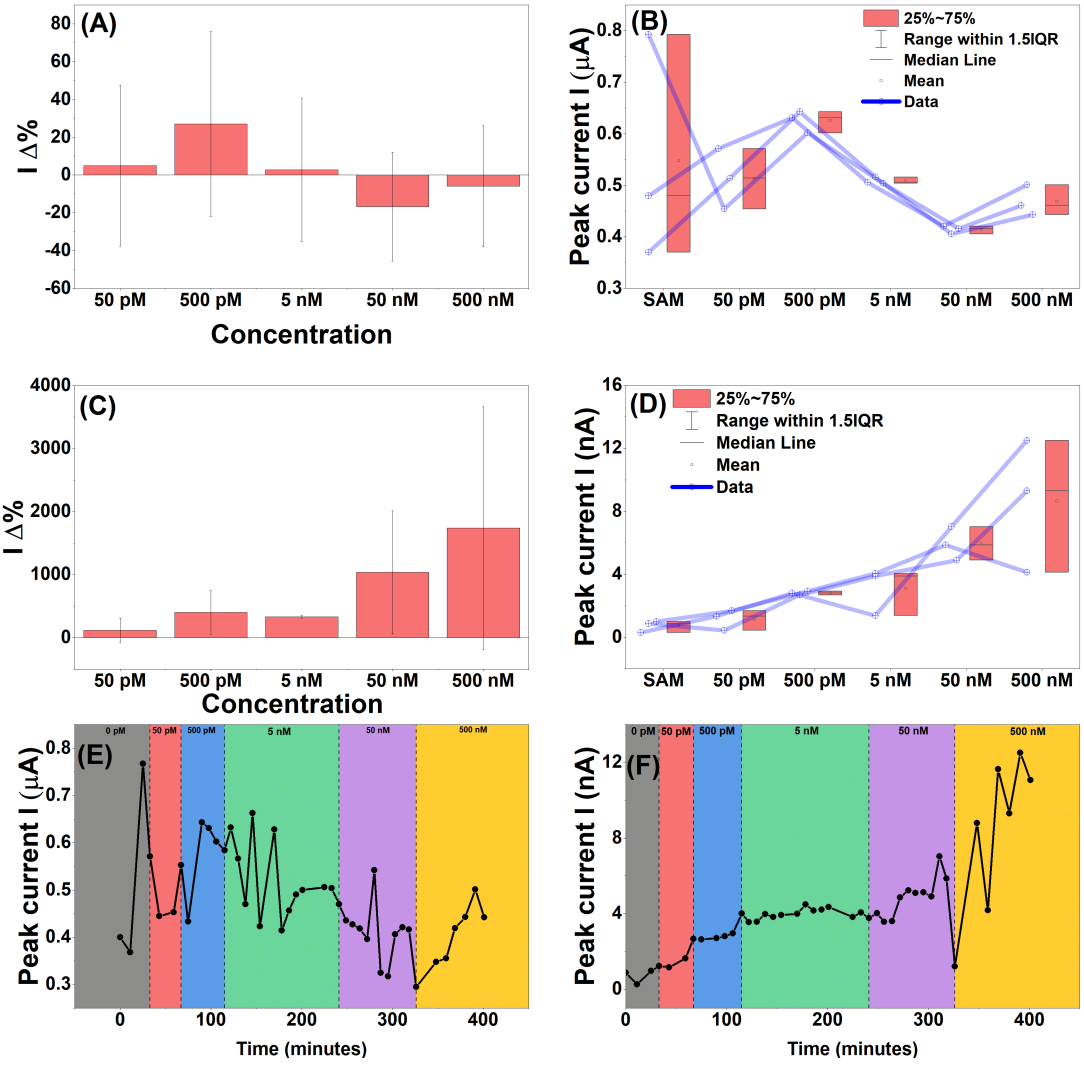

Figure 4.4: Continuous measurement of *lytA* complementary 20 bp target concentration response on fabricated microelectrodes. Mean DPV peak current percentage change response to increasing target concentration on 30 μm fabricated electrodes using 5 mM redox buffer (A). The corresponding DPV peak current raw data (B). Mean DPV peak current percentage change in response to increasing target concentration on 30 μm fabricated electrodes using 0.02 mM redox buffer (C). The corresponding DPV peak current raw data (D). Continuous DPV peak current response of 5 mM redox buffer (redox buffer 4) (E) and 0.02 mM buffer (redox buffer 2 Table 4.2) (F). Averages were taken from 3 repeated measurements for each target concentration. n = 3.

For the 0.02 mM experiment, the mean DPV current percentage change response showed a dose response (Figure 4.4C) except for 5 nM being absent from the trend. The DPV

peak current data showed that the SAM produced a smaller data spread when compared to the 5 mM experiment (Figure 4.4D) and that likely differences between SAM and target were apparent at 500 pM. Also, note that the currents recorded were in the lower nA range and the 5 mM redox was in the high nA range, this was obviously because the 0.02 mM redox solution was 250 times more dilute and the current was linearly dependent on redox concentration Eqn 1.8. This lower current range allowed for larger percentage changes thus demonstrating higher sensitivity. It also appeared to substantially reduce fluctuations in measurements (Figure 4.4F) with exception of the last concentration and time points. This could be due to noise introduced to the system or the electrode beginning to show a destabilising effect after being submerged in redox buffer and target DNA for a long period of time. The reason why the 0.02 mM experiments showed a smoother response could be due to the microelectrodes sensitive behaviour being realised by utilising low redox buffer concentrations. There was another point to note, that the current response to increasing target in the 0.02 mM redox had an increasing behaviour while the 5 mM had a decreasing behaviour (see Section 4.4 for discussion).

The macroelectrodes were less demanding to multiplex and so average responses from 2 electrodes for DPV and 3 electrodes for EIS electrodes were possible. The discrepancy between electrode numbers was due to difficulty in obtaining a DPV response on one electrode. The mean DPV current percentage change showed a decreasing response to increasing target concentration in 0.1 mM redox buffer (Figure 4.5A). There was a significant current decrease at 5 nM, this was due to longer time intervals between the 500 pM and 5 nM measurements, allowing the current to decrease further, this can be seen in (Figure 4.5E) as a large time section (100-250 minutes) at 5 nM. The reason for the longer interval was due to the current signal spiking after the addition of 5 nM target (Figure 4.5E). A pause was implemented to establish if the current behaviour would return to the original current behaviour (before 5 nM current spike). Eventually, the slope returned to a suitable gradient beginning at 200 minutes, the 240-minute measurement was used for the current analysis. This time point measured significantly less current than the final 500 pM time point, explaining the large percentage change

responses in Figure 4.5A and Figure 4.5E. The errors were reduced compared to the microelectrodes, the raw DPV data showed small data spreads and a likely difference of all target stages from the SAM stage (Figure 4.5B). EIS data was able to be circuit fitted showing immediately that the macroelectrodes had a more stable response than the microelectrodes. The mean R_{ct} percentage change confirmed the current response with an increasing dose behaviour (Figure 4.5C). The raw R_{ct} data showed a large spread that resulted in no significant differences between SAM and target stages (Figure 4.5D). An example of one of the electrodes continuous measurement response was shown in (Figure 4.5E) It demonstrated the overall current decrease response to target concentration. It appeared to reach saturation at 500 nM with the measurements levelling off after 350 minutes.

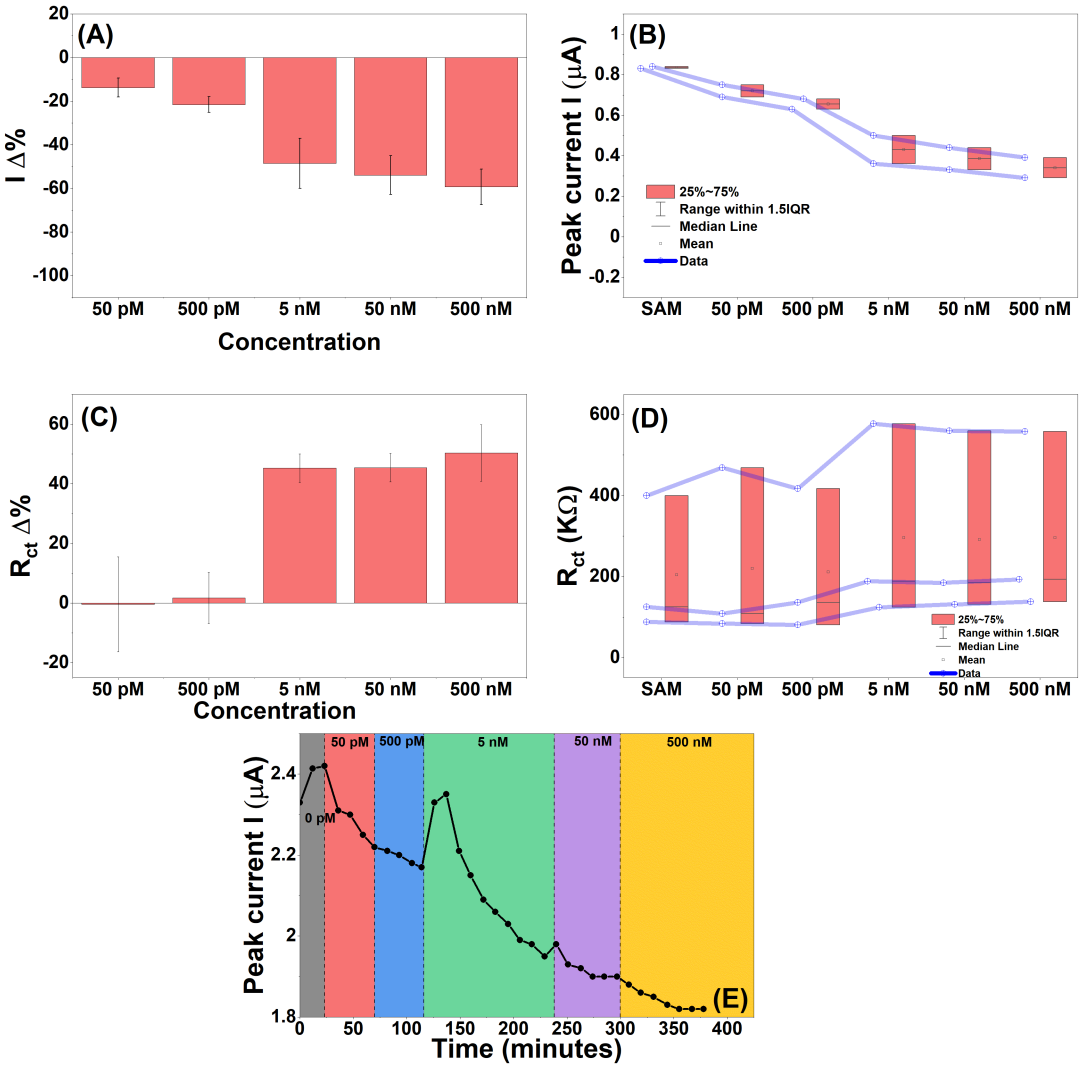

Figure 4.5: Continuous measurement of *lytA* complementary 20 bp target concentration response on macroelectrodes. Mean DPV peak current percentage change in response to increasing target concentration (A). The corresponding DPV peak current raw data (B). Mean R_{ct} percentage change in response to increasing target concentration(C). The corresponding R_{ct} raw data (D). Continuous DPV peak current response (E). 0.1 mM redox buffer (Redox buffer 3 Table 4.2) was used. n = 2 for DPV and n = 3 for EIS.

For all these continuous experiments on micro and macro electrodes, there were spikes present in the continuous plots directly after target addition this was due to a convection mechanism caused by stirring of the solution to incorporate the target concentrations quickly. This was unfortunately necessary due to the large amount of solution required

to perform these experiments. If a smaller volume was possible the diffusion alone would have been sufficient. Because of this, only measurements beyond a suitable amount of time allowing for the system to settle were used.

From these experiments, it was clearly demonstrated that the *lytA* sequences were not the cause of the poor performances seen on some of the custom-fabricated microelectrodes. Low redox buffer concentrations on the microelectrodes allowed for good electrochemical responses to target DNA with macroelectrodes confirming these target responses. The *lytA* probe was able to successfully detect complementary target DNA at multiple concentrations, with 50 pM being the lowest on macroelectrodes, and 500 pM the lowest on microelectrodes. It was the microelectrodes themselves introducing undesired behaviour and other experiments performed by colleagues using these microelectrodes were seeing the same issues. One issue found by others, were holes in the gold substrate that would then act as multiple electrodes instead of one singular electrode. This was a fabrication issue and steps were taken to resolve them. With a new batch, a final check of the custom microelectrodes was performed.

4.3.3 A final Check of Custom Microelectrodes

Four 30 μm custom fabricated microelectrodes were tested using 50 pM target DNA in 0.02 mM redox buffer. The responses from all four were not suitable for the analysis techniques previously used. The EIS Nyquist plot for the electrodes (Figure 4.6A) showed various responses. Some responded with quick semi-circle suppression (E3), others with a linear response (E4). The DPV response confirmed this (Figure 4.6B) with all electrodes showing no peak behaviour. It was obvious these electrodes had significant issues. The decision was made to discontinue the *lytA* work on these electrode platforms. In time these electrodes were made suitable by continued work by colleagues that fabricated them. By this time, development had already begun on the PCBs discussed in Chapter 3 that would allow for higher throughput, so investigating their suitability using *lytA* DNA was the next logical step. A change from MCH to MCP was employed. This was due to the improved performance (Appendix C.1) in comparison to (Figure 4.5).

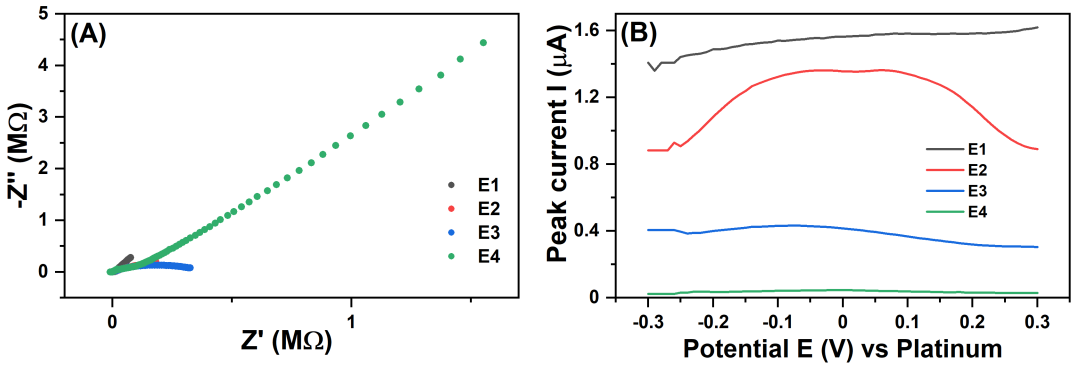

Figure 4.6: Final check of *lytA* complementary target 20 bp response on fabricated electrodes. EIS Nyquist responses from 4 custom microelectrodes to 50 pM target using 0.02 mM redox buffer (A). The corresponding DPV response (B).

4.3.4 *lytA* Detection using Custom PCB Electrodes

The performance of *lytA* sequences on custom PCBs was important for the development of a suitable biosensor platform. *lytA* was used in (Section 3.3.3) to analyse the performance of the PCBs so the reader is referred back to this section for analysis of the behaviour of *lytA* on PCBs P1-P4. This section will add more analysis to the chosen sensor platform PCB P4.

PCB P4's mean current percentage change in response to various *lytA* target DNA increased in a dose-dependent fashion. The 5 pM stage slightly bucked this trend and at 50 pM the trend reversed, continuously decreasing to final target concentration (Figure 4.7A) see Section 4.4 for a possible explanation. The raw peak current data showed a large data spread for most stages resulting in likely differences between the SAM stage and 30 pM to 50 nM concentrations, the rest were likely similar (Figure 4.7B). Square wave voltammetry was also implemented due to its improved abilities (see section 1.7.4) over DPV. The SWV results were found to produce similar percentage change magnitudes and trends (Figure 4.7C). The raw SWV peak current data also followed the same trend as DPV with the only noticeable difference being a reduction in outliers (Figure 4.7D). Likely differences were also similar, with the range still between 30 pM

and 50 nM.

The mean R_{ct} percentage change showed an increasing dose response with 5 pM again quickly departing from the response, the trend reversal at 50 pM was evident just as with DPV and SWV (Figure 4.7E) the magnitude of the percentage change with EIS was much larger than DPV and SWV, 250 % compared to 30 %. Raw R_{ct} values (Figure 4.7F) showed that there were multiple outliers. If these were excluded in the percentage change analysis, the magnitudes would have been lower but accompanied by improved errors. Likely differences between SAM and target started at 10 pM and ranged to 50 nM. EIS was the best performing measurement technique having the largest magnitude percentage changes, increased group differences between target stages and SAM stage and smaller data spreads for each stage. Further analysis on the performance of *lytA* on PCB P4 was conducted by performing linear regression of the linear region between 10 pM to 50 pM using this information to calculate limits of detection LoD (Section 1.11.3). DPV gave a Y_{LoD} = 47.4 μA (R^2 = 0.96841) which corresponded to an X_{LoD} = 10.4 pM. SWV gave a Y_{LoD} = 62.7 μA (R^2 = 0.95465) which corresponded to an X_{LoD} = 12.39 pM. EIS gave a Y_{LoD} = 1072.9 Ω (R^2 = 0.99392) which corresponded to an X_{LoD} = 4.5 pM. These X_{LoD} values were in agreement with the concentrations demonstrated to have likely differences from the box plot data. There was a second linear region in the DPV, SWV and EIS data, consisting of 4 data points from 0 to 2 pM. The X_{LoD} values for these ranged between 251 - 433 fM. This indicated that using smaller target concentrations was possible and could result in the ability to detect femtomolar levels of 20 bp complementary *S. pneumoniae* DNA. A PNA based PCB device for rapid and high sensitivity DNA quantification recently reported a limit of detection of 57 fM [215]. The sensor presented in this work saw comparable results (251 - 433 fM if using a lower linear range) without the need for costly PNA reagents and utilising a simple SAM modification process.

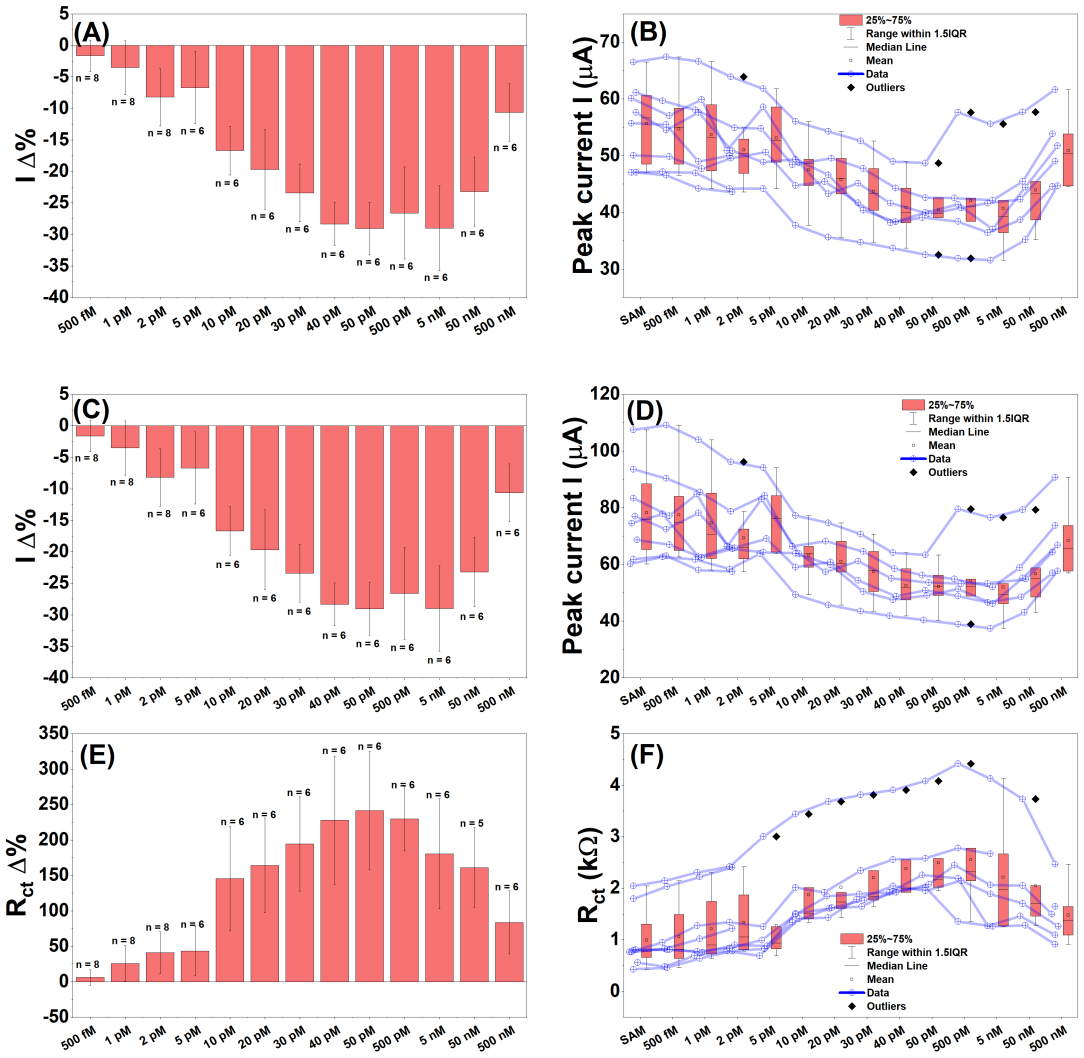

Figure 4.7: *lytA* complementary 20 bp target response on prototype PCB 4. Mean DPV peak current percentage change in response to increasing target concentration (A). The corresponding raw data (B). Mean SWV peak current percentage change in response to increasing target concentration (C). The corresponding raw data (D) Mean R_{ct} percentage change in response to increasing target concentration (E). The corresponding raw data (F). 5 mM redox buffer (redox buffer 4 Table 4.2) was used. n = 5-8.

4.3.5 PCR amplification of Genetic Sequences

With a suitable platform established and successful detection of 20 bp complementary target *lytA* DNA in PBS established. The probe sequence was next subjected to longer

DNA target fragments in PBS to more precisely replicate the DNA lengths that a sensor would be required to deal with in a point of care setting. For this a 235 bp sequence (amplified from *S. pneumoniae* genomic DNA) that contained the 20 bp complementary sequence in the middle of this larger sequence. The reason for it being in the middle and not at the ends of the sequence was due to the primer design from the researchers [213]. It was also beneficial at this stage to investigate specificity of the *lytA* probe sequence. Negative controls were also implemented utilising 115 bp OXA amplicons.

Table 4.4: List of PCR amplifications.

Amplifying	**Length (bp)**	**Qubit quantification (μg/ml)**
(1) *lytA* (*S. pneumoniae*)		
+	235	14.1
-	NA	0.9
(2) *lytA* (*S. pneumoniae*) DIG		
+	235	3.29
-	NA	2.57
(3) *lytA* (*S. pneumoniae*) Asymmetric		
+	235	6.73
-	NA	0.399
(4) *lytA* (*S. pneumoniae*) Asymmetric DIG		
+	235	8.73
-	NA	1.11
(5) *oxa* (*E. coli*)		
+	115	11.3
-	NA	2.78
(6) *oxa* (*E. coli*) DIG		
+	115	4.89
-	NA	2.75
(7) *oxa* (*E. coli*) Asymmetric		
+	115	5.13
-	NA	2.16
(8) *oxa* (*E. coli*) Asymmetric DIG		
+	115	46.4
-	NA	2.23

lytA 235 bp PCR amplification

The positive amplified *lytA* PCR mixture was tested using a Qubit4 fluorometer giving a concentration of 14.1 μg/ml (Table 4.4) and the negative (no genomic DNA template) mixture 0.9 μg/ml. This demonstrated clear discrimination between the positive PCR mixture the negative confirming successful PCR amplification of the positive control. This quantification could not confirm if it was the desired DNA sequence that was amplified only that there was some amplified nucleic acid material present. An elec-

trophoresis gel was therefore performed on both positive and negative samples (Figure 4.8). There was no visible band in the negative lane confirming no DNA was significantly amplified. A visible band between 200 bp - 300 bp on the reference ladder was present in the positive lane, confirming that the amplified material was consistent with being the desired 235 bp amplicon.

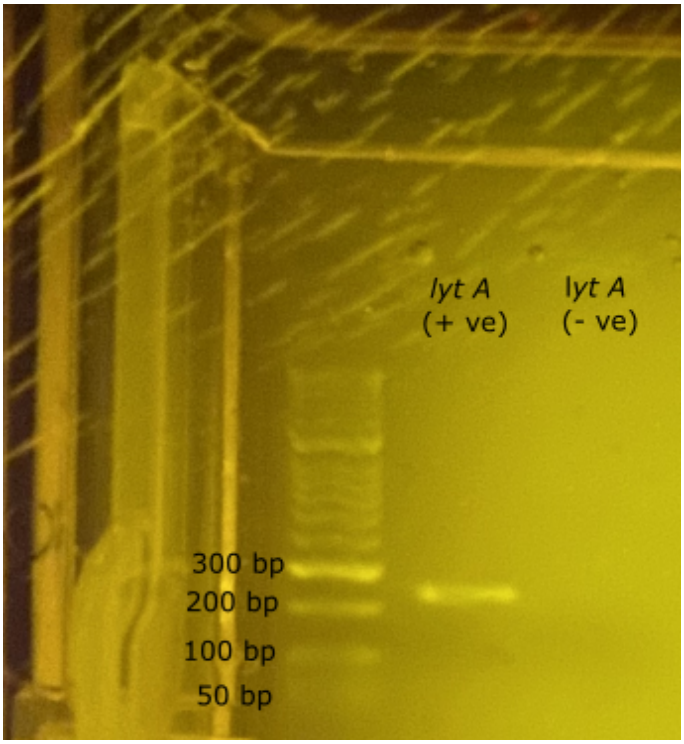

Figure 4.8: *lytA* amplicon electrophoresis gel. Positive sample showed a band between the 300 bp and 200 bp ladder reference consistent for a 235 bp amplicon. The negative showed no visible band. The distortion is due to condensation on the plastic lid.

OXA 115 bp PCR amplification

Similarly, for the OXA amplifications, the positive PCR mixture showed a concentration of 11.3 μg/ml and the negative 2.78 μg/ml (Table 4.4). Again the positive was much higher than the negative confirming nucleic acid amplification. The electrophoresis gel showed no visible band in the negative lane and a visible band in the positive lane at the lower end between 100 - 200 bp (Figure 4.9) which was consistent with a sequence of 115 bp long as desired. Note that the distorted appearance was due to water vapour

condensing on the plastic. This data showed successful amplification of the amplicons and allowed for specificity testing to commence.

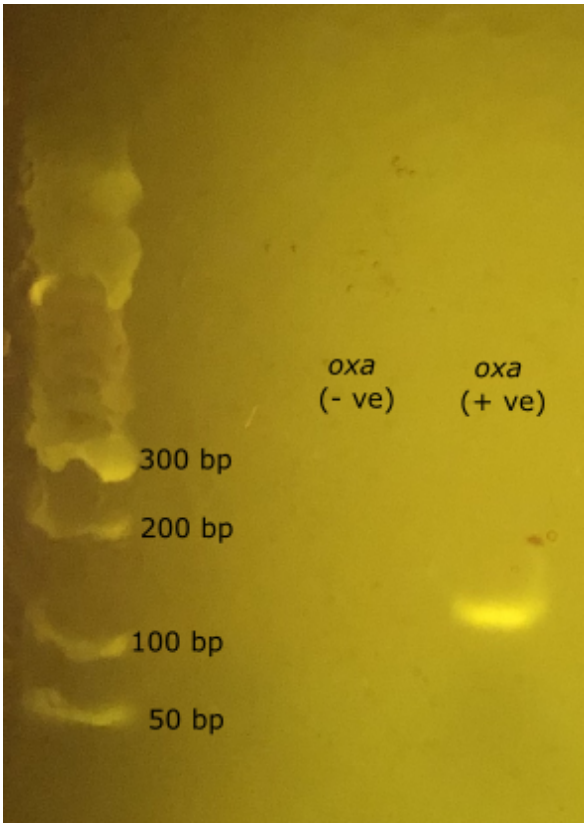

Figure 4.9: *oxa* amplicon electrophoresis gel. The positive sample showed a band between the 200 bp and 100 bp ladder reference consistent for a 115 bp amplicon. The negative showed no visible band.

Asymmetric and asymmetric DIG-labelled *lytA* and OXA PCR amplification

Amplifications of DIG-labelled *lytA* and OXA, as well as asymmetric OXA, did not attain as successful quantification's (Table 4.4). The positives were lower and the negatives slightly higher. The other PCR reactions showed better quantifications with asymmetric DIG-labelled OXA being very high 46.4 μ/ml and its negative low. Electrophoresis gels of these samples showed that all *lytA* samples failed to display any positive or negative bands (Figure 4.10). DIG-labelled OXA showed bands in both positive and negative lanes indicating the negative was contaminated. Asymmetric OXA had no bands and asymmetric DIG-labelled OXA showed a band in the positive but

not negative. This behaviour was attributed to a pipetting error leading to inconclusive results for this electrophoresis experiment. Whilst the gel was unable to confirm amplification, the quantifications from the Qubit showed that there were likely amplicons present. Experiments utilising these amplicons were still performed, using the results from these experiments to potentially confirm successful amplicon production.

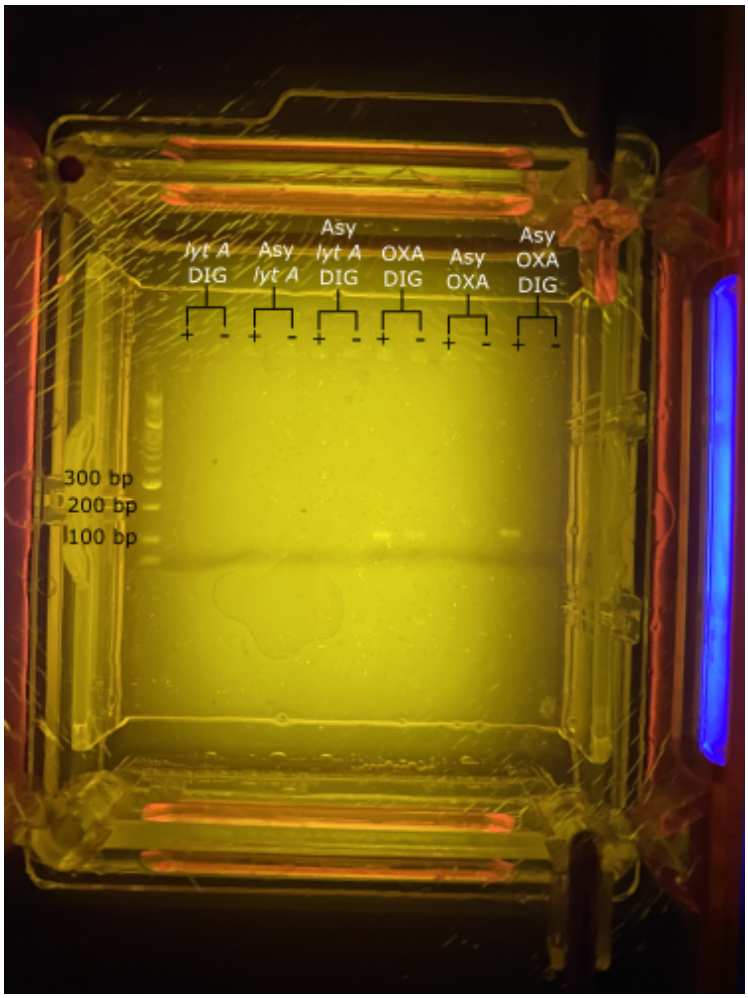

Figure 4.10: Asymmetric and DIG-labelled amplicon electrophoresis gel. All *lytA* PCRs failed to show any positive or negative bands. OXA DIG showed positive and negative bands and asymmetric OXA DIG showed a band in the positive lane.

4.3.6 *lytA* Genetic Amplicons in PBS

lytA 235 bp amplicon in PBS

lytA amplicon was diluted in PBS making various target concentrations. After heating for 5 minutes at 95 °C to denature the DNA into single stranded DNA, the amplicon target solutions were incubated on the electrodes for 15 minutes. The mean DPV percentage change in response to increasing target concentration displayed an initial increase then a gradual decrease (Figure 4.11A). There was a lack of clear dose-dependence and the presence of overlapping errors. The DPV raw current data confirmed this with a lack of any significant differences between SAM and target stages (Figure 4.11B). A similar response was found for SWV with the percentage changes lacking dose response and accompanied with overlapping errors (Figure 4.11C) The initial response was found to decrease, however, contrary to the DPV behaviour, remained that way for all target concentrations. There appeared to be an absence of differences between SAM and target stages, with the introduction of more outliers (Figure 4.11D).

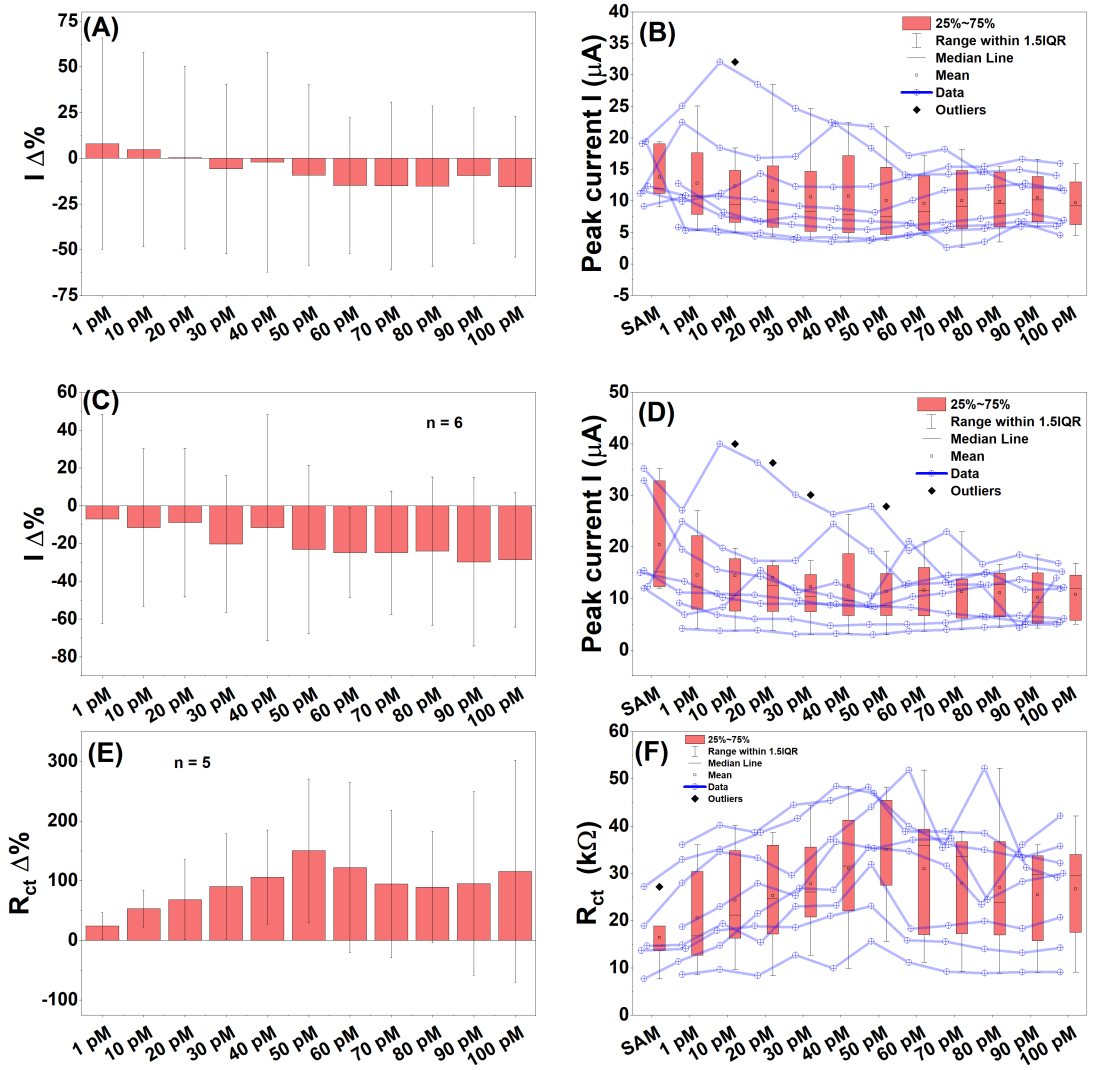

Figure 4.11: *lytA* 235 bp amplicon target response. Mean DPV peak current percentage change in response to increasing target concentration (A). The corresponding DPV peak current raw data (B). Mean SWV peak current percentage change in response to increasing target concentration (C). The corresponding SWV peak current raw data (D) Mean R_{ct} percentage change in response to increasing target concentration (E). The corresponding R_{ct} raw data (F). 2 mM redox buffer used (redox buffer 5 Table 4.2). n = 8.

EIS gave the best response with the mean R_{ct} percentage change showing a dose response from 1 pM to 50 pM (Figure 4.11E). The trend reversal phenomena appeared again at 50 pM. R_{ct} raw data had large data spreads for the target stages but the SAM stage

had a relatively small spread allowing for likely differences between SAM and target from 20 pM - 50 pM (Figure 4.11F). This EIS data confirmed the successful detection of the 235 bp *lytA* amplicon in PBS.

Asymmetric *LytA* and OXA amplicons in PBS

The Asymmetric amplicons were incubated on separate PCBs (positive and negative) for 15 minutes in PBS. Heating was not required as the asymmetric reaction should produce single stranded DNA for immediate presentation to the sensor. The mean DPV percentage changes displayed a decreasing dose response to increasing positive (*lytA*) target concentrations (Figure 4.12). The negative (OXA) also showed a dose response and produced a slightly larger response than the positive. The normalised DPV data confirmed that there were no statistical differences between the positive and negative amplicons (Figure 4.12B). The errors and data spreads were improved over the first amplicon experiment. The SWV response was again similar to DPV resulting in similar dose response's for both control groups (Figure 4.12C), with the magnitude of percentage change for SWV compared to DPV being larger. Potential likely differences were apparent between the control groups at 20 and 40 pM (Figure 4.12D). This indicated that the negative was successfully detected over the positive, which was not the intended outcome. This did nevertheless, demonstrate the potential of SWV as a more sensitive measurement technique compared to DPV.

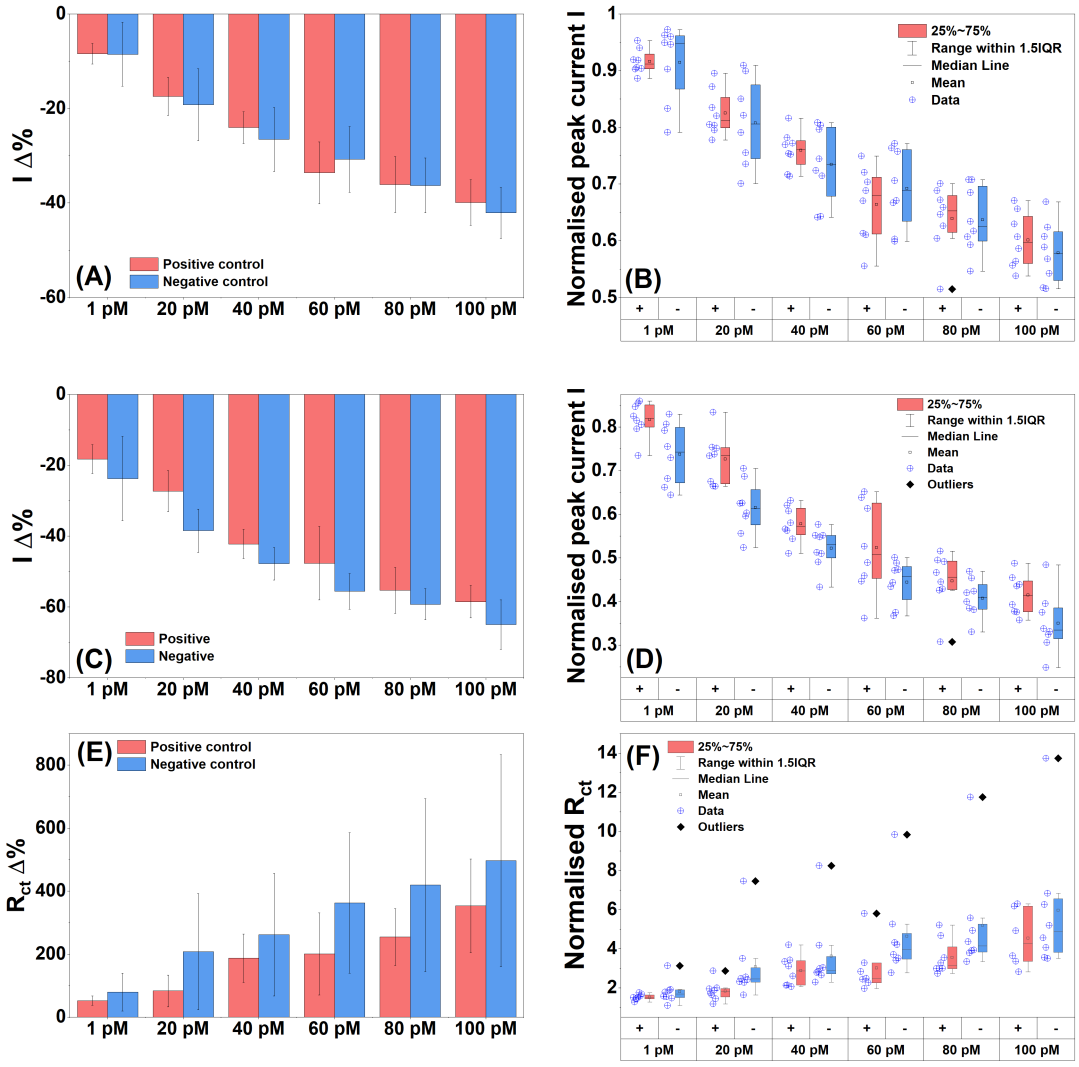

Figure 4.12: *lytA* 235 bp asymmetric amplicon target response. Mean DPV peak current percentage change in response to increasing target concentration (A). The corresponding raw data (B). Mean SWV peak current percentage change in response to increasing target concentration (C). The corresponding raw data (D) Mean R_{ct} percentage change in response to increasing target concentration (E). The corresponding raw data (F). 2 mM redox buffer used (redox buffer 5 Table 4.2). n = 8

The EIS data showed dose responses for both control groups with the negative having the larger response (Figure 4.12E). There were large errors accompanied in some positive stages and most negative stages. The normalised R_{ct} showed this could be accounted for by one outlier electrode that if discounted would give potential likely difference at

20 and 60 pM (Figure 4.12F). Again the percentage change data includes this outlier for full transparency and a reminder to the reader that better error performance was achievable by statistically rejecting this data point.

These results can be explained by non-specific biofouling of the surface. Examining (Table 4.4) showed Asymmetric *lytA* and OXA both amplified some material to approximately equivalent levels (6.73 and 5.13 μg/ml) respectively. The electrophoresis gel for both showed no indication of bands in their lanes which suggested that the specific DNA material was not present in the sample. If this were true then both PCBs exposed to the *lytA* positive and OXA negative were in reality receiving various concentrations of non-specific proteins and nucleotide mixtures that composed the PCR solutions. The responses seen here would then easily be explained as a biofouling dose response of these protein/nucleotide contaminants with none or insufficient quantities of amplicons present.

Asymmetric DIG-labelled *lytA* and OXA amplicons in PBS

40 pM positive and negative amplicons were incubated on the electrodes for 15 minutes at 50 °C washed and then incubated with HRP tagged anti DIG antibody at room temperature for 30 minutes. The mean DPV percentage change showed that both controls decreased (Figure 4.13A). The positive decreased more than the negative -40 % vs -10 %. The normalised DPV peak currents confirmed this behaviour resulting in a likely difference between the controls demonstrating successful specific detection of 40 pM asymmetric DIG-labelled *lytA* DNA (Figure 4.13B). Mean R_{ct} percentage change showed an increase in response target 100 % vs 40 % (Figure 4.13C). The normalised R_{ct} data supported this and was on the verge of a likely difference (Figure 4.13D).

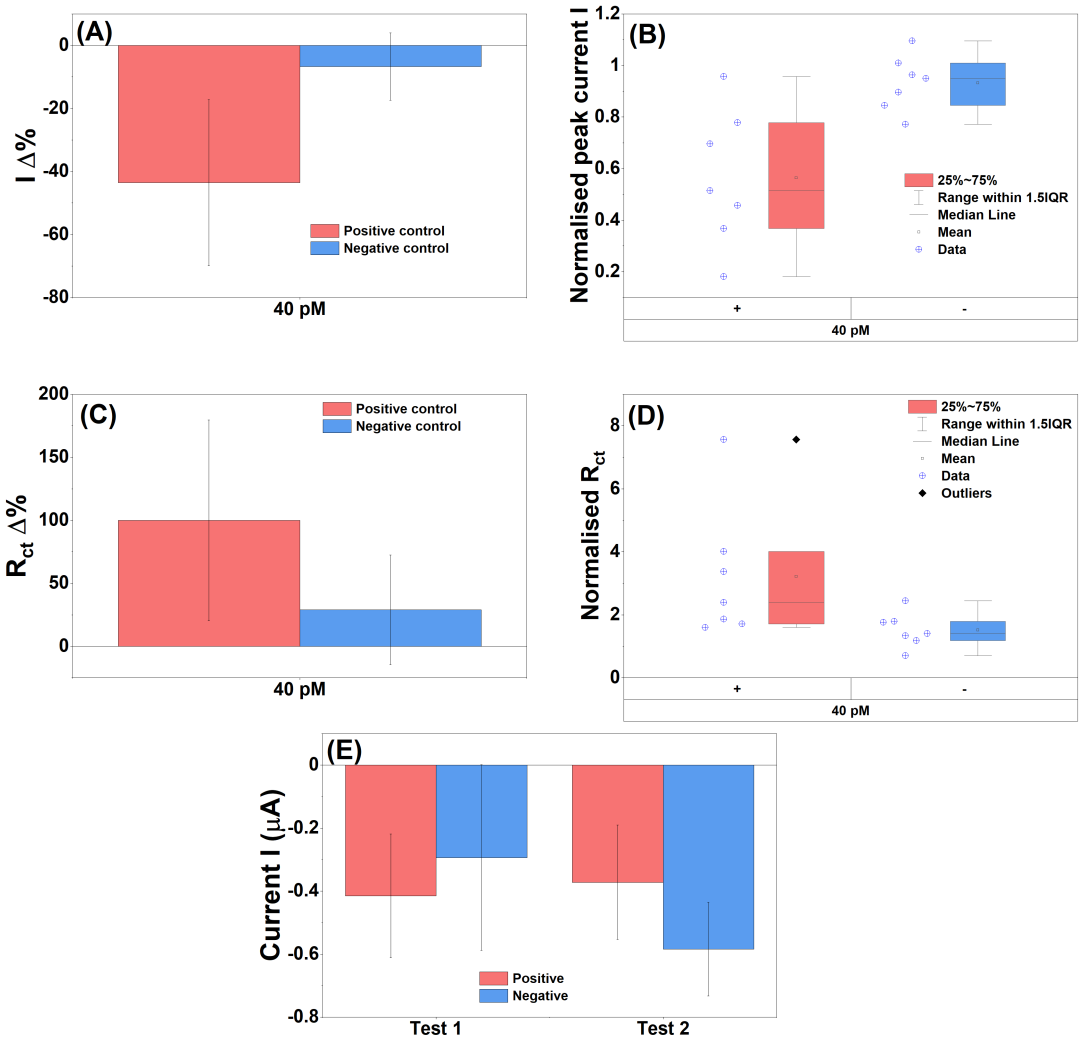

Figure 4.13: Asymmetric DIG-labelled amplicons in PBS (*lytA* 235 bp vs OXA 115 bp). Mean DPV peak current percentage change in response to 40 pM (A). The corresponding raw data (B). Mean R_{ct} percentage change in response to 40 pM (C). The corresponding raw data (D). Chronoamperometry response to 20 minutes in TMB test 1 then a rewash and re-application of TMB for 20 minutes (E). 2 mM redox buffer used (redox buffer 5 Table 4.2). n = 8

The PCBs were washed after the previous measurements and TMB was applied for 20 minutes. The TMB solution turned blue confirming the presences of HRP. Chronoamperometry was performed producing a current decrease for both positive and negative controls (Figure 4.13 Test 1). There was no differences between the controls. To ensure

that the unspecifically bound HRP was properly removed a second wash incorporating 20 seconds of 1 x PBS, 20 seconds 0.05 % tween and then 20 seconds of 0.1 x PBS was performed and reapplication of TMB for 20 minutes was undertaken. The response again showed a current decrease for both controls with the negative decreasing more than the positive (Figure 4.13 Test 2) producing no differences between the groups. This chronoamperometry method produced TMB colour reactions for both control groups solutions when only the positive control should. This meant that the HRP anti DIG antibodies were present on the negative control and were unspecifically bound, with multiple washing attempts unable to successfully remove them. This method proved to be unsuccessful and was discontinued.

4.3.7 *lytA* Genetic Amplicon in Human Serum

With successful specific detection of full complementary 20 bp and 235 bp normal PCR and asymmetric DIG-labelled amplicons in PBS and the information learned from these experiments, the next logical step was to attempt detection of the 235 bp amplicon (amplified from *S. pneumoniae* genomic DNA) in a clinically relevant analogue.

Normal 235 bp *lytA* and 115 bp OXA PCR product was heated to 95 °C for 5 minutes and then spiked into 100 % human serum. The serum samples were incubated on the electrodes for 15 minutes, tween washed and then tested. The mean DPV peak current percentage change displayed a dose dependant response to increasing target with 20 pM failing to follow the trend (Figure 4.14A). The negative control also showed a dose-dependent response. The normalised DPV data confirmed the percentage changes with the 20 pM verging on a likely difference between the two controls (Figure 4.14B). The other target concentrations showed no differences. The mean SWV peak current percentage changes showed a slight improvement over DPV with more pronounced differences between control groups (Figure 4.14C). Dose dependence was again present for both control groups. The normalised data showed that 1 and 20 pM control groups were likely different and 60, 80 and 100 pM were close to being different (Figure 4.14D).

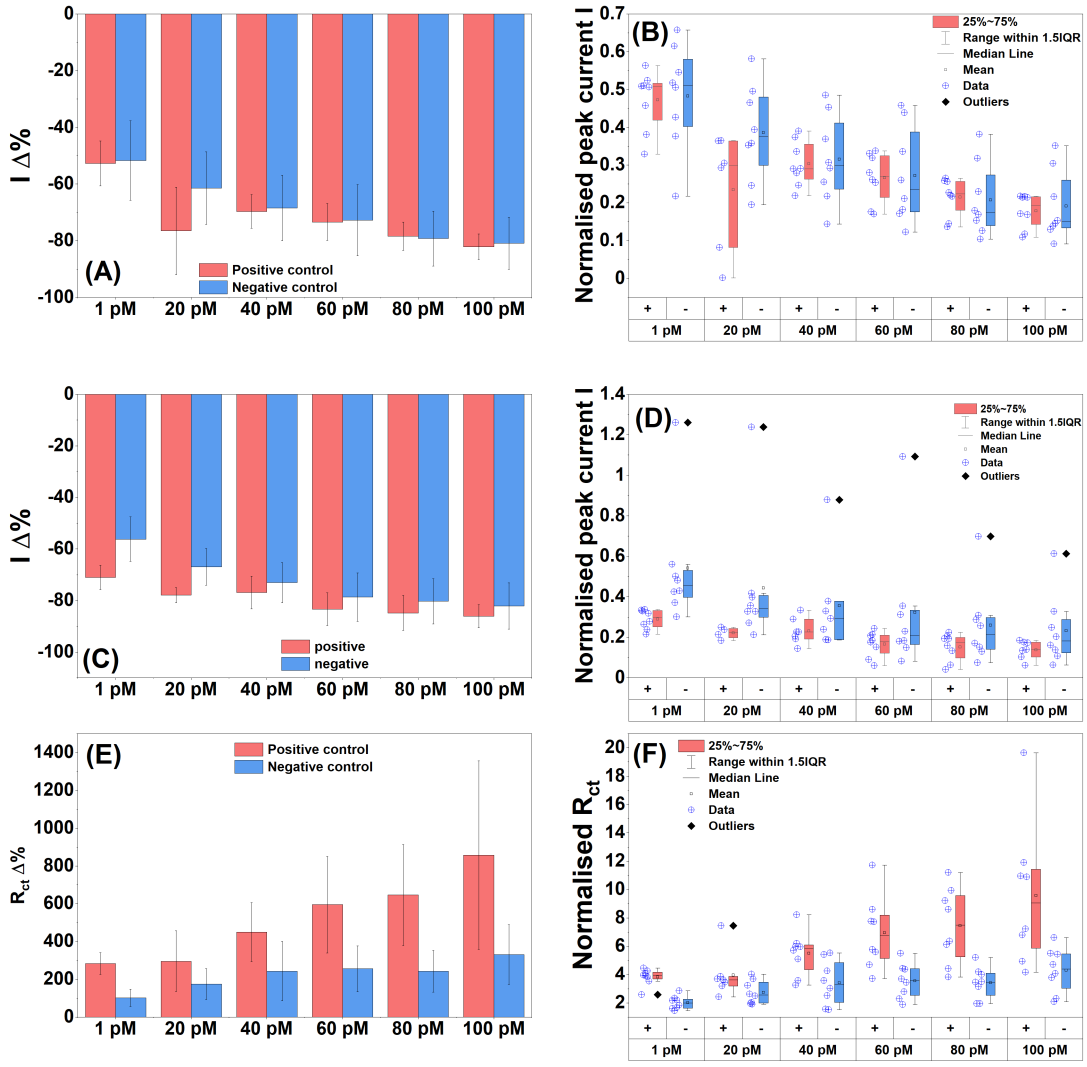

Figure 4.14: PCR amplicons in human serum (*lytA* 235 bp vs OXA 115 bp). Mean DPV peak current percentage change in response to increasing target concentration (A). The corresponding normalised DPV current raw data (B). Mean SWV peak current percentage change in response to increasing target concentration (C). The corresponding normalised SWV current raw data (D) Mean R_{ct} percentage change in response to increasing target concentration (E). The corresponding normalised R_{ct} raw data (F). 2 mM redox buffer used (redox buffer 5 Table 4.2). n = 8

EIS again proved to be the best measurement technique. The mean R_{ct} percentage change showed increasing dose dependence for the positive control (Figure 4.14E). The negative control increased until 40 pM then remained constant until 100 pM where

it then increased slightly. Therefore, the negative control did not produce a strong dose response and the sensor demonstrated anti-biofouling properties. The normalised Mean R_{ct} data showed likely differences between positive and negative groups for 1, 60, 80 and 100 pM (Figure 4.14)F. Some positive target stages were likely different from each other indicating a strong signal response to target DNA while no differences were found within the negative control group, meaning they were all likely equivalent further reinforcing the anti-biofouling performance of the sensor. The limit of detection values for the various measurement techniques were calculated. DPV had a Y_{LoD} = 0.38 μA (R^2 = 0.96058) which corresponded to an X_{LoD} = 23 pM. SWV gave a Y_{LoD} = 0.23 μA (R^2 = 0.90212) which corresponded to an X_{LoD} = 30 pM. EIS gave a Y_{LoD} = 4.35 Ω (R^2 = 0.96093) which corresponded to an X_{LoD} = 18 pM. These X_{LoD} These X_{LoD} values were in agreement with the concentrations demonstrated to have likely differences from the box plot data, with the exception of EIS which was able to successfully detect target DNA at 1 pM which was significantly lower than the calculated LoD. This is a vast improvement on current culture methods which regularly return no culture positive after multiple hours of incubation. This sensor also out preforms the pneumococcal urinary antigen test in terms of time to result, expense and complexity. The time to result are both 15 minutes but this should be easily reduced on this sensor system. The sensor does not require to be at specific temperature nor do the sample and reagents [205]. This sensor comprises of sample addition, wash, redox addition and then result, reducing the complexity of the assay. The antigen test requires sample and multiple reagents. Antigen tests are relatively expensive approximately in £3 - £5 whereas this sensor would likely be in the region of pence if it aligns its manufacture protocol with that of glucose strip production which is demonstrated in the next section for a covid-19 sensor. Other tests on the market include a magnetogenosensor assay for *lytA* that was able to obtain a limit of detection of 1100 pM [213]. Other examples of reported S. pneumoniae sensors include a DNA-Antibody nanostructure assay ($\approx$ 3.26 pM) [216], polymer based genosensor ($\approx$ 1E6 pM) [217], synergism strategy for gene sequence sensing (0.0005 pM) [218] and versatile loop-mediated isothermal amplification with a sensitivity of 0.173 pM [219]. The sensor developed in this work demonstrated

similar or improved sensitivity to the devices reported. It was also able to achieve this in complex human serum with reduced time to result utilising less complicated functionalisation strategies on an easily manufacturable device. The sensors above that demonstrate low pM detection used complex devices, materials and methods to achieve this. Table 4.5 summarises the comparisons with sensors from literature. The developed sensor demonstrated excellent responses for such a simple device and would hopefully continue showing such responses with testing of reduced concentrations and incubation times.

Table 4.5: Table of comparisons of *S pneumoniae* sensors. MB = Magnetic beads. HS = Human serum. LCT = Lowest concentration tested

Sensor	Label free	Cost	Complexity	LOD	Time to result	Other
Cell culture	Yes	Relatively cheap	Simple	NA	upto 72 hours	Low positivity rate Specialist staff Lab required
PCR	Yes	Expensive PCR machine	Relatively simple	NA	hours	Specialist staff Lab required
UAT [208]	Yes	≈ £5	Lab required Multiple stages Sample temp equilibrium	Sensitivity 78 - 89 % Specificity 95 %	15 mins	May not be generalisable 1 Test/device
Magnetosensor [213]	No	Expensive MB ≈ £2.65/test Sensor ≈ £2/test	Complex MB modification Biotinylate probe	1100 pM	5 hours	Non complex sample 1 Test/device LCT =1000 pM
DNA antibody [216]	No	Expensive Lab electrodes ≈ £hundreds	Tetrahedron DNA construction 5 stage functionalisation complex materials days to complete	3.26 pM	> 30 mins	Real samples 1 Test/device Lab required LCT = 0.028 pM
Polymer genosensor [217]	Yes	Expensive Custom lab electrodes	Relatively simple Requires electropolymerisation	1E6 pM	20 mins @ 55 °C	1 Test/device non complex sample
Synergisim gene sequence [218]	No	Expensive Lab electrodes ≈ £hundreds	Multiple labelled probes	0.0005 pM	20 - 60 mins	1 Test/device LOD calculated in 100 % PBS 100 nM detection in 50 % HS
Loop mediated isothermal amplification [219]	No	amplification kit ≈ £2.80/test UV source Mobile app	Microchip microfluidics portable but bulky magnetic beads	0.173	≈ 2 hours	1 Test/device
DNA Lab-on-PCB [215]	Yes	PNA ≈ £ hundreds	Lab based microfluidics	0.057 pM	5 mins continuous flow	LCT 0.1 = pM simple 15 bp oligo Not *S pneumoniae* sensor non complex sample
This device	Yes	≈ £ 0.2	Simple Standard DNA functionalisation	1 pM ≈ 0.3 pM with second fit	15 mins	LCT 1 pM 235 bp amplicon tested in 100 % HS 8 Tests/device Further optimisation possible

These results demonstrated that SWV could partially, and EIS could fully successfully and specifically detect an unlabelled 235 bp *lytA* amplicon amplified from *S. pneumoniae* full genomic DNA over a range of concentrations from 1 pM - 100 pM in 15 minutes at room temperature. Clinically relevant blood levels that can result in life-threatening infections can be as low as 1 - 10 colony-forming units per millilitre of blood (cfu/ml)

[220]. This equates to approximately attomolar (aM) levels of genetic material for detection. The sensor had shown possible femtomolar LoDs and should comfortably be able to detect these femtomolar concentrations. Attomolar ranges would be a challenge to achieve nevertheless until the sensor is tested with these concentrations no feasibility conclusions can be made. If the sensor was unable demonstrate detection at these small concentrations then PCR amplification would have to be employed to amplify the DNA to detectable levels. This would be easily accomplished as PCR amplification was already employed for target sequence production for these experiments. Therefore, the infrastructure already existed and had been successfully demonstrated. Two hours of amplification were required to produce nanomolar levels of target DNA with the sensor demonstrating picmolar capabilities. Consequently the attomolar DNA would only require amplification to picomolar levels shortening the current amplification times used. This would result in the successful detection of clinically relevant levels of *S. pneumoniae* in under 2 hours.

4.4 Trend Reversal and Redox Concentration Current Behaviour

It must be stated that it is not possible at present to advance a full explanation for the dose response reversal trend. It was a secondary consideration to the research so left uninvestigated. A possible explanation is presented here.

The trends shown in this section have a few common characteristics. The reversal always appeared to happen at the 50 pM target concentration for both 20 bp and 235 bp sequences. This was always after 6-8 applications of lower concentrations that incorporated testing and wash steps in between. Other experiments implementing larger concentrations had surpassed the 50 pM range and not shown any trend reversals. Therefore, the most likely cause was due to the multiple incubations, washes and testing destabilising the probe DNA. Firstly the sensor responded with decreasing current (increasing impedance) as the rate reaction of hybridisation K_{on} dominated over the dehybridisation reaction rate K_{off}, blocking the surface and giving the expected trend.

Then as the binding sites filled, the multiple washes, incubations and testing destabilised the probe DNA reducing its binding affinity and ability for target hybridisation, presenting as a saturation at 50 pM. When the next concentration was applied, K_{on} was severely reduced or non-existent and K_{off} became the dominant process. With every incubation of higher target concentrations, the sensor donated the target to solution rather than the other way round causing a current decrease (impedance increase) i.e the trend reversal. This was only one theory that fits the results and requires further investigation.

A possible theory as to why 0.02 mM redox buffer affected a current increase while 5 mM experienced a decrease could be due to the ions self-blocking the passages to the electrode surface. When the solvated anion nears the negatively charged DNA backbones they will experience a repulsion. If the concentration of anions is small then there may be minimal interaction between the DNA and anion which allows a relatively unimpeded flow to the surface. This mechanism may also act to trap the anions in the DNA SAM so that increasing the DNA concentration does not result in a current decrease as the trapped ions can then facilitate a current response.

Conversely, a higher anion concentration could result in the DNA interacting with many anions at once, leading to a blockage made from coalesced anions. Since few anions make it past the DNA a decrease in current results and little to no trapping of anions occur. Further increasing the DNA concentration strengthens this anion blockage resulting in more current decreases.

It has been shown that electrochemical response to target binding has a dependence on the ionic strength of measurement buffer [221]. The ferri/ferrocyanide redox couple used in this work contributes to buffer ionic strength due to the 3- and 4- charges, therefore reducing the concentration may make the system sensitive explaining the 0.02 mM redox buffers improved performance.

4.5 Limitations and Future Work

There were some minor interface issues with PCB P4 and the multiplexer during early experimentation leading to a small number of sub-optimal electrode responses. These were quickly resolved with consultation with the PCB and interface manufacturer. Possible future work could be to redesign the PCB interface making it more ergonomic and easier to switch between PCB cleaning and PCB measuring configurations. This would be a quality of life upgrade, not affecting the interface performance.

Covid lockdown prevented the further analysis of the *lytA* PCB biosensor. Future experiments could investigate the expanded use of asymmetric amplicons, whole genomic DNA detection in spiked human serum and finally, clinical samples. The sensor displayed impressive performances and most probably would have continued this behaviour into further investigations outlined above. The sensor platform could also be adapted to develop detection methods for other pathogens, *N. meningitidis* and *H. influenzae* are of particular interest due to their fastidious behaviour and serious effects on patient health.

4.6 Conclusions

Taking a sequence from the *lytA* gene of *S. pneumoniae*, probe and full complementary 20 bp sequences were constructed and utilised to rapidly electrochemically detect the bacterial presence of *S. pneumoniae*. Custom fabricated microelectrodes, gold standard macroelectrodes and custom designed PCBs were shown not to be suitable detection platform for this *lytA* probe DNA. The 20 bp complementary target DNA was successfully detected using these devices but the performance was sporadic and each device displayed too many drawbacks to justify further use. Following a lengthy prototyping stage, P4 was identified as the most promising sensor array because of its highly flexible design. It allowed for high experimental throughput and production of large data sets, ensuring statistical reliability when interpreting results.

Successful 20 bp target detection was shown in PBS samples using this device, resulting

in a limit of detection of 4.5 pM. Longer target sequences were created using PCR to better replicate the reality of how DNA from lysed bacteria would be presented to the biosensor. These amplicons were created in various formats: normal double stranded DNA, asymmetric (single stranded DNA) and asymmetric DIG-labelled *lytA* target amplicons. Accompanying these amplicons were equivalent negative control amplicons using the OXA gene from *E. coli*. Successful detection of normal PCR amplicon and asymmetric DIG-labelled amplicon samples in PBS was achieved. Other asymmetric PCR products in PBS were unable to be detected most probably due to insufficient quantity and contamination of amplicons of both positive and negative controls. No likely differences between positive and negative controls were found and could be explained by non-specific biofouling.

Chronoamperometry testing attempted to utilise the DIG label and accompanying HRP anti DIG antibodies but no likely differences between the controls were apparent. The HRP adhered to all surfaces on the sensor for both controls and was unable to be sufficiently removed, resulting in this method being unusable.

Finally, 235 bp of normal PCR amplicon (amplified from *S. pneumoniae* genomic DNA) was spiked into 100 % human serum and was detected at 1 - 100 pM ranges in 15 minutes at room temperature using EIS. SWV showed some promise by detecting the *lytA* amplicon at 20 pM. For clinically relevant levels of *lytA*, detection at attomolar concentrations of DNA would likely be required. This was still to be tested at the time of writing. If the sensor was unable to directly detect such small levels then PCR amplification would be employed to amplify the DNA to detectable levels. This had already been shown to work as amplification of genomic DNA was used to create the target DNA samples. This would push the successful detection time of *S. pneumoniae* to under 2 hours. The sensor also demonstrated equal or improved performances to those reported in the literature.

This work successfully demonstrated the development of a biosensor able to detect 1 pM of *lytA* amplicon from *S. pneumoniae* in a complex sample within 15 minutes at room temperature. It should not be difficult to reduce the detection time, detect lower

concentrations, and show suitable performance in clinical samples with further research on this biosensor.

Chapter 5

Electrochemical detection of SARS-CoV-2 (Enzymatic biosensor)

5.1 Introduction

SARS-CoV-2 is the name designated to the virus that can result in coronavirus disease (COVID-19). The virus became apparent to health authorities in China in late 2019 and was declared a public health emergency on 30th January 2020. The virus spread around the globe at pace and on the 11th of March gained pandemic status by the World Health Organisation [128, 222]. COVID-19 can also progress to sepsis [14], this is viral sepsis rather than bacterial. There are clinical differences between manifestations of COVID-19 and bacterial sepsis, an example of this is the near-total loss of the mucociliary escalator of the tracheobronchial tree which can lead to damage of the ciliated respiratory epithelium predisposing the patient to superinfections, similar to that seen in influenza pneumonia. These differences tend to quantitative rather than qualitative [223, 224]. That is, clinicians have encountered these disease manifestations before in sepsis patients but not with the regularity currently seen. It is therefore important that treatment follow the sepsis guidelines as well as COVID-19 guidelines. The difficulty is knowing when one condition has abated and the other continues, making treatment modifications difficult. One of the major issues during the pandemic has been

diagnostics. Assay quantity, reagent costs and time to result have been of particular issue. Solutions to these issues published in academia have been experimental, reagent intensive with no current route to manufacture.

SARS-CoV-2 is between 50 and 200 nm in diameter and has four major structural proteins [225]. The protein responsible for binding to cell surfaces that express angiotensin converting enzyme 2 (ACE2) is known as spike glycoprotein. The affinity between these two proteins has been shown to be in the low nanomolar range [226]. Due to this high affinity it is possible to use ACE2 as a receptor molecule for the spike protein in a biosensor format. ACE2 has a hydrophobic region in its structure that facilitates insertion into cell membranes [227]. This means biosensor surfaces can be potentially functionalised with ACE2 via adsorption involving hydrophobic interactions. The use of ACE2 also adds the benefit of being mutation resistant as it exploits the interaction with the spike protein. In this chapter it was shown that combining the PCB technology and fluorous SAM surface modification discussed in chapters 2 and 3, that a dense amphiphobic fluorous SAM was successfully formed on the biosensor surface. A reduction of surface fouling [228] was also achieved due to the density and amphiphobic properties of the constructed SAM. This PFDT containing amphiphobic SAM was then functionalised with ACE2 via amphiphobic physisorption creating a PFDT-ACE2 complex ready for spike protein detection. This sensor used EIS to detect binding from recombinant SARS-CoV-2 spike protein and positive and negative samples of inactivated SARS-CoV-2 from a fully validated molecular standards kit and clinical samples (Figure 5.1). A key advantage of this design was that it was label free. The sensor was designed with up-scaling and manufacturing in mind using two simple productions steps (1) facile SAM formation and (2) ACE2 functionalisation. The work here was demonstrated on a low cost sensor system, with the ability of efficient assay transfer to more mass manufacturable devices such as printed devices or glucose format sensors. This would establish the ability for high volume production of a diagnostic with potential for widespread, rapid point of need use.

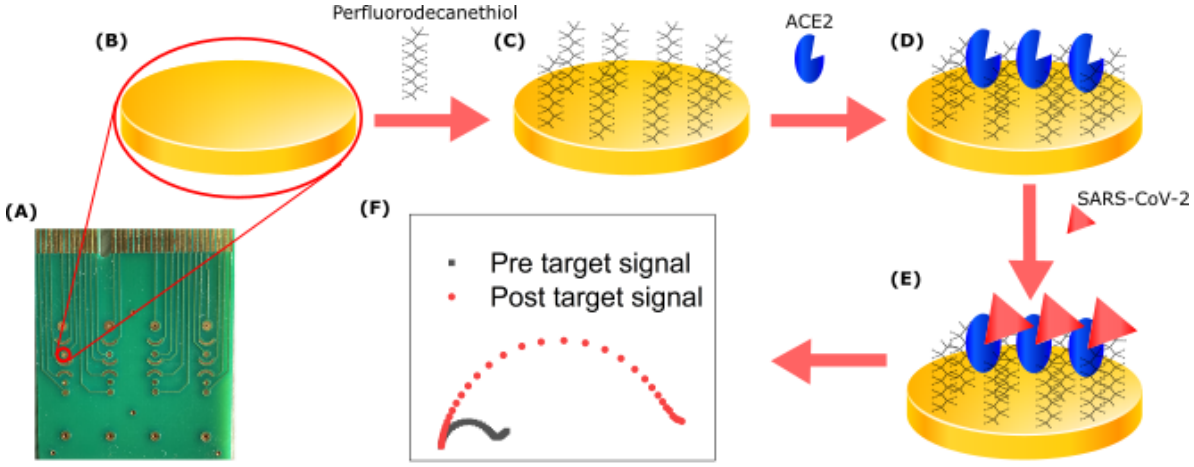

Figure 5.1: Image of the 8 times Au working electrode PCB based sensor array with on-chip Au counter and reference electrodes (A). Representations of the Au sensor surface in the following states: clean (B), PFDT functionalised and (C) ACE2 functionalised (D) and with binding of SARS-CoV-2 spike protein or inactivated virus (E). Example Nyquist plots showing the signal from an ACE2 functionalised sensor (black) and following exposure to recombinant SARS-CoV-2 spike protein (red) (F).

5.2 Materials & Methods

All measurements were taken using a PalmSens4 potentiostat running PSTrace software from Alvatek electrochemical solutions (Houten, Netherlands). The electrodes used were SEP1 BIOTIP multichannel electrode PCB platform discussed in Chapter 3, 1.6 mm diameter gold polycrystalline macroelectrodes (referred to macroelectrodes in this section) using a 1.6 mm platinum macroelectrode as combined counter and reference electrode. Both purchased from (IJ Cambria Llanelli, UK).

5.2.1 Chemicals

Chemicals used in this work are listed in Table 5.1.

Table 5.1: List of chemicals used in this work.

Chemical	Abbreviation	Supplier
De-ionised water (resistivity $\geq$ 18 MΩcm)	DI	Sigma-Aldrich
Ethanol		Sigma-Aldrich
Hydrogen peroxide	H_2O_2	Sigma-Aldrich
Perfluorodecanethiol	PFDT	Sigma-Aldrich
Phosphate buffered saline tablets	PBS	Sigma-Aldrich
Potassium hydroxide	KOH	Sigma-Aldrich
Potassium ferricyanide	$K_3[Fe(CN)_6]$	Sigma-Aldrich
Potassium ferrocyanide	$K_4[Fe(CN)_6]$	Sigma-Aldrich
Sulfuric acid	H_2SO_4	Sigma-Aldrich
Toluene	C_7H_8	Sigma-Aldrich
3,3,,5,5,-Tetramethylbenzidine	TMB	Sigma-Aldrich

5.2.2 Buffers

Buffers and their compositions used in this work are shown in Table 5.2. De-ionised water (5.1) was used to make all aqueous solutions.

Table 5.2: List of buffers used and their compositions

Buffer	Composition
Acid piranha solution	18 M H_2SO_4 and 30 % H_2O_2 (ratio = 3:1 v/v)
Redox buffer	5 mM Potassium ferricyanide/Potassium ferrocyanide in 1 x PBS
Rinse buffer	1 x PBS

5.2.3 Biological reagents

A list of biological reagents used and where they were manufactured/purchased is presented in Table 5.3.

Table 5.3: List of biological reagentsand their manufacturer

Reagent	Abbreviation	Manufacturer
Angiotensin converting enzyme 2	ACE2	Abcam
HRP conjugated spike protein	Spike-HRP	The Native Antigen Company
HRP conjugated streptavidin	Streptavidin-HRP	Bio-techne
Inactivated severe acute respiratory syndrome coronavirus 2	SARS-CoV-2	Randox laboratories Ltd

5.2.4 Preconditioning

SEP1 BIOTIP multichannel electrode PCB platforms were cleaned according to the supplied protocol. This consisted of a 15-minute submersion in a solution of 50 mM KOH in H_2SO_4 30 % (v/v) at room temperature. The PCB was then rinsed with DI water and dried using compressed air. The PCB was then electrochemically cleaned by submerging in 50 mM KOH (DI water as solvent) with an external platinum counter electrode (Metrohm, Runcorn, UK) and 3M NaCl Ag/AgCl reference electrode (IJ Cambria, Llanelli, UK). Cyclic voltammetry was performed on all working electrodes on the PCB using the following parameters: the potential window was -1.2 to 0.6 V, scan rate of 0.1 V/s and 15 scans per electrode. The PCB was then rinsed with DI water and dried again using compressed air. Gold polycrystalline macroelectrodes were submerged for 15 minutes in piranha solution as an organic material removal method. They were then electrochemically cleaned in 0.1 M H_2SO_4 using cyclic voltammetry with a potential window of -0.6 - 1.6 V at 0.1 V/s 20 scans per electrode. This setup used the same reference and counter electrodes as the PCBs used during cleaning.

5.2.5 Fluorous SAM and ACE2 Immobilisation

The SAM solution was prepared by magnetically stirring toluene and adding PFDT until a 1 mM solution was formed. Stirring aids in dispersing the PFDT throughout the solution. Fluorocarbons can have low miscibility in organic solvents and have a propensity for self-interaction forming separate phases via the fluorous effect [171, 172, 186]. The PCBs were orientated horizontally in a small glass petri dish and the PFDT solution added to cover the PCB with excess solution. Toluene evaporates quickly, by using excess solution and a film covering reduced evaporative losses. The PCBs and gold polycrystalline macroelectrodes were incubated overnight at room temperature, then rinsed with DI water (10-second water bottle flow per electrode) and dried with compressed air. All work with toluene was performed in a suitable fume hood with proper halogenated solvent waste (contaminated by PFDT during SAM formation) disposal routes. ACE2 was diluted from stock in 1 x PBS to 1 μg/ml and 10 μl aliquots were applied to each working electrode on the PCB and macroelectrode and left to incubate

for 1 hour at room temperature. Following incubation, the electrodes were rinsed with 1 x PBS (10-second water bottle flow per electrode) and dried with compressed air.

5.2.6 Protein Target Detection using PCBs

A series of dilutions of the positive control HRP conjugated SARS-CoV-2 spike protein and negative controls of similar sized proteins (HRP conjugated streptavidin and IL-6) were incubated at room temperature for 30 minutes on the PCB sensor arrays with rinsing with 1 x PBS (10 seconds water bottle flow per electrode) and EIS measurements between each concentration incubation. HRP conjugated SARS-CoV-2 spike protein and IL-6 concentrations used were 1, 10, 50 and 100 ng/ml (all dilutions in 1 x PBS). HRP conjugated streptavidin was obtained as part of an ELISA kit and the concentration was not disclosed. The accompanying instructions recommended a 1:40 dilution for ELISA assays. The series of dilutions used (1:100, 1:75, 1:50, 1:25 and 1:5) were distributed about the 1:40 recommended dilution.

5.2.7 Inactivated Virus Detection

For detection of inactivated virus, a clinical molecular standards kit for SARS-CoV-2 (Qnostics) was purchased. The kit contained positive and negative samples of the virus present in a complex "transport medium" representative of a clinical sample. A series of dilutions of the positive control (inactivated virus + transport medium and human cells) was incubated for 30 mins at room temperature on the PCBs. The concentrations used were 10^2, 10^3, 10^4, 10^5 and 10^6 dC/ml (digital copies per ml). Due to the small volume of solutions provided, the negative control (transport medium + human cells) was incubated twice for 30 minutes at room temperature. Room temperature incubations were chosen to replicate the operational environmental conditions likely required for a diagnostic device. The PCBs were rinsed with 1 x PBS (10 seconds wash bottle flow per electrode) and EIS measurements performed between each incubation.

5.2.8 SARS-CoV-2 Clinical Samples

Clinical Samples were diagnostic swabs submitted to the NHS West of Scotland Specialist Virology Centre for SARS-CoV2 testing. Samples were provided by NHS GGC Biorepository. They were anonymised surplus samples and no patient identifiable data was available to the researchers. The work was preformed under NHS GGC Biorepository ethics for the collection of surplus samples, rec. 16/WS/0207.

Clinical samples stored in viral PCR sample solution (VPSS) and viral transport media (VTM) were tested. Negative clinical samples were patient samples that returned negative test results from PCR. For clinical sample testing, the sensors were functionalised as before however, without the ACE2 immobilisation stage. 20 μl of clinical sample was added to a 180 μl of premade solution that resulted in a final solution of 10 times diluted clinical sample + 5 mM redox buffer + 1 μg/ml ACE2 + 1 x PBS. This was left for 30 minutes at room temperature to allow for the ACE2 and virus to bind sufficiently. A baseline was taken using 5 mM redox buffer then the sample solution was added across the working and joint reference/counter electrodes and tested. The first clinical samples used, were tested at different times from application to the device: immediately, 6.5 minutes and 13 minutes. All other samples after this were tested immediately. Clinical samples were obtained from and tested in the clinical microbiology category 3 bio-safety laboratory at NHS Glasgow Royal Infirmary.

5.2.9 Fluorocarbon SAM Functionalisation Investigation

All experiments used the same PFDT, ACE2 and HRP conjugated SARS-CoV-2 spike protein target concentrations as previous experiments. The negative control (HRP conjugated streptavidin) used similar concentrations to the previous streptavidin work for two experiments, then changed to a 1:3 dilution utilising repeated incubations for the final two experiments. PFDT incubation times used were 1, 5, 10, 30, 45, 60 minutes as well as overnight incubation. ACE2 incubation times were 1 hour as in previous experiments. Target incubation times were 30 minutes as in previous experiments. Some PFDT and ACE2 incubations were performed at 4 °C and 25 °C. Two experiments

utilised the original PFDT and ACE2 reagents used in previous experiments, and in another two experiments, refreshed PFDT and ACE2 reagents were used. These were purchased from the same suppliers and were in the same concentrations. The explanation of what conditions were used in each experiment is explained in the results section.

5.3 Results & Discussion

5.3.1 ACE2 Immobilisation

For these initial experiments, the SAM forming process was not investigated as PFDT had been shown to form on various electrodes in the past and with time constraints it was prudent to allocate our time to investigating new reagents such as ACE2. SAM forming conditions were eventually investigated (and presented later Section 5.3.4) following a short period of assay performance deterioration which was remedied. An examination into the amphiphobic physisorption of ACE2 into the PFDT SAM structure was conducted. 1 μg/ml ACE2 solution was incubated on the PFDT SAM modified electrodes for 1 hour at room temperature. This affected small impedance increases (Figure 5.2).

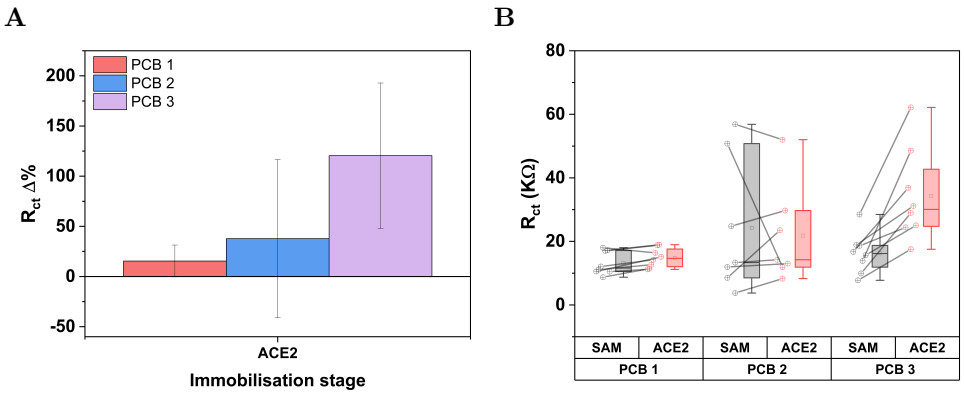

Figure 5.2: Bar graph showing R_{ct} percentage change in response to ACE2 addition versus the SAM stage (A). Box plot showing R_{ct} values of ACE2 functionalised surfaces versus the SAM functionalised stage (B). n = 8 for all PCBs except PCB 2 with n = 7.

The mean percentage change ranged from 15 % to 120 % for the three tested PCBs (Figure 5.2A). This is supported by the raw R_{ct} behaviour for the PCBs (Figure 5.2B) with 21 of the 23 electrodes tested showing increases. Impedance changes could be small

in magnitude as evidenced by the signals measured with PCB1, or large as was the case for PCB 3. This was likely due to the PFDT SAM, with each layer being topologically different due to the variable nature of the SAM formation process discussed in chapters 2, 3 and 4. This will lead to differing amounts of ACE2 being amphiphobically adsorbed. This behaviour of relatively small signal changes upon adsorption into the SAM surface was also present for the fluorous tagged probe in Chapter 2 providing further evidence that these adsorption events do not necessarily affect large signal changes.

It was clear that all electrodes showed a response to ACE2 adsorption in line with the expected behaviour of impedance increases due to more biomolecular material blocking the electrode surface. Although these results confirmed ACE2 adsorption, they could not confirm if the ACE2 was bound in the correct conformation with its receptor sufficiently exposed for efficient ligand binding to occur. This was investigated next in a series of viral target ligand experiments.

5.3.2 Spike Protein Binding

The spike protein was the principal surface protein of SARS-CoV-2 that bound ACE2 facilitating viral RNA transfer into host cells. The spike-ACE2 binding was therefore highly specific. Spike protein was used to test the fluorous SAM-ACE2 complex formed on the macroelectrodes and PCBs. By introducing spike protein to the complex multiple questions were investigated:

- Is ACE2 in the correct conformation to facilitate binding?
- If the ACE2 can facilitate binding what is the sensitivity of the biosensor?
- Can it specifically detect spike protein?

HRP conjugated spike protein and HRP conjugated streptavidin protein

It was shown using PFDT-ACE2 functionalised macroelectrodes incubated in HRP conjugated spike protein and HRP conjugated streptavidin that a large visual distinction between the two occurred in the presence of TMB (Appendix D.1). This demonstrated a strong binding affinity for spike protein. To progress further towards a usable device

these two proteins were then tested on the PCB electrodes using a more quantitative technique, EIS. After a 30 minute incubation in HRP conjugated spike protein all concentrations stages showed impedance increases (Figure 5.3A) indicated by increasing charge-transfer semi-circle size. The mean percentage change vs ACE2 stage also steadily increased (Figure 5.3B). The minimum increase was 96 % and the maximum 156 %. These results confirmed that HRP conjugated spike protein was binding to the ACE2 present in the SAM. This answered the question of whether ACE2 was in a suitable conformation in the PFDT-SAM to facilitate ligand binding.

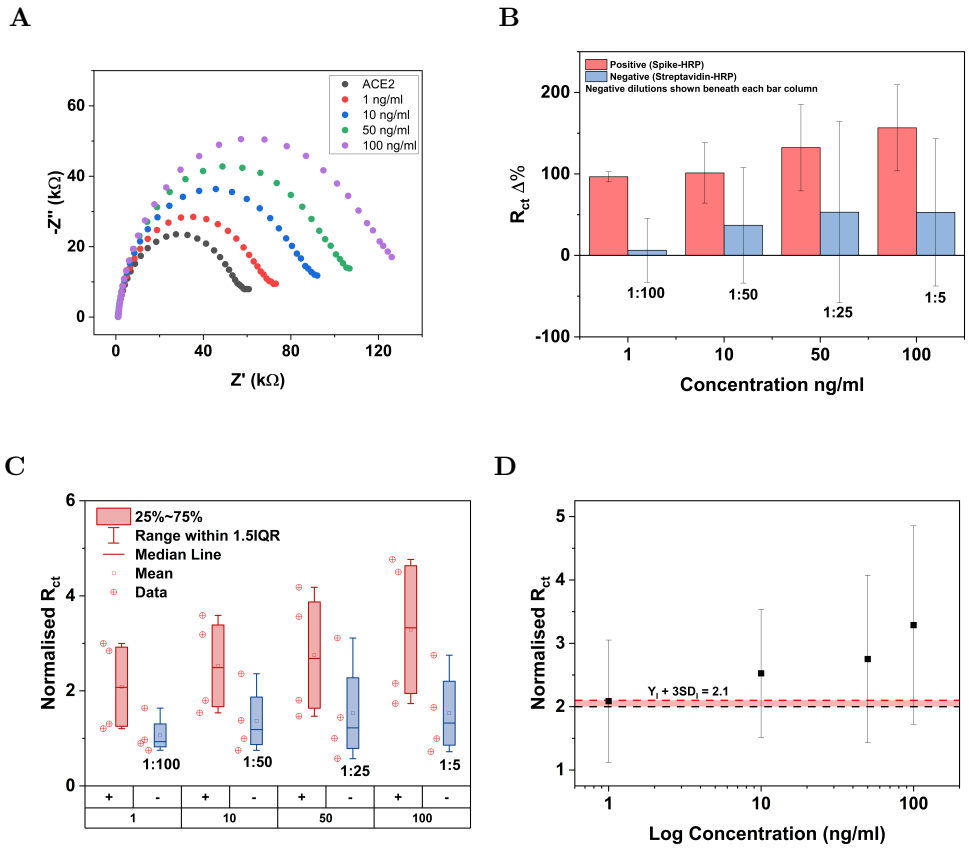

Figure 5.3: Nyquist plot showing the impedance responses to increasing concentrations of HRP conjugated spike protein (A). Bar chart showing the mean percentage change vs ACE2 stage in response to the addition of HRP conjugated spike and streptavidin (B). Box plot showing the normalised (against ACE2 values) R_{ct} values of HRP conjugated spike and streptavidin proteins (C). The dose response curve for HRP conjugated spike protein (D). EIS settings (E_{dc} vs OCP = 0.0 V, frequency range: 1 Hz to 100 kHz. n = 4 for all measurements. This data was first presented in publication [229]

Specificity investigations of the ACE2-HRP conjugated spike protein employed the use of a negative control (HRP conjugated streptavidin). The mean percentage change due to the negative control ranged from 6.2 % to 52.8 % (Figure 5.3B, blue). At each concentration stage, the negative control response was smaller than the positive control and displayed a plateau at the higher concentrations with the final two values being 53.1 % and 52.8 %. The normalised raw data also showed similar trends (Figure 5.3C) with the positive control concentrations all likely different from the ACE2 signal and none of the negative control concentrations different from the ACE2 signal. This meant that the positive was a confirmed response to specific binding and the negative was indistinguishable from the ACE2 baseline, demonstrating a lack of response to non-specific proteins.

At all concentrations the positive and negative controls were also likely different from each other, again reinforcing that the positive signal was a successful detection of HRP conjugated spike protein and rejection of the HRP conjugated streptavidin contaminant. These results answered the questions posed: ACE2 was in a suitable conformation via physisorption into the PFDT layer and was able to specifically bind the various concentrations of positive target ligands resulting in a dose dependent signal response. The strong amphiphobic nature of the PFDT SAM was also able to act as an anti-biofouling agent on the sensor evidenced by the lower negative control signals and their lack of likely differences between baseline, other negative concentrations and positive signals. This anti-biofouling did not result in complete removal of negative signal as that would be unrealistic, the signals produced by the negative control were then likely due to small amounts being adsorbed into the PFDT-ACE2 complex.

The decision to use HRP conjugated streptavidin as a negative control was for two reasons. Firstly, it was similar in size (104 kDa) to HRP conjugated spike protein (154 kDa) and should have similar effects to the spike protein allowing for suitable comparison. Secondly, since the spike protein had an HRP enzyme integrated into its structure. It was necessary to have a negative control that also contained an HRP enzyme to be able to account for any role that HRP would have on the measured signals

of the binding proteins. It was also worth mentioning that the stock concentration of the HRP conjugated streptavidin was in the region of 1 mg/ml [229]. Thus the dilutions were more concentrated than the positive by at least one order of magnitude. This again illustrated the performance of the PFDT at reducing fouling. The sensor signal response performance was gauged using Y_{LOD} and X_{LOD} (Section1.11.3). The Y_{LOD} = 2.1 (R^2 = 0.99342) (Figure 5.3D). The lowest concentration measured lay on the threshold of this limit with all other concentrations comfortably above it. This limit had a corresponding X_{LOD} = 1.06 ng/ml for HRP conjugated spike protein.

HRP conjugated spike protein and IL-6

With the promising results showing strong HRP conjugated spike protein affinity and confirmation that the HRP did not play a significant role in the output signal. It was beneficial to retest the HRP conjugated spike protein binding to ascertain the repeatability of this complex sensor system. In addition, a different negative control was included, one that is present in the body and will likely be a contaminant in clinical samples. Interleukin-6 (26 kDa) was chosen for this purpose. Being a myokine (released by skeletal muscle cells in response to muscular contractions) and cytokine (proteins important in cell signalling), IL-6 is present in the body under most circumstances, especially after exercise. Many injuries and diseases including bacterial and viral infections have inflammatory and immunological responses caused by IL-6. It has been reported that elevated levels of IL-6 present in advanced COVID-19 warranting the name cytokine storm [135]. Patients that progressed to acute respiratory distress syndrome (ARDS) had a median IL-6 concentration of 7.39 pg/ml [229, 230, 231] and patients that died had a median of 11.4 pg/ml [229, 231, 232]. For this experiment, the number of electrodes tested for each control group was increased from n = 4 to n = 8 i.e a control group per PCB.

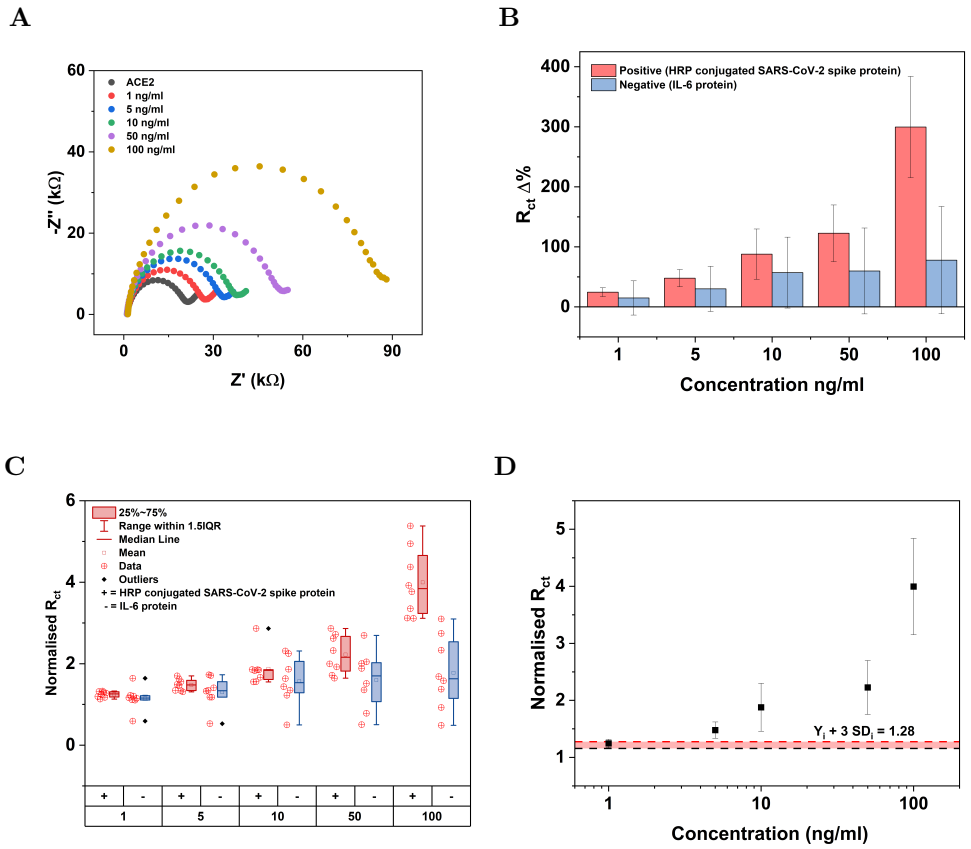

Figure 5.4: Nyquist plot showing the impedance responses to increasing concentrations of HRP conjugated spike protein (A). Bar chart showing the mean percentage change vs ACE2 stage in response to the addition of HRP conjugated spike and IL-6 (B). Box plot showing the normalised (against ACE2 values) R_{ct} values of HRP conjugated spike and IL-6 proteins (C). The dose response curve for HRP conjugated spike protein (D). n = 8 for all measurements. This data was first presented in publication [229]

As before for the HRP conjugated spike protein, the impedance increased with increasing target concentration (Figure 5.4A). This was supported by mean R_{ct} percentage changes (Figure 5.4B,red) ranging from 24.4 % to 300 %. This was in good agreement with previous experiments showing a similar trend (Figure 5.3B, red) and as such was further evidence that the HRP conjugated spike protein was successfully bound to the ACE2 present in the PFDT-ACE2 complex [229]. The IL-6 negative control showed suppressed mean R_{ct} percentage changes ranging from 14 % to 77 % (Figure 5.4B, blue) with the 10 and 50 ng/ml concentrations having similar values 57 % and 59 % respectively.

The normalised R_{ct} data (versus ACE2) showed there are likely differences between the positive and negative groups for 1, 50 and 100 ng/ml concentrations (Figure 5.4C). Confirming again that the HRP conjugated spike protein was successfully detected even in the presence of biofouling signals from the negative control. All positive control concentrations were likely different from each other, tentatively suggesting that perhaps with more data and calibration that sample measurements could estimate the concentration of spike protein present, potentially leading to a gauge of viral load.
All negative control groups except 1 ng/ml were not likely different and can all be considered as one general response due to biofouling. This demonstrated the sensor's strong anti-biofouling properties being able to suppress a dose dependent negative control signal. This was all the more impressive since these IL-6 concentrations were 10^3 to 10^5 (100 ng/ml) times higher than that measured in COVID-19 patients serological samples, which is larger still than the amounts that would be present in respiratory and saliva samples which this device was targeted.

The normalised R_{ct} Y_{LOD} was found to be 1.21 (R^2 = 0.99) (Figure 5.4D). This was a small improvement over that seen in the previous section (Y_{LOD} = 2.1). Only the 1 ng/ml concentration data point intercepted this limit, possibly making this concentration an unreliable detection. The corresponding X_{LOD} was 1.68 ng/ml, again similar to that seen in the previous section (X_{LOD} = 1.06).

SARS-CoV-2 antigen biosensors have been recently reported in the literature. Electrochemical sensors have shown good sensitivity with graphene and gold nanostars achieving a detection limit of 1.68E-22 μg/ml [233] and molecular imprinted polymers detecting nucleocapsid (15 fM)[234]. Nucleocapsid antigen-detecting half-strip lateral flow assay demonstrated a limit of detection of 0.65 ng/ml[235]. The sensor developed in this work showed comparable performance and clinical relevance.

This second experiment demonstrated and confirmed many characteristics that the first experiments with HRP conjugated streptavidin had shown. It was shown that HRP conjugated spike HRP was successfully detected at the same concentrations for a second time evidenced by dose dependent responses which meant not only was this target

ligand-receptor binding repeatable but consequently, so to was the successful formation of the PFDT-ACE2 complex allowing for this to occur. Discrimination between positive and negative controls was again demonstrated, evidenced by likely differences between the positive and negative R_{ct} responses, with the added effect of negative signal suppression demonstrating anti-biofouling properties. The likely differences between the positive control concentrations potentially allow for a calibrated indication of viral load. The normalised average behaviour always appeared to tend to repeatable results which were further demonstrated by Y_{LOD} and X_{LOD} displaying similar values to that shown in the previous section evidencing the repeatability of this sensor and protocols.

5.3.3 Virus Binding

Having shown the ability of the PCB sensor functionalised with a PFDT-ACE2 complex to successfully bind individual SARS-CoV-2 spike glycoproteins, as well as being able to discriminate the glycoprotein signal from contaminants at significantly higher concentrations, the focus was shifted towards whole SARS-CoV-2 virus detection. This was achieved by examining the responses of inactivated virus, VPSS and VTM clinical samples. Bringing the sensor into a domain that is more representative of real world scenarios that a final device would be required to deal with.

Inactivated SARS-CoV-2 detection

A logarithmic dilution series of inactivated whole virus suspended in transport medium was tested against a negative control consisting of the same transport medium without virus. The exact composition of the medium was proprietary information from the supplier but in general was composed of buffers to maintain the virus, lysed human cells and proteins in order to replicate the diversity and complexity of real clinical samples. As with the preceding experiments the R_{ct} values increased with viral concentration (Figure 5.5A). The mean R_{ct} percentage changes ranged from 106 % to 211 % (Figure 5.5B, red) with the latter corresponding to the second highest concentration value as the highest concentration tested produced a decrease to 168 %. This was likely due to displacement of virus/virus and ACE2 complex or a subsequent reordering or des-

orption of the SAM as a result of being in the proximity of large and repeated viral concentrations over successive experiments [229]. This result again demonstrated a dose dependent response to the target (virus) confirming detection of whole virus.

Due to the volume of supplied negative control, only two applications were possible. The first negative control was incubated at the same time, duration and with similar conditions as the first positive concentration. The second application was in time with the second positive concentration. The mean R_{ct} percentage changes for the negative control were almost identical 114.4 % and 113.9 % (Figure 5.5B, blue). These two incubations of negative control equated to 1 hour in the presence of the transport medium. This was significantly longer than the times required for a final point of care device. It appeared that the negative control produced a large signal but one that saturates immediately. The lack of dose dependence and the rapid saturation of the negative control response was demonstrated, yet again, displaying the anti-biofouling properties of the PFDT-ACE2 complex.

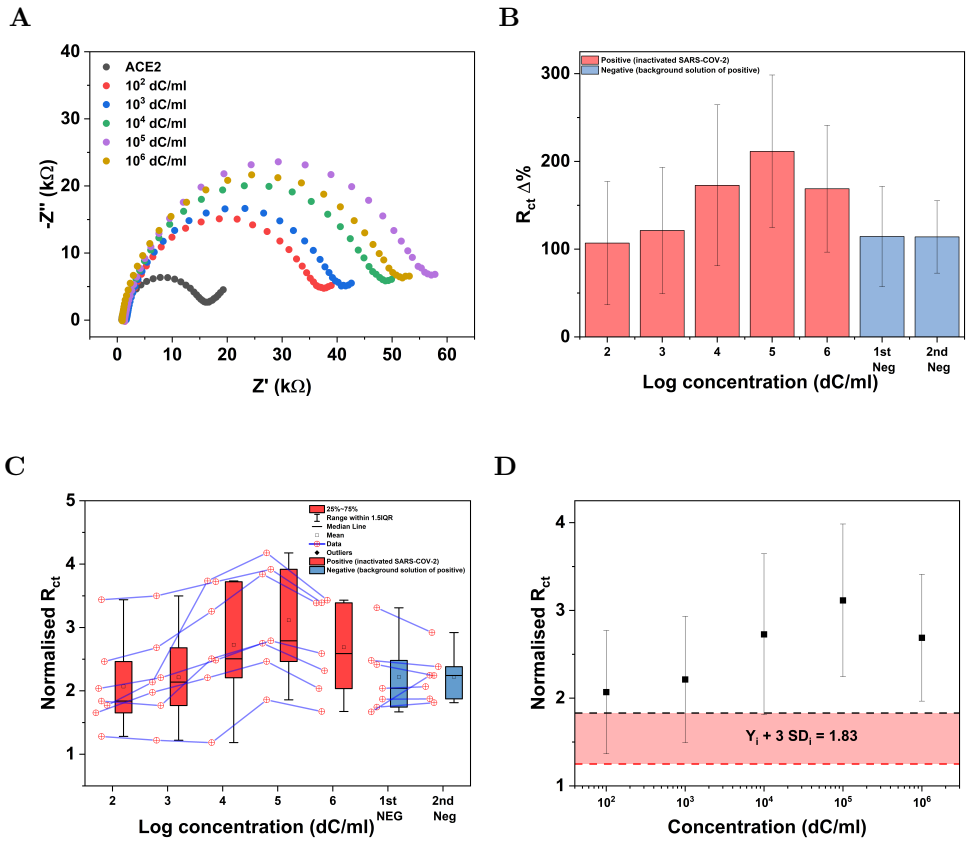

Figure 5.5: Nyquist plot showing the impedance responses to increasing concentrations of inactivated SARS-CoV-2 virus (A). Bar chart showing the mean percentage change vs ACE2 stage in response to the addition of inactivated SARS-CoV-2 virus and transport medium negative control (B). Box plot showing the normalised (against ACE2 values) R_{ct} values of inactivated SARS-CoV-2 virus and transport medium negative control (C). The dose response curve for inactivated SARS-CoV-2 virus (D). n = 7 for all measurements. This data was first presented in the publication [229].

The normalised R_{ct} data showed that the 10^2 and 10^3 dC/ml positive control concentrations were likely not significantly different from the negative control but the other positive controls likely were. This suggested that the sensor could reliably discriminate viral concentrations of 10^3 dC/ml and above. Clinical levels of SARS-CoV-2 range from 10^4 to 10^{11} RNA copies/ml [236, 237]. This places the sensor within the clinically relevant range.

As seen in previous experiments there were no likely differences between the negative control stages reinforcing the anti-biofouling capabilities (Figure 5.5C, blue). There were

also no likely differences between the positive groups like with the HRP conjugated spike protein vs IL-6 case (Figure 5.5, red). This was not of primary importance, nor was it a goal of the research. It would have simply been a bonus.

Analysis of sensor performance showed a Y_{LOD} of 1.83 (R^2 = 0.96064) (Figure 5.5D). This was again similar to the two previous spike protein experiments showing excellent and consistent performance across multiple PCBs and target conditions. The corresponding X_{LOD} was found to be 37.8 dC/ml. In these experiments, the sensor demonstrated the ability to successfully detect SARS-CoV-2 inactivated virus above 10^4 and can discriminate the virus from a negative control in clinically relevant ranges. All within a 30 minute incubation period.

Numerous SARS-CoV-2 biosensor approaches have been developed and reported recently. Magnetic beads, carbon black electrodes and multiple antibodies were employed to achieve a detection limit of 6.5 plaque-forming units per ml in whole virus [238]. An ultrasensitive super sandwich-type assay has been presented to detect viral RNA from SARS-CoV-2 with an LoD of 200 copies per ml[239], and a FET biosensor capable of detecting spike protein with a LoD of 242 copies per ml in transport medium has also been reported [240]. The sensor developed here demonstrated comparable and clinically relevant sensitivity (LoD for inactivated virus of 37.8 copies per ml)

SARS-CoV-2 clinical samples

Upon addition of VPSS clinical sample, the mean R_{ct} percentage change for the positive control decreased immediately (Figure 5.6A). The negative control showed a larger decrease than the positive. The sensor was able to respond instantly to sample addition with longer solution application times showing little to no performance improvement. The Normalised R_{ct} data showed the clear significant differences between the positive and negative samples (Figure 5.6B) with the 0-minute measurement's two-sample T-test showing a P = 1.22E-7 with a significance level set at 0.05.

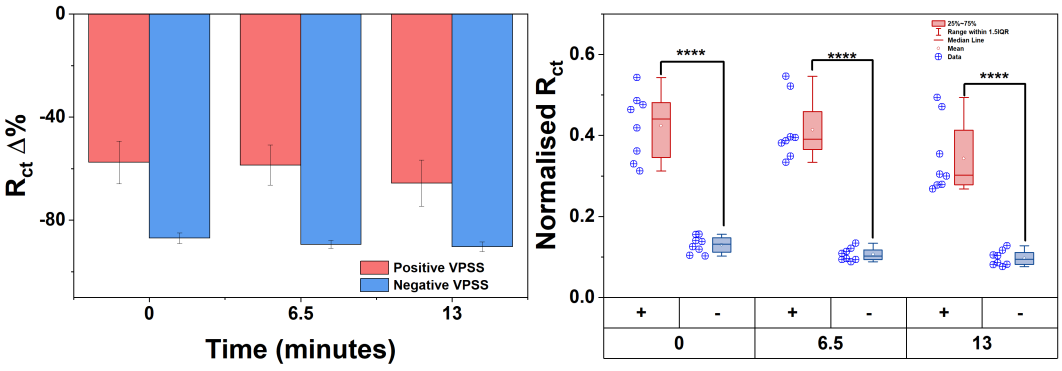

Figure 5.6: Bar chart showing the mean R_{ct} percentage change vs SAM stage in response to the addition of positive and negative VPSS clinical samples(A). Measurements were taken immediately (0 minutes), at 6.5 minutes and 13 minutes. Corresponding raw R_{ct} data from (C). n = 8. 4 asterisks = $p \leq 0.0001$.

These results demonstrated a clear detection of the positive clinical sample over the negative clinical sample. The direction of signal response changed from an increasing one in previous experiments to decreasing one in these experiments. This was due to two main factors: (1) The SAM generated with new reagents replacing the original degraded reagents, changing the behaviour of the biosensor, this is fully discussed in the next section. (2) VPSS and VTM contain chemicals, including well-known surfactants (which may have introduced a background effect into the assay signal) designed to disrupt pathogen membranes and envelopes. The fluorous SAM on the biosensor acted as a synthetic membrane so these chemicals likely had some disruptive behaviour opening up the SAM allowing for easier redox transport to the surface resulting in impedance decreases. Due to the strongly interacting fluorous molecules, the SAM was still able to maintain functionality by binding the ACE2-virus resulting in a surface blocking behaviour which resulted in the positive control having smaller signal decreases than the negative.

Eight VTM clinical samples were tested. The hospital researchers did not initially reveal the PCR results of each sample except for VTM 4 (positive) and VTM 13 (negative) which were required for additional experimentation. The mean R_{ct} percentage changes showed decreases for all samples (Figure 5.7A). The normalised R_{ct} data confirmed the

percentage changes and showed likely differences for VTM 1 vs all samples and VTM 7, 2 and 6 vs VTM 13 and 15 (Figure 5.7B). From this data, using the disclosed results of VTM 4 and 13 and using the theory that positive samples show smaller signal decreases compared to negative samples. The remaining four positive samples and two negative samples were correctly predicted in this blind experiment. VTM 4, by chance, was the positive sample disclosed from the beginning. If this was not the case, it would have been categorised as a negative sample. This was the only sample that opposed the trend. With some likely differences between positive and negative samples as well as sample positivity and negativity correctly predicted. The biosensor showed its potential as a rapid SARS-CoV-2 detection platform. Preliminary calculations showed sensitivity = 80 % and specificity = 67 %. One sample data point VTM 4, prevented the sensitivity and specificity from both being 100 %. This demonstrated improved performances over RT-PCR (sensitivity = 73 % and specificity = 61 %) [138] and antigen lateral flow assays (sensitivities reported between 52 % and 63 % for untrained staff following instructions and between 73 % and 85 % for medical and lab staff) [241]. Table 5.4 summarises some comparison of SARS-CoV-2 sensors from literature.

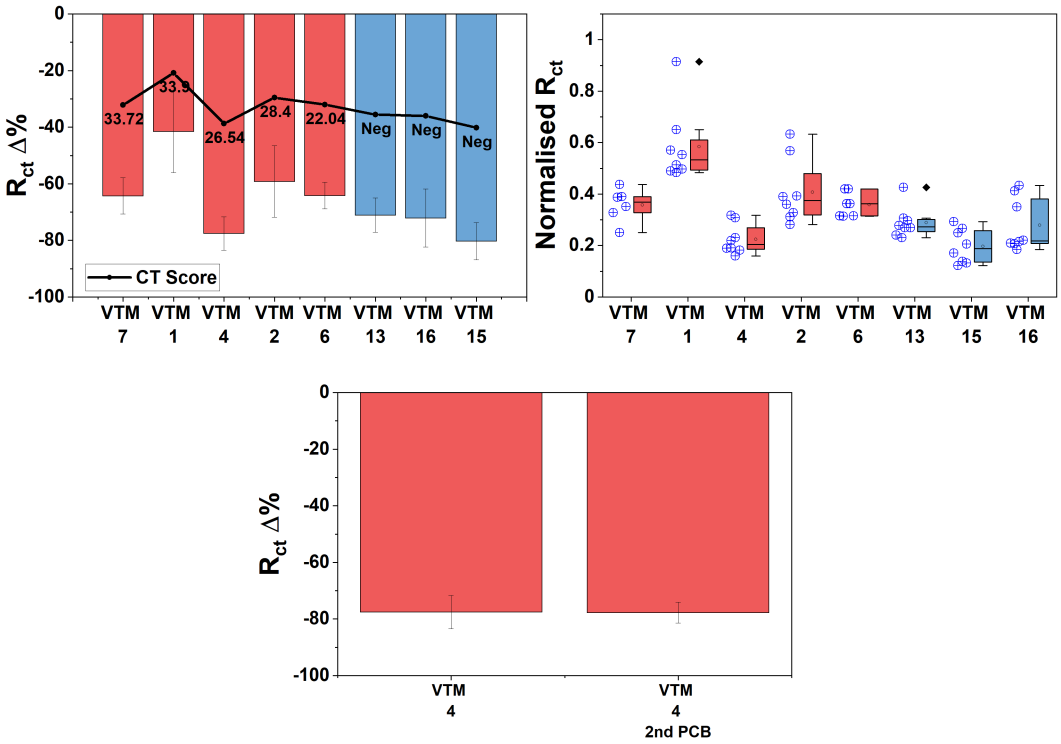

Figure 5.7: Bar chart showing the mean R_{ct} percentage change vs SAM stage in response to the addition of Positive and negative VTM clinical samples(A). Measurements were taken instantly. The overlaid line graph represents the corresponding CT scores for each positive sample. Corresponding raw R_{ct} data from (C). Mean R_{ct} percentage change of VTM 4 applied to separate devices, showing inter-device consistency. n = 8.

The cycle threshold (CT) values determined from the PCR on the samples were also provided with low values indicating higher viral loads. Figure 5.7A displays the overlaid CT scores, there was no apparent correlation between CT score and R_{ct} change. The inter-device consistency was also investigated with two PCB devices receiving VTM 4. The mean R_{ct} percentage changes for both showed a high degree of consistency -77.5 % vs -77.8 % (Figure 5.7C).

Table 5.4: Table of comparisons of SARS-CoV-2 sensors. LF = Lateral flow. LCT = Lowest concentration tested

Sensor	Label free	Cost	Complexity	LOD	Time to result	Other
RT-PCR	Yes	Expensive PCR machine	relatively simple	Sensitivity 73 % Specificity 61 %	hours	Not mutation proof Specialist staff Lab required
Antigen LF	No	≈ £5/test	Complex preparation	Sensitivity 52 % untrained 63 % trained Specificity 73 % trained 85 % trained	30 mins	Not mutation proof Manufacturable at scale 1 test/device
Gold nano star [233]	No	Expensive Sensor ≈ £2/test	Complex surface modification gold nano star production	Sensitivity 95 % Specificity 60 %	1 mins	difficult to manufacture Not mutation proof 1 Test/device
MIP[234]	Yes	NA custom made	Complex Sensor fabrication Mobile app	2.2 pg/ml	> 30 mins	difficult to manufacture Not mutation proof 1 Test/device LCT = 0.7 pM/ml
Half strip LF [235]	No	Expensive ≈ £5/test	Complex preparation	650 pg/ml	not reported	Manufacturable at scale 1 Test/device Not mutation proof
This sensor	Yes	Cheap £0.20/test	Simple two stage preparation compatible with glucose production protocols	1.68 ng/ml spike protein 37.8 dC/ml virus Sensitivity 80 % Specificity 67 %	15 mins	8 Test/device Manufacturable at scale Mutation proof further optimisation possible

5.3.4 Fluorocarbon SAM Functionalisation

Due to a pause between experiments, some new optimisations had to be performed on the boards and reagents. These optimisations quickly narrowed down issues with PFDT SAM formation evidenced by large impedances on the order of MΩ instead of tens to hundreds of kΩ. This introduced significant noise in the measurements making circuit fitting difficult. The performance of the device at the ACE2 functionalisation stage was also compromised and experiments were done to investigate the source of errors in the assay data.

SAM formation using original reagents in toluene and ethanol

To investigate these issues the SAM forming process using the original reagents was explored in two diluents: the previously used toluene, and ethanol at various incubation times. These results were quantified firstly by the R_{ct} signals and the amount of noise in the Nyquist plots. Then ACE2 and target experiments were carried out to determine

if the formed SAMs were able to facilitate the detection process as before.

Figure 5.8A showed the R_{ct} percentage change (vs clean stage) response due to 1 mM PFDT incubated at room temperature for various times for both ethanol and toluene. After 1-minute toluene showed a 15 % R_{ct} increase while ethanol experienced a 400 % increase. This placed the toluene R_{ct} values in the range 0.9 - 2 kΩ and the ethanol values 8 - 14 kΩ (Figure 5.8B). As a reminder, the overnight incubation in toluene values for the previous experiments had values in the range 20 - 150 kΩ and was the desired target range to obtain. This range was achieved in 5 minutes for ethanol and 30 minutes for toluene. In general, both diluents displayed increasing R_{ct} values for every incubation time including overnight. The overnight values for toluene were in the range of 70 - 400 kΩ which was close to the desired range but was slightly higher. Ethanol ranged between 0.17 - 2 MΩ, this was too high and signal noise was evident in the Nyquist plots. From this information, it was apparent that ethanol facilitates denser SAM formation compared to toluene. This was in agreement with literature where ethanol was shown to form tightly packed SAMs [242]. From here the quality of the SAM was investigated by first incubating the overnight formed SAMs with ACE2 and then spike protein target as was done in the previous successful experiments.

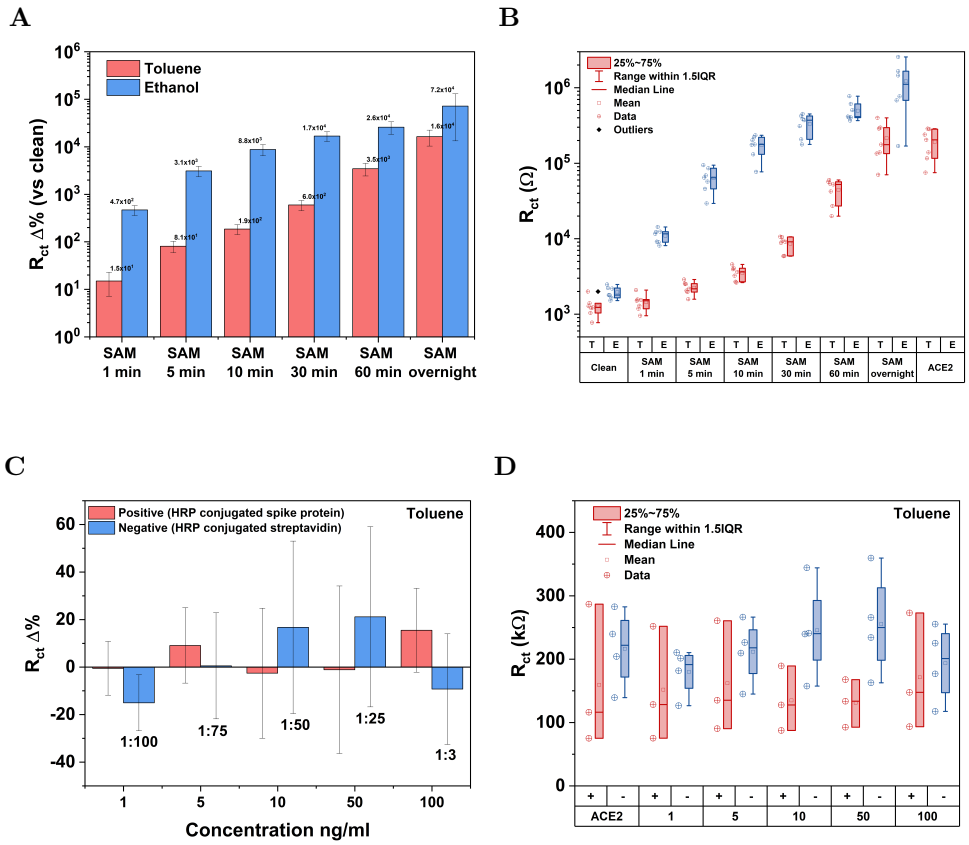

Figure 5.8: Bar chart showing the mean R_{ct} percentage change vs clean stage in response to the addition of 1 mM PFDT for various incubation times in ethanol and toluene (A). Box plot showing the R_{ct} values in response to addition of 1 mM PFDT for various incubation times in ethanol and toluene (B). Bar chart showing the mean R_{ct} percentage change vs ACE2 stage (toluene formed SAM) in response to the addition of various concentrations of SARS-CoV-2 HRP conjugated spike protein (positive) and HRP conjugated streptavidin (negative) (C). Streptavidin dilutions are shown under the corresponding columns. Box plot showing the R_{ct} values for the same conditions in (D). Ethanol EIS data could not be circuit fitted due to excess noise and therefore no bar or box plot available. n = 7 for all SAM data measurements for both ethanol and toluene. n = 3 for positive toluene target data and n = 4 for negative toluene data.

The ACE2 R_{ct} value slightly decreased compared to the overnight SAM signal for toluene. This was not the behaviour found in previous experiments which showed small to sizeable increases. This alludes to the issue of SAM quality and ACE2 degradation. If the SAM had degraded ACE2 adsorption would decline due to lack of suitable amphiphobic surface to interact. This would lead to minimal binding and the signal

would remain relatively unchanged as in (Figure 5.8B). Coincidentally if the SAM was suitable and the ACE2 had degraded such that the hydrophobic tail was ineffective the same results would occur. The evidence at this stage was not sufficient to confirm any hypothesis.

R_{ct} signal changes varied for both positive and negative data sets upon the addition of target sample. There were no likely differences between positive and negative groups or between the target and ACE2 responses (Figure5.8D). Previously it was found that there was almost always a likely difference between ACE2 and target responses as would be required for successful detection. The errors on these were also large and no discernible pattern was apparent (Figure 5.8C). This data confirmed the absence of specific binding of spike protein and produced a significant biofouling signal from the negative control. This was likely due to insufficient SAM formation diminishing its capacity to adsorb ACE2 and block surface biofouling.

Overnight incubations for both toluene and ethanol did not result in R_{ct} values the in desirable impedance range previously seen. As a result, formation of the SAMs at time frames corresponding to these desired R_{ct} values was investigated using the SAM formation times from Figure 5.8A. Ethanol was at the desired R_{ct} value range after 5 mins and toluene after 30 mins. The PCBs were subsequently incubated as before for these time durations. The resulting SAM R_{ct} values for ethanol were 21 - 162 kΩ and 8 - 13 kΩ for toluene. Toluene was unable to reach desired range, with ethanol better situated. To check the quality of these SAMs, ACE2 was again functionalised, the responses for both diluents showed the average R_{ct} percentage change decreased (Figure 5.9A). Toluene experienced a larger decrease -26 % than ethanol -7 %. This again did not follow the expected signal increases and was further evidence that there were issues with PFDT SAM formation. Large signal increases for the negative control and small percentage changes for the positive control (Figures 5.9B and C), demonstrated that the SAM was again not offering suitable anti-biofouling and a lack of ACE2 adsorption resulting in little specific spike protein binding.

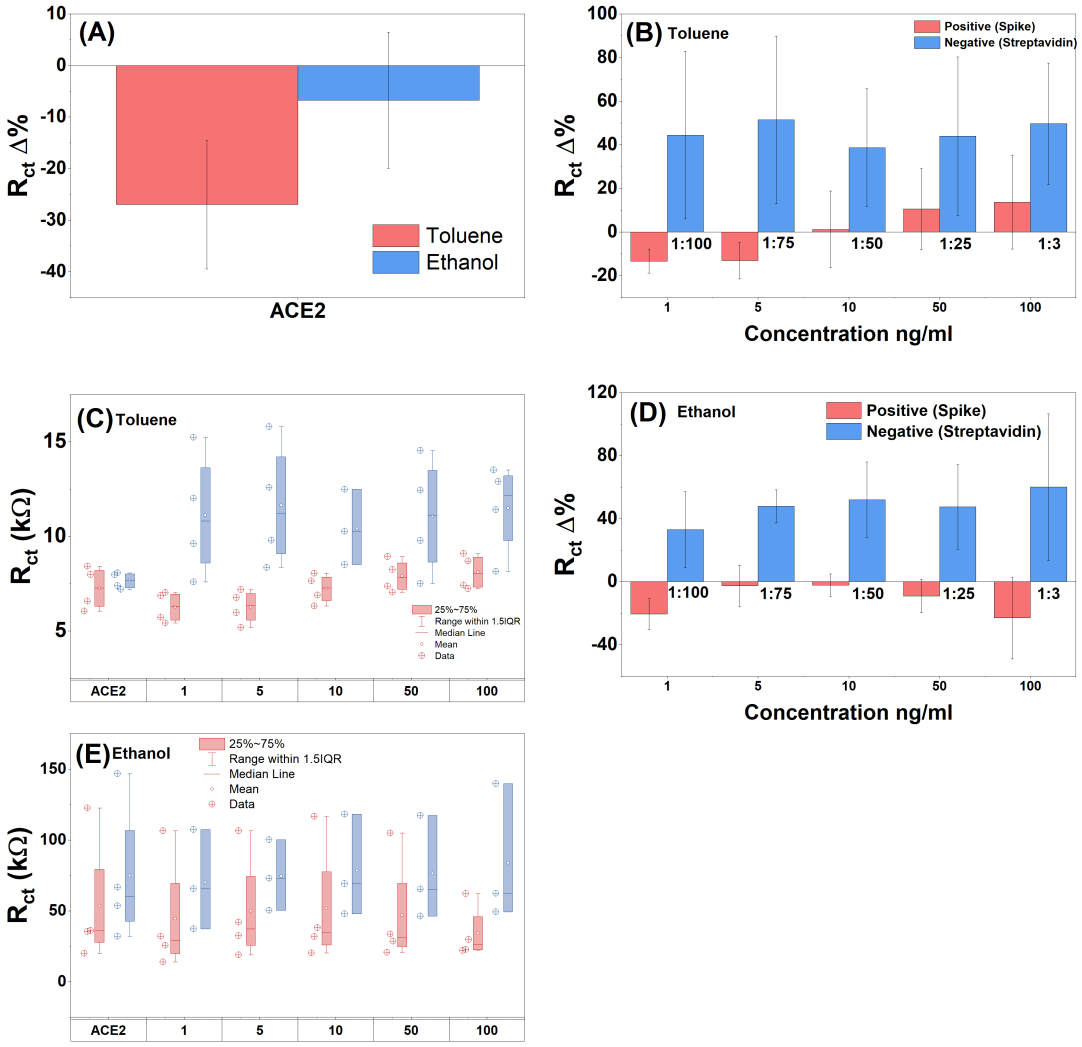

Figure 5.9: Bar chart showing the mean R_{ct} percentage change vs SAM stage in response to the addition of 1 μg/ml ACE2 for 1-hour incubation for the ethanol and toluene PFDT formed SAMs (A). Bar chart showing the mean R_{ct} percentage change vs ACE2 stage (toluene formed SAM) in response to the addition of various concentrations of SARS-CoV-2 HRP conjugated spike protein (positive) and HRP conjugated streptavidin (negative) (B). Corresponding raw R_{ct} data from (A) in box plot configuration (C). Bar chart showing the mean R_{ct} percentage change vs ACE2 stage (ethanol formed SAM) in response to the addition of various concentrations of SARS-CoV-2 HRP conjugated spike protein (positive) and HRP conjugated streptavidin (negative) (D). Corresponding raw R_{ct} data from (D) in box plot configuration (E). n = 8 for (A) and n = 4 for all other data.

Ethanol responses were similar with large negative signal increases however, all positive

signals decreased (Figures 5.9D and E). From the box plots (Figure 5.9C and E) it was apparent that none of the positive data for both ethanol and toluene diluents was likely different from the ACE2 stage and could not be confirmed as a detection. The negative responses for toluene were likely different from the ACE2 stage reinforcing the lack of performance on this PCB during the experiment. Ethanol negatives were not different but contributed a high negative response.

At this stage, there was sufficient evidence that PFDT was causing many issues and that ACE2 was a possible contributor to these problems. New PFDT and ACE2 were purchased. Investigating ethanol as a diluent was discontinued. Ethanol displayed the potential to be a suitable diluent and with further work should provide performance that offers the ability to work with a wider array of products due to its less destructive nature compared to toluene. Time constraints did not allow for its investigation to continue and toluene showed slightly improved performances and allowed for a more direct comparison to all the previous experiments.

SAM formation using refreshed reagents in toluene

With refreshed PFDT and ACE2 reagents acquired investigation into SAM formation and ACE2 adsorption was continued. In this iteration, incubation temperature dependence was explored. The experiments discussed at the beginning of this chapter were performed in a warm lab during the summer. When the experiments began to show a decline in responses, most were performed in a new lab that was susceptible to outside temperatures. At the time, the temperatures were lower due to it being autumn/winter. The incubation time chosen for these experiments was 45 minutes. This was from the evidence of the previous experiment where 30 minutes was not quite enough to elevate the R_{ct} values into the desired range for toluene. Overnight incubation was not investigated here as to dedicate full attention to properly exploring the suitability of quick SAM formation times. After 45 minute incubations in PFDT at 4 °C and 25 °C R_{ct} values for both temperature groups were found to be similar with 4 °C PCB ranging between 2 - 10 kΩ and 25 °C being between 3 - 14 kΩ (Figure 5.10A). There was no conclusive difference between these groups and as such could be concluded that for the

temperatures tested there was no significant temperature dependence for PFDT SAM formation. These R_{ct} ranges were close to that of the previous experiment with the original PFDT reagent. The extra time did not foster higher values and so it could not be concluded if the new PFDT resulted in better SAM performance. ACE2 incubation and target response would help determine this.

The normalised ACE2 (vs SAM) R_{ct} values for both temperature groups were also similar (Figure 5.10B). On average the 4 °C group had a slight decrease compared to the SAM and 25 °C group had a slight increase. The two groups were not likely different but were close to possible likeliness. Consequently for the temperatures tested there was no temperature dependence on ACE2 adsorption performance. These results also demonstrated an improved signal response due to ACE2 adsorption compared to the previous section displaying either a very minimal signal decreases or slight signal increase coming more in line with experiments before the pause in experiments. This was evidence that SAM was more suitably formed.

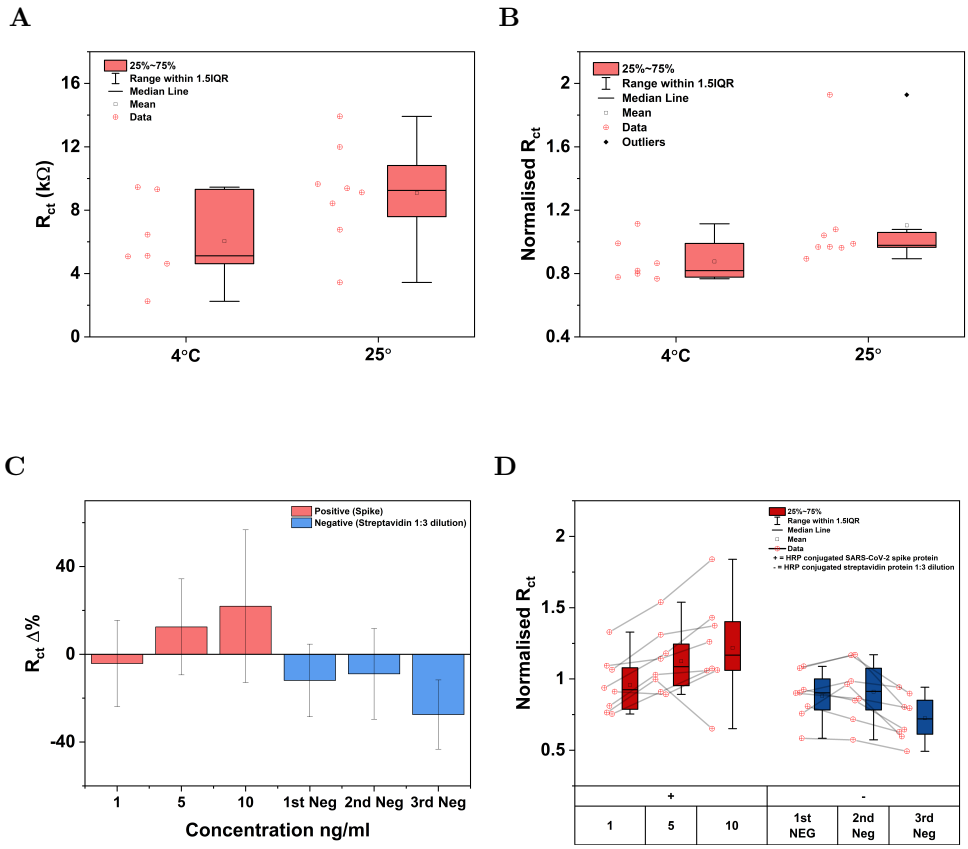

Figure 5.10: Box plot showing the raw R_{ct} values in response to addition of 1 mM PFDT for 45 minutes toluene at 4 °C and 25 °C (A). Box plot showing the normalised (vs SAM) R_{ct} values in response to addition of 1 μg/ml ACE2 for 1 hour incubation at 4 °C and 25 25 °C (B). Bar chart showing the mean R_{ct} percentage change vs ACE2 stage in response to addition of various concentrations of SARS-CoV-2 HRP conjugated spike protein (positive) and repeated incubations of 1:3 dilution HRP conjugated streptavidin (negative) (C). Corresponding normalised (vs ACE2) R_{ct} values (D). n = 8 for all data measurements.

Incubation's in the positive SARS-CoV-2 spike protein concentrations saw a return of the dose response (Figure 5.10C). The average R_{ct} percentage change began with a decrease at 1 ng/ml then increased for 5 and 10 ng/ml. The negative control was not incubated in different concentrations like previous experiments instead it was incubated in the strongest concentration 1:3 dilution multiple times. This made sample preparation easier and exposed the SAM to more extreme fouling conditions. This was decided due to time factors. If the SAM could demonstrate anti-biofouling responses for this

strong concentration over multiple incubations then it should have equal or better responses for smaller concentrations. The negative control showed a decrease in average R_{ct} percentage change response as had been seen in the earlier experiments. The first two incubations were consistent but the third saw a larger decrease. The 10 ng/ml positive control was likely different from all negative controls (Figure 5.10D). The box plots of the negative further showed the consistency of the first two incubations. From this experiment, it was concluded that the new PFDT and ACE2 improved the issues that were present in previous experiments. The SAM still did not appear to suitably form, evidenced by the negative responses and the errors present on both positive and negative controls. This was likely due to the quick SAM formation time not allowing for a uniform and densely packed SAM to facilitate improved ACE2 adsorption and anti-biofouling consistency.

Testing the new reagents after an overnight PFDT incubation showed that the SAM R_{ct} values were in the range of 3 - 6.2 kΩ for the positive PCB and 4 - 6 kΩ for the negative board (Figure 5.11A). Note that although the data in (Figure 5.11A) was split into positive and negative sections, the clean, SAM and ACE2 stages were all equally prepared using the same reagents, the labelling was a way to mark the boards for use at the target stage. These ranges were small and not within the range seen in the experiments before the pause. As was seen from the time dependence on SAM formation (Figure 5.8A) the SAM signals increase with time then after a certain point decrease during overnight incubation. This is in agreement with the literature that SAM formation is best achieved over a longer incubation to allow two stages of formation to take place. An initial quick stage that increases the impedance and then a longer reorganisation stage that takes tens of hours and that gives uniformity to the SAM (see Section1.8). This did not explain why the overnight of this experiment was so low compared to the summer experiments. The answer to this was discovered a few weeks after the SAM investigation came to an end. PFDT freezes at 15 °C, consequently, it was permanently frozen during storage in the lab. During the summer the temperature was sufficient to maintain PFDT as a liquid well above its freezing temperature, making it instantly usable. When the temperatures dropped during autumn a thawing process

was required before pipetting. This was initially done with a hot plate that raised the PFDT above its freezing point. It was using this procedure that SAM issues became apparent. It was later discovered that the PFDT was not sufficiently above the freezing temperature and would begin to freeze in the pipette resulting in poor injection volumes into the toluene diluent. In later experiments, the PFDT was raised to 25 °C then added to the toluene. Something that was standardised going forward. This resulted in a return to the previous summer R_{ct} ranges. So the critical aspect of SAM formation had been found to be the storage temperature for PFDT rather than the temperature of the incubation step in toluene.

Even though the SAM R_{ct} in this experiment were low their quality was investigated again using ACE2 and target incubations. The ACE2 R_{ct} values increased for both PCBs (Figure 5.11A). This was a return to the behaviour demonstrated during the successful summer experiments and was evidence that the SAM was optimally formed and the ACE2 was sufficiently adsorbing.

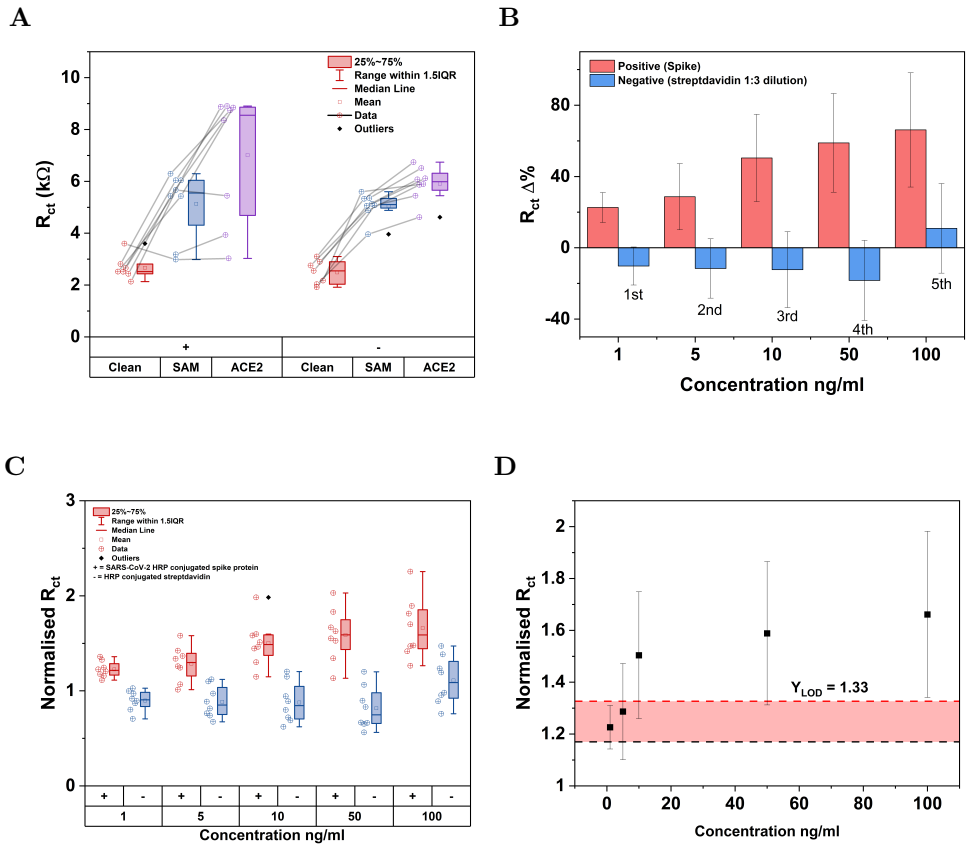

Figure 5.11: Box plot showing the raw R_{ct} values in response to clean. overnight 1 mM PFDT incubation forming SAM complex and 1 hour 1 μg/ml ACE2 incubation (A). Bar chart showing the mean R_{ct} percentage change vs ACE2 stage in response to the addition of various concentrations of SARS-CoV-2 HRP conjugated spike protein (positive) and repeated incubations of 1:3 dilution HRP conjugated streptavidin (negative) (B). Corresponding normalised (vs ACE2) R_{ct} values (C). Dose response curve for inactivated SARS-CoV-2 HRP conjugated spike protein (D). n = 8 for all data measurements.

After positive target incubation, the dose response was again apparent for all concentrations (Figure 5.11B). This showed that the ACE2 was present in the SAM and was binding the target spike protein. The negative average R_{ct} percentage changes were consistently negative for four of the incubations and positive for the fifth. This showed the anti-biofouling properties returned although with negative signal changes instead of positive ones in the previous summer. It was not possible to fully investigate the underlying explanation for the signal decreases observed with negative samples however, with

new reagents this might have been a new SAM behaviour becoming the new expected SAM response.

The results demonstrated a performance and consistency well beyond the intended operating scope. The box plot data showed that all positive data was likely different from the negative data indicating good specificity of the device. All incubations with negative samples were not likely different from one other with exception of the fifth incubation which was potentially likely different. This further reinforced the fact that the device consistently suppressed negative control responses. As a final analysis, the dose response curve was plotted (Figure 5.11D). The $Y_{LOD} = 1.33$ ($R^2 = 0.938$) which was in the region of the previous summer experiments. The first two positive concentrations lay inside this limit and the 10 and 50 ng/ml errors just overlap with this region suggesting the 1 and 5 ng/ml concentrations may be questionable and the 10 and 50 ng/ml are most likely fine but caution must be taken. The corresponding $Y_{LOD} = 4.94$ ng/ml was a couple of ng/ml off the values of the previous summer. This experiment demonstrated the PCBs return to the behaviour previously witnessed during earlier experiments. This was suitable evidence that the new reagents solved the decline in performance due to reagent degradation, bringing the sensor back to a consistent and functional level.

5.4 Conclusion

The preparation and testing of an uncomplicated and straightforwardly produced electrochemical biosensor for SARS-CoV-2 were demonstrated. The sensor consisted of a base SAM composed entirely of PFDT with ACE2 amphiphobically absorbed into the layer. It was possible, using solutions of HRP-conjugated spike protein (positive) and HRP conjugated streptavidin and IL-6 (negatives) to detect the viral spike protein in a sensitive, specific and dose-dependant manner. Detection and discrimination of inactivated SARS-CoV-2 virus present in a complex medium (cell culture lysate from a clinical respiratory assay validation kit) was demonstrated to confirm the PFDT-ACE2 layer provided the sensitivity, specificity and resistance to biological fouling necessary for a useful biosensor for SARS-CoV-2. The lower signal change and saturation effect from

negative samples demonstrated weak interaction with the PFDT-ACE2 layer. VPSS clinical samples showed a significant difference from the negative control p = 1.22E-7. VTM samples showed some significant differences P = 1.089E-4 with preliminary results of sensitivity = 80 % and specificity = 67 % with one data point preventing 100 % for both. The sensor was shown to be clinically relevant and comparable to other devices reported in the literature. These results were obtained at room temperature 30 minutes after each sample was presented to the sensor. There was every confidence the time to result could be easily reduced to 5 minutes and even better discrimination between positive and negative samples with further optimisation. This biosensor showed an impressive performance at detecting all SARS-CoV-2 elements and the virus itself against multiple negative controls, a renewal of reagents changing the SAM behaviour midway through experiments and with limited resources and manpower in a very short period of time.

Biosensors offer an enticing route to sensitive and low cost detection of biological analytes, with the glucose biosensor being a prominent example allowing quick and easy monitoring of blood glucose levels. Facilities that can mass manufacture very large quantities of these sensors produce millions of sensors per day. This results in unit costs of 20 UK pence [243]. There are few diagnostic technologies able to match this performance and value. In contrast, the biosensor demonstrated in this work required a simple two-stage preparation of 1) PFDT immobilisation on low cost PCB electrodes and 2) ACE2 adsorption into the PFDT. These stages are compatible with current glucose sensor manufacturing protocols, providing rapid translation to a glucose sensor format. This allows for a low cost mutation proof Covid-19 assay utilising CE marked materials and measurement devices to be widely and rapidly distributed for point of care testing.

Chapter 6

Conclusions and Future Work

The goal of this thesis was to enhance the understanding and performance of electrochemical biosensors in detecting pathogens causing sepsis and hyperinflammation. Chapters 2 and 3lay the groundwork for an electrochemical biosensor by discovering a suitable sensor platform to undergo biofunctionalisation. The work in Chapter 2 investigated the potential sensitivity, signal to noise ratio, and sample volume improvements that microelectrodes offer. Using 25 μm diameter glass pulled microelectrodes an optimal cleaning protocol of acid piranha submersion followed by fine mechanical polishing of decreasing alumina powder grit sizes (0.3, 0.1 and 0.05 mm) was shown. Electrochemical detection of DNA employed two methods: 1) A ssDNA probe-MCH SAM based surface modification where both probe and MCH were covalently bonded to the electrode surface. 2) PFDT fluorous SAM modified surface that facilitated binding of probe DNA modified with a fluorous ponytail via the fluorous effect. In agreement with the literature, it was found that establishing reliable and repeatable SAM formation, leading to consistent changes when challenged with target DNA was difficult. At this point, the decision was made to advance onto a PCB platform because of the advantages associated with these systems. The fluorous SAM work provided some optimism with the potential for reuse by removal of probe and target via solvent washing and subsequent probe re-functionalisation and target hybridisation. Microelectrodes undermined the quality of these results and revisiting this fluorous DNA work using PCBs would

be very beneficial. In Chapter 4, custom fabricated microelectrodes were examined. These showed an improvement over the glass pulled microelectrodes but suffered from fabrication issues that ultimately lead to poor performances. This work determined that microelectrodes were difficult to operate for DNA biosensing under the conditions tested.

In Chapter 3, attempts were made to make electrochemical biosensing more streamlined by developing a plug and play electrode format that not only simplified operational use but increased the number of testable electrodes. This was achieved by examining multiple custom PCB designs with various gold plating and preconditioning techniques. The optimal custom PCB design used a combination of electroless plating and electroplating followed by a 10-second submerging in acid piranha (Figure 3.1C). The increased electrode number (n = 8) contributed better statistical information and provided some promising DNA biosensor results. This design was not chosen as a suitable biosensor platform as it was unable to consistently give good responses. This was due to issues with gold coverage on the electrode surface. With more time to optimise the gold plating process, this sensor would have achieved consistent performances, but with pressing time constraints, it was decided to move to a commercially available device which became available during the course of this research. The PCB produced by BIOTIP was employed as the biosensing platform to facilitate pathogen detection as it demonstrated consistent cleaning responses and good initial DNA sensing results.

Future work for these two chapters could continue to examining glass pulled microelectrodes to improve performances and continue optimisation of the gold plating process on the custom PCB. However, a more ambitious but achievable goal would be to combine the custom PCB format with a microelectrode system. Improvement of the gold plating procedure could be realised by employing a hard gold plating technique (nickel sub-layer) on the PCB. This was hypothesised to be a contributing factor to the consistency issues and should help solve that problem. Secondly, shrink the electrodes to a microelectrode level ($< 30\ \mu$m). A company has already been identified with the ability to produce 30-micron feature sizes on PCBs. If these two milestones were realised, then

it would be beneficial to increase the number of electrodes on the device, a distinct advantage of using microelectrodes. This would allow for a Lab-on-Chip device, basically a panel of tests that can be run consecutively. If voltammetric testing was utilised then these tests can take advantage of the microelectrodes ability to facilitate very fast CV, DPV and SWV allowing for rapid testing. Multiple pathogen recognition elements, biomarker recognition and susceptibility testing are a few examples of assays that could be potentially present on a single Lab-on-Chip device.

Chapters 4 and 5 took the work from the previous chapters and developed DNA and enzymatic biosensors on the chosen PCB device. In Chapter 4 a *S. pneumoniae* DNA biosensor was developed using a ssDNA probe-MCP SAM functionalised on the electrode surface as a recognition element for target sequences. The target sequences were taken from a section of DNA encoding the major autolysin (*lytA*) gene. This was firstly achieved by using a 20 bp complementary target sequence diluted in PBS. This was then increased to a 235 bp sequence by amplifying *S. pneumoniae* genomic DNA. This was detected in both PBS and human serum. For human serum detection, the sensor was able to demonstrate a dose response and a minimum detection concentration of 1 pM (smallest concentration tested) in 15 minutes at room temperature. The sensor was also able to discriminate the *lytA* sequence from a 115 bp OXA (*E. coli*) sequence negative control. Clinically relevant levels of DNA are likely at the attomolar level. These levels were not tested, but if the sensor was unable to directly detect such small amounts of DNA then PCR amplification could be incorporated. This was already shown to work as PCR amplification used to create the 235 bp DNA sequence. From the amplification times required in the creation of these sequences, it was estimated that a sensor utilising this format would be able to successfully detect *S. pneumoniae* in under 2 hours. This was a quicker, simpler and more sensitive device than a similar *lytA* biosensor [213].

Future work for this device would benefit from examining lower *lytA* concentrations in human serum to determine if attomolar level detection is possible. If not possible, then development of a PCR step perhaps even incorporated on the PCB itself would be desirable. Blood purification methods using specialist PCR kits rather than regular

PCR methods could reduce complexity and improve sensitivity of the device for clinical sample use. Detection of full genomic DNA and then clinical samples would then follow. If it could be determined that DNA hybridisation rapidly then reducing the 15-minute incubation time could be easily achieved.

The work in Chapter 5 brought together concepts and information from all previous chapters to develop a SARS-CoV-2 electrochemical enzymatic biosensor in a matter of a few months at the behest of the Chief Scientist Office of Scotland. Experience dealing with biological material and difficulties encountered with complex diluents was further developed from the basis established in Chapter 4. The PCB platform discovered and optimised in Chapter 3 was employed as the sensor platform to investigate SARS-CoV-2 detection. The PFDT fluorous SAM used on the microelectrodes in Chapter 2 was employed to form a dense amphiphobic layer that was conducive to hydrophobic physisorption of ACE2. By amalgamating all the previous work, this biosensor was able to demonstrate a dose response to recombinant HRP conjugated spike proteins and inactivated virus samples in a complex human medium. Discrimination between spike protein and, IL-6 and HRP conjugated streptavidin negative controls (both at concentrations beyond what is experimentally used and levels found in the body) was seen. Discrimination between inactivated virus and a blank negative solution containing human cells and proteins were also found. The results showed specific binding between ACE2 and targets while also displaying strong anti-biofouling properties of the PFDT SAM. Finally, the biosensor was able to demonstrate significant differences between positive and negative clinical samples in VPSS P = 1.22E-7 and VTM P = 1.089E-4. Preliminary calculations gave a sensitivity = 80 % and specificity = 67 %. Only one data point prevented both sensitivity and specificity from being 100 %. The clinical samples had also been freeze/thawed multiple times and spent 6 weeks in the fridge. As a result, these samples likely experienced degradation affecting the results.

Future work for this biosensor could include further optimisation of the PFDT SAM by employing a less aggressive (toluene dissolves many types of plastics used in sensor development) diluent, for example, ethanol. Migrating the fluorous surface modifications

onto a more manufacturable glucose like electrode system would ready the sensor for mass production and quicker deployment. This should not be difficult as this surface chemistry was designed with this in mind. Adding extra assays for detection of cold, flu and protein biomarkers would make the device even more versatile at excluding COVID related patients with the common ailments that mimic the disease.

Overall, the work carried out was fruitful and informative. Key findings from the thesis were:

1. Microelectrodes were difficult to operate for DNA biosensing under the conditions tested.
2. The fluorous DNA chemistry showed promise for the development of easily functionalised and regenerable biosensor surfaces.
3. The PCB format produced a well functioning DNA biosensor without the variation and unusual signal behaviours seen from microelectrodes.
4. The fluorous PFDT SAM layer developed proved to be an effective vehicle for rapid immobilisation of ACE2 and led to the development of a novel biosensor for SARS-CoV-2.

Important sub findings were:

1. Variation is a significant issue in SAM based DNA biosensors as evidenced by the bar charts and signal spreads produced in this work.
2. Clinical samples introduce further complexity in terms of signal changes and variation but the sensors developed for *S. pneumoniae* and SARS-CoV-2 were able to be measured successfully in complex samples.

Through combination of fluorous surface modification and a PCB sensor array, two biosensor systems which could be useful for the detection of sepsis and SAR-CoV-2 were produced.

Appendix A

Examining Microelectrodes as a Sensor Platform

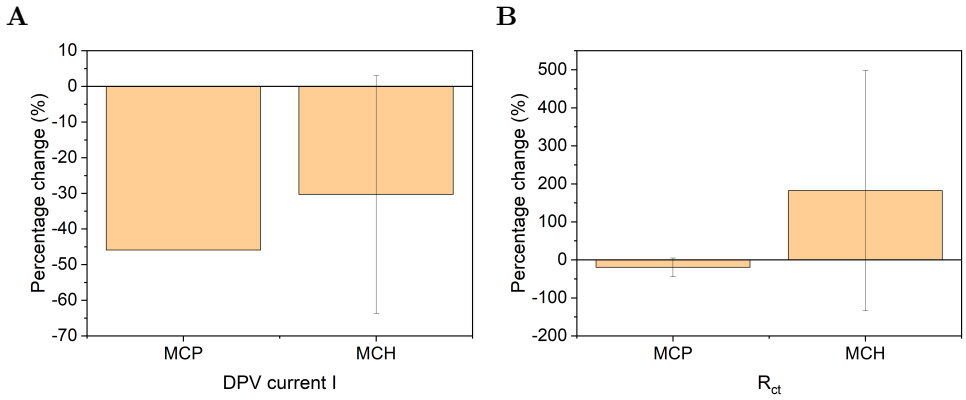

Figure A.1: DPV signal percentage change between clean electrode surface and the two SAM treatments MCP and MCH on microelectrode (A). The corresponding EIS signal percentage change (B). (E_{dc} vs OCP = 0.0 V, frequency range: 0.1 Hz to 100 kHz). Measurements taken in redox buffer 1 (vs platinum). n = 1 for MCP (electrode failure) and n = 2 for MCH

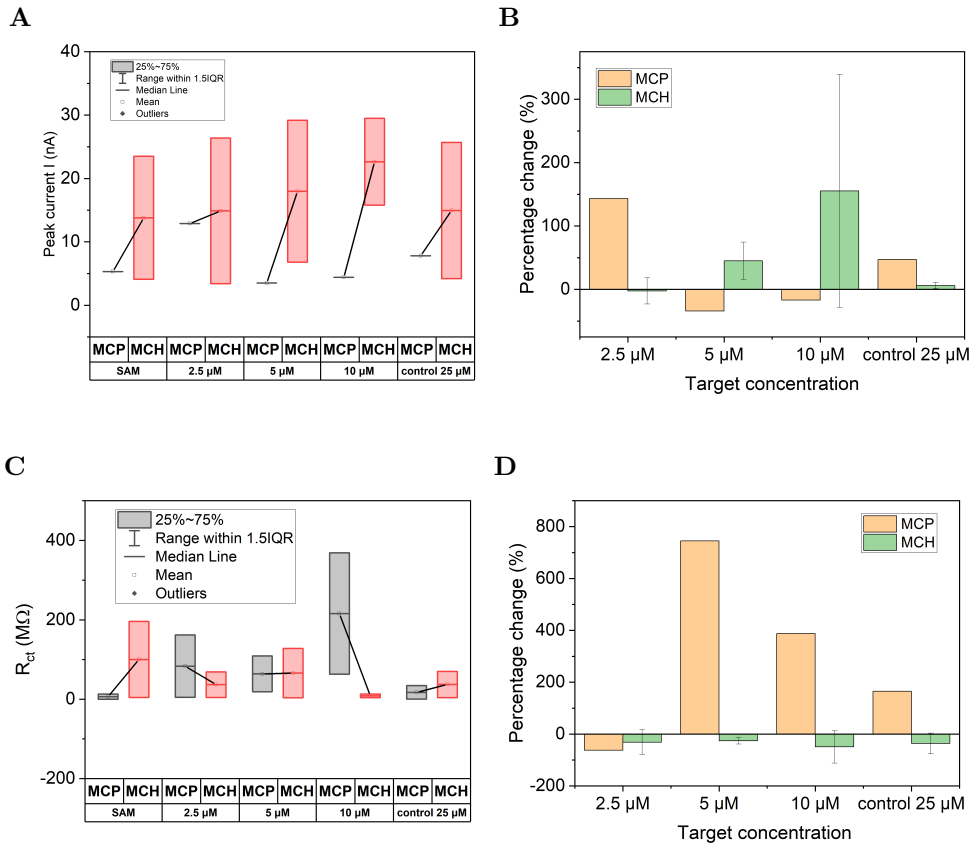

Figure A.2: Box chart of MCP and MCH data for SAM, 2.5 μM, 5 μM, 10 μM and control stages (A), DPV signal percentage changes for target DNA stages vs SAM stage (B) corresponding EIS box chart data (C) and EIS signal percent change (D). Measurements taken in redox buffer 1. EIS settings (E_{dc} vs OCP = 0.0 V, frequency range: 0.1 Hz to 100 kHz). (Vs platinum). Note MCP n =1 for both DPV and EIS. MCH n = 2 for both.

Appendix B

Printed Circuit Boards as Biosensors

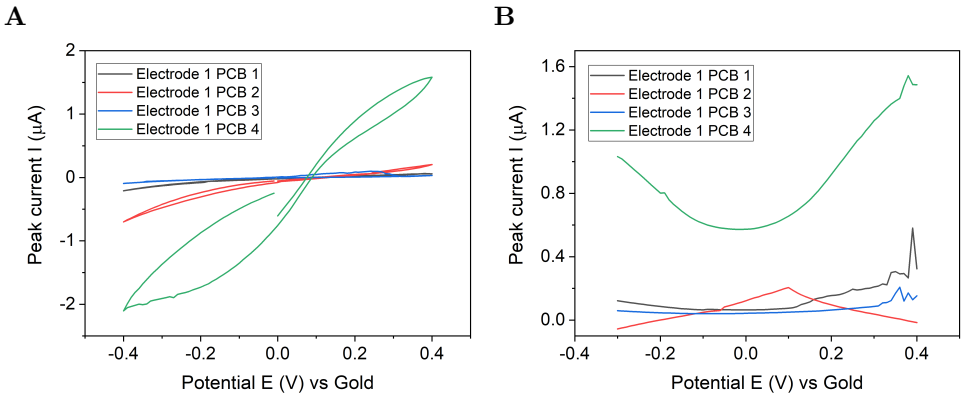

Figure B.1: CV response of PCB P2 (A), DPV response (B) to fresh out of the box PCB P2 boards (no cleaning). Measurements taken in 5 mM redox buffer. Note that it is one electrode from each board

Appendix C

Electrochemical Detection of *S. pneumoniae*

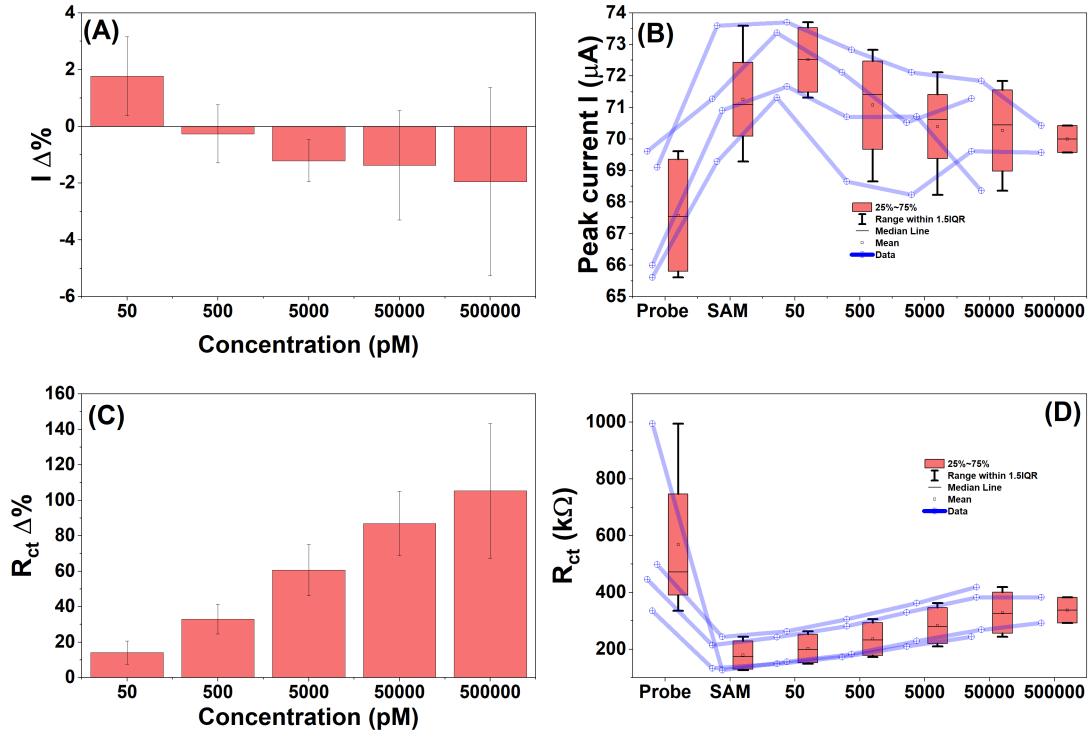

Figure C.1: *lytA* complementary 20 bp target response on macroelectrodes using MCP. Mean DPV peak current percentage change in response to increasing target concentration (A). The corresponding DPV peak current raw data (B). Mean R_{ct} percentage change in response to increasing target concentration (C). The corresponding R_{ct} raw data (D). 1 mM redox buffer (redox buffer 1 Table 4.2) n = 4

Appendix D

Electrochemical Detection of SARS-CoV-2

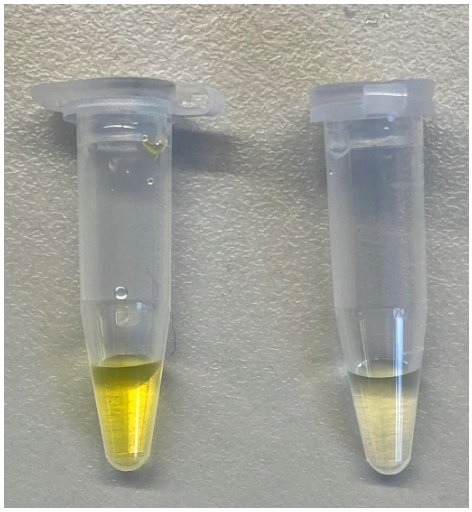

Figure D.1: Visual discrimination between the positive HRP conjugated spike protein (Left) and the HRP conjugated streptavidin (Right). Evidencing the strong binding affinity of the spike protein and the strong anti-biofouling properties of the fluorous SAM.

References

[1] Bone RC, Balk RA, Cerra FB, Dellinger RP, Fein AM, Knaus WA, et al. Definitions for sepsis and organ failure and guidelines for the use of innovative therapies in sepsis. Chest. 1992;101(6):1644–1655.

[2] Levy MM, Fink MP, Marshall JC, Abraham E, Angus D, Cook D, et al. 2001 sccm/esicm/accp/ats/sis international sepsis definitions conference. Intensive Care Medicine. 2003;29(4):530–538.

[3] Singer M, Deutschman CS, Seymour CW, Shankar-Hari M, Annane D, Bauer M, et al. The third international consensus definitions for sepsis and septic shock (sepsis-3). JAMA. 2016;315(8):801–810.

[4] van der Poll T, van de Veerdonk FL, Scicluna BP, Netea MG. The immunopathology of sepsis and potential therapeutic targets. Nature Reviews Immunology. 2017;17(7):407.

[5] Angus DC, Linde-Zwirble WT, Lidicker J, Clermont G, Carcillo J, Pinsky MR. Epidemiology of severe sepsis in the United States: analysis of incidence, outcome, and associated costs of care. Critical Care Medicine. 2001;29(7):1303–1310.

[6] Weiss SL, Fitzgerald JC, Pappachan J, Wheeler D, Jaramillo-Bustamante JC, Salloo A, et al. Global epidemiology of pediatric severe sepsis: the sepsis prevalence, outcomes, and therapies study. American Journal of Respiratory and Critical Care Medicine. 2015;191(10):1147–1157.

[7] Rudd KE, Johnson SC, Agesa KM, Shackelford KA, Tsoi D, Kievlan DR, et al.

Global, regional, and national sepsis incidence and mortality, 1990–2017: analysis for the Global Burden of Disease Study. The Lancet. 2020;395(10219):200–211.

[8] Martin GS, Mannino DM, Eaton S, Moss M. The epidemiology of sepsis in the United States from 1979 through 2000. New England Journal of Medicine. 2003;348(16):1546–1554.

[9] Kumar G, Kumar N, Taneja A, Kaleekal T, Tarima S, McGinley E, et al. Nationwide trends of severe sepsis in the 21st century (2000-2007). Chest Journal. 2011;140(5):1223–1231.

[10] Zimmerman JE, Kramer AA, Knaus WA. Changes in hospital mortality for United States intensive care unit admissions from 1988 to 2012. Critical Care. 2013;17(2):R81.

[11] Hospital Admitted Patient Care Activity, 2016-17 [Online monograph]. NHS Digital; 2017 [cited 14/10/2017]. Available from: `https://digital.nhs.uk/catalogue/PUB30098`.

[12] Summary Hospital-level Mortality Indicator (SHMI) - Deaths associated with hospitalisation, England, April 2016 - March 2017 [Online monograph]. NHS Digital; 2017 [cited 14/10/2017]. Available from: `https://digital.nhs.uk/catalogue/PUB30092`.

[13] Sepsis affects 260,000 people every year [Online monograph]. The UK Sepsis Trust; 2017 [cited 14/10/2017]. Available from: `https://sepsistrust.org/`.

[14] covid-19-recovery-response [Online monograph]. The UK Sepsis Trust; 2020 [cited 18/01/2021]. Available from: `https://sepsistrust.org/covid-19-recovery-response/`.

[15] Vincent JL, Moreno R, Takala J, Willatts S, De Mendonça A, Bruining H, et al. The SOFA (Sepsis-related Organ Failure Assessment) score to describe organ dysfunction/failure. Intensive Care Medicine. 1996;22(7):707–710.

[16] Churpek MM, Snyder A, Han X, Sokol S, Pettit N, Howell MD, et al. qSOFA,

SIRS, and early warning scores for detecting clinical deterioration in infected patients outside the ICU. Am J Respir Crit Care Med. 2016;195(7):906–911.

[17] Mellhammar L, Linder A, Tverring J, Christensson B, Boyd JH, Sendi P, et al. NEWS2 is superior to qSOFA in detecting sepsis with organ dysfunction in the emergency department. Journal of Clinical Medicine. 2019;8(8):1128.

[18] Hecker A, Uhle F, Schwandner T, Padberg W, Weigand M. Diagnostics, therapy and outcome prediction in abdominal sepsis: current standards and future perspectives. Langenbeck's Archives of Surgery. 2014;399(1):11–22.

[19] Sepsis: recognition, diagnosis and early management management NICE guideline [Online monograph]. NICE; 2017 [cited 20/10/2017]. Available from: `https://www.nice.org.uk/guidance/ng51`.

[20] Lee A, Mirrett S, Reller LB, Weinstein MP. Detection of bloodstream infections in adults: how many blood cultures are needed? Journal of Clinical Microbiology. 2007;45(11):3546–3548.

[21] Dellinger RP, Levy MM, Rhodes A, Annane D, Gerlach H, Opal SM, et al. Surviving Sepsis Campaign: international guidelines for management of severe sepsis and septic shock, 2012. Intensive Care Medicine. 2013;39(2):165–228.

[22] Vincent JL, Sakr Y, Sprung CL, Ranieri VM, Reinhart K, Gerlach H, et al. Sepsis in European intensive care units: results of the SOAP study. Critical Care Medicine. 2006;34(2):344–353.

[23] Raad I, Hanna H, Maki D. Intravascular catheter-related infections: advances in diagnosis, prevention, and management. The Lancet Infectious Diseases. 2007;7(10):645–657.

[24] Peralta G, Rodríguez-Lera MJ, Garrido JC, Ansorena L, Roiz MP. Time to positivity in blood cultures of adults with *Streptococcus pneumoniae* bacteremia. BMC Infectious Diseases. 2006;6(1):79.

[25] Shah SS, Downes KJ, Elliott MR, Bell LM, McGowan KL, Metlay JP. How long

does it take to “rule out” bacteremia in children with central venous catheters? Pediatrics. 2008;121(1):135–141.

[26] Leggieri N, Rida A, Francois P, Schrenzel J. Molecular diagnosis of bloodstream infections: planning to (physically) reach the bedside. Current Opinion in Infectious Diseases. 2010;23(4):311–319.

[27] Afshari A, Schrenzel J, Ieven M, Harbarth S. Bench-to-bedside review: Rapid molecular diagnostics for bloodstream infection-a new frontier? Critical Care. 2012;16(3):222.

[28] Donelli G, Vuotto C, Mastromarino P. Phenotyping and genotyping are both essential to identify and classify a probiotic microorganism. Microbial Ecology in Health and Disease. 2013;24(1):20105.

[29] Brenner DJ, Fanning GR, Rake AV, Johnson KE. Batch procedure for thermal elution of DNA from hydroxyapatite. Analytical Biochemistry. 1969;28:447–459.

[30] Ley JD, Cattoir H, Reynaerts A. The quantitative measurement of DNA hybridization from renaturation rates. The FEBS Journal. 1970;12(1):133–142.

[31] Crosa JH, Brenner DJ, Falkow S. Use of a single-strand specific nuclease for analysis of bacterial and plasmid deoxyribonucleic acid homo-and heteroduplexes. Journal of Bacteriology. 1973;115(3):904–911.

[32] Takayuki Ezaki EY Yasuhiro Hashimoto. Fluorometric deoxyribonucleic acid-deoxyribonucleic acid hybridization in microdilution wells as an alternative to membrane filter hybridization in which radioisotopes are used to determine genetic relatedness among bacterial strains. International Journal of Systematic and Evolutionary Microbiology. 1989;39(3):224–229.

[33] Vaneechoutte M, Rossau R, De Vos P, Gillis M, Janssens D, Paepe N, et al. Rapid identification of bacteria of the *Comamonadaceae* with amplified ribosomal DNA-restriction analysis (ARDRA). FEMS Microbiology Letters. 1992;93(3):227–233.

[34] Collins M, Rodrigues U, Ash C, Aguirre M, Farrow J, Martinez-Murcia A, et al.

Phylogenetic analysis of the genus *Lactobacillus* and related lactic acid bacteria as determined by reverse transcriptase sequencing of 16S rRNA. FEMS Microbiology Letters. 1991;77(1):5–12.

[35] Hertel C, Ludwig W, Pot B, Kersters K, Schleifer KH. Differentiation of *lactobacilli* occurring in fermented milk products by using oligonucleotide probes and electrophoretic protein profiles. Systematic and Applied Microbiology. 1993;16(3):463–467.

[36] Gürtler V, Stanisich VA. New approaches to typing and identification of bacteria using the 16S-23S rDNA spacer region. Microbiology. 1996;142(1):3–16.

[37] Woese C, Stackebrandt E, Macke T, Fox G. A phylogenetic definition of the major eubacterial taxa. Systematic and Applied Microbiology. 1985;6(2):143–151.

[38] Woese CR. Bacterial evolution. Microbiological Reviews. 1987;51(2):221.

[39] Schwartz DC, Cantor CR. Separation of yeast chromosome-sized DNAs by pulsed field gradient gel electrophoresis. Cell. 1984;37(1):67–75.

[40] Tenover FC, Arbeit RD, Goering RV, Mickelsen PA, Murray BE, Persing DH, et al. Interpreting chromosomal DNA restriction patterns produced by pulsed-field gel electrophoresis: criteria for bacterial strain typing. Journal of Clinical Microbiology. 1995;33(9):2233.

[41] Janssen P, Coopman R, Huys G, Swings J, Bleeker M, Vos P, et al. Evaluation of the DNA fingerprinting method AFLP as a new tool in bacterial taxonomy. Microbiology. 1996;142(7):1881–1893.

[42] Tonolla M, Benagli C, Rossi V, Fragoso C, Petrini O. MALDI-TOF MS: a new laboratory option for the diagnosis of clinical infections. Pipette. 2010;3:6–10.

[43] Singhal N, Kumar M, Kanaujia PK, Virdi JS. MALDI-TOF mass spectrometry: an emerging technology for microbial identification and diagnosis. Frontiers in microbiology. 2015;6:791.

[44] Arnaud C, Burger F, Steffens S, Veillard NR, Nguyen TH, Trono D, et al. Statins

reduce interleukin-6–induced C-reactive protein in human hepatocytes. Arteriosclerosis, Thrombosis, and Vascular Biology. 2005;25(6):1231–1236.

[45] Peisajovich A, Marnell L, Mold C, Du Clos TW. C-reactive protein at the interface between innate immunity and inflammation. Expert Review of Clinical Immunology. 2008;4(3):379–390.

[46] ten Oever J, Tromp M, Bleeker-Rovers CP, Joosten LA, Netea MG, Pickkers P, et al. Combination of biomarkers for the discrimination between bacterial and viral lower respiratory tract infections. Journal of Infection. 2012;65(6):490–495.

[47] Haran JP, Beaudoin FL, Suner S, Lu S. C-reactive protein as predictor of bacterial infection among patients with an influenza-like illness. The American Journal of Emergency Medicine. 2013;31(1):137–144.

[48] Povoa P, Almeida E, Moreira P, Fernandes A, Mealha R, Aragao A, et al. C-reactive protein as an indicator of sepsis. Intensive Care Medicine. 1998;24(10):1052–1056.

[49] Lelubre C, Anselin S, Zouaoui Boudjeltia K, Biston P, Piagnerelli M. Interpretation of C-reactive protein concentrations in critically ill patients. BioMed Research International. 2013;2013.

[50] Greenberg SB. Infections in the immunocompromised rheumatologic patient. Critical Care Clinics. 2002;18(4):931–956.

[51] Ansar W, Ghosh S. C-reactive protein and the biology of disease. Immunologic Research. 2013;56(1):131–142.

[52] Morgenthaler N, Struck J, Chancerelle Y, Weglöhner W, Agay D, Bohuon C, et al. Production of procalcitonin (PCT) in non-thyroidal tissue after LPS injection. Hormone and Metabolic Research. 2003;35(05):290–295.

[53] Nylen ES, Whang KT, Snider RH, Steinwald PM, White JC, Becker KL. Mortality is increased by procalcitonin and decreased by an antiserum reactive to

procalcitonin in experimental sepsis. Critical Care Medicine. 1998;26(6):1001–1006.

[54] Meisner M. Update on procalcitonin measurements. Annals of Laboratory Medicine. 2014;34(4):263.

[55] Prucha M, Bellingan G, Zazula R. Sepsis biomarkers. Clinica Chimica Acta. 2015;440:97–103.

[56] Rhodes A, Evans LE, Alhazzani W, Levy MM, Antonelli M, Ferrer R, et al. Surviving sepsis campaign: international guidelines for management of sepsis and septic shock: 2016. Intensive Care Medicine. 2017;43(3):304–377.

[57] Assink-de Jong E, De Lange DW, Van Oers JA, Nijsten MW, Twisk JW, Beishuizen A. Stop Antibiotics on guidance of Procalcitonin Study (SAPS): a randomised prospective multicenter investigator-initiated trial to analyse whether daily measurements of procalcitonin versus a standard-of-care approach can safely shorten antibiotic duration in intensive care unit patients-calculated sample size: 1816 patients. BMC Infectious Diseases. 2013;13(1):178.

[58] Kitamura K, Kangawa K, Eto T. Adrenomedullin and PAMP: discovery, structures, and cardiovascular functions. Microscopy research and Technique. 2002;57(1):3–13.

[59] Brain SD, Grant AD. Vascular actions of calcitonin gene-related peptide and adrenomedullin. Physiological Reviews. 2004;84(3):903–934.

[60] Struck J, Tao C, Morgenthaler NG, Bergmann A. Identification of an adrenomedullin precursor fragment in plasma of sepsis patients. Peptides. 2004;25(8):1369–1372.

[61] Önal U, Valenzuela-Sánchez F, Vandana KE, Rello J. Mid-regional pro-adrenomedullin (MR-proADM) as a biomarker for sepsis and septic shock: narrative review. In: Healthcare. vol. 6. Multidisciplinary Digital Publishing Institute; 2018. p. 110.

[62] Buendgens L, Yagmur E, Ginsberg A, Weiskirchen R, Wirtz T, Jhaisha SA, et al. Midregional Proadrenomedullin (MRproADM) Serum Levels in Critically Ill Patients Are Associated with Short-Term and Overall Mortality during a Two-Year Follow-Up. Mediators of Inflammation. 2020;2020.

[63] Franco DM, Arevalo-Rodriguez I, i Figuls MR, Zamora J. Interleukin-6 for diagnosis of sepsis in critically ill adult patients. The Cochrane Database of Systematic Reviews. 2015;2015(7).

[64] Hack CE, Hart M, Van Schijndel R, Eerenberg A, Nuijens J, Thijs L, et al. Interleukin-8 in sepsis: relation to shock and inflammatory mediators. Infection and Immunity. 1992;60(7):2835–2842.

[65] Sarris AH, Kliche KO, Pethambaram P, Preti A, Tucker S, Jackow C, et al. Interleukin-10 levels are often elevated in serum of adults with Hodgkin's disease and are associated with inferior failure-free survival. Annals of Oncology. 1999;10(4):433–440.

[66] Heper Y, Akalın E, Mıstık R, Akgöz S, Töre O, Göral G, et al. Evaluation of serum C-reactive protein, procalcitonin, tumor necrosis factor alpha, and interleukin-10 levels as diagnostic and prognostic parameters in patients with community-acquired sepsis, severe sepsis, and septic shock. European Journal of Clinical Microbiology and Infectious Diseases. 2006;25(8):481–491.

[67] Kellum JA, Kong L, Fink MP, Weissfeld LA, Yealy DM, Pinsky MR, et al. Understanding the inflammatory cytokine response in pneumonia and sepsis: results of the Genetic and Inflammatory Markers of Sepsis (GenIMS) Study. Archives of Internal Medicine. 2007;167(15):1655–1663.

[68] Wong HR, Cvijanovich N, Wheeler DS, Bigham MT, Monaco M, Odoms K, et al. Interleukin-8 as a stratification tool for interventional trials involving pediatric septic shock. American Journal of Respiratory and Critical Care Medicine. 2008;178(3):276–282.

[69] Prucha M, Herold I, Zazula R, Dubska L, Dostal M, Hildebrand T, et al. Signifi-

cance of lipopolysaccharide-binding protein (an acute phase protein) in monitoring critically ill patients. Critical Care. 2003;7(6):R154.

[70] Lamping N, Dettmer R, Schröder N, Pfeil D, Hallatschek W, Burger R, et al. LPS-binding protein protects mice from septic shock caused by LPS or gram-negative bacteria. Journal of Clinical Investigation. 1998;101(10):2065.

[71] Zweigner J, Gramm HJ, Singer OC, Wegscheider K, Schumann RR. High concentrations of lipopolysaccharide-binding protein in serum of patients with severe sepsis or septic shock inhibit the lipopolysaccharide response in human monocytes. Blood. 2001;98(13):3800–3808.

[72] Villar J, Pérez-Méndez L, Espinosa E, Flores C, Blanco J, Muriel A, et al. Serum lipopolysaccharide binding protein levels predict severity of lung injury and mortality in patients with severe sepsis. PLOS ONE. 2009;4(8):e6818.

[73] Tschaikowsky K, Hedwig-Geissing M, Schmidt J, Braun GG. Lipopolysaccharide-binding protein for monitoring of postoperative sepsis: complemental to C-reactive protein or redundant? PLOS ONE. 2011;6(8):e23615.

[74] Deitcher SR, Eisenberg PR. Elevated concentrations of cross-linked fibrin degradation products in plasma: an early marker of Gram-negative bacteremia. Chest. 1993;103(4):1107–1112.

[75] Iba T, Gando S, Murata A, Kushimoto S, Saitoh D, Eguchi Y, et al. Predicting the severity of systemic inflammatory response syndrome (SIRS)-associated coagulopathy with hemostatic molecular markers and vascular endothelial injury markers. Journal of Trauma and Acute Care Surgery. 2007;63(5):1093–1098.

[76] Goebel PJ, Williams JB, Gerhardt RT. A Pilot Study of the Performance Characteristics of the D-dimer in Presumed Sepsis. Western Journal of Emergency Medicine. 2010;11(2):173.

[77] Frances Talaska Fischbach MBD. A Manual of Laboratory and Diagnostic Tests. 8th ed. Philadelphia: Lippincott Williams & Wilkins; 2009.

[78] Rodelo JR, De la Rosa G, Valencia ML, Ospina S, Arango CM, Gómez CI, et al. D-dimer is a significant prognostic factor in patients with suspected infection and sepsis. The American Journal of Emergency Medicine. 2012;30(9):1991–1999.

[79] Endo S, Suzuki Y, Takahashi G, Shozushima T, Ishikura H, Murai A, et al. Presepsin as a powerful monitoring tool for the prognosis and treatment of sepsis: a multicenter prospective study. Journal of Infection and Chemotherapy. 2014;20(1):30–34.

[80] Masson S, Caironi P, Spanuth E, Thomae R, Panigada M, Sangiorgi G, et al. Presepsin (soluble CD14 subtype) and procalcitonin levels for mortality prediction in sepsis: data from the Albumin Italian Outcome Sepsis trial. Critical Care. 2014;18(1):R6.

[81] Popov D, Plyushch M, Ovseenko S, Abramyan M, Podshchekoldina O, Yaroustovsky M. Prognostic value of sCD14-ST (presepsin) in cardiac surgery. Kardiochirurgia i Torakochirurgia Polska= Polish Journal of Cardio-Thoracic Surgery. 2015;12(1):30.

[82] Shozushima T, Takahashi G, Matsumoto N, Kojika M, Okamura Y, Endo S. Usefulness of presepsin (sCD14-ST) measurements as a marker for the diagnosis and severity of sepsis that satisfied diagnostic criteria of systemic inflammatory response syndrome. Journal of Infection and Chemotherapy. 2011;17(6):764–769.

[83] Takeuchi O, Akira S. Pattern recognition receptors and inflammation. Cell. 2010;140(6):805–820.

[84] Bone RC. Sir isaac newton, sepsis, SIRS, and CARS. Critical Care Medicine. 1996;24(7):1125–1128.

[85] Reinhart K, Bauer M, Riedemann NC, Hartog CS. New approaches to sepsis: molecular diagnostics and biomarkers. Clinical Microbiology Reviews. 2012;25(4):609–634.

[86] Chan JK, Roth J, Oppenheim JJ, Tracey KJ, Vogl T, Feldmann M, et al.

Alarmins: awaiting a clinical response. The Journal of Clinical Investigation. 2012;122(8):2711.

[87] Deutschman CS, Tracey KJ. Sepsis: current dogma and new perspectives. Immunity. 2014;40(4):463–475.

[88] Kollef KE, Schramm GE, Wills AR, Reichley RM, Micek ST, Kollef MH. Predictors of 30-day mortality and hospital costs in patients with ventilator-associated pneumonia attributed to potentially antibiotic-resistant gram-negative bacteria. CHEST Journal. 2008;134(2):281–287.

[89] Limaye AP, Kirby KA, Rubenfeld GD, Leisenring WM, Bulger EM, Neff MJ, et al. Cytomegalovirus reactivation in critically ill immunocompetent patients. JAMA. 2008;300(4):413–422.

[90] Otto GP, Sossdorf M, Claus RA, Rödel J, Menge K, Reinhart K, et al. The late phase of sepsis is characterized by an increased microbiological burden and death rate. Critical Care. 2011;15(4):R183.

[91] Moore FA, Moore EE. Evolving concepts in the pathogenesis of postinjury multiple organ failure. Surgical Clinics of North America. 1995;75(2):257–277.

[92] Gentile LF, Cuenca AG, Efron PA, Ang D, McKinley BA, Moldawer LL, et al. Persistent inflammation and immunosuppression: a common syndrome and new horizon for surgical intensive care. The Journal of Trauma and Acute Care Surgery. 2012;72(6):1491.

[93] Morgan MP, Szakmany T, Power SG, Olaniyi P, Hall JE, Rowan K, et al. Sepsis patients with first and second-hit infections show different outcomes depending on the causative organism. Frontiers in Microbiology. 2016;7:207.

[94] Vincent JL, Abraham E. The last 100 years of sepsis. American Journal of Respiratory and Critical Care Medicine. 2006;173(3):256–263.

[95] Sørensen OE, Borregaard N. Neutrophil extracellular traps-the dark side of neutrophils. The Journal of Clinical Investigation. 2016;126(5):1612–1620.

[96] Yipp BG, Kubes P. NETosis: how vital is it? Blood. 2013;122(16):2784–2794.

[97] Czaikoski PG, Mota JMSC, Nascimento DC, Sônego F, Melo PH, Scortegagna GT, et al. Neutrophil extracellular traps induce organ damage during experimental and clinical sepsis. PLOS ONE. 2016;11(2):e0148142.

[98] Opal S, Poll T. Endothelial barrier dysfunction in septic shock. Journal of Internal Medicine. 2015;277(3):277–293.

[99] Darwish I, Liles WC. Emerging therapeutic strategies to prevent infection-related microvascular endothelial activation and dysfunction. Virulence. 2013;4(6):572–582.

[100] Tressel SL, Kaneider NC, Kasuda S, Foley C, Koukos G, Austin K, et al. A matrix metalloprotease-PAR1 system regulates vascular integrity, systemic inflammation and death in sepsis. EMBO Molecular Medicine. 2011;3(7):370–384.

[101] Sanchez T. Sphingosine-1-phosphate signalling in endothelial disorders. Current Atherosclerosis Reports. 2016;18(6):31.

[102] Claushuis TA, van Vught LA, Scicluna BP, Wiewel MA, Klouwenberg PMK, Hoogendijk AJ, et al. Thrombocytopenia is associated with a dysregulated host response in critically ill sepsis patients. Blood. 2016;127(24):3062–3072.

[103] de Stoppelaar SF, van't Veer C, van der Poll T, et al. The role of platelets in sepsis. Thromb Haemost. 2014;112(4):666–677.

[104] Merle NS, Noe R, Halbwachs-Mecarelli L, Fremeaux-Bacchi V, Roumenina LT. Complement system part II: role in immunity. Frontiers in Immunology. 2015;6.

[105] Guo RF, Ward PA. Role of C5a in inflammatory responses. Annu Rev Immunol. 2005;23:821–852.

[106] Shao Z, Nishimura T, Leung L, Morser J. Carboxypeptidase B2 deficiency reveals opposite effects of complement C3a and C5a in a murine polymicrobial sepsis model. Journal of Thrombosis and Haemostasis. 2015;13(6):1090–1102.

[107] Amaral A, Opal SM, Vincent JL. Coagulation in sepsis. Intensive Care Medicine. 2004;30(6):1032–1040.

[108] Nieman MT. Protease-activated receptors in hemostasis. Blood. 2016;128(2):169–177.

[109] Danese S, Vetrano S, Zhang L, Poplis VA, Castellino FJ. The protein C pathway in tissue inflammation and injury: pathogenic role and therapeutic implications. Blood. 2010;115(6):1121–1130.

[110] Warren BL, Eid A, Singer P, Pillay SS, Carl P, Novak I, et al. High-dose antithrombin III in severe sepsis: a randomized controlled trial. JAMA. 2001;286(15):1869–1878.

[111] Bernard GR, Vincent JL, Laterre PF, LaRosa SP, Dhainaut JF, Lopez-Rodriguez A, et al. Efficacy and safety of recombinant human activated protein C for severe sepsis. New England Journal of Medicine. 2001;344(10):699–709.

[112] Abraham E, Reinhart K, Opal S, Demeyer I, Doig C, Rodriguez AL, et al. Efficacy and safety of tifacogin (recombinant tissue factor pathway inhibitor) in severe sepsis: a randomized controlled trial. JAMA. 2003;290(2):238–247.

[113] Boomer JS, To K, Chang KC, Takasu O, Osborne DF, Walton AH, et al. Immunosuppression in patients who die of sepsis and multiple organ failure. JAMA. 2011;306(23):2594–2605.

[114] Hotchkiss RS, Monneret G, Payen D. Sepsis-induced immunosuppression: from cellular dysfunctions to immunotherapy. Nature Reviews Immunology. 2013;13(12):862–874.

[115] Venet F, Pachot A, Debard AL, Bohe J, Bienvenu J, Lepape A, et al. Human CD4+ CD25+ regulatory T lymphocytes inhibit lipopolysaccharide-induced monocyte survival through a Fas/Fas ligand-dependent mechanism. The Journal of Immunology. 2006;177(9):6540–6547.

[116] Scumpia PO, Delano MJ, Kelly-Scumpia KM, Weinstein JS, Wynn JL, Winfield

RD, et al. Treatment with GITR agonistic antibody corrects adaptive immune dysfunction in sepsis. Blood. 2007;110(10):3673–3681.

[117] Pastille E, Didovic S, Brauckmann D, Rani M, Agrawal H, Schade FU, et al. Modulation of dendritic cell differentiation in the bone marrow mediates sustained immunosuppression after polymicrobial sepsis. The Journal of Immunology. 2011;186(2):977–986.

[118] Hotchkiss RS, Tinsley KW, Swanson PE, Grayson MH, Osborne DF, Wagner TH, et al. Depletion of dendritic cells, but not macrophages, in patients with sepsis. The Journal of Immunology. 2002;168(5):2493–2500.

[119] Kapoor G, Saigal S, Elongavan A. Action and resistance mechanisms of antibiotics: A guide for clinicians. Journal of Anaesthesiology, Clinical Pharmacology. 2017;33(3):300.

[120] Duval RE, Grare M, Demoré B. Fight against antimicrobial resistance: We always need new antibacterials but for right bacteria. Molecules. 2019;24(17):3152.

[121] Luther A, Urfer M, Zahn M, Müller M, Wang SY, Mondal M, et al. Chimeric peptidomimetic antibiotics against Gram-negative bacteria. Nature. 2019;576(7787):452–458.

[122] Antibiotics summary [Online monograph]. Kamal S; 2015 [cited 14/11/2017]. Available from: `https://rb.gy/skpfn1`.

[123] The Merck Manual of Diagnosis and Therapy. 19th ed. Whitehouse Station, NJ: Merck & Co and Merck Sharp & Dohme; 2011.

[124] GGC Medicines Adult Therapeutics Handbook [Online reference material]. GGC Medicines; 2017 [cited 15/01/2018]. Available from: `http://handbook.ggcmedicines.org.uk/guidelines/infections/`.

[125] Kadioglu A, Weiser JN, Paton JC, Andrew PW. The role of *Streptococcus pneumoniae* virulence factors in host respiratory colonization and disease. Nature Reviews Microbiology. 2008;6(4):288–301.

[126] Rouphael NG, Stephens DS. *Neisseria meningitidis*: biology, microbiology, and epidemiology. Neisseria meningitidis: Advanced Methods and Protocols. 2012:1–20.

[127] King P. *Haemophilus influenzae* and the lung (Haemophilus and the lung). Clinical and Translational Medicine. 2012;1(1):10.

[128] WHO Director-General's opening remarks at the media briefing on COVID-19 11 March 2020 [Online monograph]. World Health Organisation; 2020 [cited 23/07/2020]. Available from: `https://rb.gy/0blyoy`.

[129] Decaro N. Alphacoronavirus‡. In: Tidona C DG, editor. The Springer Index of Viruses. New York: Springer New York; 2011. p. 371–383.

[130] Decaro N. Betacoronavirus‡. In: Tidona C DG, editor. The Springer Index of Viruses. New York: Springer New York; 2011. p. 385–401.

[131] Boopathi S, Poma AB, Kolandaivel P. Novel 2019 coronavirus structure, mechanism of action, antiviral drug promises and rule out against its treatment. Journal of Biomolecular Structure and Dynamics. 2020;39(9):3409–3418.

[132] Sheleme T, Bekele F, Ayela T. Clinical presentation of patients infected with coronavirus disease 19: a systematic review. Infectious Diseases: Research and Treatment. 2020;13:1178633720952076.

[133] Kakodkar P, Kaka N, Baig M. A comprehensive literature review on the clinical presentation, and management of the pandemic coronavirus disease 2019 (COVID-19). Cureus. 2020;12(4).

[134] Rousan LA, Elobeid E, Karrar M, Khader Y. Chest x-ray findings and temporal lung changes in patients with COVID-19 pneumonia. BMC Pulmonary Medicine. 2020;20(1):1–9.

[135] Leisman DE, Ronner L, Pinotti R, Taylor MD, Sinha P, Calfee CS, et al. Cytokine elevation in severe and critical COVID-19: a rapid systematic review,

meta-analysis, and comparison with other inflammatory syndromes. The Lancet Respiratory Medicine. 2020.

[136] Gustine JN, Jones D. Immunopathology of Hyperinflammation in COVID-19. The American Journal of Pathology. 2020;191(1):4–17.

[137] Sinha P, Matthay MA, Calfee CS. Is a "cytokine storm" relevant to COVID-19? JAMA Internal Medicine. 2020;180(9):1152–1154.

[138] Vinh DB, Zhao X, Kiong KL, Guo T, Jozaghi Y, Yao C, et al. Overview of COVID-19 testing and implications for otolaryngologists. Head & Neck. 2020;42(7):1629–1633.

[139] Two, Three and Four-probe Instrument [Online monograph]. Gamry instruments; 2021 [cited 14/6/21]. Available from: `https://rb.gy/tbpmbt`.

[140] Paunovic M, Schlesinger M. Fundamentals of Electrochemical Deposition. 2nd ed. The ECS Series of Texts and Monographs. New Jersey: John Wiley & Sons; 2006.

[141] Bard AJ, Faulkner LR, Leddy J, Zoski CG. Electrochemical Methods: Fundamentals and Applications. 2nd ed. New York: Wiley; 1980.

[142] Lovrić M. Square-Wave Voltammetry. In: Scholz F, editor. Electroanalytical Methods: Guide to Experiments and Applications. Berlin: Springer Berlin Heidelberg; 2002. p. 111–136.

[143] Adamson AW, Gast AP, et al. Physical Chemistry of Surfaces. 6th ed. New York: Wiley; 1997.

[144] Ulman A. Formation and structure of self-assembled monolayers. Chemical Reviews. 1996;96(4):1533–1554.

[145] Nuzzo RG, Allara DL. Adsorption of bifunctional organic disulfides on gold surfaces. Journal of the American Chemical Society. 1983;105(13):4481–4483.

[146] Bain CD, Troughton EB, Tao YT, Evall J, Whitesides GM, Nuzzo RG. Formation

of monolayer films by the spontaneous assembly of organic thiols from solution onto gold. Journal of the American Chemical Society. 1989;111(1):321–335.

[147] Shimazu K, Yagi I, Sato Y, Uosaki K. In situ and dynamic monitoring of the self-assembling and redox processes of a ferrocenylundecanethiol monolayer by electrochemical quartz crystal microbalance. Langmuir. 1992;8(5):1385–1387.

[148] Peterlinz KA, Georgiadis R. In situ kinetics of self-assembly by surface plasmon resonance spectroscopy. Langmuir. 1996;12(20):4731–4740.

[149] Yang DF, Wilde C, Morin M. Studies of the electrochemical removal and efficient re-formation of a monolayer of hexadecanethiol self-assembled at an Au (111) single crystal in aqueous solutions. Langmuir. 1997;13(2):243–249.

[150] Nuzzo RG, Zegarski BR, Dubois LH. Fundamental studies of the chemisorption of organosulfur compounds on gold (111). Implications for molecular self-assembly on gold surfaces. Journal of the American Chemical Society. 1987;109(3):733–740.

[151] Love JC, Estroff LA, Kriebel JK, Nuzzo RG, Whitesides GM. Self-assembled monolayers of thiolates on metals as a form of nanotechnology. Chemical Reviews. 2005;105(4):1103–1170.

[152] Nishida N, Hara M, Sasabe H, Knoll W. Thermal desorption spectroscopy of alkanethiol self-assembled monolayer on Au (111). Japanese Journal of Applied Physics. 1996;35(11R):5866.

[153] Bürgi T. Properties of the gold–sulphur interface: from self-assembled monolayers to clusters. Nanoscale. 2015;7(38):15553–15567.

[154] Overlayer Structures & Surface Diffraction [Online monograph]. Queen Mary University London; 1996 [cited 27/11/2017]. Available from: `http://www.chem.qmul.ac.uk/surfaces/scc/s6_4g.htm`.

[155] Dubois LH, Nuzzo RG. Synthesis, structure, and properties of model organic surfaces. Annual Review of Physical Chemistry. 1992;43(1):437–463.

[156] Ulman A, Eilers JE, Tillman N. Packing and molecular orientation of alkanethiol monolayers on gold surfaces. Langmuir. 1989;5(5):1147–1152.

[157] Lisdat F, Schäfer D. The use of electrochemical impedance spectroscopy for biosensing. Analytical and Bioanalytical Chemistry. 2008;391(5):1555.

[158] Levicky R, Herne TM, Tarlov MJ, Satija SK. Using self-assembly to control the structure of DNA monolayers on gold: a neutron reflectivity study. Journal of the American Chemical Society. 1998;120(38):9787–9792.

[159] Shen H, Mark JE, Seliskar CJ, Mark Jr HB, Heineman WR. Blocking behavior of self-assembled monolayers on gold electrodes. Journal of Solid State Electrochemistry. 1997;1(2):148–154.

[160] Kafka J, Pänke O, Abendroth B, Lisdat F. A label-free DNA sensor based on impedance spectroscopy. Electrochimica Acta. 2008;53(25):7467–7474.

[161] Corrigan DK, Schulze H, McDermott RA, Schmüser I, Henihan G, Henry JB, et al. Improving electrochemical biosensor performance by understanding the influence of target DNA length on assay sensitivity. Journal of Electroanalytical Chemistry. 2014;732:25–29.

[162] Riedel M, Kartchemnik J, Schöning MJ, Lisdat F. Impedimetric DNA Detection-Steps Forward to Sensorial Application. Analytical Chemistry. 2014;86(15):7867–7874.

[163] Degefa TH, Kwak J. Electrochemical impedance sensing of DNA at PNA self assembled monolayer. Journal of Electroanalytical Chemistry. 2008;612(1):37–41.

[164] Keighley SD, Estrela P, Li P, Migliorato P. Optimization of label-free DNA detection with electrochemical impedance spectroscopy using PNA probes. Biosensors and Bioelectronics. 2008;24(4):906–911.

[165] Macpherson JV, Beeston MA, Unwin PR. Imaging local mass-transfer rates within an impinging jet and studies of fast heterogeneous electron-transfer kinetics using

the microjet electrode. Journal of the Chemical Society, Faraday Transactions. 1995;91(5):899–904.

[166] Heinze J. Ultramicroelectrodes in electrochemistry. Angewandte Chemie International Edition. 1993;32(9):1268–1288.

[167] Boxplot [Online figure]. Stipak B; 2007 [cited 14/04/2020]. Available from: `http://web.pdx.edu/~stipakb/download/PA551/boxplot_files/boxplot4.jpg`.

[168] Miller J, Miller JC. Statistics and Chemometrics for Analytical Chemistry. 6th ed. Harlow, United Kingdom: Pearson Education; 2010.

[169] Pletcher D. A First Course in Electrode Processes. 2nd ed. Cambridge, UK: RSCPublishing; 2009.

[170] Compton RG, Banks CE. Understanding Voltammetry. 3rd ed. London, UK: World Scientific Publising Europe Ltd; 2018.

[171] Gladysz JA, Curran DP, Horváth IT. Handbook of Fluorous Chemistry. Weinheim, Germany: WILEY-VCH Verlag GmBH & Co. KGaA; 2004.

[172] Cametti M, Crousse B, Metrangolo P, Milani R, Resnati G. The fluorous effect in biomolecular applications. Chemical Society Reviews. 2012;41(1):31–42.

[173] Fischer LM, Tenje M, Heiskanen AR, Masuda N, Castillo J, Bentien A, et al. Gold cleaning methods for electrochemical detection applications. Microelectronic Engineering. 2009;86(4-6):1282–1285.

[174] Daniele S, Bragato C. From macroelectrodes to microelectrodes: Theory and electrode properties. In: Environmental analysis by electrochemical sensors and biosensors. Springer; 2014. p. 373–401.

[175] Konopka S, McDuffie B. Diffusion coefficients of ferri-and ferrocyanide ions in aqueous media, using twin-electrode thin-layer electrochemistry. Analytical Chemistry. 1970;42(14):1741–1746.

[176] García-Miranda Ferrari A, Foster CW, Kelly PJ, Brownson DA, Banks CE. De-

termination of the electrochemical area of screen-printed electrochemical sensing platforms. Biosensors. 2018;8(2):53.

[177] Cox JT, Guerrette JP, Zhang B. Steady-state voltammetry of a microelectrode in a closed bipolar cell. Analytical Chemistry. 2012;84(20):8797–8804.

[178] Petrovic S. Cyclic voltammetry of hexachloroiridate (IV): an alternative to the electrochemical study of the ferricyanide ion. The Chemical Educator. 2000;5(5):231–235.

[179] Vogt S, Su Q, Gutièrrez-Sànchez C, Nöll G. Critical view on electrochemical impedance spectroscopy using the ferri/ferrocyanide redox couple at gold electrodes. Analytical Chemistry. 2016;88(8):4383–4390.

[180] Standard Operating Procedures for Cyclic Voltammetry [Online monograph]. Graham D; 2020 [cited 23/03/2020]. Available from: `https://sop4cv.com/index.html`.

[181] Cancino J, Machado SA. Microelectrode array in mixed alkanethiol self-assembled monolayers: Electrochemical studies. Electrochimica Acta. 2012;72:108–113.

[182] Mendes R, Carvalhal R, Kubota L. Effects of different self-assembled monolayers on enzyme immobilization procedures in peroxidase-based biosensor development. Journal of Electroanalytical Chemistry. 2008;612(2):164–172.

[183] Campuzano S, Pedrero M, Montemayor C, Fatás E, Pingarrón JM. Characterization of alkanethiol-self-assembled monolayers-modified gold electrodes by electrochemical impedance spectroscopy. Journal of Electroanalytical Chemistry. 2006;586(1):112–121.

[184] Štulík K, Amatore C, Holub K, Mareček V, Kutner W. Microelectrodes. Definitions, characterization, and applications. Pure Appl Chem. 2000;72(8):1483–1492.

[185] Sheffer M, Vivier V, Mandler D. Self-assembled monolayers on Au microelectrodes. Electrochemistry Communications. 2007;9(12):2827–2832.

[186] Flynn GE, Withers JM, Macias G, Sperling JR, Henry SL, Cooper JM, et al.

Reversible DNA micro-patterning using the fluorous effect. Chemical Communications. 2017;53(21):3094–3097.

[187] Xu Y, Jiang Y, Cai H, He PG, Fang YZ. Electrochemical impedance detection of DNA hybridization based on the formation of M-DNA on polypyrrole/carbon nanotube modified electrode. Analytica Chimica Acta. 2004;516(1-2):19–27.

[188] Ito T, Hosokawa K, Maeda M. Detection of single-base mismatch at distal end of DNA duplex by electrochemical impedance spectroscopy. Biosensors and Bioelectronics. 2007;22(8):1816–1819.

[189] Keighley SD, Li P, Estrela P, Migliorato P. Optimization of DNA immobilization on gold electrodes for label-free detection by electrochemical impedance spectroscopy. Biosensors and Bioelectronics. 2008;23(8):1291–1297.

[190] Sheffer M, Vivier V, Mandler D. Self-assembled monolayers on Au microelectrodes. Electrochemistry Communications. 2007;9(12):2827–2832.

[191] Jacobs M, Muthukumar S, Selvam AP, Craven JE, Prasad S. Ultra-sensitive electrical immunoassay biosensors using nanotextured zinc oxide thin films on printed circuit board platforms. Biosensors and Bioelectronics. 2014;55:7–13.

[192] Jolly P, Rainbow J, Regoutz A, Estrela P, Moschou D. A PNA-based Lab-on-PCB diagnostic platform for rapid and high sensitivity DNA quantification. Biosensors and Bioelectronics. 2019;123:244–250.

[193] Dutta G, Jallow AA, Paul D, Moschou D. Label-Free Electrochemical Detection of *S. mutans* Exploiting Commercially Fabricated Printed Circuit Board Sensing Electrodes. Micromachines. 2019;10(9):575.

[194] Moschou D. Lab-on-a-PCB. Nexus Media Communications Ltd.; 2016Jun;122(1962).

[195] Jobst G, Moser I, Svasek P, Varahram M, Trajanoski Z, Wach P, et al. Mass producible miniaturized flow through a device with a biosensor array. Sensors and Actuators B: Chemical. 1997;43(1-3):121–125.

[196] Bhavsar K, Fairchild A, Alonas E, Bishop DK, La Belle JT, Sweeney J, et al. A cytokine immunosensor for Multiple Sclerosis detection based upon label-free electrochemical impedance spectroscopy using electroplated printed circuit board electrodes. Biosensors and Bioelectronics. 2009;25(2):506–509.

[197] Elgrishi N, Rountree KJ, McCarthy BD, Rountree ES, Eisenhart TT, Dempsey JL. A practical beginner's guide to cyclic voltammetry. Journal of Chemical Education. 2017;95(2):197–206.

[198] Klotz D. Negative capacitance or inductive loop?–A general assessment of a common low frequency impedance feature. Electrochemistry Communications. 2019;98:58–62.

[199] Park S, Kang SW, Kim K. Competition between ionic adsorption and desorption on electrochemical double layer capacitor electrodes in acetonitrile solutions at different currents and temperatures. Journal of Power Sources. 2017;372:8–15.

[200] Muhammad RD, Oza-Frank R, Zell E, Link-Gelles R, Narayan KV, Schaffner W, et al. Epidemiology of invasive pneumococcal disease among high-risk adults since the introduction of pneumococcal conjugate vaccine for children. Clinical Infectious Diseases. 2013;56(5):e59–e67.

[201] Drijkoningen J, Rohde G. Pneumococcal infection in adults: burden of disease. Clinical Microbiology and Infection. 2014;20:45–51.

[202] Li Y, Weinberger DM, Thompson CM, Trzciński K, Lipsitch M. Surface charge of *Streptococcus pneumoniae* predicts serotype distribution. Infection and Immunity. 2013;81(12):4519–4524.

[203] Dockrell DH, Whyte MK, Mitchell TJ. Pneumococcal pneumonia: mechanisms of infection and resolution. Chest. 2012;142(2):482–491.

[204] Chavanet P. Pneumococcus infections: is the burden still as heavy? Médecine et Maladies Infectieuses. 2012;42(4):149–153.

[205] Pneumococcal Urinary Antigen Testing (UAT) [Online monograph]. Tankesh-

war A; 2017 [cited 10/06/2021]. Available from: https://microbeonline.com/pneumococcal-urinary-antigen-testing-uat-principle-procedure-results/.

[206] West DM, McCauley LM, Sorensen JS, Jephson AR, Dean NC. Pneumococcal urinary antigen test use in diagnosis and treatment of pneumonia in seven Utah hospitals. ERJ Open Research. 2016;2(4).

[207] Kim B, Kim J, Jo YH, Lee JH, Hwang JE, Park MJ, et al. Prognostic value of pneumococcal urinary antigen test in community-acquired pneumonia. PLOS ONE. 2018;13(7):e0200620.

[208] Gutiérrez F, Mar M, Rodríguez JC, Ayelo A, Soldán B, Cebrián L, et al. Evaluation of the immunochromatographic Binax NOW assay for detection of *Streptococcus pneumoniae* urinary antigen in a prospective study of community-acquired pneumonia in Spain. Clinical Infectious Diseases. 2003;36(3):286–292.

[209] Lucarelli F, Tombelli S, Minunni M, Marrazza G, Mascini M. Electrochemical and piezoelectric DNA biosensors for hybridisation detection. Analytica Chimica Acta. 2008;609(2):139–159.

[210] Drummond TG, Hill MG, Barton JK. Electrochemical DNA sensors. Nature Biotechnology. 2003;21(10):1192–1199.

[211] Obregón V, García P, García E, Fenoll A, López R, García JL. Molecular peculiarities of the *lytA* gene isolated from clinical pneumococcal strains that are bile insoluble. Journal of Clinical Microbiology. 2002;40(7):2545–2554.

[212] Llull D, López R, García E. Characteristic signatures of the *lytA* gene provide a basis for rapid and reliable diagnosis of Streptococcus pneumoniae infections. Journal of Clinical Microbiology. 2006;44(4):1250–1256.

[213] Campuzano S, Pedrero M, García JL, García E, García P, Pingarrón JM. Development of amperometric magnetogenosensors coupled to asymmetric PCR for the specific detection of *Streptococcus pneumoniae*. Analytical and Bioanalytical Chemistry. 2011;399(7):2413–2420.

[214] Woodford N, Carattoli A, Karisik E, Underwood A, Ellington MJ, Livermore DM. Complete nucleotide sequences of plasmids pEK204, pEK499, and pEK516, encoding CTX-M enzymes in three major *Escherichia coli* lineages from the United Kingdom, all belonging to the international O25: H4-ST131 clone. Antimicrobial Agents and Chemotherapy. 2009;53(10):4472–4482.

[215] Jolly P, Rainbow J, Regoutz A, Estrela P, Moschou D. A PNA-based Lab-on-PCB diagnostic platform for rapid and high sensitivity DNA quantification. Biosensors and Bioelectronics. 2019;123:244–250.

[216] Wang J, Leong MC, Leong EZW, Kuan WS, Leong DT. Clinically relevant detection of *Streptococcus pneumoniae* with DNA-antibody nanostructures. Analytical Chemistry. 2017;89(12):6900–6906.

[217] Ferreira FP, Honorato-Castro AC, da Silva JV, Orellana SC, Oliveira GC, Madurro JM, et al. A novel polymer-based genosensor for the detection and quantification of *Streptococcus pneumoniae* in genomic DNA sample. Polymer Engineering & Science. 2018;58(8):1308–1314.

[218] Li F, Yu Z, Xu Y, Ma H, Zhang G, Song Y, et al. Using the synergism strategy for highly sensitive and specific electrochemical sensing of *Streptococcus pneumoniae* Lyt-1 gene sequence. Analytica Chimica Acta. 2015;886:175–181.

[219] Wang H, Ma Z, Qin J, Shen Z, Liu Q, Chen X, et al. A versatile loop-mediated isothermal amplification microchip platform for *Streptococcus pneumoniae* and *Mycoplasma pneumoniae* testing at the point of care. Biosensors and Bioelectronics. 2019;126:373–380.

[220] Kelley SO. What are clinically relevant levels of cellular and biomolecular analytes? ACS Sensors. 2017;2(2):193–197.

[221] Keighley SD, Estrela P, Li P, Migliorato P. Optimization of label-free DNA detection with electrochemical impedance spectroscopy using PNA probes. Biosensors and Bioelectronics. 2008;24(4):906–911.

[222] Novel Coronavirus – China [Online monograph]. World Health Organisation; 2020 [cited 23/07/2020]. Available from: https://www.who.int/csr/don/12-january-2020-novel-coronavirus-china/en/.

[223] Does COVID-19 Cause Sepsis? [Online monograph]. Boncyk CS, Mart MF, Ely WE; 2020 [cited 23/07/2020]. Available from: https://www.medscape.com/viewarticle/939038#vp_3.

[224] Lin HY. The severe COVID-19: A sepsis induced by viral infection? And its immunomodulatory therapy. Chinese Journal of Traumatology. 2020;23(4):190–195.

[225] Paul S. The molecular biology of coronavirus. Adv Virus Res. 2006;66(48):193–292.

[226] Lan J, Ge J, Yu J, Shan S, Zhou H, Fan S, et al. Structure of the SARS-CoV-2 spike receptor-binding domain bound to the ACE2 receptor. Nature. 2020;581(7807):215–220.

[227] Warner F, Smith A, Hooper N, Turner A. What's new in the renin-angiotensin system? Cellular and Molecular Life Sciences CMLS. 2004;61(21):2704–2713.

[228] Xu D, Su Y, Zhao L, Meng F, Liu C, Guan Y, et al. Antibacterial and antifouling properties of a polyurethane surface modified with perfluoroalkyl and silver nanoparticles. Journal of Biomedical Materials Research Part A. 2017;105(2):531–538.

[229] Vezza VJ, Butterworth A, Lasserre P, Blair EO, MacDonald A, Hannah S, et al. An electrochemical SARS-CoV-2 biosensor inspired by glucose test strip manufacturing processes. Chemical Communications. 2021;57(30):3704–3707.

[230] Wu C, Chen X, Cai Y, Xia J, Zhou X, Xu S, et al. Risk Factors Associated With Acute Respiratory Distress Syndrome and Death in Patients With Coronavirus Disease 2019 Pneumonia in Wuhan, China. JAMA Internal Medicine. 2020;180(7):934–943.

[231] Coomes EA, Haghbayan H. Interleukin-6 in COVID-19: a systematic review and meta-analysis. Reviews in medical virology. 2020;30(6):1–9.

[232] Ruan Q, Yang K, Wang W, Jiang L, Song J. Clinical predictors of mortality due to COVID-19 based on an analysis of data of 150 patients from Wuhan, China. Intensive Care Medicine. 2020;46(5):846–848.

[233] Hashemi SA, Behbahan NGG, Bahrani S, Mousavi SM, Gholami A, Ramakrishna S, et al. Ultra-sensitive viral glycoprotein detection NanoSystem toward accurate tracing SARS-CoV-2 in biological/non-biological media. Biosensors and Bioelectronics. 2021;171:112731.

[234] Raziq A, Kidakova A, Boroznjak R, Reut J, Öpik A, Syritski V. Development of a portable MIP-based electrochemical sensor for detection of SARS-CoV-2 antigen. Biosensors and Bioelectronics. 2021;178:113029.

[235] Grant BD, Anderson CE, Williford JR, Alonzo LF, Glukhova VA, Boyle DS, et al. SARS-CoV-2 coronavirus nucleocapsid antigen-detecting half-strip lateral flow assay toward the development of point of care tests using commercially available reagents. Analytical Chemistry. 2020;92(16):11305–11309.

[236] Zhang Y, Odiwuor N, Xiong J, Sun L, Nyaruaba RO, Wei H, et al. Rapid molecular detection of SARS-CoV-2 (COVID-19) virus RNA using colorimetric LAMP. MedRxiv. 2020.

[237] Wölfel R, Corman VM, Guggemos W, Seilmaier M, Zange S, Müller MA, et al. Virological assessment of hospitalized patients with COVID-2019. Nature. 2020;581(7809):465–469.

[238] Fabiani L, Saroglia M, Galatà G, De Santis R, Fillo S, Luca V, et al. Magnetic beads combined with carbon black-based screen-printed electrodes for COVID-19: A reliable and miniaturized electrochemical immunosensor for SARS-CoV-2 detection in saliva. Biosensors and Bioelectronics. 2021;171:112686.

[239] Zhao H, Liu F, Xie W, Zhou TC, OuYang J, Jin L, et al. Ultrasensitive

supersandwich-type electrochemical sensor for SARS-CoV-2 from the infected COVID-19 patients using a smartphone. Sensors and Actuators B: Chemical. 2021;327:128899.

[240] Seo G, Lee G, Kim MJ, Baek SH, Choi M, Ku KB, et al. Rapid detection of COVID-19 causative virus (SARS-CoV-2) in human nasopharyngeal swab specimens using field-effect transistor-based biosensor. ACS Nano. 2020;14(4):5135–5142.

[241] Deeks JJ, Raffle AE. Lateral flow tests cannot rule out SARS-CoV-2 infection. BMJ. 2020;371. Available from: `https://www.bmj.com/content/371/bmj.m4787`.

[242] Love JC, Estroff LA, Kriebel JK, Nuzzo RG, Whitesides GM. Self-assembled monolayers of thiolates on metals as a form of nanotechnology. Chemical Reviews. 2005;105(4):1103–1170.

[243] Blood glucose testing strips [Online monograph]. NICE; 2017 [cited 10/02/2021]. Available from: `https://rb.gy/nftmgg`.